Symmetric Nonaqueous Flow Batteries with Porous Separators



Kirk Smith

University of Oxford

A thesis submitted for the degree of

Doctor of Philosophy

October 2021

This thesis is dedicated to the late

Simon Robert Greiner

Olga Sarar Smith

&

Kenneth Edward Smith

"Darkness is for putting the tools away." —KES

Acknowledgements

Many friends, mentors, and family members have led me in various ways to this doctoral effort and carried me through it. The whole process has been quite unpredictable, and I never would have imagined my midwestern self in this position studying electrochemical engineering in England watching the UK stumble through Brexit right before a global pandemic hits. I would like to thank all my track and cross country coaches and teammates I've had through the years for instilling in me the endurance to push through repeated failures. For my development as a scientist, I owe my professors from the University of Tulsa as well as my advisors and labmates from all the previous research groups I was in however briefly. For my professed ethics of labor, inquiry, and service, I owe my entire extended family, particularly my sister, parents, and grandparents.

I am a much improved researcher thanks to the autonomy and critical insights bestowed upon me by Professor Monroe, for which I'm grateful. I believe I now approach problems more confidently, analytically, and with more rigor than ever before thanks to his advice and high standards for quality. Thanks to former group member Dr. James Saraidaridis for staying around to show me the ropes upon my arrival to the UK; I would have not accomplished anything close to what I eventually did without this transfer of knowledge and skill. A massive thanks to my experimental labmates Andrew Wang and Dr. Howie Chu, who listened to my various rants for years, gave feedback on countless failed hypotheses and a few correct ones, and helped me change many argon cylinders. I also owe much to past and present students Dr. Tianhong Hou, Dr. Priyamvada Goyal, Taeho Jung, and Alexander Van-Brunt, as well as Professor David Howey, his group, and its alumni.

I'd also like to thank anyone who listened to me complain about how my research wasn't working (there are too many of you to list—but Liam and Claudia probably heard the most), and anyone who ever helped prepare a meal for me while I was completing this effort. Special thanks to the extended Viking Forest crew who lodged me in Cumbria (the best county) during the early months of the pandemic while the university was closed.

The final months of thesis writing were particularly difficult because of unforeseen events. During that time I relied heavily on my family, and also my partner Anne Coleman—whose love and support I'm extremely grateful for.

Abstract

Symmetric flow batteries use a single electrolyte formulation instead of the usual two and offer simplified manufacture and operation, the possibility to use low-cost porous separators in place of ion-exchange membranes, and elimination of certain failure modes. Furthermore, using nonaqueous solvents in lieu of water enables exploration of redox species that support cell potentials beyond the electrochemical window of aqueous electrolytes. This thesis aims to assist in minimizing the levelized cost of storage for symmetric nonaqueous flow batteries through informed electrolyte development, materials selection, and device operation.

Illustrating the large design space of flow battery electrolytes permits the definition of "symmetric" for the present application. A zero-dimensional model for flow batteries with porous separators is developed which incorporates self-discharge behavior. Coupling this model to technoeconomic equations reveals the basic tradeoffs inherent to using porous separators along with two promising active species approaches for symmetric flow battery electrolytes: salts of coordinated transition metal-ligand complexes and synthetically simple, soluble aromatic compounds used in a mixed electrolyte configuration. The technoeconomic analysis explores membrane cost/performance tradeoffs pertinent to symmetric systems using porous separators.

Successfully implementing symmetric electrolytes of any composition requires original approaches to measurement and control of transport phenomena in the membrane due to shifts in relative contribution of different driving forces for crossover and self-discharge *vs.* traditional flow batteries. Real-time estimation techniques and reservoir balancing methods are developed to measure and control these convoluted phenomena. Common perceived failure modes of benchtop flow batteries and methods to deconvolute capacity fade mechanisms are discussed.

The established nonaqueous redox-active species vanadium acetylacetonate is used as a representative compound to demonstrate that, counter to current literature, the primary failure mode of nonaqueous flow batteries is confined to resistance growth in the separator and not electrolyte or electrode degradation. Methods to further understand and mitigate this failure mode are discussed, and solubilities of cosolvent systems are explored to improve energy density. Iron bipyridine salts are revisited and found to succeed in symmetric flow battery operation subject to separator degradation constraints, prompting the study of more affordable counteranions.

Contents

List of Figures **vii**

List of Acronyms **xiii**

1 Symmetric RFBs: Fundamentals, Model, & Technoeconomics **1**

1.1 Traditional RFB Construction 2
1.2 Taxonomy of Flow Batteries 6
1.3 Focus on Symmetric Systems 11
1.3.1 Disproportionation 12
1.3.2 Mixed Electrolytes 13
1.4 Motivation for Porous Separators 15
1.5 Model for Porous-Separator RFBs 17
1.5.1 Derivation 18
1.5.2 Behavior 24
1.6 Technoeconomics 35
1.6.1 Capital Expenditure 36
1.6.2 Levelized Cost of Storage 44
1.6.3 Technoeconomics of Porous Separator RFBs 46
1.7 Thesis Objectives & Structure 52

2 Measurement & Control for RFBs with Porous Separators **55**

2.1 Introduction 55
2.2 Real-time Measurement of Self-Discharge 56
2.2.1 Materials & Methods 58
2.2.2 Results 59
2.3 Reservoir-Volume Control System 61
2.3.1 Materials & Methods 62
2.3.2 Results 66
2.4 General Cell Design Developments 72
2.5 Conclusion 75

3 $V(acac)_3$ Development & Separator Fouling **77**
3.1 Introduction . . . 77
3.1.1 Context . . . 78
3.2 Solvent Manipulation for Energy Density . . . 79
3.2.1 Solubility & Conductivity Results . . . 84
3.2.2 Cycling Results . . . 90
3.3 Degradation in $V(acac)_3$ systems . . . 93
3.3.1 Effect of Anion Substitution . . . 97
3.3.2 Effect of $V(acac)_3$ Recrystallization . . . 100
3.3.3 Effect of Different Separator Materials . . . 102
3.3.4 Effect of Porous Electrode Replacement . . . 104
3.3.5 Double Reference Electrode Experiments . . . 107
3.3.6 Discussion . . . 124
3.3.7 Approaches to Deconvolute Degradation Phenomena . . . 128
3.4 Conclusion . . . 131

4 Iron-Based Electrolytes **132**
4.1 Introduction . . . 132
4.2 Synthesis . . . 135
4.3 Voltammetry . . . 137
4.4 Solubility . . . 143
4.5 Cycling . . . 144
4.5.1 HVC Cutoff, Celgard 4560 . . . 144
4.5.2 Double RE Celgard 4560 . . . 146
4.5.3 Long-term Cycling with Replaceable Cellulose Separators . . . 150
4.6 Fouling Observations and Discussion . . . 159
4.7 Conclusion . . . 161

5 Conclusion **162**

Appendices

A Flow Cell and Hermetically Sealed Reservoir Drawings **167**

B Publications and Presentations Given **172**

References **174**

List of Figures

1.1 RFBs compared to other electrochemical devices in terms of reversibility and configuration (adapted from [1]) . . . 3
1.2 A traditional RFB unit cell . . . 4
1.3 A traditional RFB stack with three unit cells . . . 5
1.4 Classification of flow batteries by half-cell configuration . . . 7
1.5 Electrochemical stability windows of aqueous and nonaqueous solvents *vs.* saturated calomel electrode from [27] . . . 10
1.6 A disproportionation flow battery . . . 13
1.7 A conventional asymmetric flow battery on the left and on the right, a symmetric flow battery using a mixed electrolyte . . . 14
1.8 Schematic for model of porous separator flow battery self-discharge showing applied and self-discharge currents (not to scale) . . . 19
1.9 Schematic for model of porous separator flow battery self-discharge showing carbon felt porosity ϕ, cell thickness t_{cell}, and cell geometric area A_{cell} (not to scale) . . . 20
1.10 Polarization experimental datapoints and best-fit curve for 0.1 M vanadium acetylacetonate ($V(acac)_3$) flow cell showing no apparent kinetic limitations in the low-current-density region with untreated carbon felt electrodes, using the experimental methods of Saraidaridis and Monroe [69] . . . 25
1.11 Representative charge-discharge simulation for a standard $V(acac)_3$ benchtop experiment . . . 26
1.12 Model charge/discharge curves as applied current density varies . . . 29
1.13 Model efficiencies as applied current density varies . . . 30
1.14 Model charge/discharge curves as self-discharge current density varies with fixed applied current density of $40\,\text{mA}\,\text{cm}^{-2}$ . . . 31
1.15 Model charge/discharge curves as self-discharge current density varies with fixed applied current density of $40\,\text{mA}\,\text{cm}^{-2}$ . . . 32
1.16 Model charge/discharge curves as ASR varies . . . 32
1.17 Model efficiencies as ASR varies . . . 33
1.18 Model charge/discharge curves as flowrate varies . . . 34
1.19 Model efficiencies as flowrate varies . . . 34

1.20 Capital cost of representative flow battery architectures based on (a)symmetry, salt configuration (salt-splitting, rocking chair), and mixed electrolyte/disproportionation configuration 43
1.21 Simulated charge/discharge curve for a hypothetical 1 MW, 100 MWh flow battery 47
1.22 Capital and levelized costs of a porous separator flow battery *vs.* nominal cell potential 48
1.23 Capital and levelized costs of a porous separator flow battery *vs.* real discharge duration 49
1.24 Capital and levelized costs of a porous separator flow battery *vs.* applied current density 50
1.25 Capital and levelized costs of a porous separator flow battery *vs.* self-discharge current density 51
1.26 Hypothetical cost-performance relationship across the spectrum of expensive, selective IEMs to cheap, high-self-discharge porous separators 52
1.27 Capital and levelized costs of a porous separator flow battery *vs.* self-discharge current density using the cost-performance relationship from Fig. 1.26 53

2.1 Voltage and estimated state-of-charge (SOC) of cell undergoing self-discharge 59
2.2 Self-discharge flux and current density for a three hour period of self-discharge estimated by the adaptive observer 60
2.3 Overview of experimental setup for active balancing of electrolyte volumes in flow battery reservoirs. Pictures of **a)** the experimental setup and **b)** the level sensing image processing script during a flow battery experiment. 62
2.4 Cycle efficiencies and discharge energy capacities plotted simultaneously with imbalance and PID pump speed output control signal. . 67
2.5 Voltage profiles of charge-discharge cycles during active balancing. A 10 second open-circuit hold is performed between charge and discharge steps. 68
2.6 Intracycle imbalance and individual reservoir volumes during a stable, balanced period of cycling. Each reservoir had 5 mL of electrolyte initially. 69
2.7 Image-based mechanical balancing of multiple flow cells and reservoirs simultaneously with one camera 72
2.8 Camera feed of setup in Fig. 2.7 showing the virtual sight tubes and level measurement 73
2.9 Exploded view of the cell used in this thesis 75

2.10 Experimental flow cell running in glovebox 76

3.1 Plot of densitometry results showing variation in density with mass fraction of $V(acac)_3$ for pure ACN at 20°C, recorded by Luke Petit 85
3.2 Variation in solubility limit of $V(acac)_3$ in ACN/DO solvent mixture with increasing mole fraction of DO. (blue) theoretical relationship (red) experimental data 87
3.3 Plot showing variation in density of the ACN/DO solvent mixture with increasing mole fraction of 1,3-dioxolane (1,3-DO) for (dark blue) no $V(acac)_3$ (light blue) 0.1 M $V(acac)_3$ (red) 0.7 M $V(acac)_3$, recorded by Luke Petit 88
3.4 Cyclic voltammogram of (red) 0.5 M $TEABF_4$ in ACN with 0.1 M $V(acac)_3$ active species (blue) 0.4 M $TEABF_4$ in 0.3 ACN 0.7 DO by mole fraction with 0.1 M $V(acac)_3$ active species, glassy carbon working electrode, silver/silver nitrate reference, scan rate 400 mVs^{-1}, 25°C, recorded by Luke Petit 89
3.5 Experimental setup of a test cell running without reservoirs in order to minimize solvent evaporation, and because the peristaltic pump tubing occupied sufficient electrolyte volume to facilitate testing . . 91
3.6 Charge/discharge profiles of high concentration $V(acac)_3$ experiment run with peristaltic pumps and no reservoirs 92
3.7 Efficiencies of cycles presented in 3.6 92
3.8 Charge/discharge profiles of a representative $V(acac)_3$ system with tetraethylammonium tetrafluoroborate ($TEABF_4$) support undergoing fouling with a constant voltage cutoff of 2.5 V 96
3.9 Efficiencies of the charge/discharge cycles presented in Fig. 3.8 . . . 97
3.10 Cyclic voltammograms of $V(acac)_3$ with either $TEABF_4$ or tetraethylammonium perchlorate ($TEAClO_4$) supporting electrolyte in acetonitrile (ACN) over their entire electrochemical stability windows, GC WE, Pt CE, Ag/Ag^+ RE, scan rate 400 $mV\,s^{-1}$ 98
3.11 Charge/discharge profiles of a representative $V(acac)_3$ system with $TEAClO_4$ support undergoing fouling with a constant voltage cutoff of 2.5 V 99
3.12 Efficiencies of the charge/discharge cycles presented in Fig. 3.11 . . 99
3.13 Charge/discharge profiles of a flow cell with $V(acac)_3$ purified by recrystallization 101
3.14 Efficiencies of the charge/discharge cycles presented in Fig. 3.13 . . 102
3.15 Charge/discharge profiles of a $V(acac)_3$ flow cell with an Anodisc alumina separator 103

3.16 Efficiencies of the charge/discharge cycles for a $V(acac)_3$ cell with an Anodisc alumina separator presented in Fig. 3.15 103
3.17 Charge/discharge profiles of a $V(acac)_3$ flow cell with a cellulose Dreamweaver Silver 20 separator 104
3.18 Efficiencies of the charge/discharge cycles of a $V(acac)_3$ flow cell with a cellulose Dreamweaver Silver 20 separator presented in Fig. 3.17 . 105
3.19 Charge/discharge profiles of a degraded $V(acac)_3$ flow cell immediately before (black) and immediately after (red) undergoing an electrode swap 106
3.20 Efficiencies of the charge/discharge cycles on either side of and including those presented in Fig. 3.19. Electrode replacement occurs after cycle 40. 106
3.21 Schematic showing double reference electrode setup in a flow battery, with one reference electrode in each reservoir 108
3.22 Double reference separator fouling experiment with $V(acac)_3$ and Celgard 4560, with OCP hold and diode test in between half-cycles. Red lines show the positive and negative half-cell potentials, which all lie on top of each other. 110
3.23 Efficiencies of Celgard 4560 separator fouling experiment from Fig. 3.22 111
3.24 Bode plot of impedance spectra from Celgard 4560, $V(acac)_3$ separator fouling experiment 111
3.25 Nyquist plot of impedance spectra from Celgard 4560, $V(acac)_3$ separator fouling experiment 112
3.26 Current-voltage relationship of ionic diode membrane fouling signature for $V(acac)_3$ flow cell with Celgard 4560 113
3.27 Double reference separator fouling experiment with $V(acac)_3$ and Anodisc alumina separator, with OCP hold and diode test in between half-cycles. Red lines show the positive and negative half-cell potentials, which all lie on top of each other. 114
3.28 Efficiencies of alumina separator fouling experiment from Fig. 3.27 . 115
3.29 Bode plot of impedance spectra from alumina, $V(acac)_3$ separator fouling experiment 115
3.30 Nyquist plot of impedance spectra from alumina, $V(acac)_3$ separator fouling experiment 116
3.31 Close-up Nyquist plot of first 250 cycles of impedance spectra from alumina, $V(acac)_3$ separator fouling experiment 116
3.32 Current-voltage relationship of $V(acac)_3$ flow cell with alumina separator, showing absence of ionic diode effect seen with Celgard in Fig. 3.26 118

3.33 Anodisc alumina separators used in $V(acac)_3$ double reference electrode separator fouling experiment. Left separator faced negative electrode, right separator faced positive electrode. Separators were rinsed thoroughly with neat ACN before photo was taken. 119
3.34 Full and half-cell (red) potentials of a $V(acac)_3$ flow battery held at 2.3 V for half-hour steps with a diode test 120
3.35 Closer look at the diode test portion of 3.34 121
3.36 Bode plots of the impedance spectra from the 2.3 V hold degradation experiment 121
3.37 Nyquist plots of the impedance spectra from the 2.3 V hold degradation experiment 122
3.38 Reservoir levels and applied pump duty cycle over the course of the 2.3 V hold degradation experiment 122
3.39 Proposed mechanism of porous separator fouling in RFBs resulting in increased coulombic and decreased voltaic efficiencies over time . 125

4.1 Voltammetry of iron (II) triflate in ACN in black, showing irreversible Fe^{2+}/Fe^{3+} couple and Fe^{2+}/Fe^{0} plating stripping in black, and in red, after ligation by 2,2'–bipyridine (bpy), enabling (quasi)reversible Fe^{2+}/Fe^{3+} and absence of plating/stripping negative couple. $400\,mV\,s^{-1}$, GC WE, Pt CE, Ag/Ag^{+} RE. 137
4.2 Cyclic voltammetry of iron (II) tris(2,2'–bipyridine) ($[Fe(bpy)_3]^{2+}$) triflate in ACN with various cutoffs, showing sequential ligated bpy reductions. $100\,mV\,s^{-1}$, GC WE, Pt CE, Ag/Ag^{+} RE. 139
4.3 Differential pulse voltammetry of $[Fe(bpy)_3]^{2+}$ triflate in ACN showing the iron II/III positive couple, as well as all sequential ligated bpy reductions to their radical anions, and possibly dianions. $400\,mV\,s^{-1}$, GC WE, Pt CE, Ag/Ag^{+} RE. Scan from +1 to –3 V *vs.* Ag/Ag^{+} . 141
4.4 A comparison of $V(acac)_3$ and $[Fe(bpy)_3]^{2+}$ in ACN, $100\,mV\,s^{-1}$, GC WE, Pt CE, Ag/Ag^{+} RE. 142
4.5 A comparison of $V(acac)_3$ and $[Fe(bpy)_3]^{2+}$ in ACN with a ferrocene reference couple at scanrates of 25, 50, 75, 100, 200, 300, 400, and 500 $mV\,s^{-1}$, GC WE, Pt CE, Ag/Ag^{+} RE. 142
4.6 109 charge/discharge profiles of 0.1 M iron (II) tris(2,2'–bipyridine) triflate ($[Fe(bpy)_3]^{2+}(CF_3SO_3)_2$) in ACN without supporting electrolyte. $20\,mA\,cm^{-2}$, 2.6 V cutoff 145
4.7 Charge/discharge efficiencies of Fig. 4.6 145
4.8 Bode plots of EIS scans taken every 10 cycles during experiment of Fig. 4.6 146

4.9 Nyquist plots of EIS scans taken every 10 cycles during experiment of Fig. 4.6. Noise in the low-frequency response appears in the final cycles, with a heavily fouled separator, indicating the EIS settings are likely no longer suitable for the system. 147
4.10 Over 50 charge/discharge profiles of 0.1 M $[Fe(bpy)_3]^{2+}(CF_3SO_3)_2$ in ACN without supporting electrolyte. 20 mA cm^{-2} to 25% theoretical SOC, open-circuit hold between cycles 148
4.11 Charge/discharge efficiencies of Fig. 4.10 148
4.12 Half-cell data from Fig. 4.10 showing constant and repeatable Nernstian behavior and lack of overpotential growth from electrode surfaces to bulk solutions 149
4.13 Over 150 charge/discharge profiles of 0.1 M $[Fe(bpy)_3]^{2+}(CF_3SO_3)_2$ in propylene carbonate (PC) without supporting electrolyte. Dreamweaver Silver 40 cellulose separator, 5 mA cm^{-2} to 25% theoretical SOC, 30s OCP hold 152
4.14 Charge/discharge efficiencies of 4.13 152
4.15 Charge/discharge profiles of 0.1 M $[Fe(bpy)_3]^{2+}(CF_3SO_3)_2$ in PC without supporting electrolyte, in same cell as Fig. 4.13 with new separator. Dreamweaver Silver 40 cellulose separator, 5 mA cm^{-2} to 25% theoretical SOC for first 15 cycles, then 10 mA cm^{-2} to to 50% theoretical SOC, 30s OCP hold 154
4.16 Charge/discharge efficiencies of Fig. 4.15 154
4.17 Initial charge/discharge profiles of 0.1 M $[Fe(bpy)_3]^{2+}(CF_3SO_3)_2$ in PC without supporting electrolyte, in same cell as Fig. 4.15 with new separator. Dreamweaver Silver 20 cellulose separator, 20 mA cm^{-2} to 50%, 30s OCP hold 156
4.18 Charge/discharge profiles of 0.1 M $[Fe(bpy)_3]^{2+}(CF_3SO_3)_2$ in PC without supporting electrolyte, in same cell as Fig. 4.15 with new separator after initial cycles of Fig. 4.17. Dreamweaver Silver 20 cellulose separator, 40 mA cm^{-2} to 50% SOC, 30s OCP hold 157
4.19 Charge/discharge efficiencies of Fig. 4.18 157
4.20 Charge/discharge profiles of 0.1 M $[Fe(bpy)_3]^{2+}(CF_3SO_3)_2$ in PC without supporting electrolyte, in same cell as Fig. 4.18 with new separator. 4 pieces of Dreamweaver Silver 40 cellulose separator, 5 mA cm^{-2} to 25% SOC, 30s OCP hold 158
4.21 Charge/discharge efficiencies of Fig. 4.20 159
4.22 Fouled Celgard 4560 separators with adsorbed active species in their pores after stirring and sonicating in neat ACN. $V(acac)_3$ on left, $[Fe(bpy)_3]^{2+}(CF_3SO_3)_2$ on right 160

List of Acronyms

$[Fe(bpy)_3]^{2+}$ iron (II) tris(2,2'–bipyridine). 132–137, 139, 141–143, 147, 150, 161, 163–165

$[Fe(bpy)_3]^{2+}(CF_3SO_3)_2$ iron (II) tris(2,2'–bipyridine) triflate. 127, 135, 137–141, 144, 145, 148, 150–152, 154, 156–161, 163

1,3-DO 1,3-dioxolane. 82–84, 86–90, 144

$acac^-$ acetylacetonate. 134

ACN acetonitrile. 80–90, 94–96, 98, 108, 109, 118, 119, 132, 133, 135–142, 144, 145, 147, 148, 150, 151, 160, 161, 163

BF_4^- tetrafluoroborate. 95, 97, 98, 126, 133, 135, 143, 144

BMIMTFSI (1-butyl, 3-methyl)imidazolium bis(trifluoromethanesulfonyl)imide. 80

bpy 2,2'–bipyridine. 133, 134, 136–139, 141, 143, 163

CE coulombic efficiency. 27

$CF_3SO_3^-$ trifluoromethanesulfonate, or triflate. 133, 135, 143, 144

$CH_3CO_2^-$ acetate. 135

$CH_3SO_3^-$ methanesulfonate, or mesylate. 135, 143, 144

ClO_4^- perchlorate. 97, 98, 133

DMC dimethylcarbonate. 80

DME dimethoxyethane. 82, 84, 94, 100, 144

DMF dimethylformamide. 80, 82, 84, 144

DMSO dimethyl sulfoxide. 82, 84, 144

EC ethylene carbonate. 86

EE energy efficiency. 27

IEM ion exchange membrane. 15–18, 29, 30, 51, 52, 164

LCOS levelized cost of storage. 44, 51

PC propylene carbonate. 139, 144, 150–152, 154–158, 161, 163

SOC state-of-charge. 20, 21, 23, 28, 36, 38, 56, 57, 59–61, 64, 70, 88, 104, 109, 110, 112, 119, 123, 124, 130, 146, 148, 151, 152, 154, 157, 158, 165

$TBABF_4$ tetrabutyllammonium tetrafluoroborate. 80, 81

$TBAPF_6$ tetrabutylammonium hexafluorophosphate. 80, 81, 100

$TEABF_4$ tetraethylammonium tetrafluoroborate. 24, 58, 80, 81, 83, 84, 88, 90, 94, 96, 98, 100, 109, 139, 147

$TEAClO_4$ tetraethylammonium perchlorate. 98, 99, 108

THF tetrahydrofuran. 80, 144

$V(acac)_3$ vanadium acetylacetonate. 24–26, 53, 58, 75, 77–101, 103–106, 109–116, 118–120, 135, 141, 142, 144, 146, 147, 150, 159–163

VE voltaic efficiency. 27

$VO(acac)_2$ vanadyl acetylacetonate. 94, 100

1

Symmetric RFBs: Fundamentals, Model, & Technoeconomics

Contents

1.1 Traditional RFB Construction 2
1.2 Taxonomy of Flow Batteries 6
1.3 Focus on Symmetric Systems 11
1.3.1 Disproportionation 12
1.3.2 Mixed Electrolytes 13
1.4 Motivation for Porous Separators 15
1.5 Model for Porous-Separator RFBs 17
1.5.1 Derivation 18
1.5.2 Behavior 24
1.6 Technoeconomics 35
1.6.1 Capital Expenditure 36
1.6.2 Levelized Cost of Storage 44
1.6.3 Technoeconomics of Porous Separator RFBs 46
1.7 Thesis Objectives & Structure 52

Symmetric redox-flow batteries (RFBs) exist within a wider RFB design landscape that has not yet settled on formal definitions or classifications of various system architectures. Symmetric RFBs of various types which are capable of utilizing porous separators must therefore be placed in the correct context to understand their merits and drawbacks relative to other system architectures. In order to clarify both the literature and the present work, the RFB design space will now be defined

and categorized in order to place symmetric RFBs in their appropriate context.

1.1 Traditional RFB Construction

Effective grid-scale energy storage requires systems with sufficient capacity, power, and efficiency metrics that provide guaranteed performance on the timescale of decades at a competitive levelized cost of energy stored. RFBs possess intrinsic advantages over other electrochemical approaches to storage, including decoupled power-energy relationships, constant liquid-phase operation, use of ubiquitous chemical process equipment, and a paucity of degradation pathways. Numerous RFB configurations and chemistries exist, with development status spanning from academic groups modeling and synthesizing new redox active molecules to companies operating and installing systems up to and above the 100 MW and 100 MWh levels.

The major disadvantage of traditional all-liquid RFBs compared to conventional secondary batteries is their relatively low energy density, with many chemistries' theoretical maximums below $50\,\mathrm{Wh\,L^{-1}}$ [1]. This characteristic limits RFBs to stationary energy storage primarily. While the all-liquid nature of RFBs does preclude them from common secondary battery degradation pathways related to intercalation and morphological changes from plating/stripping electrodes, RFBs can suffer from other degradation modes not limited to state-of-charge drift, heterogeneous and homogeneous side reactions of the electrolytes, membrane degradation, and corrosion of the bipolar plates [2]. Additionally, while system-level comparisons are obscured by differing balance-of-plant and usage requirements, compared to traditional lithium-ion chemistries at the unit cell level, flow batteries have somewhat lower round-trip energy efficiencies [3].

In the context of electrochemical energy conversion and storage devices, RFBs are secondary rechargeable batteries with continuous forced convection analogous to fuel cells and electrolyzers, with the important exception that they are closed liquid-based systems exchanging only heat and electrical work with their surroundings. A visual depiction summarizing the role RFBs play relative to their other electrochemical counterparts is shown in Fig. 1.1.

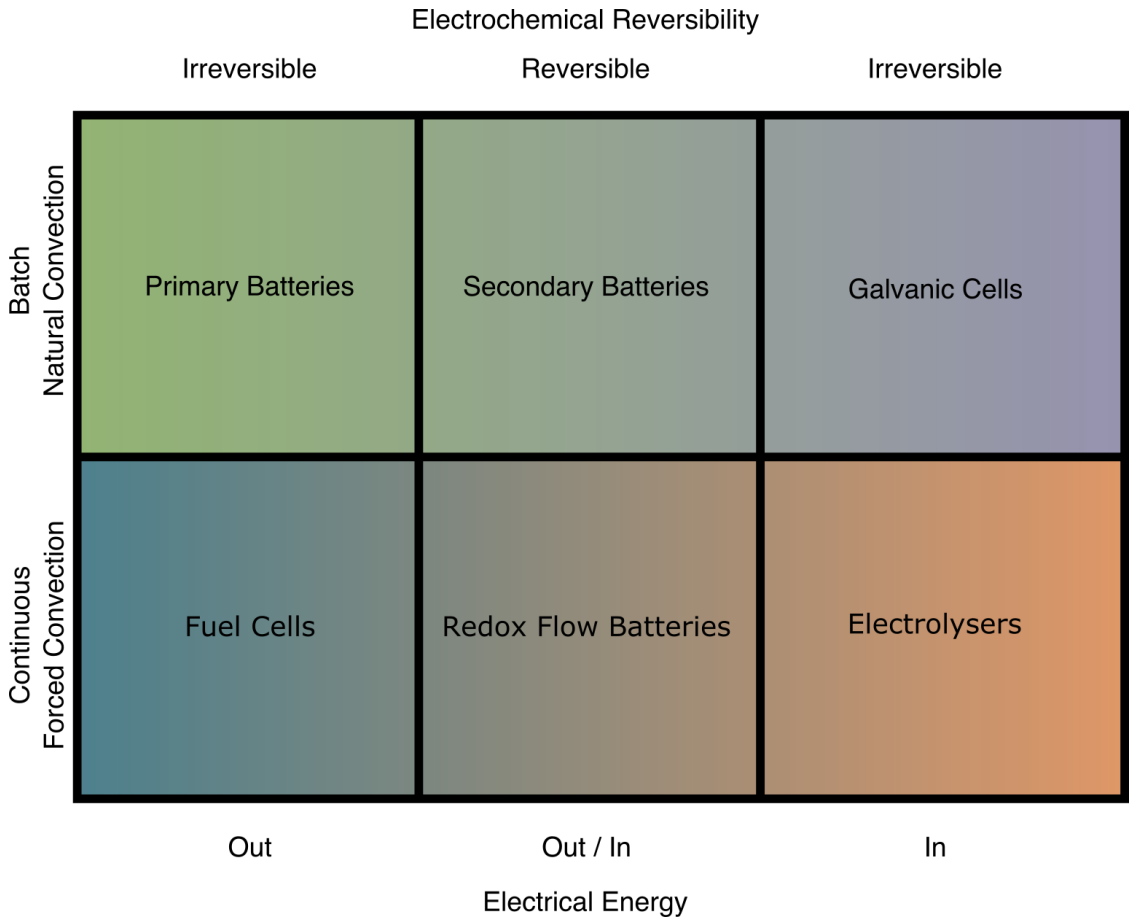


Figure 1.1: RFBs compared to other electrochemical devices in terms of reversibility and configuration (adapted from [1])

Traditional, all-liquid RFBs consist fundamentally of two electrochemical half-cells connected to an external electrical load/source as shown in Fig. 1.2. These half-cells exist as two discrete fluid chambers, each with an inlet and outlet, and contain a porous solid electrode (usually carbon felt or paper) which provides a high surface area for heterogeneous electrochemical reactions with redox-active molecules dissolved in a liquid electrolyte. The electrolytes of each half-cell are physically separated but ionically connected *via* a membrane or separator that ideally permits only ion transport between the electrolytes. This ionic connection completes the electrochemical circuit between the half-cells and facilitates the redox reaction of the redox-active molecules (active species) in each half-cell.

The liquid electrolytes are each stored in separate reservoirs and are continuously pumped between their respective reservoirs and the cell. These multifunctional

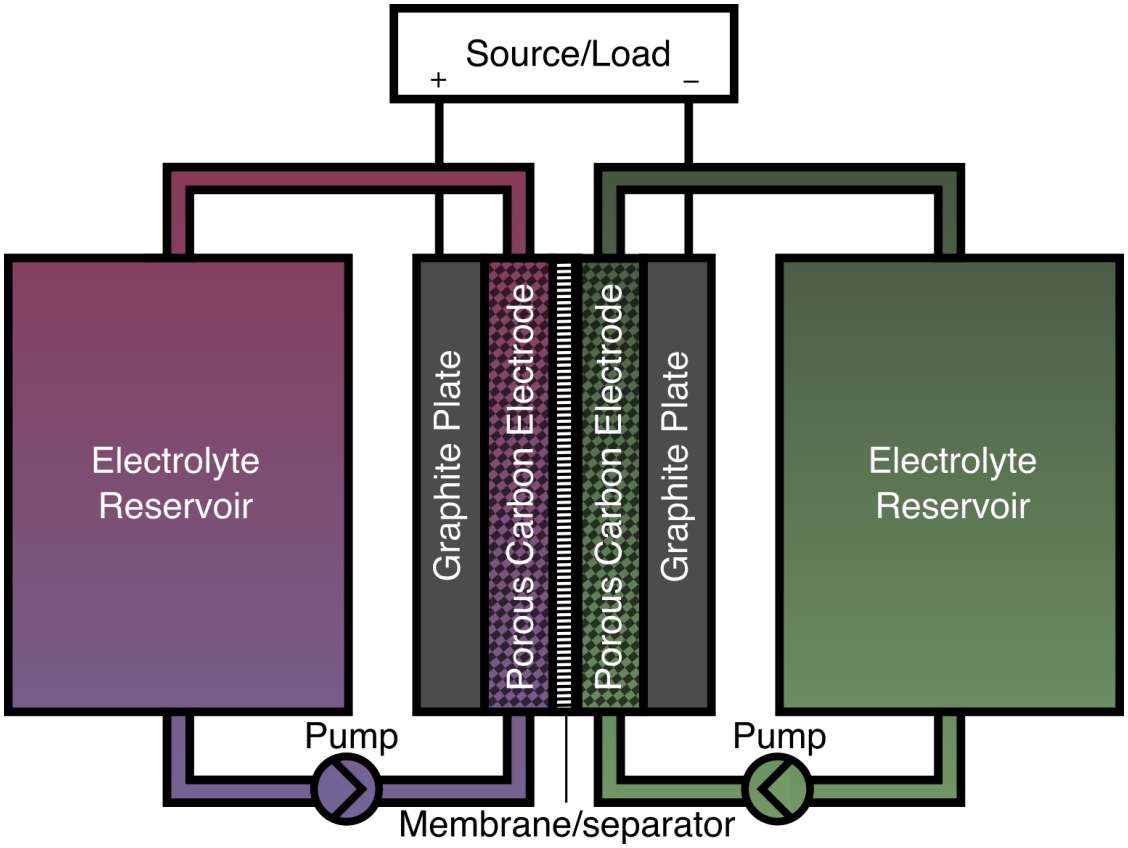


Figure 1.2: A traditional RFB unit cell

electrolytes provide ionic conductivity to the liquid phase of the cell, maintain electroneutrality *via* ion exchange between half-cells, and transport the dissolved active species to the porous-electrode surface where heterogeneous redox reactions occur. The first two of the aforementioned functionalities are typically accomplished with a supporting electrolyte, whose ions maintain electroneutrality during cell operation by travelling across the membrane. A supporting electrolyte is an acid, base, or salt added to the multicomponent electrochemical system, chiefly to increase the ionic conductivity of the solution without participating in the electrode reactions [4].

The minimum ionic strength needed in the electrolyte to maintain charge balance up to the system's maximum theoretical state-of-charge depends on the number of charges received or donated by the active species across all of its oxidation states. This minimal necessary support concentration generally may differ from the optimal concentration of salt required to achieve a desired conductivity.

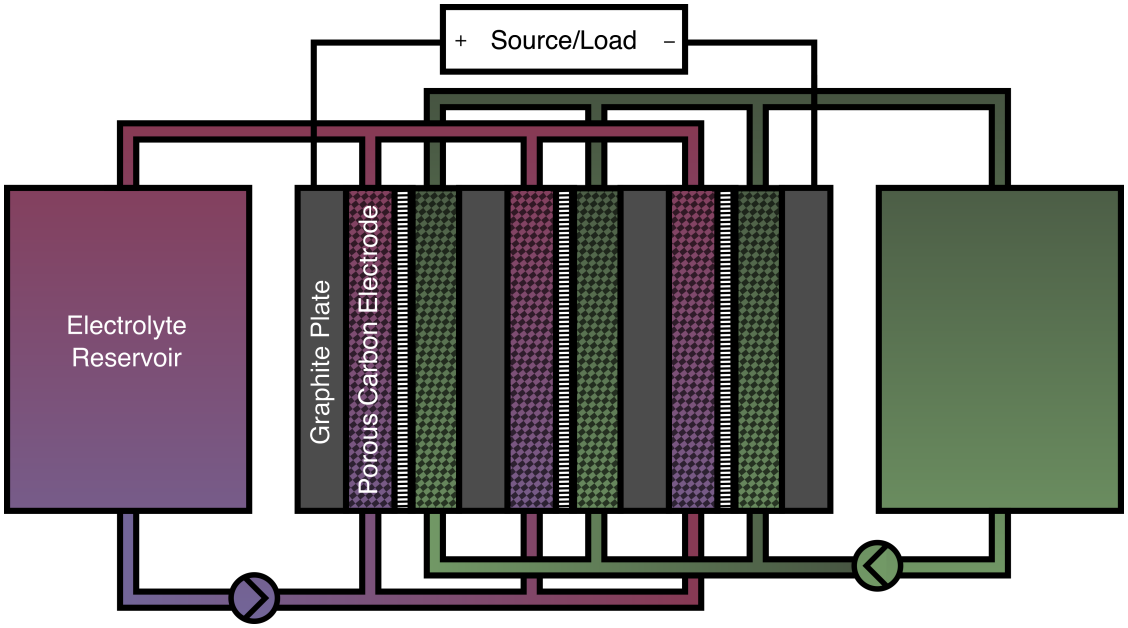


Figure 1.3: A traditional RFB stack with three unit cells

.

While lab-scale research typically consists of a single unit cell with its two half-cells, practical implementations of RFBs contain several cells. Cells are typically arranged in stacks, which connect cells electrically in series and hydraulically in parallel, as seen in Fig. 1.3.

Multiple stacks are combined into modules, all connected hydraulically in parallel with one pump circulating the electrolyte of each reservoir.

RFBs offer multiple design features unique amongst electrochemical energy storage devices. Since energy is stored in dissolved active species, the energy content of a RFB is directly proportional to the volume of electrolyte contained in the reservoir. The power capability of a RFB is directly proportional to the active surface area of the cells comprising its stacks. This decoupling of energy and power allows for independent scaling in either vector by simply increasing reservoir volume or electrode surface area, respectively, unlike conventional batteries where this relationship is fixed by the geometry of solid electrodes. This design flexibility primes RFBs for long-duration applications because adding energy capacity only requires more active species, electrolyte, and tank capacity, while stack and other power-related components remain unchanged. The long lifetimes demanded by

grid-scale storage applications require durable technologies, and traditional RFB active species always exist in the liquid state, in principle immune to mechanical degradation pathways like fatigue, dendrites, or other changes in surface morphology. Finally, RFBs offer simple recycling pathways. Active material and electrolyte can be easily drained and in some cases reused, while established recycling procedures already exist for the remaining metal and plastic mechanical components [5].

There are multiple configurations of traditional all-liquid chemistries and several hybrid RFB approaches which utilize solid active material. An overview of these classifications follows. The remainder of this chapter focuses on defining symmetric flow batteries in the context of all RFB architectures, developing a simple model for symmetric flow batteries which use porous separators, and finally ties this fundamental model to existing technoeconomic models to help guide development.

1.2 Taxonomy of Flow Batteries

Several reviews of the RFB literature exist [6–15]. There are myriad ways to design and fabricate a flow battery, especially when including hybrid flow batteries which utilize gas and/or solid reactant phases. In efforts to visualize this vast design space, RFBs have been classified using a tree-based approach [1, 9, 16]. This tree-based approach becomes cluttered due to redundant branches from the presence of multiple non-mutually exclusive attributes like active-species chemical classification (organic, coordination compounds, organic), (non)aqueous distinction, hybrid configuration, *etc.* The ability of a flow battery composition to possess multiple independent attributes mean a graphical approach such as Fig. 1.4, while not exhaustive, is more useful to intuitively and efficiently capture the entire design space with commonly used classifications.

Fig. 1.4 attempts to depict the entire RFB design space in terms of half-cell electrolyte specification. For each half-cell, a gaseous, solid, or liquid-phase redox-active compound is chosen (with at least one half-cell being liquid in order to justify status as a flow battery), along with a supporting electrolyte and solvent system. This visualization shows the entire range of categories of redox-active

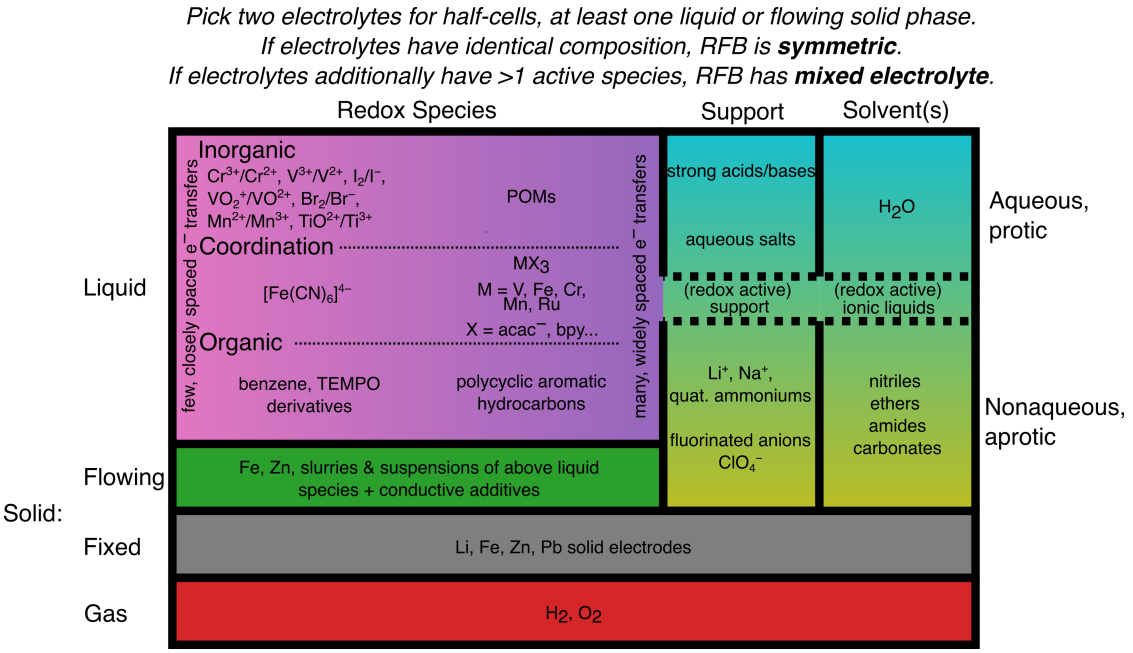


Figure 1.4: Classification of flow batteries by half-cell configuration

compounds, supporting electrolyte, and solvents available to construct flow batteries. Aqueous and nonaqueous systems have been intentionally included together under the categories "Support" and "Solvent(s)" to illustrate that water is a solvent and strong acids/bases merely supporting electrolyte, and conceptually there is no difference between aqueous/nonaqueous systems (whereas their physicochemical properties are vastly different). Also, inorganic, coordination compounds, and organic compounds with varying quantities of reversible electron transfer events are all grouped together in the liquid redox species box, in their respective sub-categories.

Symmetric RFBs, formally introduced in the next section, are also more easily depicted with Fig. 1.4, rather than introducing another set of redundant branches in a tree-based RFB design space. Symmetric RFB compounds suitable for disproportionation are visible in the many-electron-transfer region of the liquid redox species box, while a mixed electrolyte formulation can be achieved with by choosing two liquid-phase active species from the left side of the liquid redox species box (such as the popular iron/chromium mixed electrolyte system). This categorization task shows how the same group of RFB active compounds may be used

to construct flow batteries of various architectures, which would be complicated to depict with a tree-based approach.

A drawback of the approach in Fig. 1.4 is that this graphical method, unlike tree-based approaches, does not provide guidance as to suitable combinations of half-cells and active species/support/solvent systems. For example, a protic electrolyte system would not be used in conjunction with most polycyclic aromatic hydrocarbon molecules whose charged radical species are only stable in aprotic nonaqueous systems, and many inorganic salts of redox-active compounds are insoluble in nonaqueous electrolytes. Also, this approach does not include some exceptions, such as a select few totally liquid organic active species, which do not require solvent to be solubilized (though solvent would likely be needed for practical reasons to solubilize supporting electrolyte, reduce viscosity *etc.*). Still, Fig. 1.4 has been created to provide a more accessible overview of the chemical design space for flow batteries.

All RFBs contain two half-cells and a means of physically separating them while ionically connecting them, in the traditional arrangement of a divided electrochemical cell. Membranes almost exclusively accomplish this, though cells utilizing laminar flow to achieve the same end have been implemented [17–19]. Membranes may be fabricated to be selective towards cations or anions, while some are nonselective and known as porous separators. The categorical names given to separators with varying degrees of porosity are often misused according to formal definitions. The International Union of Pure and Applied Chemistry (IUPAC) defines microporous materials as those with pore sizes below 2 nm, mesoporous between 2 and 50 nm, and macroporous above 50 nm [20]. Porous materials often have a distribution of pore sizes, however, which blur these formal definitions. Furthermore, filtration membranes, commonly used as experimental porous separators, have their own nomenclature, with Noack *et al.* summarizing nanofiltration membranes as having pore sizes below 5 nm, ultrafiltration membranes between 5 and 100 nm, and microfiltration membranes between 100 nm and 10 mm [1].

Some flow batteries have membrane pore-size distributions matched to redox molecules which permit ion transport but block active species transport based on size exclusion [21].

The half-cells each typically contain one redox couple—more are possible, however, as distinct redox-active molecules can offer multiple redox events and multiple redox-active molecules may be intentionally present in an individual half-cell. Additionally, at least one half-cell must be "flowable" for a system to be reasonably labeled as a "flow' battery—either as a traditional all-liquid solution, or as a suspension of solid particles such as iron or zinc. Half-cells can be solid plates of metal such as iron [22], zinc [23], or lead [24], or gaseous phases like oxygen (for so-called "air-breathing" RFBs [10]) and hydrogen. Solid-plate half-cells do not have fully decoupled power-energy relationships. Such configurations with at least one solid phase are variously described as semi-solid, slurry, or suspension RFBs while in general any RFB without two all-liquid half cells is known as a hybrid RFB.

A given half-cell, when based on a liquid or otherwise pumpable mixture, will have an associated reservoir. Depending on the relative electrochemical potential of the given half-cell to its complementary half-cell, the reservoir mixture can be referred to for more positive compounds (which oxidize when charged) as the positive electrolyte, posolyte, or catholyte, and for more negative compounds (which reversibly reduce when charged) as the negative electrolyte, negolyte, or anolyte.

For redox-active molecules in the liquid phase and solid particles in suspension, solvent(s) and supporting compound(s) must be additionally specified. Conventional strong acids and bases are common for aqueous systems while a wide array of solvents and salts that intend to support wide electrochemical windows are used for nonaqueous systems—a selected few are depicted in Fig. 1.5. Ionic liquids can also be used as both solvent and support. The primary motivation for pursuing nonaqueous systems is achieving redox couples with a potential difference beyond that supported by water (typically 1.4 V on carbon electrodes).

To maintain electroneutrality across all states of charge, the concentration of initial unconverted active species in the electrolyte must equal the ionic strength

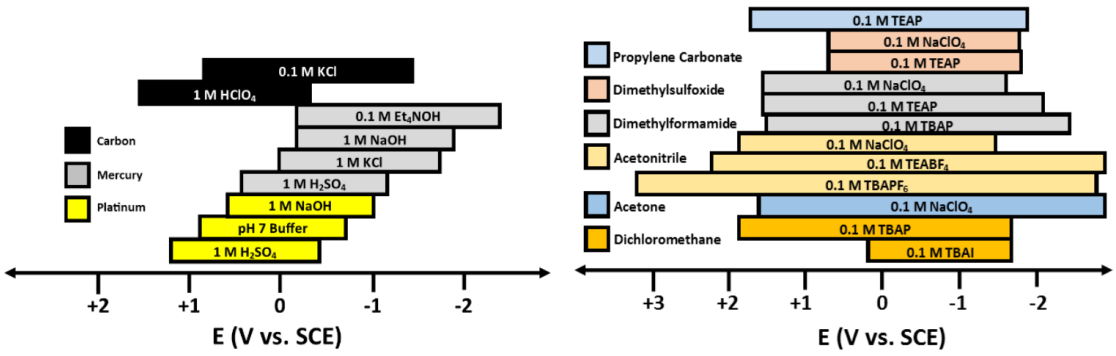


Figure 1.5: Electrochemical stability windows of aqueous and nonaqueous solvents *vs.* saturated calomel electrode from [27]

provided by the support. This means for a system with a initially neutral 1.0 M nominal concentration of an active species that donates or receives one charge during the charging process, 0.5 M of a binary monovalent salt is needed to allow for 100% theoretical conversion of actives on charging. This configuration is known as "salt-splitting," where both cations and anions of supporting electrolyte move between half-cells on charge and discharge to maintain electroneutrality [25, 26]. Active species, however, may be ionic themselves, and contain electrochemically inert counterions which can function as supporting electrolyte. If these counterions serve as the only supporting electrolyte, this configuration is known as a "rocking-chair" [25] or (additional) "supporting salt-free" configuration [25]. This rocking-chair metaphor originates from the characteristic of all the inert, non-reactive cations or anions migrating from one half-cell to the other during charge/discharge (rocking back and forth). A salt-splitting battery would have inert, non-reactive cations and anions traveling between half-cells in both direction on charge/discharge.

Two configurations not shown in Figure 1.4 are based on having undissolved solids in the electrolyte reservoirs. One approach may have a saturated supernatant circulating to and from the stack, with undissolved actives species (of potentially multiple oxidation states) remaining in the reservoir, such as Br_2 phase separation in the $ZnBr_2$ aqueous system discussed in [28] and [29]. The other configuration uses a soluble redox shuttle system and an insoluble material in the reservoirs; this configuration is called "redox-targeting" or said to be using "solid boosters"

[30–32]. Redox-active polymers or "redoxmers" have also been explored for both redox-targeting systems and membrane approaches based on size-exclusion [31].

For liquid half-cells, distinctions are made between inorganic, coordination, and organic compounds. The term "organometallic" is often used to describe what are formally (by IUPAC standards) coordination compounds, which have coordination bonds between transition metals and organic ligands. The only true organometallic compound known to be used in RFBs is ferrocene, since it contains a metal-carbon bond. Motivation for organic active species development has two main components. The possibility of eliminating the presence of metal-containing active species which require traditional resource extraction techniques offers a route for cost reduction by means of well-understood industrial organic synthesis methods. Additionally, organic active species and the organic ligands in coordination compounds offer a wide molecular design space in which structural modifications *via* organic chemistry promise the tuning of redox potentials and solubilities to enable energy-dense RFBs [33, 34].

1.3 Focus on Symmetric Systems

Symmetric flow batteries contain mixtures that are electrochemically identical in each half-cell and corresponding reservoir in the discharged state. In this configuration, active species from either reservoir that may migrate to the other reservoir through the separator do not permanently degrade the capacity of the battery. Active-species crossover in a symmetric system has the effect of reducing the coulombic efficiency of a given cycle without permanently degrading the capacity of the battery. When using an asymmetric system, active-species crossover is not necessarily reversible, because electrolytes are not supposed to be mixed. Even if using an ion-exchange membrane highly resistant to crossover, a defect or failure such as a puncture could result in the irreversible total mixing of the reservoirs. A useful discussion of crossover mitigation strategies for flow batteries is found in [35].

At times in the literature, the term "symmetric" has been used to describe an experimental technique in which the polarization behavior of single redox couple is

studied in a full flow cell by connecting the outlet of one half-cell to the inlet of the other, so that the cell can pass current without any net charge being transferred [36, 37]. In this context, the electrochemical system studied does not have a full cell reaction enabling energy storage and is therefore not technically a battery.

Despite the fact that all the half reactions involve the same metal, aqueous all-vanadium systems are not symmetric because the reservoirs are not electrochemically identical when fully discharged. The capacity loss associated with electrolyte mixing is reversible for aqueous all-vanadium RFBs, however, and can be mitigated by periodic or continuous regeneration processes. These losses occur on the order of 0.1% capacity loss per cycle at both the lab-scale and full-scale according to various sources [35, 38–40]. In this dissertation, the symmetric nature of the systems studied obviate the need for any regeneration process to restore capacity as the electrolytes never need to be unmixed or have their average oxidation states adjusted.

1.3.1 Disproportionation

To achieve a symmetric system, a disproportionation compound X can be used that supports coulombically reversible reduction and oxidation half-reaction, leading to an overall cell reaction like

$$2\,\mathrm{X} \longleftrightarrow \mathrm{X}^{+} + \mathrm{X}^{-}\,\cdot$$

Disproportionation compounds in the context of flow batteries are sometimes referred to as “bipolar” [41], “symmetric [42], “bi(-)redox” [43], or “bifunctional” [44], but the categorization implemented here provides needed clarity to the field. A schematic of a generic flow battery based on a disproportionation reaction is provided in Figure 1.6.

Inorganic compounds supporting disproportionation seem to be primarily polyoxometallates [45]. Coordination compounds based on transition metals are numerous; disproportionation compounds based on vanadium [46], chromium [47], manganese [48] have been proposed, and ligand modifications have been pursued for chromium- and vanadium-centered coordination compounds to improve redox potentials and solubility [34, 49].

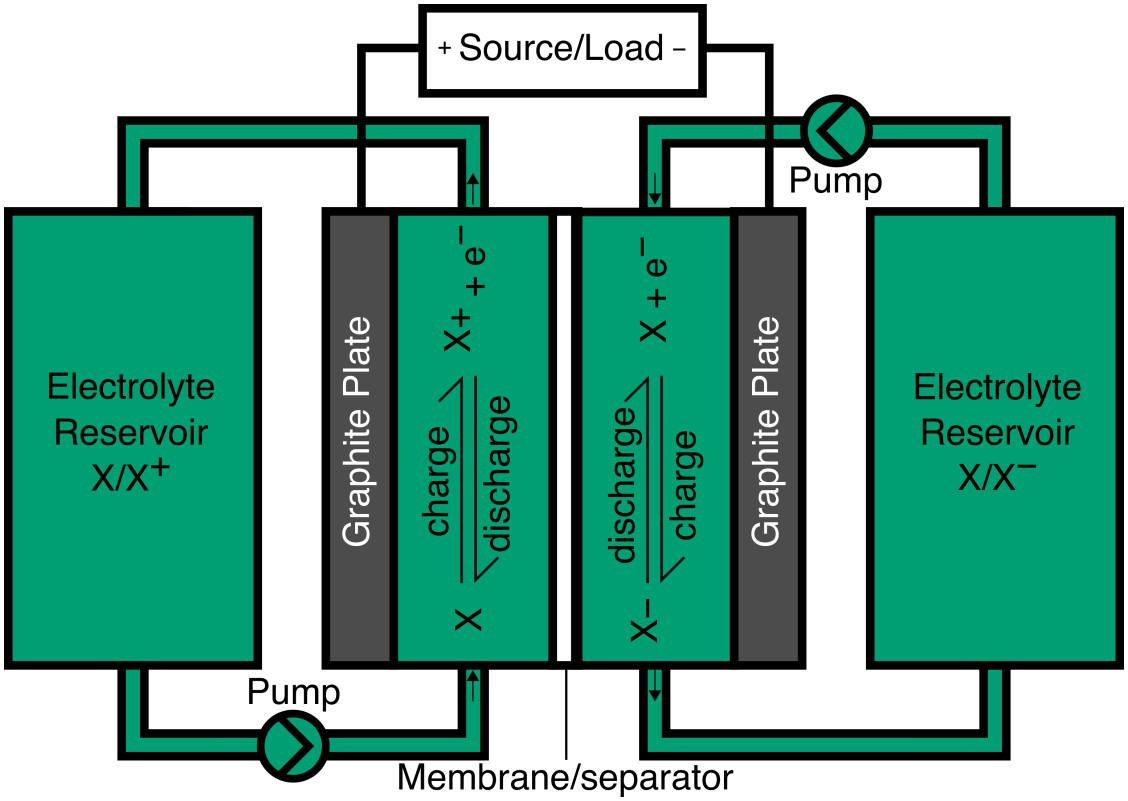


Figure 1.6: A disproportionation flow battery

Organic disproportionation compounds have been studied computationally [50] and experimentally for aqueous [51] and nonaqueous systems [41, 52–57].

1.3.2 Mixed Electrolytes

Additionally, symmetric systems may be realized in a "mixed electrolyte" configuration by using two distinct molecules A & B in solution, each providing at least one coulombically reversible reduction or oxidation corresponding to the following half-cells:

$$\mathrm{A} + \mathrm{B} \longleftrightarrow \mathrm{A}^{+} + \mathrm{B}$$
$$\mathrm{A} + \mathrm{B} \longleftrightarrow \mathrm{A} + \mathrm{B}^{-}$$

for an overall cell reaction of

$$\mathrm{A} + \mathrm{B} \longleftrightarrow \mathrm{A}^{+} + \mathrm{B}^{-}.$$

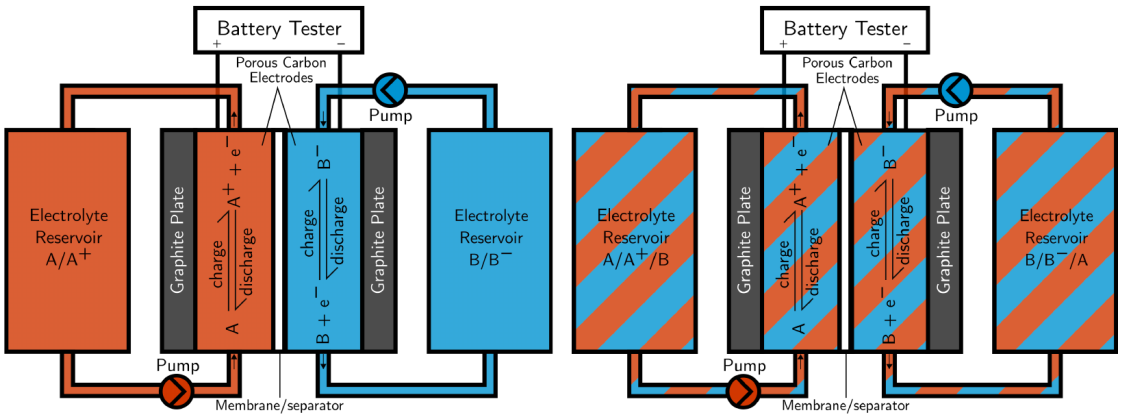


Figure 1.7: A conventional asymmetric flow battery on the left and on the right, a symmetric flow battery using a mixed electrolyte

Mixed electrolytes allow for a pseudo-disproportionation process to be realized without a singular molecule needing to provide both redox events. This can avoid synthetic cost and aid with solubility, though both molecules need to be stable across the entire potential window of both electrodes.

A visual depiction of the difference between a traditional flow battery and two symmetric flow batteries, one disproportionation, one mixed electrolyte, is shown in Figure 1.7.

The difference between the types can be additionally understood in the context of flow batteries at large in all their different configurations in Figure 1.4.

There is a historical precedent in the field of electrochemiluminescence for using two soluble redox-active molecules to provide reduction and oxidation events with widely separated potentials. Keszthelyi, Tachikawa, and Bard used thianthrene and 2,5-diphenyl-1,3,4-oxadiazole in an "mixed energy-sufficient" system in 1972 [58]. Similar to symmetric RFB development, electrochemiluminesence initially relied heavily on disproportionation compounds, and this paper demonstrated the use of disparate molecules in solution to achieve the same end. The literature on electrochemically generated chemiluminescence is concerned with classes of compounds very similar to those considered for flow batteries, and serves as useful inspiration for symmetric-flow-battery electrolytes based on disproportionation and mixed-electrolyte approaches.

Mixed electrolytes are sometimes used intentionally by researchers looking to eliminate irreversible capacity fade due to crossover in their experiments. This technique consists of taking negolytes and posolytes intended for an asymmetric flow battery and pre-mixing them, sometimes while using a porous separator [59–62]. This eliminates one source of capacity fade and allows for a closer analysis of chemical stability.

Yang *et al.* used this approach with iron sulfate and anthraquinone disulfonic acid in a mixed-electrolyte configuration [62]. Selverston *et al.* demonstrated a system with a mixed zinc–iron chloride electrolyte, utilizing a porous separator [63]. This system is additionally a hybrid flow battery, because the zinc half-cell involves electroplating. Xie *et al.* used a similar approach with zinc–cerium [64]. Notably, the Zn/Zn^{2+} half-cell often encounters problems with dendrites [1].

The aqueous iron–chromium flow chemistry is an example of an all-liquid, inorganic mixed electrolyte system by this definition.

1.4 Motivation for Porous Separators

This thesis focuses on nonaqueous symmetric flow battery chemistries, and will attempt to elucidate their performance in configurations that use porous separators to divide the unit electrochemical cell. Porous separators are the primary alternative to ion exchange membranes (IEMs) conventionally used to electronically separate the porous carbon electrodes of the unit cell while facilitating ion transport. IEMs are ionomers—polymers comprising electrically neutral monomer units with ionically charged constituent groups. The arrangement of these groups allows for selective transport of ions.

Typically, in flow battery applications, IEMs are made from fluorinated compounds. As will be emphasized later in this dissertation, fluorine-containing components are relatively expensive in the context of affordable energy storage systems. Notably, however, an IEM contributes to the power-related cost of a flow battery, which contributes marginally to system cost at long discharge times; in other words, an expensive reactor (which may use an IEM) is more justifiable than

an expensive electrolyte for present applications in grid-scale energy storage. Despite this, more affordable and sustainable cell components still deserve further study, provided any performance trade-offs are justifiable, and affordable power-related components increase the competitiveness of RFBs at shorter discharge durations.

Porous separators are thin (10s of µm) sheets with some porosity, pore sizes on the micro- or sub-micrometer scale, and (in battery applications) usually possess nonzero tortuosity. They are typically polymers of various compositions, though ceramic porous separators are possible (and are tested later in this thesis).

Olefin-based (polyethylene and/or polypropylene) porous separators are at least an order of magnitude cheaper than fluorinated IEMs: $10\,\$\,\mathrm{m}^{-2}$ *vs.* $500\,\$\,\mathrm{m}^{-2}$ in 2014, and a projected future price differential of $1\,\$\,\mathrm{m}^{-2}$–$3\,\$\,\mathrm{m}^{-2}$ *vs.* $25\,\$\,\mathrm{m}^{-2}$–$75\,\$\,\mathrm{m}^{-2}$ for IEMs [3]. Also, IEMs were initially designed for aqueous environments, so chemical compatibility with nonaqueous electrolytes is not always guaranteed—though nonaqueous-compatible IEMs are being actively developed.

Porous separators also have intrinsically different performance requirements due to the chemistries they can be used with. An asymmetric chemistry with dissimilar discharged electrolyte compositions requires an IEM to prevent irreversible mixing. As such, IEMs in this configuration must be manufactured and operate long-term without defects like pinholes or cracks which would allow mixing of electrolytes from either reservoir. A porous separator contains holes (of a defined size distribution) by design; while a large pinhole or crack would be deleterious for performance, a replacement separator costs much less than an IEM and half-cell electrolyte mixing is tolerable for a symmetric system.

While porous separators are more affordable, easier to manufacture, and more robust than IEMs, they are not without compromise. Porous separators are entirely permeable to any molecular species whose diameter is smaller than the characteristic pore size. As such, they allow supporting electrolyte, solvent, and active species of all charge states to pass through the separator (but at different rates); this means porous separators will always have a lower coulombic efficiency than IEMs, which typically have over 99% coulombic efficiency. It should be emphasized that

porous separators generally have lower area-specific cell resistances than IEMs. This conductivity improvement is much more pronounced in the domain of relatively less conductive (*vs.* aqueous) nonaqueous electrolytes. These features—lower coulombic efficiency, higher conductivity/voltaic efficiency, lower cost—create tradeoffs between reactor cost (capital cost) and reactor performance (future cash flow), which will be explored further in subsequent sections.

In full-scale systems, the use of porous separators is open for debate. At the benchtop scale, however, while they may not be the optimal solution in every case, porous separators are undeniably useful. They are affordable, chemically resistant, and forgiving compared to IEMs and can eliminate sources of failure.

1.5 Model for Porous-Separator RFBs

To understand the tradeoffs of porous separators in terms of system performance and ultimately cost, this section presents a simple zero-dimensional model of a symmetric flow battery, which introduces one key parameter to account for porous separators. This parameter is the self-discharge current density, j_{sd}, which describes the "leakiness" of the membrane towards the recombination of charged active species ideally kept as separated as possible. This section presents this model with some assumptions and presents the analytical solution. Subsequent sections integrate the model into modified technoeconomic models to explore the initially apparent tradeoffs. In Chapter 2, these assumptions are shown to be valid using a real-time measurement technique developed for purposes of separator characterization.

A flow battery is a divided electrochemical cell with forced convection; for the battery to be charged, products of the electrochemical full-cell reaction must leave the half-cells at a rate faster than they recombine through the separator. The inherently lower coulombic efficiency of flow batteries with porous separators comes from this unique background self-discharge process, and this ratio of faradaic current to self-discharge current is central to performance.

Nemani and Smith explored a two-dimensional model with physical and kinetic approximations for RFBs with non-selective separators, but the chief aim was to

focus on capacity fade from irreversible crossover, which is not present with the symmetric RFBs studied in this dissertation [65]. Darling *et al.* offer a rigorous examination of separator requirements for flow batteries, looking at both IEMs and porous separators, but again are primarily concerned with systems where the crossover of charged active species is destructive, unlike in symmetric systems [66]. Additionally, this framework by Darling *et al.* while robust, is unnecessarily complex for an initial high-level understanding of the tradeoffs inherent to symmetric RFBs with porous separators.

Existing models for flow batteries treat the case of symmetric RFBs with porous separators as an exception, if they are included at all. This is in part because, as mentioned previously, symmetric RFBs with porous separators represent one small sub-category of the vast RFB design space, and most work explicitly dedicated to their study has skewed experimental. More complex models incorporating two and three-dimensional flow through porous electrodes, Marcus-Hush kinetics, dilute or concentrated solution theory and the like will undoubtedly be useful in the future to understand symmetric RFBs with porous separators, but here a simple zero-dimensional model based on ordinary differential equations allows for facile exploration of the initial tradeoffs of these systems, especially when coupled to technoeconomic models.

1.5.1 Derivation

The following zero-dimensional model consists of two control volumes: one for a singular reservoir and one for its respective half-cell. The volume of the reservoir is assumed to be many times larger than that of the half-cell. The symmetric electrolyte configuration allows the model to consider only one half of the system. Electrolyte with an active species concentration c_0 and flowrate $\dot{V}$ travels from the reservoir with volume V_{res} and SOC_{res} to a half-cell with volume V_{cell}, geometric area A_{cell}, SOC_{cell}, and electrode porosity ϕ. In the half-cell, this portion of electrolyte receives a faradaic applied current density j_{app} and loses some charge to a self-discharge current density j_{sd} which both compete to change SOC_{cell} This

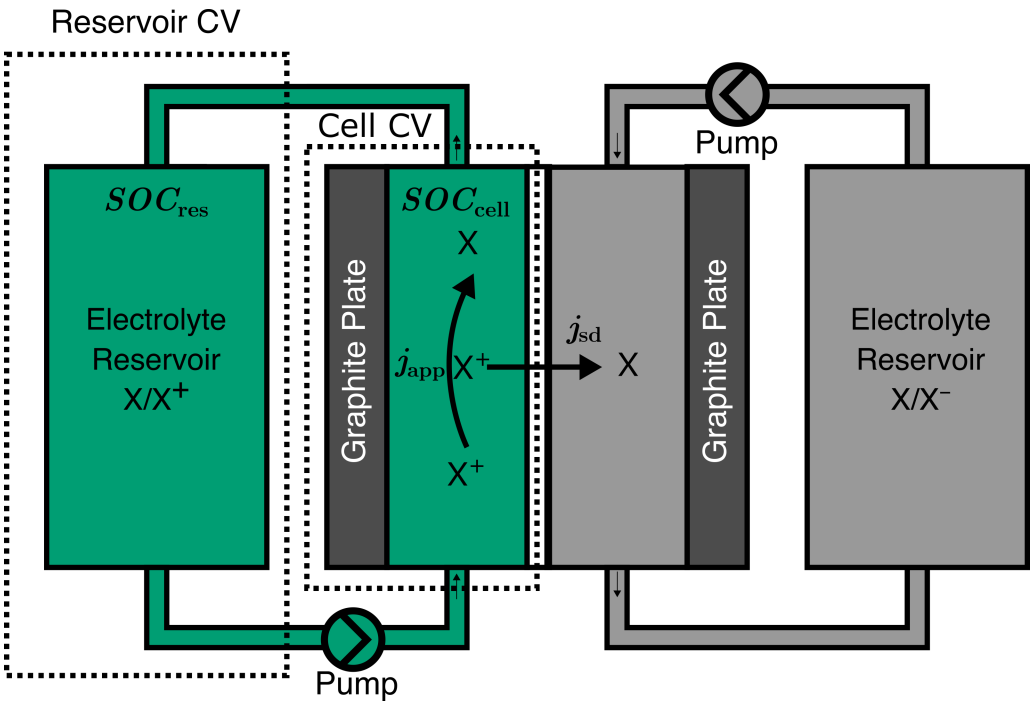


Figure 1.8: Schematic for model of porous separator flow battery self-discharge showing applied and self-discharge currents (not to scale)

self-discharge current density j_{sd} is assumed to be directly proportional to SOC_{cell}; at higher states of charge, more self-discharge is expected, and *vice versa*. This assumption is validated in Chapter 2, and will not be discussed further here. Also assumed are perfect mixing within the reservoir and the cell itself, leading to uniform states-of-charge distributions. A schematic showing the control volumes and relevant terms is shown in Figure 1.8.

A system of linear first-order ordinary differential equations describes the charge balances in the two control volumes,

$$\frac{dSOC_{res}}{dt} = \frac{\dot{V}}{V_{res} - V_{cell}}(SOC_{cell} - SOC_{res}) \tag{1.1}$$

$$\frac{dSOC_{cell}}{dt} = \frac{\dot{V}}{V_{cell}}(SOC_{res} - SOC_{cell}) - \frac{(j_{app} + j_{sd}SOC_{cell})A_{cell}}{V_{cell}c_0F.} \tag{1.2}$$

The parameters are defined in Table 1.1.

Eq. 1.1 treats the reservoir as a stirred tank with no reactions occurring; the quotient on the right-hand side of the equation is a residence time, which is multiplied by

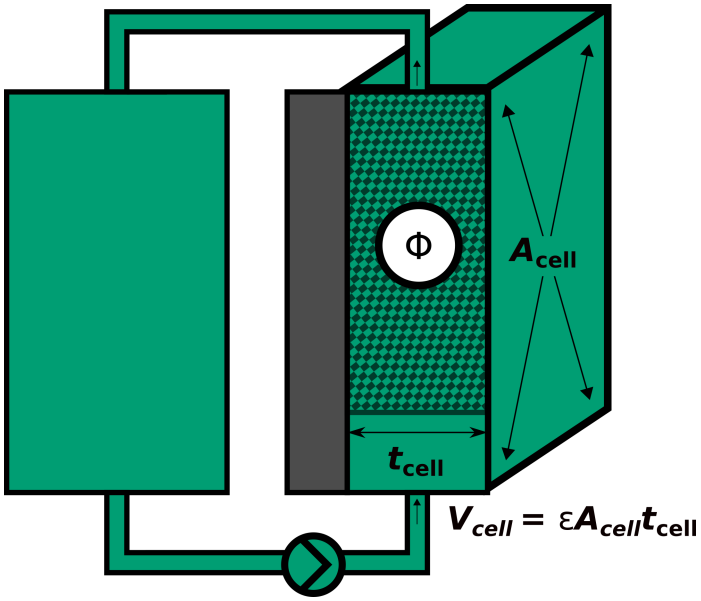


Figure 1.9: Schematic for model of porous separator flow battery self-discharge showing carbon felt porosity ϕ, cell thickness t_{cell}, and cell geometric area A_{cell} (not to scale)

the difference in states of charge entering and leaving the reservoir leading to an accumulation or depletion of reservoir SOC. Eq. 1.2 describes the reaction chamber as a stirred tank with zero order (faradaic current of charging/discharging) and first order (self-discharge) reactions occurring. The first term on the right-hand side is analogous to the right-hand side of Eq. 1.1; a residence time multiplied by a difference in charge-state, which corresponds to the stirred-tank behavior of the cell. The second term is the combined faradaic current and self-discharge term. The convention of discharge corresponding to positive current is used here. The applied current density j_{app} is independent of state of charge and concentration. The self-discharge current density j_{sd} is proposed to be dependent on the unitless SOC_{cell}, so the product of those two terms multiplied by the area of the cell A_{cell} becomes the instantaneous self-discharge current in the cell. The denominator of the second term in Eq. 1.2 normalizes the applied and self-discharge currents to the nominal amount of initial discharged active species in the cell to yield the rate of change of state of charge in the cell due to electrode and separator processes.

Solving this system of equations begins with making the substitution $V_{\text{cell}} = \phi A_{\text{cell}} t_{\text{cell}}$ to simplify notation. Also, the ratio $\frac{\dot{V}}{V_{\text{cell}}}$ appears frequently and is useful

Table 1.1: Definitions of terms in porous separator RFB self-discharge model along with their representative benchtop values

Parameter	Meaning	Units	Benchtop Values
SOC_{res}	reservoir SOC	-	0-100%
SOC_{cell}	cell SOC	-	0-100%
$\dot{V}$	volumetric flowrate	$\text{L}\,\text{s}^{-1}$	$20\ \text{mL}\,\text{min}^{-1}$
V_{res}	reservoir volume	L	16 mL
V_{cell}	cell volume	L	607 µL
A_{cell}	cell geometric area	m^2	$2.20\,\text{cm}^2$
t_{cell}	cell thickness	m	3.2 mm
ϕ	electrode porosity	-	87%
j_{app}	applied current density	$\text{A}\,\text{m}^{-2}$	$40\,\text{mA}\,\text{cm}^{-2}$
j_{sd}	self-discharge current density	$\text{A}\,\text{m}^{-2}$	$8\,\text{mA}\,\text{cm}^{-2}$
c_0	active species concentration	$\text{mol}\,\text{L}^{-1}$	$0.1\,\text{mol}\,\text{L}^{-1}$
F	Faraday's constant	$96\,485\,\text{C}\,\text{mol}^{-1}$	
$E^{\ominus}$	standard cell potential	V	2.2 V
Θ	cell potential	V	1.8-2.5 V
R	gas constant	$8.314\,\text{J}\,\text{K}^{-1}\,\text{mol}^{-1}$	
T	temperature	K	22 °C
η	overpotential	V	±300 mV

to recognize as the reciprocal residence time in the cell, compared to a similar quantity for the reservoir, $\frac{\dot{V}}{V_{\text{res}}}$. Eq. 1.1 and Eq. 1.2 can be added together and solved for $\frac{dSOC_{\text{res}}}{dt}$:

$$\frac{dSOC_{\text{res}}}{dt} = -\frac{V_{\text{cell}}}{V_{\text{res}}}\frac{dSOC_{\text{cell}}}{dt} - \frac{j_{\text{app}}A_{\text{cell}}}{V_{\text{res}}c_0F} - \frac{j_{\text{sd}}A_{\text{cell}}}{V_{\text{res}}c_0F}SOC_{\text{cell}} \tag{1.3}$$

Taking the second derivative of SOC_{cell} with respect to time yields the following expression:

$$V_{\text{cell}}\frac{d^2SOC_{\text{cell}}}{dt^2} = \dot{V}\left(\frac{dSOC_{\text{res}}}{dt} - \frac{dSOC_{\text{cell}}}{dt}\right) - \frac{j_{\text{sd}}A_{\text{cell}}}{c_0F}\frac{dSOC_{\text{cell}}}{dt} \tag{1.4}$$

Substituting Eq. 1.4 into Eq. 1.3 and rearranging to standard form yields the following second order inhomogeneous ordinary differential equation with constant coefficients:

$$\frac{d^2SOC_{\text{cell}}}{dt^2} + \left(\frac{\dot{V}}{V_{\text{res}}} + \frac{\dot{V}}{V_{\text{cell}}} + \frac{j_{\text{sd}}}{\phi t_{\text{cell}} c_0 F}\right)\frac{dSOC_{\text{cell}}}{dt} + \left(\frac{\dot{V} j_{\text{sd}}}{V_{\text{res}}\phi t_{\text{cell}} c_0 F}\right) SOC_{\text{cell}} = -\frac{\dot{V} j_{\text{app}}}{V_{\text{res}}\phi t_{\text{cell}} c_0 F} \quad (1.5)$$

Solving this initial value problem begins by finding the solution for the homogeneous problem (or, the solution with no applied current, *ie*, at open circuit):

$$\frac{d^2SOC_{\text{cell}}}{dt^2} + \left(\frac{\dot{V}}{V_{\text{res}}} + \frac{\dot{V}}{V_{\text{cell}}} + \frac{j_{\text{sd}}}{\phi t_{\text{cell}} c_0 F}\right)\frac{dSOC_{\text{cell}}}{dt} + \left(\frac{\dot{V} j_{\text{sd}}}{V_{\text{res}}\phi t_{\text{cell}} c_0 F}\right) SOC_{\text{cell}} = 0 \quad (1.6)$$

The solution has real and distinct roots when

$$\frac{\dot{V}}{V_{\text{res}}} + \frac{\dot{V}}{V_{\text{cell}}} + \frac{j_{\text{sd}}}{\phi t_{\text{cell}} c_0 F} > 2\sqrt{\frac{\dot{V} j_{\text{sd}}}{V_{\text{res}}\phi t_{\text{cell}} c_0 F,}} \quad (1.7)$$

in which case the general solution of form $SOC_{\text{cell}} = c_1 e^{\lambda_1 t} + c_2 e^{\lambda_2 t}$ has the coefficients

$$\lambda_1, \lambda_2 = \frac{1}{2}\left[- \left(\frac{\dot{V}}{V_{\text{res}}} + \frac{\dot{V}}{V_{\text{cell}}} + \frac{j_{\text{sd}}}{\phi t_{\text{cell}} c_0 F}\right) \pm \sqrt{\left(\frac{\dot{V}}{V_{\text{res}}} + \frac{\dot{V}}{V_{\text{cell}}} + \frac{j_{\text{sd}}}{\phi t_{\text{cell}} c_0 F}\right)^2 - 4\frac{\dot{V} j_{\text{sd}}}{V_{\text{res}}\phi t_{\text{cell}} c_0 F}}\right]. \quad (1.8)$$

With the general solution of the homogeneous problem, the particular solution can now be found. The nonhomogeneous part is constant, so trying $y_p = K$ gives $y_p' = y_p'' = 0$. This yields the following expression for K:

$$\frac{\dot{V} j_{\text{sd}}}{V_{\text{res}}\phi t_{\text{cell}} c_0 F} K = -\frac{\dot{V} j_{\text{app}}}{V_{\text{res}}\phi t_{\text{cell}} c_0 F} \quad (1.9)$$

$$K = -\frac{j_{\text{app}}}{j_{\text{sd}}} \quad (1.10)$$

Now, the general solution of the nonhomogenous initial value problem:

$$SOC_{\text{cell}} = c_1 e^{\lambda_1 t} + c_2 e^{\lambda_2 t} - \frac{j_{\text{app}}}{j_{\text{sd}}} \tag{1.11}$$

$$SOC_{\text{cell}}(0) = SOC_0 \tag{1.12}$$

$$\frac{dSOC_{\text{cell}}}{dt}(0) = \frac{j_{\text{sd}} SOC_0 + j_{\text{app}}}{\phi t_{\text{cell}} c_0 F} \tag{1.13}$$

$$c_1 = \frac{-\frac{j_{\text{sd}} SOC_0 + j_{\text{app}}}{\phi t_{\text{cell}} c_0 F} - \lambda_2 (SOC_0 + \frac{j_{\text{app}}}{j_{\text{sd}}})}{\lambda_1 - \lambda_2} \tag{1.14}$$

$$c_2 = SOC_0 - c_1 + \frac{j_{\text{app}}}{j_{\text{sd}}} \tag{1.15}$$

$$\tag{1.16}$$

$$\lambda_1, \lambda_2 = \frac{1}{2}\Bigg[- \left(\frac{\dot{V}}{V_{\text{res}}} + \frac{\dot{V}}{V_{\text{cell}}} + \frac{j_{\text{sd}}}{\phi t_{\text{cell}} c_0 F} \right) \pm \sqrt{\left(\frac{\dot{V}}{V_{\text{res}}} + \frac{\dot{V}}{V_{\text{cell}}} + \frac{j_{\text{sd}}}{\phi t_{\text{cell}} c_0 F} \right)^2 - 4 \frac{\dot{V} j_{\text{sd}}}{V_{\text{res}} \phi t_{\text{cell}} c_0 F}} \Bigg] \tag{1.17}$$

These above equations define an exact solution to the zero-dimensional model of a symmetric porous-separator-based flow battery with a constant faradaic applied current and some amount of self-discharge proportional to state of charge.

An output equation 1.18 can approximate the terminal voltage of the cell from SOC_{cell} using an expression that accounts for the Nernstian equilibrium potential and a current-dependent overpotential,

$$\Theta = E^{\ominus} + \frac{2RT}{F} \ln \frac{SOC_{\text{cell}}}{1 - SOC_{\text{cell}}} + \eta(j_{\text{app}}). \tag{1.18}$$

In Eq. 1.18 the Nernstian potential is dependent on SOC. A generic overpotential term, which generally accounts for kinetic overpotential, ohmic losses, and diffusion potential (concentration overpotential), is expressed as a function of applied current density. Only a rough approximation of overpotential will suffice for the present exploration; a polarization curve with the following simplified form from [67] shall be used by fitting experimental data:

$$\eta(j_{\text{app}}) = -j_{\text{app}} * \text{ASR} + c \ln \left(1 - \frac{j_{\text{app}}}{j_{\text{lim}}} \right), \tag{1.19}$$

where ASR is the area-specific ohmic resistance in $\Omega\,\mathrm{cm}^{-2}$, c is an empirical constant describing concentration overpotential in V/decade, and j_{lim} is the mass-transfer limited current density in $\mathrm{mA\,cm}^{-2}$.

Kinetic terms were omitted for the present application with $\mathrm{V(acac)_3}$ because there were no kinetic limitations present in the polarization data which allowed for fitting of kinetic terms (shown in Fig. 1.10). This is justified by the fast kinetics measured by Shinkle *et al.* who determined the positive $\mathrm{V(acac)_3/V(acac)_3^+}$ couple to have immeasurably fast kinetics "significantly faster than any electrode process in the aqueous all-vanadium flow battery" and the negative $\mathrm{V(acac)_3/V(acac)_3^-}$ couple to have kinetics on the same order as the aqueous V(IV)/V(V) couple, with the nonaqueous system having an exchange current density of $1.3\,\mathrm{A\,m}^{-2}$ on glassy carbon [68].

1.5.2 Behavior

Now, charge/discharge cycles can be simulated with the the analytical model. Voltage cutoffs typically used in charge-discharge cycling are enforced by iteratively seeking the SOC_{cell} which corresponds to the end of the half-cycle using Eq. 1.18. Cycles can also be set to fixed charge cutoffs (*ie.* stopping a charge step after a fixed time). In the model simulation the initial condition for SOC_{cell} on charge is estimated by first simulating a discharge half-cycle from 100% state of charge, which hits a voltage cutoff before arriving at 0% SOC_{cell}. This makes sure the simulation does not include the first-cycle behavior of a longer charge time due to starting from true 0% state of charge.

A representative simulation helps to demonstrate the utility of this model. To do this, experimental data for a polarization curve of a benchtop cell with 0.1 M $\mathrm{V(acac)_3}$ and 0.3 M $\mathrm{TEABF_4}$ are fit using Eq. 1.19; a comparison of experimental data and the best-fit curve is shown in Fig. 1.10. The relevant experimental procedures used in the collection of this polarization data was identical to the methods of Saraidaridis and Monroe [69]. The best-fit curve yields an empirical concentration overpotential constant c of 0.35 V/decade, cell ASR of $1.56\,\Omega\,\mathrm{cm}^{-2}$,

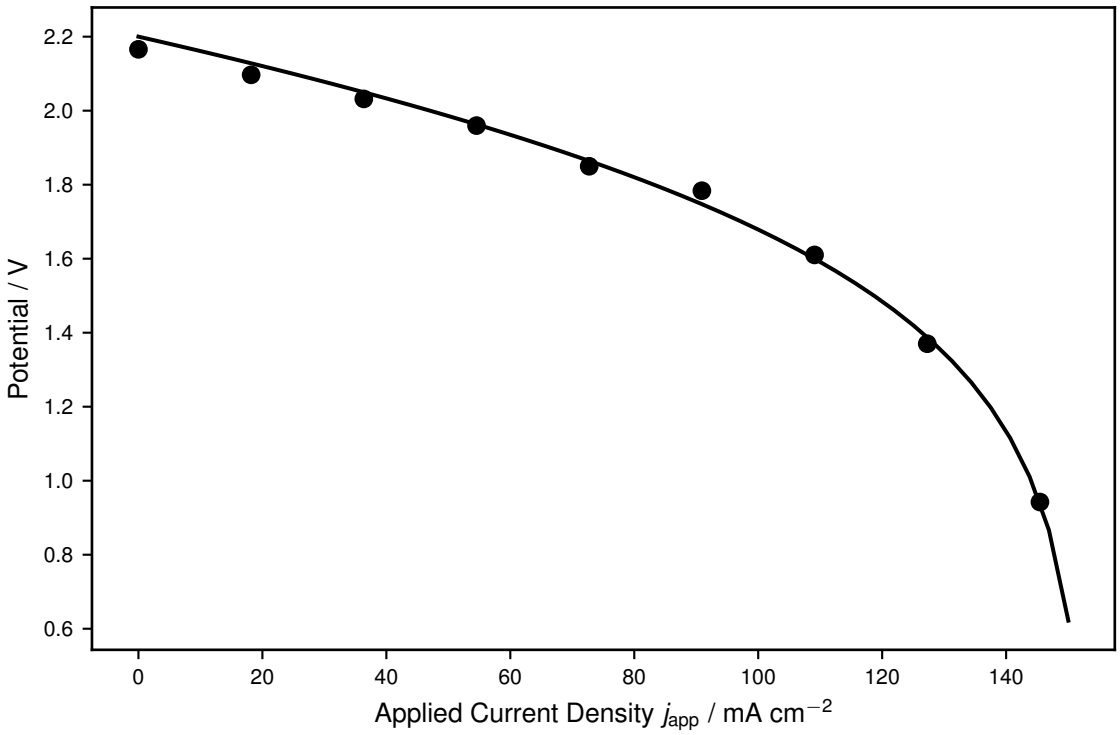


Figure 1.10: Polarization experimental datapoints and best-fit curve for 0.1 M $V(acac)_3$ flow cell showing no apparent kinetic limitations in the low-current-density region with untreated carbon felt electrodes, using the experimental methods of Saraidaridis and Monroe [69]

and limiting current j_{lim} of 153 mA cm^{-2}. These values for a real (albeit very unoptimized) symmetric nonaqueous flow cell will be used in the remainder of this chapter as a rough approximation.

Figure 1.11 serves as a representative simulation output using values for a typical benchtop $V(acac)_3$ experiment, with the polarization data above. This simulation used an applied current density of 40 mA cm^{-2}, flowrate of 20 mL min^{-1}, combined reservoir volume of 16 mL, geometric cell area of 2.2 cm, initial active species concentration of 0.1 M and high voltage cutoff of 2.7 V. These values are commensurate with the benchtop flow battery experiments described in the following chapter. Importantly, a j_{sd} value of 8 mA cm^{-2}/SOC was used, which was the value determined by the real-time measurement technique developed in the following chapter. This model output is presented here due to its utility in demonstrating how the model framework can be integrated with technoeconomic models to

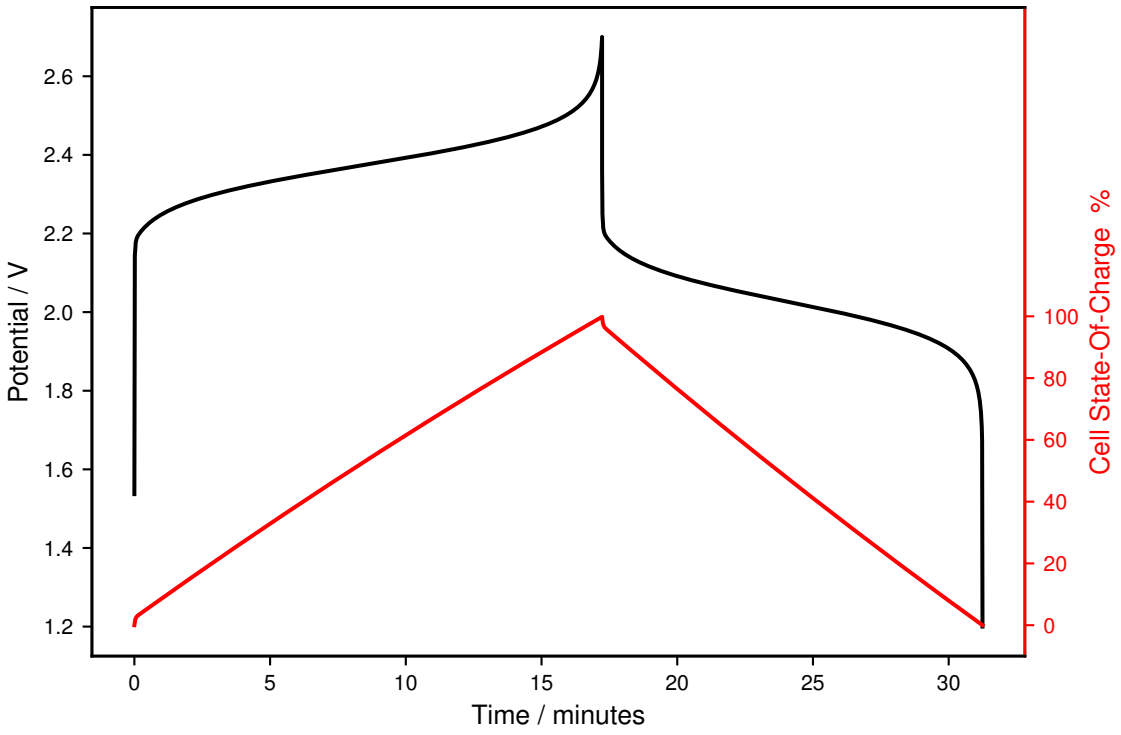


Figure 1.11: Representative charge-discharge simulation for a standard $V(acac)_3$ benchtop experiment

illustrate general and fundamental principles of symmetric flow batteries with porous separators. Simulating this charge-discharge cycle, with the iterative process to find the voltage cutoff, took approximately 10 milliseconds on a professional-grade laptop.

Analysis of the charge-discharge cycle from Fig. 1.11 yields following efficiencies: 82% coulombic, 70% voltaic, 57% energy, and 91% utilization. Energy capacity on charge is $3.5\,\mathrm{W\,h\,L^{-1}}$, and $2.5\,\mathrm{W\,h\,L^{-1}}$ on discharge.

Notably, these results come from a representative simulation of a low-concentration, highly unoptimized benchtop system of an experimental chemistry, and as such are not meant to be compared to specification of at-scale flow battery systems. The present purpose is to understand the system-level tradeoffs of various component properties and operational parameters for the previously unexplored porous-separator symmetric RFB design space. In the present system, the energetic losses are primarily due to coloumbic losses from self-discharge through the porous separator and voltaic losses from the ohmic resistance of the system. In a real system,

with a porous separator designed for the application, a both higher coulombic and voltaic efficiencies could realistically be achieved. The Celgard and Dreamweaver separators and filtration materials used as porous separators in this dissertation are not designed for RFB applications. Celgard 4560 is designed for secondary lithium-ion batteries (without convection) while the filter materials used in Ch. 3 are for dead-end filtration. A brief discussion of utilization efficiency follows.

Emphasis on Utilization Efficiency

In the reporting of standard RFB charge/discharge cycling, coulombic efficiency (CE) is defined as the ratio of coulombs accessed on discharge to coulombs applied during charge. Energy efficiency (EE) is defined as the ratio of joules accessed on discharge to joules applied during charge. Voltaic efficiency (VE) is determined by dividing the energy efficiency by the coulombic efficiency and represents the ratio of the average voltage accessed on discharge to the average voltage applied/observed on charge.

A critical performance parameter under-reported in literature relates to effective energy density. Often, the maximum solubility of an active species will be multiplied by its redox potential to report the theoretical maximum energy density. Charge/discharge cycling results are reported along with corresponding efficiency values, but not the amount of charge or energy accessed during discharge. This obscures two phenomena: capacity fade and accessible energy on discharge. A RFB chemistry can appear stable when only looking at efficiency metrics, but capacity could still fade with each cycle while maintaining commensurate efficiencies as reported by Laramie *et al.* [26]. Furthermore, by not reporting the accessible energy on discharge in comparison to the theoretical energy deliverable, the RFB community loses focus on an important research objective: converting as much of the active materials in the reservoirs as possible. RFB analysis must rigorously check how much of the active material is accessed *vs.* how much remains unconverted.

Utilization efficiency (UE) is defined as

$$\epsilon_{\mathrm{u}} = \frac{Q_{\mathrm{discharge}}}{c_0 n F V_{\mathrm{res}}}, \tag{1.20}$$

where $Q_{\text{discharge}}$ is electrical charge accessed on discharge, c_0 is the concentration of active species, n is the number of electrons transferred per molecule of active species, F is Faraday's constant, and V_{res} is the electrolyte volume of one reservoir. The term "electrochemical yield" has been used to refer to this metric in the literature [**kolesnichenkoElucidatingInstabilitiesContributing**, 45, 70, 71], but definition as an efficiency allows for more direct comparison with coulombic, voltaic, and energy efficiencies which utilization efficiency may vary in relation with.

Another way to interpret utilization efficiency is as a proxy for the maximum accessible state-of-charge, on a discharge basis. Dividing the utilization efficiency by the coulombic efficiency then gives the state-of-charge accessed during the charging step.

While no system can expect to reach its theoretical energy density due to irreversible losses from kinetic, ohmic, and concentration overpotentials, the discrepancy cannot be simply attributed to coulombic and voltaic efficiency losses. In every RFB, the system will hit the upper voltage cutoff before converting all of the active species in solution, ostensibly to prevent unwanted high-voltage side reactions and protect cell components. This steep increase in voltage at the end of charging corresponds to the vertical asymptotes predicted by the Nernst equation at 100% SOC. This phenomenon is always encountered before 100% theoretical SOC in a real RFB, because the local SOC and active-species concentrations at the electrode surface differ from their values in the reservoir. This difference can prematurely trigger the end-of-charge voltage cutoff and reduce voltaic efficiency. Voltaic inefficiency in the form of concentration overpotential *can* limit utilization efficiency due to premature voltage cutoff, though the voltaic efficiency metric itself does not *directly* affect the extent to which active species react. Voltaic and coulombic inefficiencies do not fully account for this lack of active-species utilization, though they are at times used to explain this issue, as in [72].

Now, the behavior of symmetric flow batteries with porous separators can be simulated to show qualitative trends. First, a range of current densities are simulated, holding all other parameters constant.

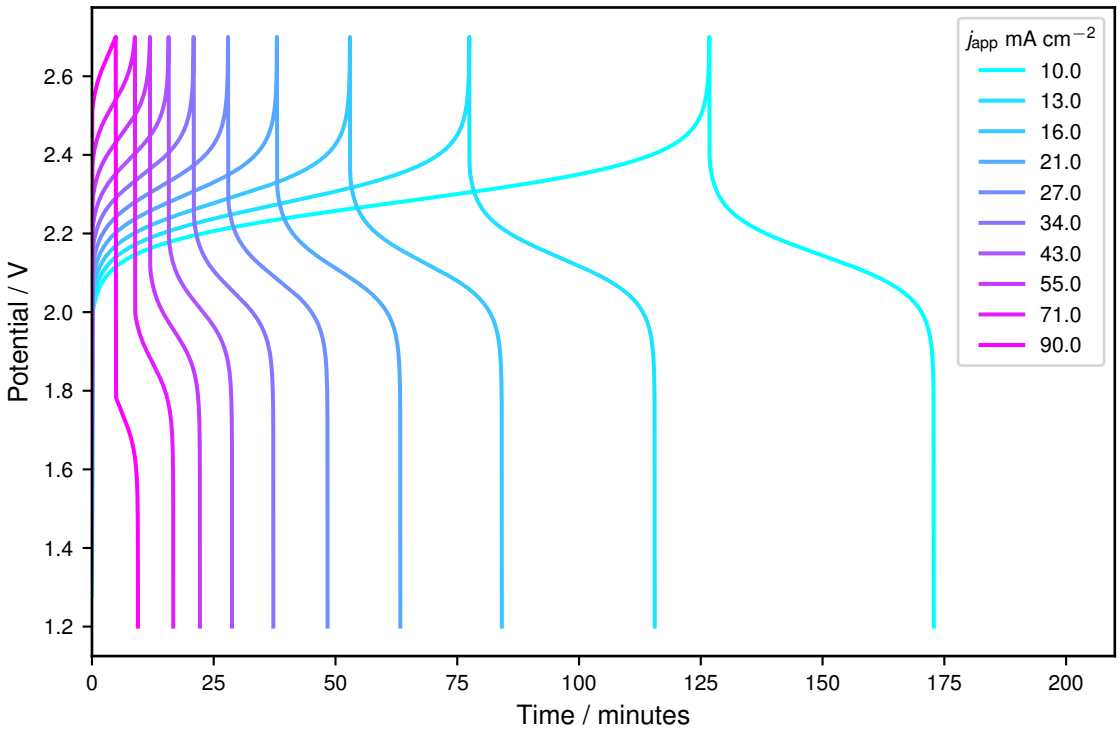


Figure 1.12: Model charge/discharge curves as applied current density varies

Applied Current Density

Sweeping the applied current density from 10 mA cm^{-2}–90 mA cm^{-2} produces the charge-discharge curves shown in Fig. 1.12, and resulting efficiencies and energy densities in Fig. 1.13.

Fig. 1.12 shows the intuitive behavior of a higher current producing a larger ohmic drop, shortening charge cycles by hitting the high voltage cutoff earlier. Fig. 1.13 lends more useful information. Local maxima at different j_{app} appear for voltaic efficiency, energy efficiency, utilization efficiency, and discharge energy density.

Note how couloumbic efficiency is monotonically increasing in the range of applied current densities. This behavior is a key characteristic of flow batteries with porous separators, because higher current densities lead to shorter cycle times, and thus less time for self discharge as the ratio $\frac{j_{app}}{j_{sd}}$ increases. IEM-based flow batteries possess intrinsically high $\frac{j_{app}}{j_{sd}}$ due to very low j_{sd}, and their coulombic efficiencies are typically >99% across their range of operating current densities. The effective absence of self-discharge for IEM-based flow batteries then means

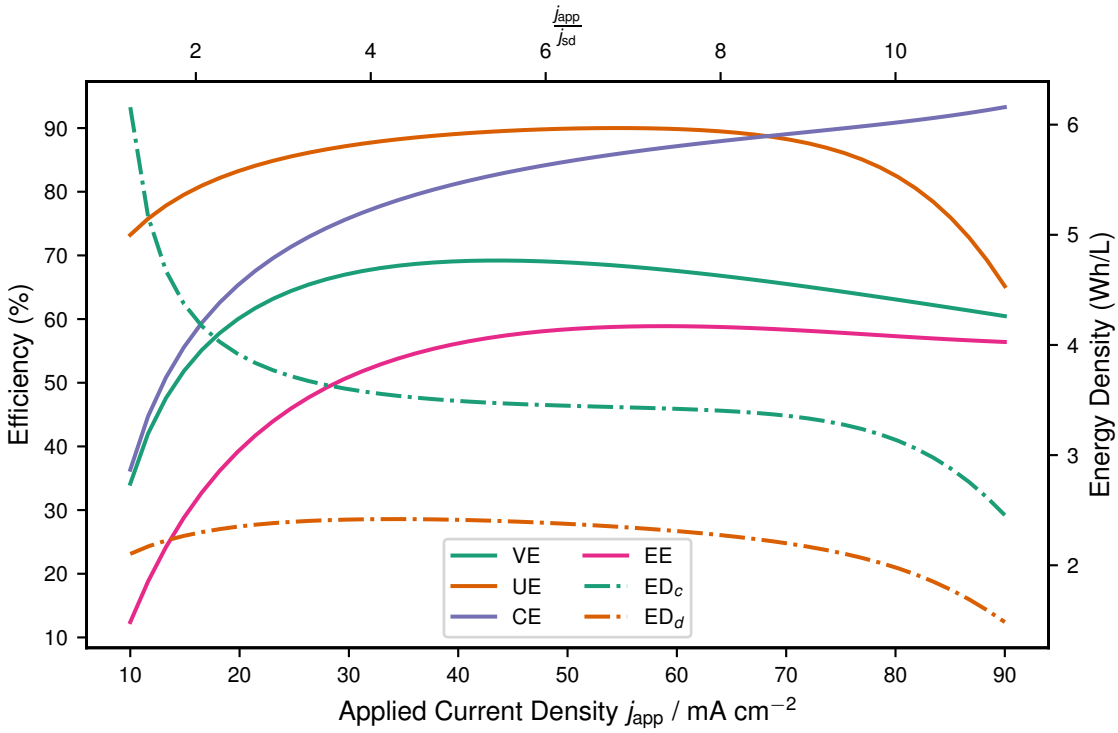


Figure 1.13: Model efficiencies as applied current density varies

voltaic and energy efficiencies typically decrease monotonically as j_{app} increases. Here, Fig. 1.13 shows local maxima in voltaic and energy efficiencies at nonzero j_{app}. This behavior is fundamental to these systems using porous separators and not found in conventional flow batteries using IEMs.

Self-Discharge Current Density

Next, the self-discharge current density is varied by orders of magnitude on either side of the previously used value of $8\,\mathrm{mA\,cm^{-2}}$ to produce the charge-discharge curves shown in Fig. 1.14 and resulting efficiencies and energy densities in Fig. 1.15.

Fig. 1.14 shows how a larger j_{sd} value produces a longer charge step and shorter discharge cycle due to the increased propensity for self-discharge. Fig. 1.15 shows entirely monotonic behavior for all curves shown. As expected, overall performance decreases in every way as self-discharge current density increases. A useful insight from this, however, is that performance remains fairly steady until a threshold roughly at $\frac{j_{app}}{j_{sd}} = 10$, after which performance drops precipitously. This

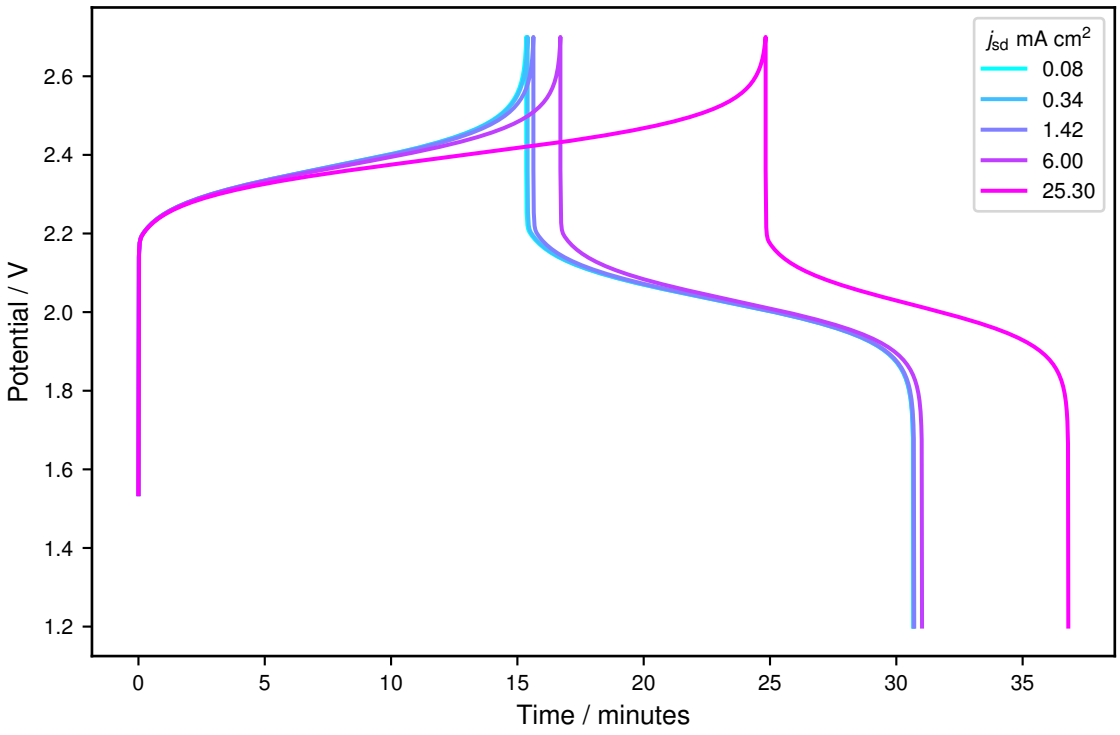


Figure 1.14: Model charge/discharge curves as self-discharge current density varies with fixed applied current density of 40 mA cm^{-2}

suggests that with technoeconomic insights, and knowledge of porous separator cost-performance tradeoffs, there may be acceptable levels of self-discharge which justify the use of porous separators.

Area-Specific Resistance

Another simple parameter to vary and observe with this model is the area-specific resistance of the cell. This is defined as the resistance of the cell normalized to the geometric area A_{cell} as shown previously in Fig. 1.9. Sweeping the ASR from $0\,\Omega\,\text{cm}^2$–$14\,\Omega\,\text{cm}^2$ produces the charge-discharge curves shown in Fig. 1.16, and resulting efficiencies and energy densities in Fig. 1.17.

Fig. 1.16 is similar to Fig. 1.12, which is understandable because both simulations are directly varying the overpotential in the cell. There are subtle differences, though: in 1.12, except for the highest current densities, the end of charge is initiated by the vertical asymptote of the nernstian charge profile, whereas in 1.16 ohmic overpotential triggers the voltage cutoff instead.

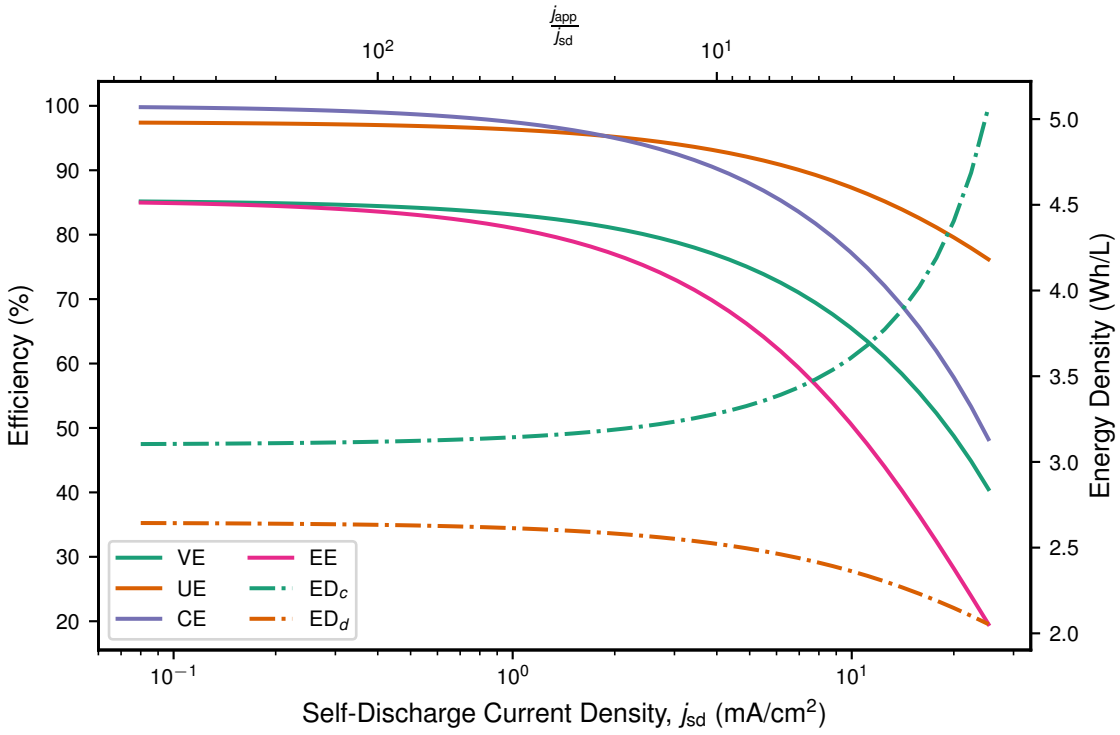


Figure 1.15: Model charge/discharge curves as self-discharge current density varies with fixed applied current density of 40 mA cm^{-2}

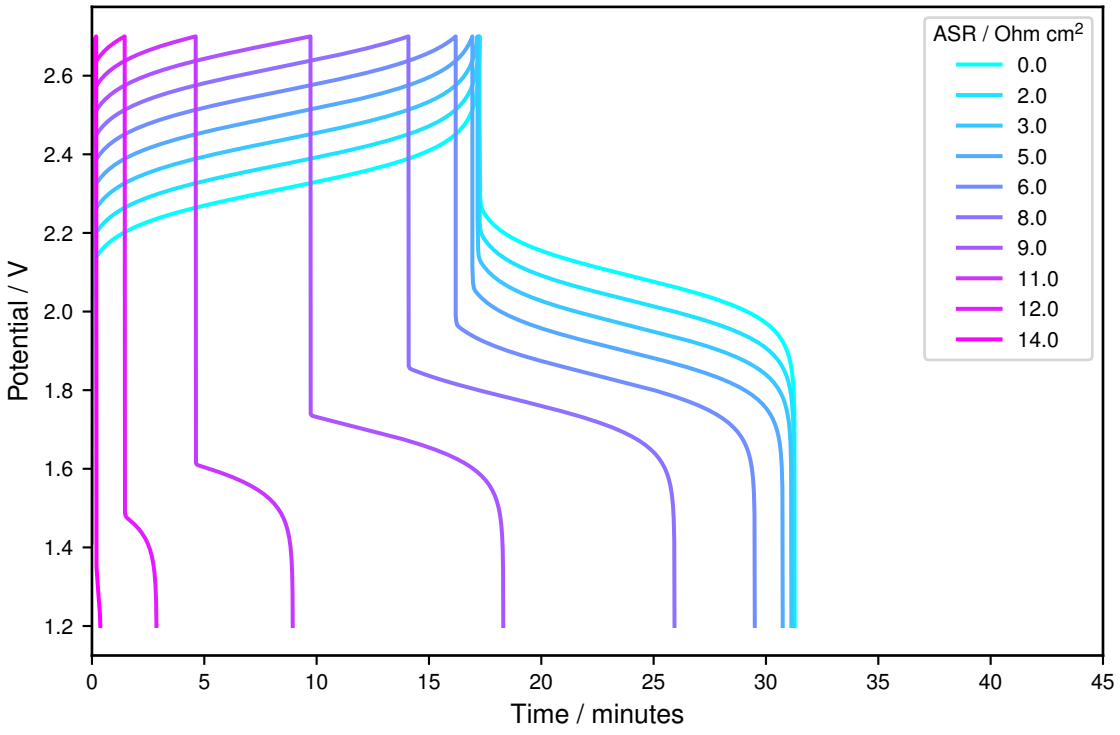


Figure 1.16: Model charge/discharge curves as ASR varies

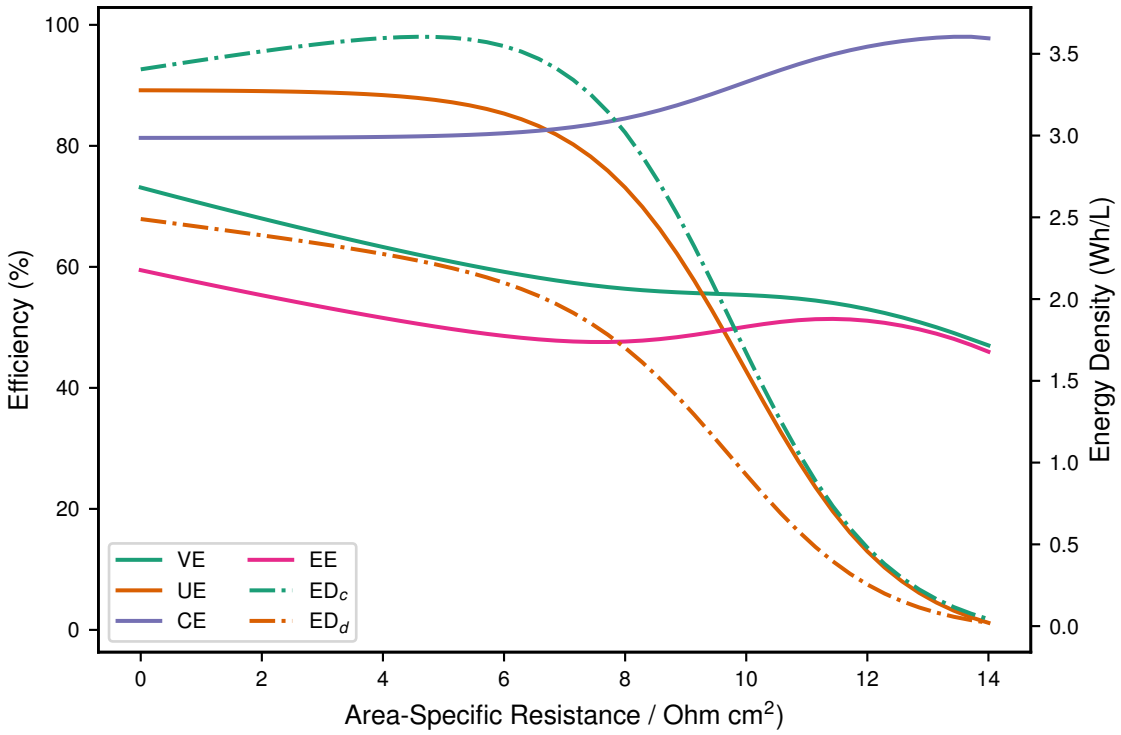


Figure 1.17: Model efficiencies as ASR varies

Fig. 1.17 is quite different from Fig. 1.13. Voltaic efficiency monotonically decreases as ASR increases. Intuitively, an ASR as close to zero as possible is desirable, but if a flow battery has a porous separator with nonzero self-discharge tendencies, the optimal applied current is not as close to zero as possible. In a real system, there are likely relationships between ASR and self-discharge, so behavior can not be directly uncoupled as presented here.

Flowrate

Varying flowrate demonstrates some interesting behavior, although it is not particularly useful in the context of the present model because the mass-transfer relationship between flowrate and limiting current is not considered. Still, the model responds to changes in flowrate, especially at low flowrates—albeit flowrates too low to be realistically used experimentally.

Fig. 1.18 shows cycle length decreasing dramatically as flowrate decreases from $1\,\mathrm{mL\,min^{-1}}$ to stagnation. In Fig. 1.19, efficiencies and energy densities are plotted

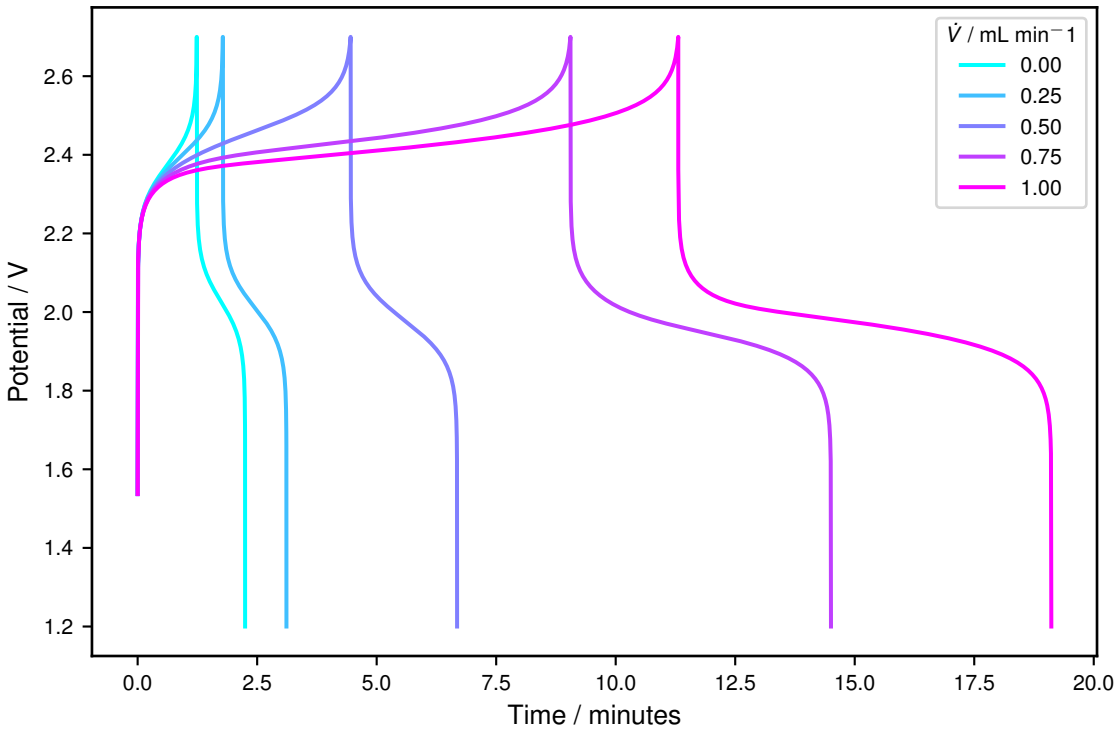


Figure 1.18: Model charge/discharge curves as flowrate varies

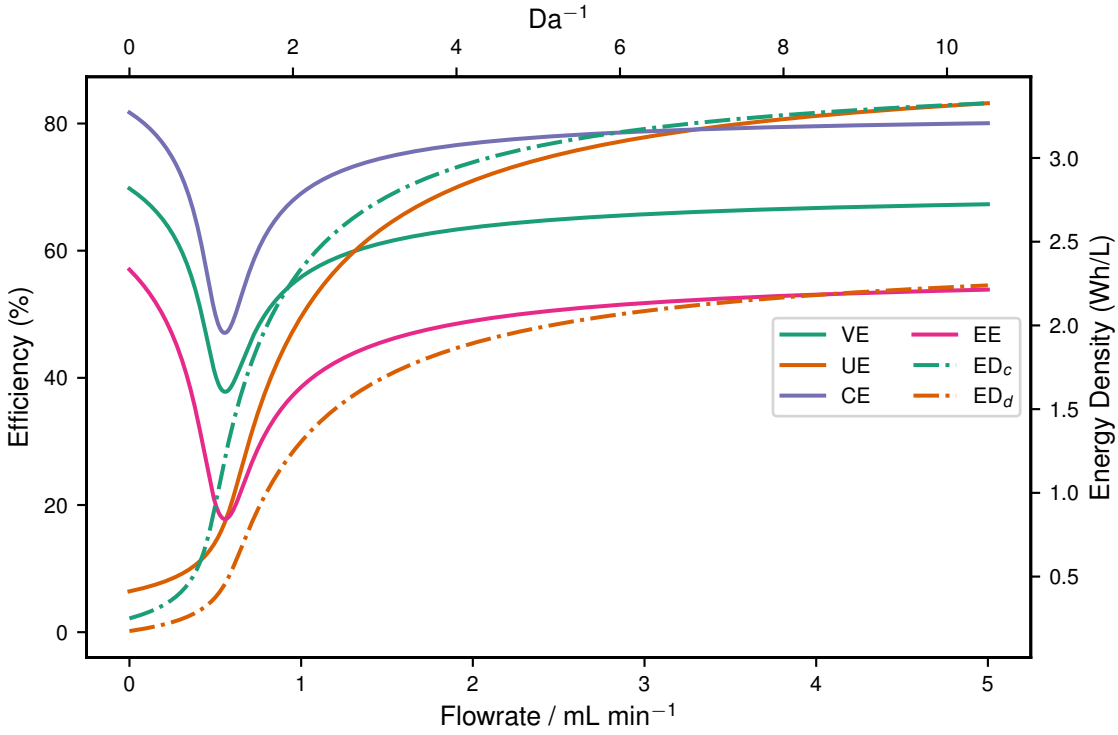


Figure 1.19: Model efficiencies as flowrate varies

against both the flowrate and the reciprocal of a dimensionless Damköhler number defined as $\mathrm{Da} = \frac{j_{\mathrm{app}} V_{\mathrm{cell}}}{c_0 F t_{\mathrm{cell}} \dot{V}}$. This Damköhler number is the ratio of the applied electrochemical reaction rate to the rate of forced convective mass transport in the cell. It is intuitive that the rate of convective mass transport in the cell should ideally be several times larger than the rate of electrochemical reactions, and Fig. 1.18 confirms this, as well as demonstrating that the model is functioning as expected. The results suggest that flow batteries must operate with $\mathrm{Da}^{-1} >> 1$, notwithstanding mass transport limitations which are not included here. For reference, the standard operating flowrate for the benchtop cell whose values are taken for this simulation are greater than or equal to $10\,\mathrm{mL\,min^{-1}}$ or a Da^{-1} of approximately 20.

The myriad performance outputs of this fundamental model for flow batteries with porous separators may now be coupled to more holistic technoeconomic models for capital cost and levelized cost of energy stored.

1.6 Technoeconomics

The present, overarching motivation for flow battery development is to find affordable, durable, grid-scale energy-storage solutions—ostensibly to allow for further use of wind and solar resources in an attempt to decarbonize and mitigate the worst effects of climate change in a way compatible with the current global economic framework, which necessitates perpetual "growth." Additionally, finding materials that do not introduce problematic supply-chain or end-of-life-disposal issues would be ideal; *ie*, finding materials which are compatible with the emerging circular economies of the world. In the absence of a "sociotechnoeconomic model," however, the current section will briefly modify and merge existing technoeconomic models for flow batteries and to quantitatively illustrate the motivation for further chapters of this thesis.

Darling *et al.* formulated the following cost equation for flow batteries [3]:

$$\frac{P_0}{E_{\mathrm{d}}} = C_{\mathrm{reactor}} + C_{\mathrm{electrolyte}} + C_{\mathrm{additional}} + C_{\mathrm{BOP}}[=]\frac{\$}{\mathrm{kWh}}, \tag{1.21}$$

where P_0 is capital expenditure in \$, E_d is energy accessed on discharge in kW h, and the terms on the right indicate the individual cost contributions of the reactor, electrolyte, additional, and balance-of-plant costs, respectively, all in \$/kWh.

Equation 1.21, widely used in recent literature to describe the economics of flow batteries, is based off the work of Newman *et al.* [73] and Poonpun and Jewell [74]. The Darling *et al.* model, known colloquially as the DG model, was later extended by Dmello *et al.* [25]. The DG model paper was widely adopted in part because of the joint academic and industrial affilitions of the authors, who gave private sector perspectives on current and future components costs. The extension by Dmello *et al.* in addition to providing sensitivity analyses of design architectures not considered in the DG model, provided all code for the model as supplementary material which eased the process of introducing modifications and/or simplifications for the present work.

1.6.1 Capital Expenditure

The following changes have been implemented from the definitions used by Darling *et al.* and Dmello *et al.*:

1. switch to mole fraction electrolyte specification (from mass fraction/other coefficients)

2. switch to mole fraction accessible electrons to account for multiple electron transfers and symmetric/mixed electrolyte systems

3. use of utilization efficiency instead of allowable SOC range

4. determination of reactor area from porous separator model outputs

These changes do not fundamentally alter the model, but allow for simplification and adaption to the systems considered in this dissertation, as well as for direct coupling to the previously described porous-separator RFB model.

Change 1 was made largely out of preference for mole fraction electrolyte composition over mass fraction, although they are easily interconvertible. Specifying

the electrolyte formulation by mole fraction, however, removes many terms from the DG model concerned with active and salt solubility, mean actives molality, mean salt molality, stoichiometric coefficients, *etc.* Rather, all that is needed is the mole fraction composition of the electrolyte, molecular weights, and constituent component costs on a mass basis. The same information is captured with either approach, but specifying the formulation by initial mole/mass fraction rather than an array of solubilities of various solution components and coefficients allows for a less cluttered model, with the relevant stoichiometric ratios captured by the respective component fractions.

Change 2 was incorporated to more easily account for mixed electrolyte and/or disproportionation systems, where there may be intentionally non-reacting active species in either reservoir or a disproportionation molecule means there is only a singular active species present on either side. This change contrasts the existing TEA literature principally focused on dissimilar electrolytes in either reservoir which transfer varying number of electrons.

Change 3 replaces the DG model's allowable SOC range χ with utilization efficiency, because in the present work, the allowable SOC range is not known *a priori* and utilization efficiency is more of a performance characteristic than an operational parameter. Also, this change leads to consistent terminology with the porous separator RFB model.

Change 4 further simplifies the model by taking outputs from the porous separator RFB model and tying them directly to the definitions of reactor area given in the DE model.

Making these changes results in the following equations to describe costs. Parameter/variable definitions are given in Table 1.2. Examining the equation for reactor cost first, c_a is the cost per unit geometric area (membrane, electrode, plate, *etc.*), $\epsilon_\mathrm{sys,d}$ is the AC system efficiency on discharge (incl. losses due to auxiliary equipment and pumping), i_d is average discharge current density, V_d is average discharge voltage, and t_d is discharge time. Reactor cost area estimation uses Eq. 1.22 which is identical to equation 5 in [3], but the present analysis can use terms

E_d, V_d, and i_d directly from the outputs of the previously described model for porous separator flow battery performance. Darling *et al.* go on to modify Eq. 1.22 to incorporate polarization behavior, which has already been taken into account.

$$C_\mathrm{reactor} = \frac{c_\mathrm{a}}{\epsilon_\mathrm{sys,d} i_\mathrm{d} V_\mathrm{d} t_\mathrm{d}} \tag{1.22}$$

Modifying equation eight from [3], a multicomponent electrolyte is specified by mole fractions (x_i), and the per-species allowable SOC range, χ, is replaced with the previously-defined utilization efficiency, ϵ_u, which succinctly captures the degree to which active species are utilized on discharge under specified (*i.e.* long-term) operating conditions. When directly coupling the previous model for porous separator flow battery behavior, ϵ_u can be omitted, as the model's output t_d will account for under-utilization of active material. The mass-specific cost of a given electrolyte component, $c_{m,i}$, is similar to the extension of the DG model [3] by Dmello *et al.* [25]. The number of electrons per mole active species as well as possible salt-configuration (ratios, rocking chair, non-monovalent salts, *etc.*) are all captured by the respective x_i, and instead the mole fraction of electrons $n_{e^-,i}$ specifies the number of available for redox states for a species. The mole fractions are evaluated as the sum of both positive and negative electrolytes. This form is useful for incorporation of additional components such as cosolvents, additional salts, surfactants, complexation agents, *etc.* in a symmetric system. The constant 2 in Eq. 1.23 accounts for the existence of two reservoirs having identical compositions in this symmetric system.

$$C_\mathrm{electrolyte} = 2 \sum_i \frac{c_{\mathrm{m},i} M_i x_i}{n_{e^-,i}} \left[\epsilon_\mathrm{sys,d} \epsilon_\mathrm{q} \epsilon_\mathrm{u} V_\mathrm{d} F \right]^{-1} \tag{1.23}$$

$$C_\mathrm{add} = \frac{c_\mathrm{add}}{t_\mathrm{d}} \tag{1.24}$$

$$C_\mathrm{BOP} = \frac{c_\mathrm{BOP}}{t_\mathrm{d}} \tag{1.25}$$

Due to the intrinsically decoupled energy/power relationship in RFBs, the unit cost of the reactor goes down as the power-related i_d and V_d terms in the

Table 1.2: Definitions of terms in present technoeconomic model

Parameter	Meaning	Units
P_0	capital cost	\$
E_d	energy on discharge	kWh
C_reactor	reactor cost	\$ kWh^{-1}
$C_\mathrm{electrolyte}$	electrolyte cost	\$ kWh^{-1}
C_add	additional cost	\$ kWh^{-1}
C_BOP	balance-of-plant cost	\$ kWh^{-1}
c_a	reactor cost per unit geometric area	\$ m^{-2}
$c_{\mathrm{m},i}$	cost of species i	\$ kg^{-1}
c_add	additional cost	\$ kW^{-1}
c_BOP	balance-of-plant cost	\$ kW^{-1}
i_d	average discharge current density	A m^{-2}
V_d	average discharge cell voltage	V
t_d	discharge time	h
M_i	molar mass of species i	kg mol^{-1}
x_i	mole fraction of species i	-
$n_{e^-,i}$	number of accessible electrons per mole i	e^-/mol
$\epsilon_\mathrm{sys,d}$	system discharge efficiency	-
ϵ_q	coulombic efficiency	-
ϵ_u	utilization efficiency	-
F	Faraday's constant	96 485 C mol^{-1}

denominator of Eq. 1.22 increase in magnitude. Importantly, the cost for nonaqueous c_a taken from [3] is much lower than that of aqueous systems, due to the possibility of substituting an olefin-based porous separator in place of a more expensive fluorinated ion exchange membrane.

The electrolyte cost $C_\mathrm{electrolyte}$ described by Eq. 1.23 is also straightforward; higher efficiencies and discharge voltages, more electrons per mole active species, and lower molecular weights/cost per unit mass components all produce a more affordable electrolyte. $c_\mathrm{additional}$ and c_BOP are both fixed values taken from [3], with average values taken for nonaqueous systems.

The intrinsic energy/power decoupling and long-term behavior of flow battery cost can be seen by examining these individual cost components in the limit of long discharge duration t_d. $C_\mathrm{electrolyte}$ is the only term without t_d in its denominator, meaning the capital cost of the entire system eventually approaches energy-related

$C_{\text{electrolyte}}$ at large t_{d} values, a basic feature of all energy/power decoupled energy storage systems.

A 3 V, 5 hour battery is considered using the nominal values from Dmello *et al.* [25], but with adjustments to the electrolyte composition. Table 1.3 defines a conventional asymmetric-flow-battery electrolyte with disparate, unmixed positive electrolytes. Note that the salt mole fraction is half the mole fraction of the individual positive and negative active species, which is the minimum value required for a binary salt. Table 1.4 defines a symmetric electrolyte using a disproportionation compound in a salt-splitting configuration. Note that in this case, the molecular weight of the disproportionation compound has doubled, and the number of electrons transferred by it is now two. Table 1.4 defines a symmetric electrolyte using a mixed electrolyte, salt splitting approach. Comparing with the asymmetric case in Table 1.3, note how the mole fractions of both the positive and negative species are doubled, yet the salt mole fraction stays the same, and the number of electrons transferred per mole actives has halved. This is inherent to the mixed-electrolyte symmetric approach, wherein half of the active species on either side are not utilized. Table 1.6 defines a symmetric electrolyte using a disproportionation compound in a rocking-chair configuration. Comparing with the symmetric, disproportionation, salt-splitting case in Table 1.4, note how there is no explicit salt species anymore and the molecular weight of the disproporationation salt has increased by another 100 g/mol to account for the increasingly bulky compound which now contains inert counterions to serve as supporting electrolyte.

Using the above equations for capital cost and values for the discussed configurations, a brief comparison of different all-liquid flow battery architectures is made in Fig. 1.20.

The cost inputs to Fig. 1.20 were chosen in order to be commensurate with the target cost breakdowns from Darling *et al.* and Dmello *et al.* which sought to determine material parameters that would achieve sub-100 $\$\,\text{kW}^{-1}\,\text{h}$ of installed capital cost. These targets were set by the US Department of Energy for long-duration energy storage in the GRIDS program in 2010 [75], and used by Darling

Table 1.3: Values for asymmetric, salt-splitting flow battery electrolyte capital cost estimation

Parameter	Meaning	Units
c_p	cost of positive species	$5\,\$\,\mathrm{kg}^{-1}$
M_p	molecular weight of positive species	$100\,\mathrm{g\,mol}^{-1}$
x_p	mole fraction of positive species	0.1
n_p	electrons per mole positive species	1
c_n	cost of negative species	$5\,\$\,\mathrm{kg}^{-1}$
M_n	molecular weight of negative species	$100\,\mathrm{g\,mol}^{-1}$
x_n	mole fraction of negative species	0.1
n_n	electrons per mole negative species	1
c_salt	cost of salt	$20\,\$\,\mathrm{kg}^{-1}$
M_salt	molecular weight of salt	$100\,\mathrm{g\,mol}^{-1}$
x_salt	mole fraction of salt	0.05
c_sol	cost of solvent	$2\,\$\,\mathrm{kg}^{-1}$
M_sol	molecular weight of solvent	$40\,\mathrm{g\,mol}^{-1}$
x_sol	mole fraction of solvent	.75

Table 1.4: Values for symmetric, disproportionation, salt-splitting flow battery electrolyte capital cost estimation

Parameter	Meaning	Units
c_d	cost of positive species	$5\,\$\,\mathrm{kg}^{-1}$
M_d	molecular weight of positive species	$200\,\mathrm{g\,mol}^{-1}$
x_d	mole fraction of positive species	0.1
n_d	electrons per mole positive species	2
c_salt	cost of salt	$20\,\$\,\mathrm{kg}^{-1}$
M_salt	molecular weight of salt	$100\,\mathrm{g\,mol}^{-1}$
x_salt	mole fraction of salt	0.05
c_sol	cost of solvent	$2\,\$\,\mathrm{kg}^{-1}$
M_sol	molecular weight of solvent	$40\,\mathrm{g\,mol}^{-1}$
x_sol	mole fraction of solvent	0.85

et al. Dmello *et al.* and many others as cost targets in 2010s. As of the writing of this dissertation, no concrete evidence exists to suggest that this target has been achieved; yet, the next decades technoeconomic targets have become nearly an order of magnitude lower, with some researchers calling for sub-$10/kWh and the US Department of Energy "Long Duration Storage Shot" program calling for $15-30/kWh, with round-trip energy efficiencies above 60%. While cost targets continue to drop, sub-$100/kWh electrochemical energy storage devices do not yet exist, and as such $100/kWh was used as a nominal target in order to be

Table 1.5: Values for symmetric, mixed electrolyte, salt-splitting flow battery electrolyte capital cost estimation

Parameter	Meaning	Units
c_p	cost of positive species	$5\,\$\,\mathrm{kg}^{-1}$
M_p	molecular weight of positive species	$100\,\mathrm{g\,mol}^{-1}$
x_p	mole fraction of positive species	0.2
n_p	electrons per mole positive species	.5
c_n	cost of negative species	$5\,\$\,\mathrm{kg}^{-1}$
M_n	molecular weight of negative species	$100\,\mathrm{g\,mol}^{-1}$
x_n	mole fraction of negative species	0.2
n_n	electrons per mole negative species	.5
c_salt	cost of salt	$20\,\$\,\mathrm{kg}^{-1}$
M_salt	molecular weight of salt	$100\,\mathrm{g\,mol}^{-1}$
x_salt	mole fraction of salt	0.05
c_sol	cost of solvent	$2\,\$\,\mathrm{kg}^{-1}$
M_sol	molecular weight of solvent	$40\,\mathrm{g\,mol}^{-1}$
x_sol	mole fraction of solvent	0.55

Table 1.6: Values for symmetric, disproportionation, rocking-chair flow battery electrolyte capital cost estimation

Parameter	Meaning	Units
c_d	cost of disproportionation salt species	$5\,\$\,\mathrm{kg}^{-1}$
M_d	molecular weight of disproportionation salt species	$300\,\mathrm{g\,mol}^{-1}$
x_d	mole fraction of disproportionation salt species	0.1
n_d	electrons per mole disproportionation salt species	2
c_sol	cost of solvent	$2\,\$\,\mathrm{kg}^{-1}$
M_sol	molecular weight of solvent	$40\,\mathrm{g\,mol}^{-1}$
x_sol	mole fraction of solvent	0.9

compatible with existing RFB technoeconomic literature which has used this same target in recent years.

Fig. 1.20 shows constant power-related costs for all configurations, which is expected as the only parameters varied are those defined in the preceding tables which specify the electrolyte composition. The total cost of asymmetric and disproportionation salt-splitting approaches are both close to \$100/kWh, with the individual electrolyte contributions being \$48.4/kWh and \$49.9/kWh, respectively. The mixed electrolyte has an electrolyte cost of \$64.0/kWh, while that for the rocking-chair approach is \$41.4/kWh.

These estimates are quite rough ones, with no effort made to obtain synthetic cost

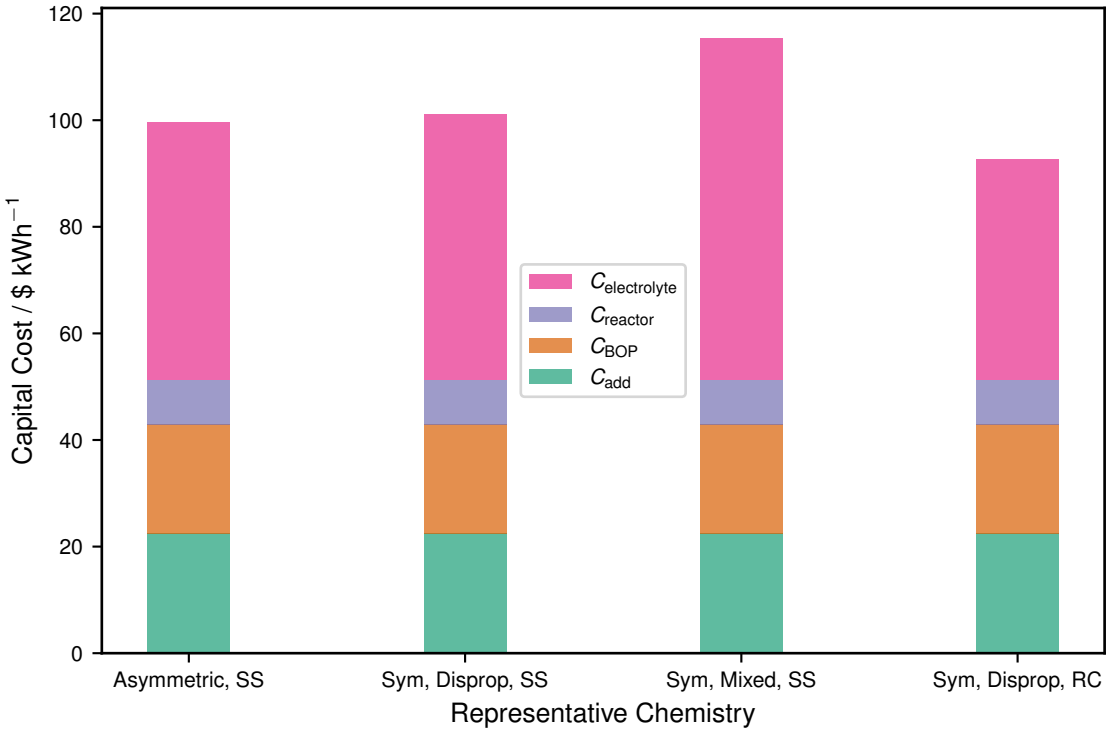


Figure 1.20: Capital cost of representative flow battery architectures based on (a)symmetry, salt configuration (salt-splitting, rocking chair), and mixed electrolyte/disproportionation configuration

estimates. Interestingly, asymmetric and symmetric disproportionation approaches are almost equal, essentially because the disproportionation molecule can be thought of as being the synthesis product of the union of the disparate positive and negative species from the asymmetric system. This synthesis process is likely to incur some additional cost. However, the asymmetric approach must use a more expensive IEM, which is not considered here.

The mixed-electrolyte approach is the most expensive, understandably so because it contains significantly underutilized dissolved active species. The point emphasized here, however, is that if the active species are sufficiently cheap (and the values used here are estimated future costs from [25]), overpaying for *twice* the amount otherwise needed only incurs an additional electrolyte cost of approximately 32% compared to an asymmetric system, which uses half the amount of unmixed active species in either reservoir. As discussed in [25], the most expensive electrolyte

component on a mass-basis for conventional nonaqueous systems is the (typically) fluorinated supporting salt, not the active species.

This leads into the final point to be made from Fig. 1.20, which is that the rocking-chair approach obtains the lowest electrolyte cost. Assuming the same mass-specific cost for the singular solute in the rocking-chair approach, but a much higher molecular weight, ultimately leads to a lower cost than any other approach considered. The proposition of a supporting-salt free flow battery is elegant, as such a system contains only one solute and a solvent, and the solute contains an active ion that possesses both positive and negative redox activity and a counterion (or ions).

1.6.2 Levelized Cost of Storage

Capital cost is not the only consideration for the technoeconomics of an energy-storage project; operation and maintenance expenditures, discount rates, project lifetimes, and other cash flows all create a fuller picture of the viability of a proposed technology. Incorporating all of these factors leads to a more insightful metric known as levelized cost of storage (LCOS), with units of \$/kWh per cycle.

The ARPA-E DAYS program [76] defined levelized cost of storage as (using ϵ for efficiency to be consistent within this chapter):

$$LCOS = \left[\left(\frac{1}{\epsilon_{\mathrm{RTE}}}-1\right)P_{\mathrm{C}}\sum_{t=1}^{T}\frac{n_{\mathrm{c}}(t)}{(1+r)^t}+\sum_{t=1}^{T}\frac{O\&M(t)}{(1+r)^t}+\left(\frac{C_{\mathrm{E}}}{\epsilon_{\mathrm{d}}}+\frac{C_{\mathrm{P}}}{t_{\mathrm{d}}}\right)\right]*\left[\sum_{t=1}^{T}\frac{n_{\mathrm{c}}(t)}{(1+r)^t}\right]^{-1}. \tag{1.26}$$

Parameter/variable definitions are given in Table 1.7.

The target metric for the DAYS program was to have the round-trip cost of storing energy, or LCOS, be no more than \$ 0.05 per kWh of energy stored, so that energy could be economically sold wholesale at a price of 0.075 \$/kWh. This equation considers the number of cycles per year a storage technology can deliver at its rated discharge duration, maintenance costs, cost of input energy, and the time value of money. Further analysis will plot LCOS alongside capital costs because of the simplicity and increased relevance of doing so.

Table 1.7: Definitions of terms relevant for levelized cost of storage analysis

Parameter	Meaning	Units
ϵ_{RTE}	round-trip efficiency	-
P_{C}	price of charging energy	0.025 \$/kWh
t	year index	-
T	project lifetime	20 years
n_{c}	number of cycles/year	-
r	discount rate	10%
$O\&M$	operation & maintenance cost	\$/kWh
C_{E}	energy capital cost	\$/kWh
ϵ_{d}	system discharge efficiency	-
C_{P}	power capital cost	\$/kW
t_{d}	discharge duration	hours

Presently, no operation or maintenance costs are considered - the majority of flow-battery literature on maintenance is concerned with correcting average oxidation state drift, chiefly due to hydrogen evolution in aqueous chemistries [40, 77–81]. Part of the motivation for studying nonaqueous flow batteries is the significantly wider electrochemical window for operation and availability of aprotic solvent systems, which negate this source of oxidation state drift. Additionally, symmetric-flow-battery construction should also help alleviate any maintenance procedures, due to the inherent resistance to crossover and mixing. Put another way, if a nonaqueous flow chemistry is worth pursuing, it should have smaller expected operation and maintenance expenditures than an aqueous system, and this could be possible with a nonaqueous symmetric system that has no oxidation state drift or capacity-fade mechanisms.

Albertus *et al.* [29] expanded on the DAYS FOA [76] LCOS equations by including an additional revenue stream from capacity payments and splitting operating cost into variable and fixed portions, and storage-media replacement costs. These additions are omitted here because the present focus is on observing the behavior of porous-separator flow batteries as it relates to LCOS in the simplest case.

Nothing introduced here yet is significantly novel or unintuitive. Rather, the modifications made to existing literature allow for more facile comparison of the symmetric-disproportionation and mixed-electrolyte systems described previously.

1.6.3 Technoeconomics of Porous Separator RFBs

Some basic behavior of the capital-cost model defined presently will now be demonstrated for a representative nonaqueous chemistry similar to that defined in [25], so that parameters can be varied with the technoeconomic model directly tied to the porous separator model.

According to [82], long-duration storage should be modeled at 100 hrs at a practical minimum, so a hypothetical benchmark nonaqueous system is created for a 1 MW, 100MWh battery with a 3 V cell potential and 1 M actives concentration. This prioritizes energy-related costs over power-related ones. The trade-offs of a porous separator, however, influence both energy and power. Energy is more important in this discussion, and lowering the coulombic efficiency of a system increases the required volume of electrolyte. So, 100 hours as a benchmark functions for the present purpose.

With the presently defined porous-separator performance model, discharge time is not known *a priori*; rather, the reservoir volume and applied current are predetermined and the self-discharge behavior determines the actual simulated discharge time. Additionally, in the current model, cell area and applied current are predetermined, and average discharge power density is an output of the simulation. In order to guarantee an exact discharge time and power density, the model could be solved iteratively until convergence, but this is not necessary for the following parameter sweeps.

Assuming 3 V, 1.0 M actives, and a power density of 1.3 $\mathrm{kW\,m^{-2}}$ (following table 3 from [3]), initial estimates of 770 $\mathrm{m^2}$ for reactor area and 1.3 ML for an individual reservoir volume are obtained to correspond to a 1 MW, 100 MWh battery. A flowrate of 57 $\mathrm{L\,s^{-1}}$is chosen to give a Damköhler number of 20, and other values are extrapolated from benchtop experiments. Electrolyte specification is identical to Table 1.3. Again, the intention here is to merely explore the technoeconomic behavior of flow batteries with porous separators in a semi-quantitative way to observe qualitative trends.

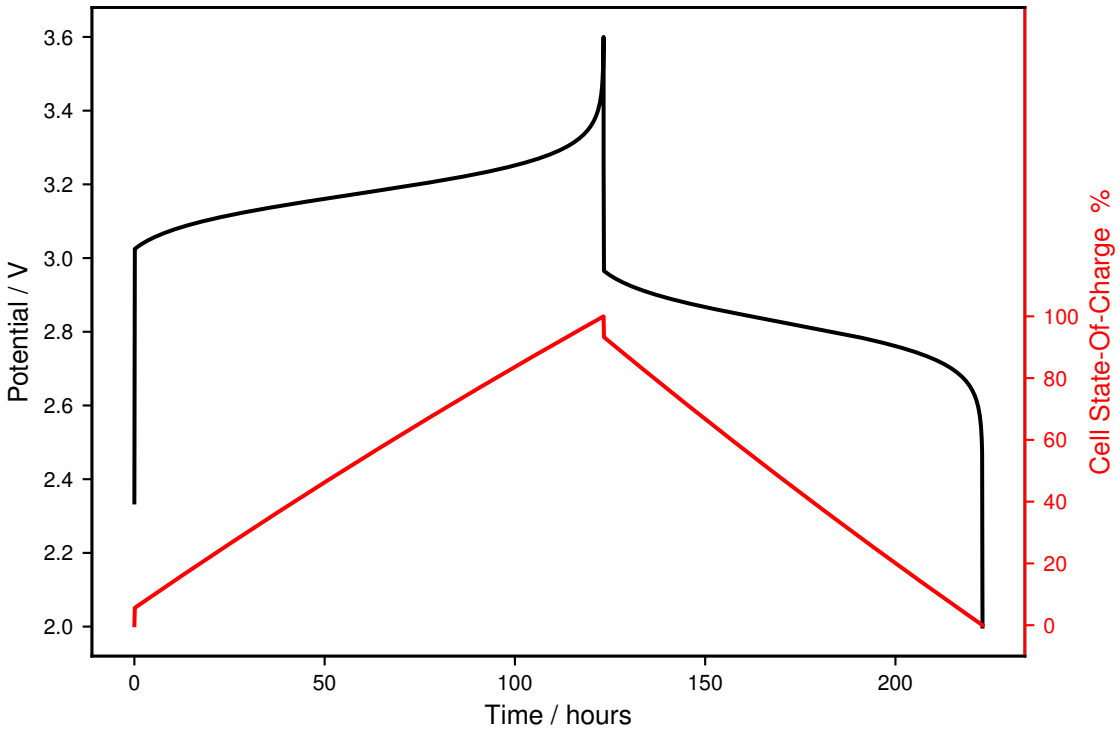


Figure 1.21: Simulated charge/discharge curve for a hypothetical 1 MW, 100 MWh flow battery

The simulation output using these values produces the simulation output shown in Fig. 1.21 for a hypothetical 1 MW, 100 MWh symmetric nonaqueous battery using a porous separator. Analysis of the charge-discharge cycle from Fig. 1.21 yields following efficiencies: 81% coulombic, 71% voltaic, 58% energy, and 87% utilization. Energy capacity on charge is $46\,\mathrm{W\,h\,L^{-1}}$, and $33\,\mathrm{W\,h\,L^{-1}}$ on discharge. Average discharge power is 867 kW. This corresponds to a C_{add} of \$1.13/kWh, C_{BOP} of \$1.03/kWh, C_{reactor} of \$1.02/kWh, $C_{\mathrm{electrolyte}}$ of \$34.9/kWh, summing to a total capital cost of \$38.1/kWh. These capital costs lead to a LCOS of 0.029 \$/kWh-cycle. Many assumptions have led to these numbers, but this LCOS is conveniently below the stated target of 0.05 \$/kWh-cycle from [76], leaving 0.02 \$/kWh-cycle of overhead for factors not yet considered, like pumping costs and operation/maintenance costs.

In the following figures, because of the long nominal discharge duration of 100 hours, the capital cost (and consequently LCOS) is dominated largely by the electrolyte cost, which serves as the price floor for any flow-battery chemistry.

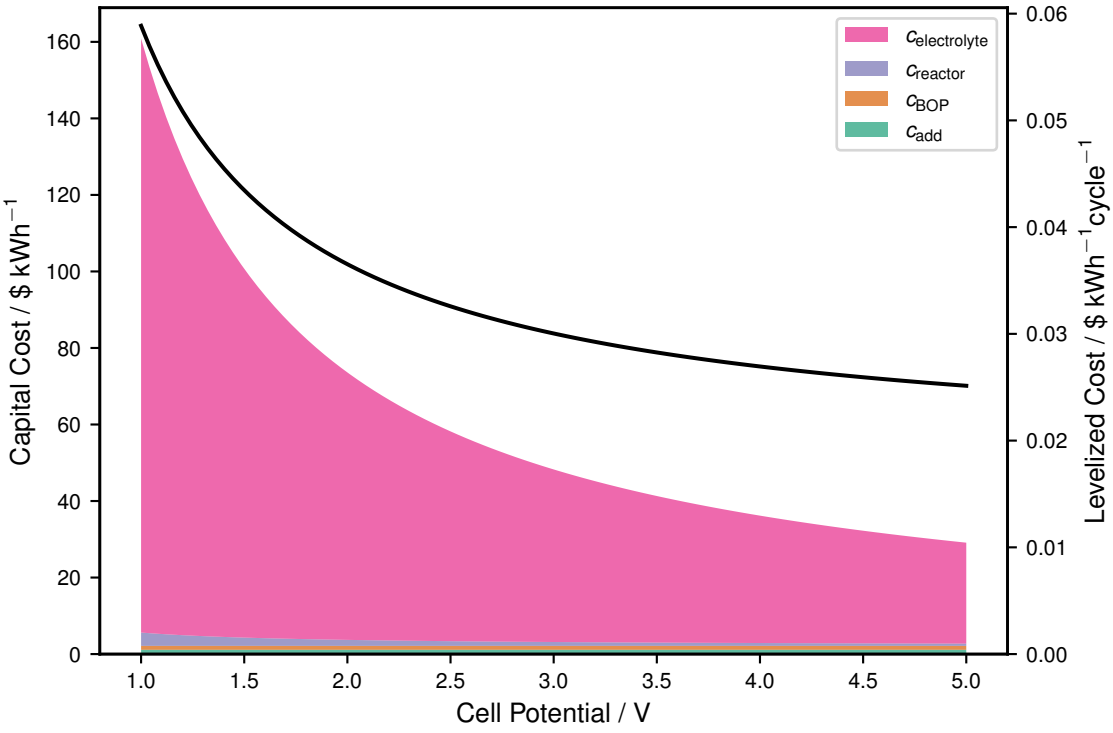


Figure 1.22: Capital and levelized costs of a porous separator flow battery *vs.* nominal cell potential

Figure 1.22 demonstrates the intrinsic $1/V^2$ behavior of both capital and levelized cost decrease as cell voltage increases in a flow battery—porous-separator flow batteries are no exception.

Figure 1.23 shows an expected decrease in capital cost as discharge time is varied from approximately one hour to 250 hours, as the total capital cost eventually approaches that of the electrolyte alone. Levelized cost slowly increases, however, which seems counterintuitive. With a longer cycle time, however, fewer cycles per year occur. In Eq. 1.26 for levelised cost of energy stored per cycle, the number of cycles n_c per year is in the denominator and numerator, but not for every term. Notably, n_c is not in the numerator's term for capital cost, and so at long discharge times, the denominator of the entire quotient becomes larger faster than the numerator becomes smaller, resulting in a gradual but not extreme increase in LCOS. As mentioned previously, the only revenue stream considered here is arbitrage, so this only serves as an illustrative example.

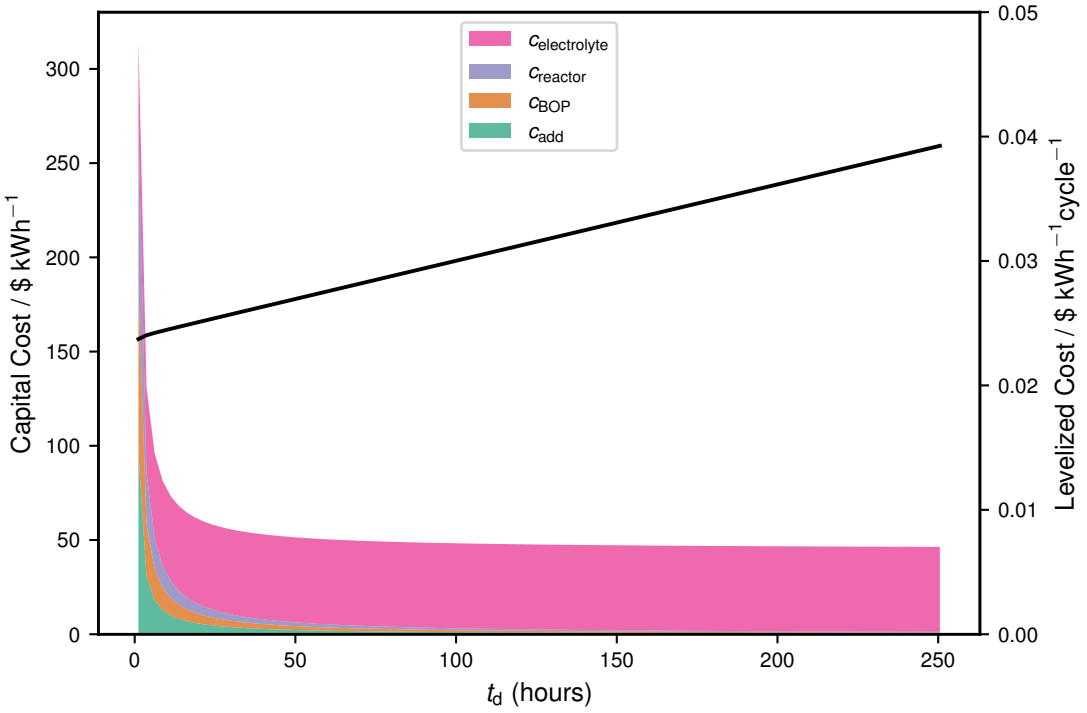


Figure 1.23: Capital and levelized costs of a porous separator flow battery *vs.* real discharge duration

Fig. 1.24 shows slightly more interesting behavior than the previous figures. Looking back at Fig. 1.13, recall how there local maxima at different applied current densities for the various efficiencies. Fig. 1.24 demonstrates how these combine to form one local minima for capital cost, and another for levelized cost. Looking only at capital cost would suggest operation at a lower current density is optimal, while levelized cost suggests a higher, wider economical operating window exists for applied current density. Uneconomical operation occurs at too high or too low current densities.

Straightforward behavior occurs is also shown in Fig. 1.25. Capital and levelized cost increase monotonically as self-discharge current density increases. Beyond a self-discharge current density of approximately 10 mA cm^{-2}, levelized cost of storage increases beyond the target value from [76] of \$0.05 per kWh-cycle. Realistically, though, better-performing separators with lower self-discharge will likely cost more. IEMs do cost an order of magnitude more than porous separators [3], but enable coulombic efficiencies near unity.

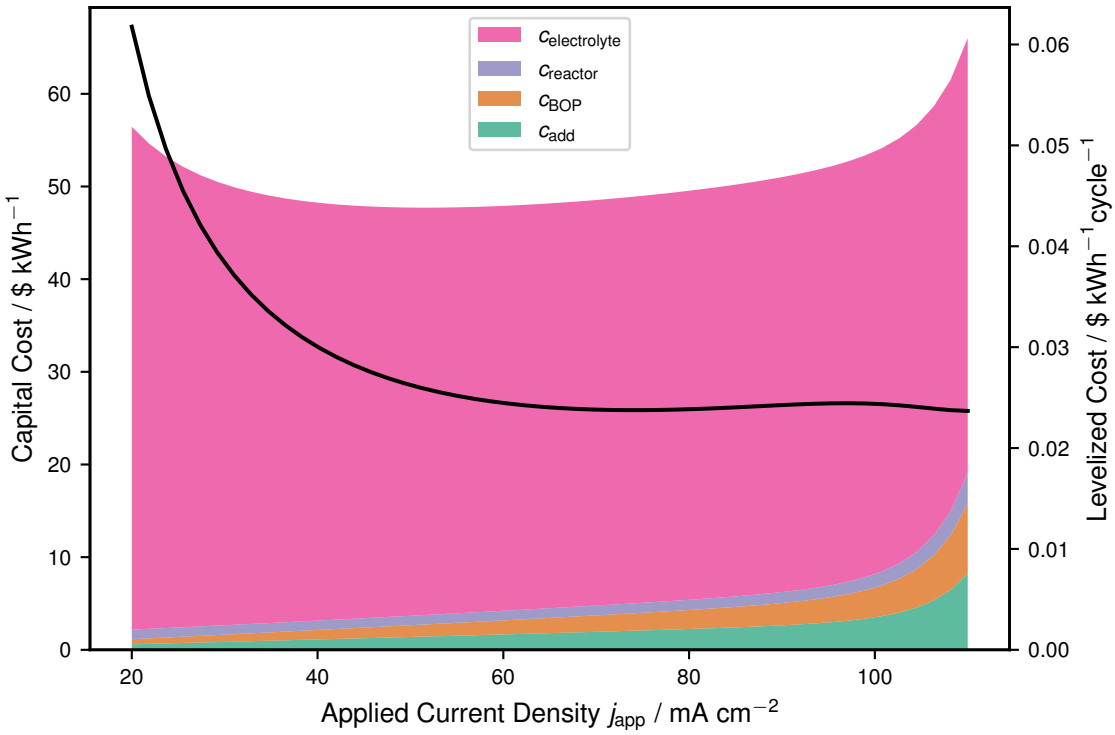


Figure 1.24: Capital and levelized costs of a porous separator flow battery *vs.* applied current density

In order to capture this tradeoff and how it trickles down from electrochemical performance to capital and levelized cost, the artificial cost-performance relationship shown in 1.25 has been constructed, where an exaggerated premium for separator performance has been added on top of the base c_{area} value for nonaqueous systems of \$107.5 per square meter.

Fig. 1.27 shows how the relationship in Fig. 1.26 follows through to capital and levelized costs.

Notably, even for a 100-hour battery which is used as the benchmark for the present simulations, reactor cost constitutes the majority of capital cost for the more expensive c_{area}, lower j_{sd} region on the left side of Fig. 1.27. Yet, the levelized cost is still quite low in this region, and reaches a local minimum at a lower rate of self-discharge (more expensive separator) than the capital-cost minimum. Presumably, with a very long discharge time, one can afford expensive high-performance power-related components, because they drop to zero in the limit of infinite discharge times.

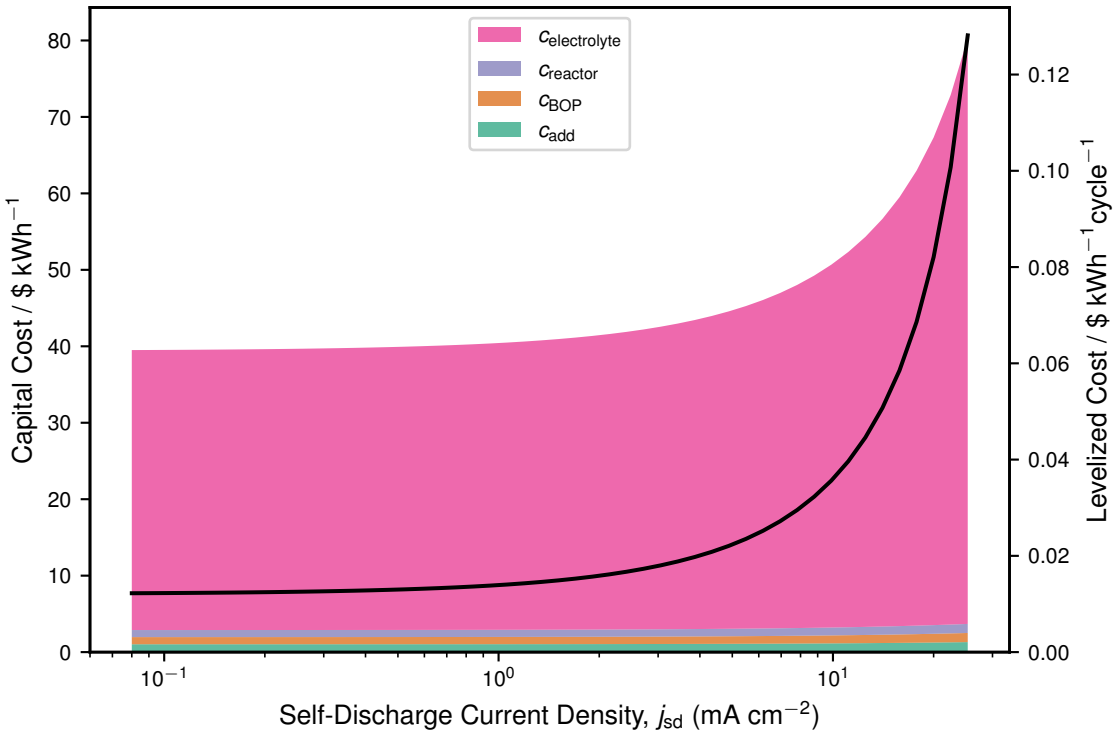


Figure 1.25: Capital and levelized costs of a porous separator flow battery *vs.* self-discharge current density

Numerous practical factors still motivate the exploration of RFBs separated by porous separators, however. IEMs designed for nonaqueous environments are not yet available. If a separator/membrane needed replacing, a porous separator would incur much lower operation and maintenance costs than an IEM. Also, in short-to-medium duration applications (for which definitions vary widely), the reactor cost can still contribute significantly to the overall capital— cost, and cheaper, lower-performance reactors may be competitive depending on the cost model. Fig. 1.27 shows how there exists a window in which capital cost is below \$100/kWh and LCOS below \$0.05/kWh/cycle. While the minimum of each curve are not at the same j_{sd}, the value of LCOS at the capital cost absolute minimum is not much higher than the value of the LCOS absolute minimum.

LCOS is not the singular technoeconomic objective function to be minimized. If a porous separator leads to a much lower capital cost, a somewhat higher but permissible LCOS, lower O&M costs, then it very well may be suitable for a

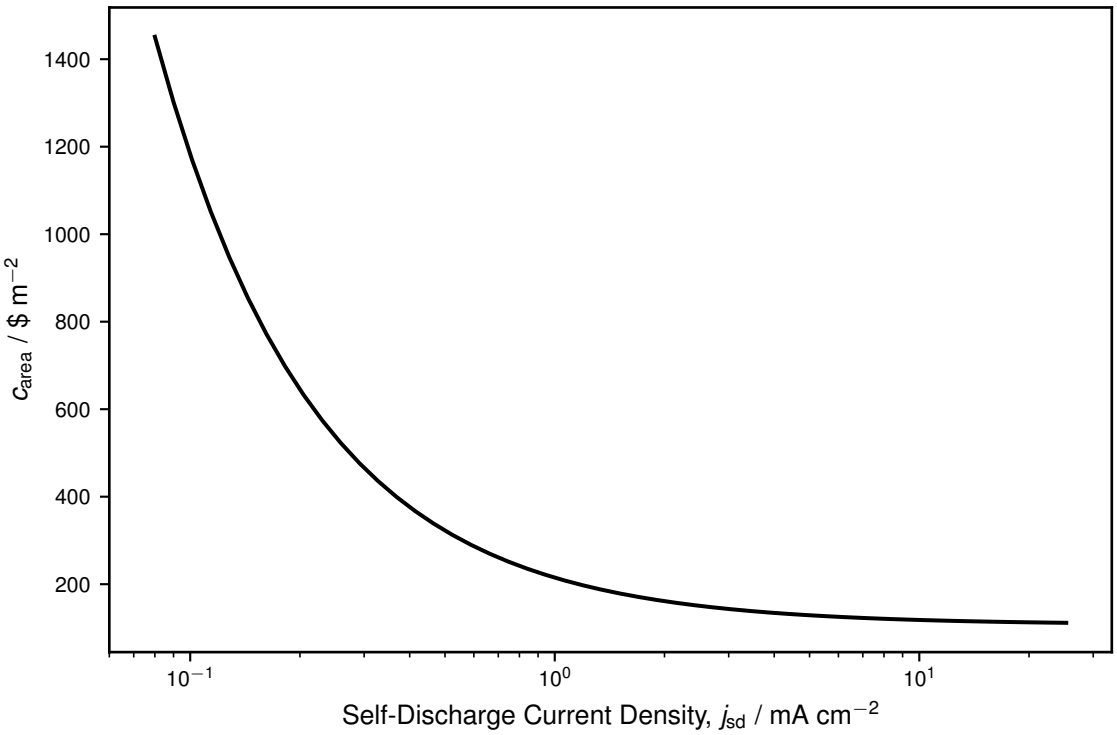


Figure 1.26: Hypothetical cost-performance relationship across the spectrum of expensive, selective IEMs to cheap, high-self-discharge porous separators

grid-scale RFB installation, and as such is deserving of further study.

1.7 Thesis Objectives & Structure

In this chapter, symmetric flow batteries have been placed within the context of the wider RFB design space along and relevant definitions clarified. An elementary model has been developed for symmetric RFBs with porous separators that experience higher than normal levels of self-discharge and coupled to existing technoeconomic models for capital and levelized costs of stored energy.

Chapter 2 focuses on the practical aspects of constructing and running these systems on the benchtop scale, which are different to typical benchtop RFBs using IEMs. These aspects includes monitoring and measuring the self-discharge of the RFB in real time, and maintaining long-term volume balance of the RFB's reservoirs. The experimental methods developed in Chapter 2 underpin Chapters 3 and 4.

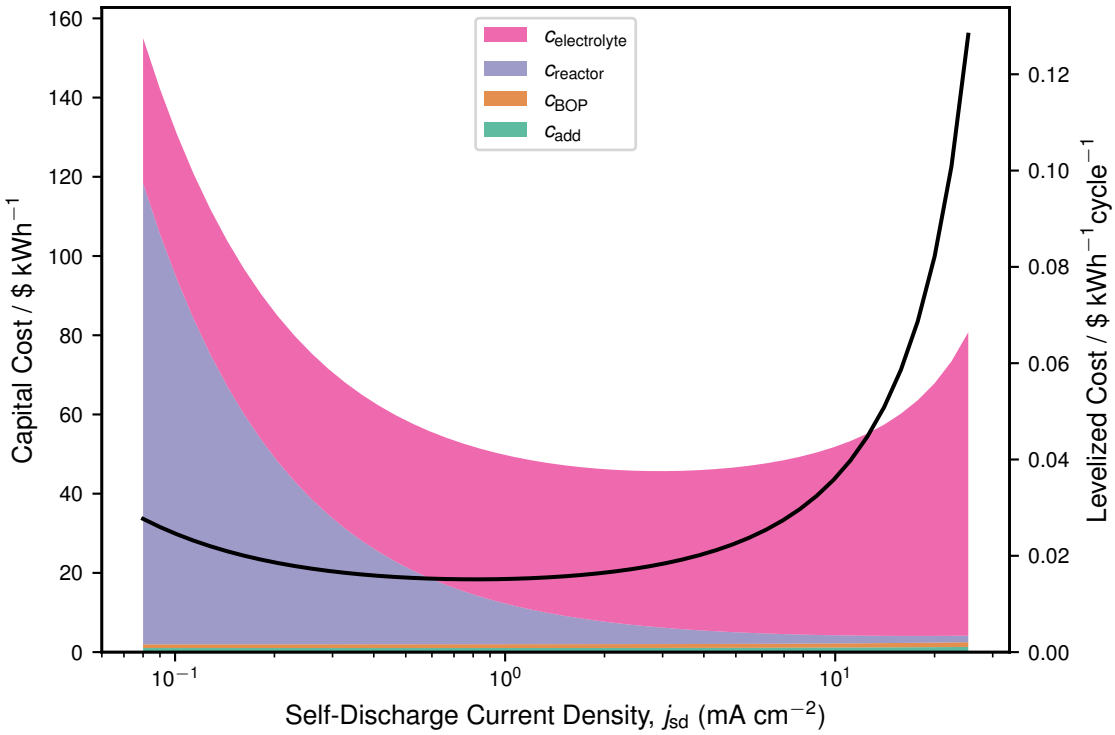


Figure 1.27: Capital and levelized costs of a porous separator flow battery *vs.* self-discharge current density using the cost-performance relationship from Fig. 1.26

Chapter 3 focuses on the V(acac)$_3$ system as a model for symmetric RFBs with porous separators. Some initial attempts to increase the energy density of the electrolyte through cosolvent manipulation are included. The second section of this chapter is the core effort of this dissertation—an investigation into the unpredictable degradation of V(acac)$_3$ RFBs not yet fully understood in the literature. Empirical observations lead to the formation of a hypothesis of separator pore-clogging, prompting novel double-reference-electrode experiments which serve as initial validation.

This hypothesis maintains that, counter to current literature, the studied nonaqueous electrolytes and carbon felt electrodes are chemically stable at nonzero states-of-charge. Said hypothesis is further validated in Chapter 4 where nonaqueous iron electrolytes are synthesized, characterized, and studied with similar methods as in Chapter 3. Similar separator pore-clogging phenomena are observed with the iron-based systems as they are in the vanadium-based systems of Chapter 3.

With a basic understanding of the domain of flow batteries, and more specifically flow batteries using porous separators to enable symmetric electrolytes in the non-aqueous regime, attention now turns to measurement and control of experimentally observable phenomena on the benchtop scale.

2

Measurement & Control for RFBs with Porous Separators

Contents

2.1 Introduction 55
2.2 Real-time Measurement of Self-Discharge 56
2.2.1 Materials & Methods 58
2.2.2 Results 59
2.3 Reservoir-Volume Control System 61
2.3.1 Materials & Methods 62
2.3.2 Results 66
2.4 General Cell Design Developments 72
2.5 Conclusion 75

2.1 Introduction

Compared to conventional aqueous flow batteries using an ion exchange membrane, flow batteries with porous separators show clearly distinct behavior, including a higher rate of self-discharge, as discussed in Chapter 1, and a faster rate of volume imbalance between reservoirs. This is because the non-selective separator permits transport of all species, including solvent. Moreover, if the electrolyte is nonaqueous, oxidation-state drift may be less severe than aqueous systems due to the wider

electrochemical stability window and aprotic nature of the solvents, but chemical incompatibility of cell components and electrolyte leakage may be more pronounced because of differences in the chemical environment and electrolyte viscosity. In this chapter, methods to monitor the rate of self-discharge through a current-interrupt technique, to monitor and control reservoir imbalance, and to seal nonaqueous benchtop flow cells effectively are discussed.

2.2 Real-time Measurement of Self-Discharge

When charging and discharging benchtop flow batteries with porous separators, coulomb-counting cannot be used to estimate state of charge because some charged active species will recombine through the separator during operation. Since coulombic inefficiency in porous-separator RFBs owes largely to electrolyte crossover, counting the number of coulombs passed to the system will not accurately reflect charge state. A different approach could use the open-circuit-potential (OCP) *vs.* SOC relationship to determine how much charge is retained in the system. For most experimental electrolytes tested at the benchtop scale, however, these relationships do not exist. Thus, the problem of estimating charge-state poses a conundrum, seeming to require simultaneous estimation of charge-state and the rate of self-discharge through the membrane, without assuming too many functional forms in the process. This issue partially motivated the development of the model presented in Chapter 1.

In a RFB, the concentration of the oxidized and reduced compounds in either electrolyte tank is directly proportional to the state-of-charge of the system. This means as the state-of-charge in the cell increases, the concentration of reduced products on one side and oxidized products on the opposite side of the membrane increases proportionally. If self-discharge occurred as a Fickian diffusion process (as a first-order approximation), this would imply more self-discharge occurs as the state-of-charge increases due to the increasing concentration (activity) gradient across the porous separator. Thus, this motivated the assumption that self-discharge current density j_{sd} was directly proportional to the state-of-charge in the cell.

To test this assumption, a technique was developed to estimate both SOC and self-discharge in real time from experimental data. By charging a flow battery to some unknown state of charge and then letting it self-discharge at open circuit while watching the open-circuit potential decay, this technique could be used to both observe the rate of self-discharge and to see if a cell chemistry exhibits an ideal Nernstian OCP–SOC relationship.

Intra-departmental collaboration with fellow researchers Dr. Pedro Ascencio and Prof. Dave Howey led to the creation of an adaptive observer control technique which was published as a conference paper [83].

A system held at open circuit naturally tends towards equilibrium through self-discharge. In the case of a symmetric RFB with a porous separator, the equilibrium state consists of fully discharged electrolytes with identical chemical compositions in both reservoirs. Self-discharge through the porous separator of a flow battery may be a function of several factors intrinsic to the membrane itself and the electrolyte itself (across all charge-states) as well as unique interaction parameters between the membrane and electrolyte, bulk and boundary layer flow conditions, *etc.* A reasonable overarching driving force for this self-discharge could be Fickian diffusion processes across the membrane, owing to the increasingly large difference in active-species and supporting-salt concentrations (and activities) as state of charge increases.

The technique developed in [83] avoids making assumptions as to the form of self-discharge, essentially changing the second term in Eq. 1.2 to be a generic active-species crossover flux $\dot{N}$ which has units of SOC per unit time. Essentially, Eq. 1.2 and 1.1 become the following:

$$\frac{dSOC_{\text{res}}}{dt} = \frac{\dot{V}}{V_{\text{res}} - \varepsilon V_{\text{cell}}}(SOC_{\text{cell}} - SOC_{\text{res}}) \tag{2.1}$$

$$\frac{dSOC_{\text{cell}}}{dt} = \frac{\dot{V}}{\varepsilon V_{\text{cell}}}(SOC_{\text{res}} - SOC_{\text{cell}}) - \dot{N} \tag{2.2}$$

These equations are then shown to guarantee convergence when used to estimate SOC_{cell} and $\dot{N}$ dynamically in an adaptive observer approach, described in [83]. With

this mathematical proof of convergence demonstrated, actual use of the technique consists of a two-step process. First, gains are calculated using predetermined values for the system, such as reservoir volume, flowrate, concentration, equilibrium cell potential, *etc.* The process of calculating these gains in a way that guarantees convergence is a convex optimization problem requiring conic solvers and is described properly in [83]. These gains are calculated once, and then used in the adaptive observer to estimate the functional-formless self-discharge flux $\dot{N}$. The adaptive observer itself is more straightforward, and involves solving an initial value problem derived from Eqs. 2.1 & 2.2 using the gains calculated from the initial optimization at each timestep of experimental data (the process of calculating the correct gains, which only happens once and *a priori*, is more complex). This produces estimates of the self-discharge rate $\dot{N}$ and the system's state of charge in real-time.

This self-discharge flux $\dot{N}$ can be divided by the estimated SOC_{cell} at every timestep to produce an estimate of j_{sd}, thereby testing the assumption of a self-discharge current density that is directly proportional to cell state of charge. An example of this entire experimental procedure follows.

2.2.1 Materials & Methods

The self-discharge experiment was performed inside an argon-filled glovebox (Pure-Lab, Inert Technologies, USA) with 0.1 M $V(acac)_3$(98%, Strem, UK) as the active species dissolved in anhydrous acetonitrile (ACN, 99.8%, Sigma, UK) dried over molecular sieves (3 Å, Sigma-Aldrich, USA) with 0.2 M $TEABF_4$ (Sigma, 99%, UK) used as a supporting salt. A flow cell designed for nonaqueous electrolytes was used with 2.20 cm^2 of active area and reservoir volumes of 18 mL each. The flowrate of 9 mL/min corresponds to a reactor residence time of 4.65 s when using electrodes with a porosity ε of 0.87. Porous carbon felt electrodes (Alfa-Aesar, UK) compressed 50% to a final thickness of 3.17 mm were used in a flow-through configuration alongside impervious bipolar graphite plates (GraphiteStore, USA). A polypropylene porous separator (Celgard 4650, Celgard, USA) was used to separate the counter-current electrolyte flow inside the cell. Peristaltic pumps (MasterFlex, Cole-Palmer,

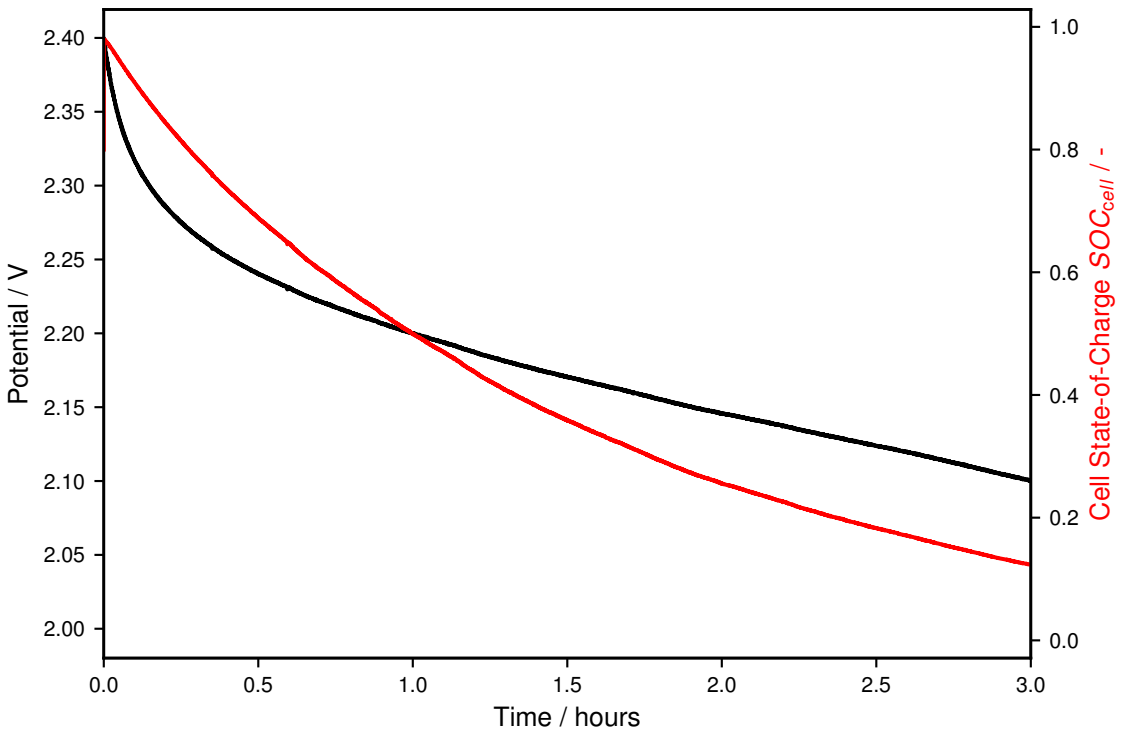


Figure 2.1: Voltage and estimated SOC of cell undergoing self-discharge

USA) circulated electrolyte through the half-cells using polytetrafluoroethylene (PTFE) tubing with perfluoroalkoxy alkane (PFA) compression fittings. Wetted materials in the system consisted entirely of PTFE, PFA, polypropylene, impervious graphite, and carbon felt.

As preconditioning procedure, the flow battery used in the experiment was cycled three times at $20\,\mathrm{mA\,cm^{-2}}$ between 3 V and 1 V. After this, the battery was charged up to the 3 V (voltage cutoff) to let it self-discharge at open circuit.

The code repository referenced in [83] contains a MATLAB script which calculates the gains needed to use the adaptive observer. In the code repository for this thesis, that code has been rewritten in Python and uses the corresponding Python packages for convex optimization instead.

2.2.2 Results

Fig. 2.1 shows the voltage profile of the cell self-discharging at open circuit (black) and the estimated state of charge from the adaptive observer.

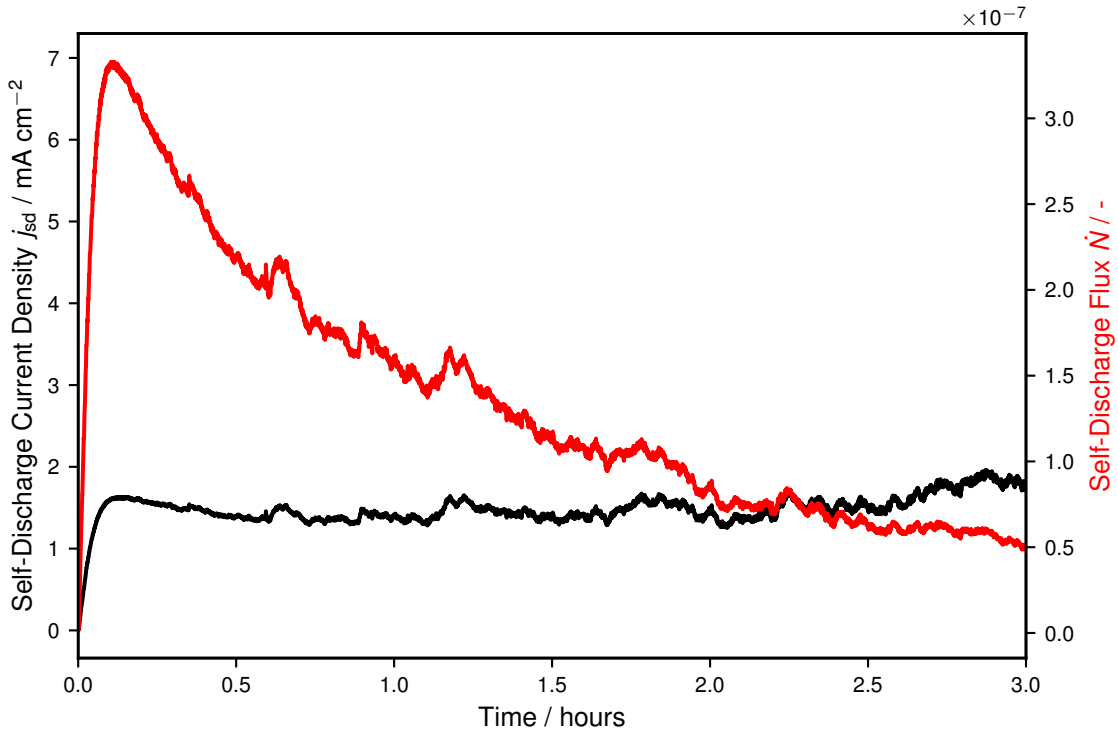


Figure 2.2: Self-discharge flux and current density for a three hour period of self-discharge estimated by the adaptive observer

Fig. 2.1 shows what appears to be an exponential decay of state of charge over time as the voltage of the cell traverses down the Nernstian plateau. Note the intersection of the curves at the equilibrium cell potential of 2.2 V and 50% state of charge. Fig. 2.2 shows the estimated self-discharge flux $\dot{N}$ (unitless), and an estimated self-discharge current density j_{sd} proportional to state of charge.

The exponential decay of state of charge seems validated by the nearly-constant j_{sd} calculated here, which is just under $2\,\text{mA}\,\text{cm}^{-2}$ for the three hours shown in the figure. Equation 1.11, the general solution to the porous separator RFB model, indicates state-of-charge at open-circuit is expected to decay as a sum of exponentials in time. All other terms constituting the coefficients of these exponentials are constants—if j_{sd} is indeed constant, then this self-discharge process is one of exponential decay with constant coefficients, which Fig. 2.2 appears to validate.

Note the very small magnitude of the self-discharge flux $\dot{N}$ estimated here— on the order of 0.00001% SOC per second. This experimentally observable constant

Table 2.1: Methods to manage bulk volume imbalance between reservoirs in redox flow batteries

Mechanism	Mode	Rebalance Fluid Path	Reference
Mechanical	Periodic, Active	External	Most benchtop experiments
Mechanical	Continuous, Passive	External	[84, 85]
Mechanical	Continuous, Active	Through Membrane	This work, [38, 86]
Osmotic	Continuous, Passive	N/A	[77, 87]

j_{sd} value led to the assumption of constant j_{sd} for the analytical solution developed in Chapter 1 and subsequent technoeconomic analysis.

2.3 Reservoir-Volume Control System

Several methods have been proposed for managing both differences in volumes and average oxidation states between electrolyte reservoirs in flow batteries. Volume imbalance, however, may be more severe in nonaqueous systems, especially if a porous separator is used instead of an ion exchange membrane. The driving forces for bulk electrolyte volume imbalance include mechanical and osmotic pressure as well as species-varying electroosmotic drag and SOC-varying properties such as density and viscosity, which influence the previously mentioned processes. These processes can result in bulk volume changes both within a single cycle and cumulatively across several charge-discharge cycles. The latter cumulative effect can be negated through an appropriate volume balancing scheme, and can eliminate a troubling (albeit reversible) source of capacity fade during cycling experiments in order to help deconvolute other possible failure mechanisms, if any.

Strategies to manage volume imbalance are summarized in Table 2.1. These include periodic and continuous external mechanical transfers of bulk electrolyte, continuous internal balancing of electrolyte by adjusting hydraulic pressure across the membrane (actively or passively), and mitigation of bulk imbalance by balancing average intra-cycle osmotic pressures with an additional solute.

This section describes an image-based mechanical balancing method to maintain volume-balanced reservoirs during uninterrupted charge-discharge cycling by regulat-

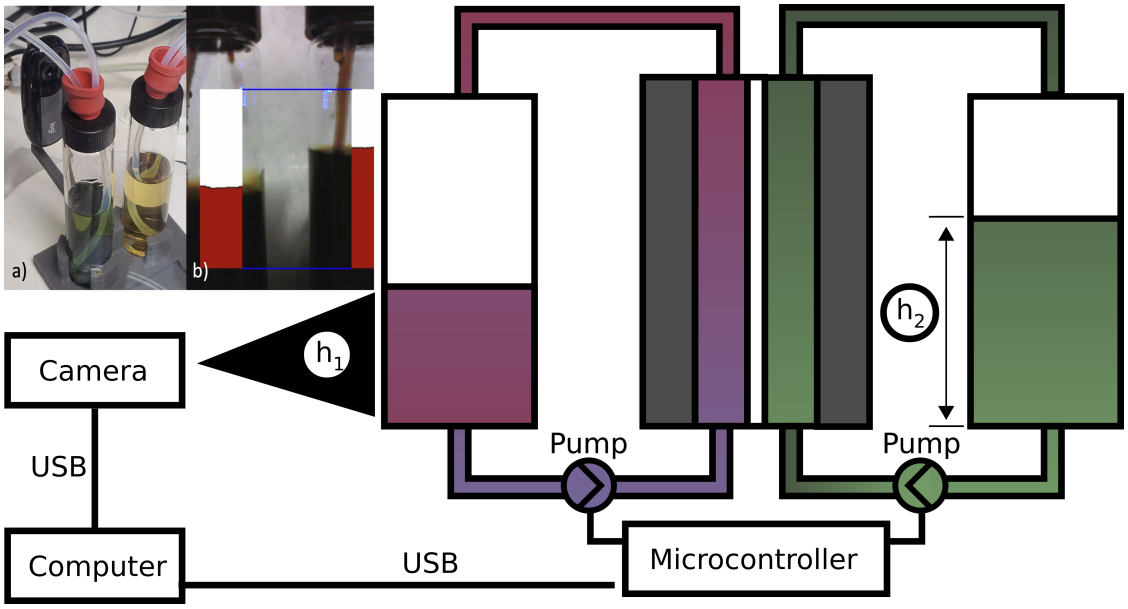


Figure 2.3: Overview of experimental setup for active balancing of electrolyte volumes in flow battery reservoirs. Pictures of **a)** the experimental setup and **b)** the level sensing image processing script during a flow battery experiment.

ing the hydraulic pressure across the cell membrane. The approach uses an external USB camera to measure the electrolyte volume in each reservoir. The difference in volume is used as the input to a PID controller, which controls a pressure-modulating output. In the present configuration this output is the difference in flowrates between the two pumps. Other implementations could use a control valve in either electrolyte flow path or the reservoir-headspace differential pressure as a PID control output, enabled by using an experimental setup similar to [38]. Pumps used in RFB experiments often have some form of external speed control input, and the approach implemented here uses no additional hardware beyond a USB camera and microcontroller, and avoids introducing additional wetted components in the flow path. A schematic of the system is shown in Figure 2.3.

2.3.1 Materials & Methods

Acetonitrile (HPLC grade, Fisher, UK) and diethyl ether (puriss, Honeywell, Germany) were sparged with argon and dried over 4 Å molecular sieves (Sigma-Aldrich, USA). After sparging, acetonitrile was dispensed over an activated alumina

column with a solvent purification system (Inert PureSolv, USA) before storage over molecular sieves. Both solvents were confirmed anhydrous using Karl-Fisher coulometry. All experiments were conducted in an argon-filled glovebox with $<$ 1.0 ppm O_2 and H_2O (PureLab, Inert Technologies, USA) using 0.1 M vanadium acetylacetonate ($V(acac)_3$)) in acetonitrile while using 0.3 M tetraethylammonium tetrafluoroborate (Sigma, 99%, UK) as a supporting salt. Vanadium acetylacetonate ($V(acac)_3$, 98%, Strem, UK) was recrystallized from hot acetonitrile and washed three times with diethyl ether before vacuum drying at ambient temperature while strictly avoiding exposure to ambient air.

The flow-cell construction was the same as is described in the subsequent section of this chapter. Celgard 4560 was used as a porous separator, and sealed between the carbon felt electrodes with laser-cut 1/8" expanded PTFE gasket material (GORE, USA). Compression was approximately 70% of the initial thickness after using a torque wrench set to 25 in-lb on the four bolts of the cell. Resin-impregnated graphite (Graphitestore.com, USA) was used for current collectors contacting the carbon felts. All inlets and outlets were arranged to establish a counter-current fluid flow in the cell. One channel of an Ivium Octostat potentiostat was used as a battery cycler.

Chemically compatible diaphragm pumps (model FF-12, 1/4-28 fittings, DCB-4 wire control, FS 60X PEEK prefilter, KNF Neuberger, UK) were used in all experiments. A 24 V 1.25 A wall power supply was used to power the pumps. A Teensy 3.5 microcontroller received control input from a PC, and was used both to control pump duty cycles and monitor pump speeds. A USB webcam (Logitech, C505E, 2MP) was aimed at the reservoirs and video output was processed on the PC using the OpenCV Python library ([88]) to determine reservoir levels. Various Python scripts facilitated communication and data logging between the PC, USB camera, and microcontroller. Relevant firmware/software files can be found on GitHub at https://github.com/kirkpsmith/rfb-volume-balancing.

After consideration of other techniques for measuring liquid levels in the reactant reservoirs, image-based monitoring was chosen both because of its simplicity and because its contact-free nature avoided chemical compatibility requirements. To

facilitate sensing of reservoir levels, clear or opaque reservoirs (or an external sight tube) are required, and the electroyte must be a different color from the background reservoir/headspace at every state of charge. (NB: Sensing of optically clear liquids could be possible with extension of the sensing code.) The liquid-level sensor functions by first prompting the user to select sensing areas from the camera feed which correspond to virtual sight tubes; the user draws a rectangular box on the image for each reservoir, with the stipulation that the box contains both electrolyte and headspace over an adequate sensing range. These virtual sight tubes are then calibrated to a known height from any external volumetric graduations on the reservoirs or prior knowledge of the vessel's height/volume relationship. Here, the reservoirs were cylindrical vials, so a constant horizontal cross-section was assumed, such that the fluid volume in the reservoirs tracked linearly with the liquid-surface height.

Binary image thresholding is used to convert each frame from the camera into black and white. Further image processing manipulates the sensed area to remove any irregularities, such as droplets adhered on the reservoir walls. The height of the processed sensed area is then converted to a volume using the reference volume/height relationship and time-averaged over a 60 second period to filter the effects of liquid-level fluctuations from stirring, or from electrolyte splashing in from the cell outlet tubing or reservoir inlet tubing. Upon cell assembly, when a known volume of electrolyte is evenly split between reservoirs, the level sensor calibrates itself against this known volume so absolute volume measurements can be made incorporating the piping and reactor-chamber volumes. This enables tracking of relative changes between reservoirs and absolute volumes of each reservoir, to monitor electrolyte leakage, solvent evaporation, and/or SOC dependent volume changes of individual reservoirs.

This 60 second time-averaged signal of the real-time volume of each reservoir is then averaged over a time period corresponding to twice the expected cycle length before being sent to the PID controller. This last constraint prevents the controller from responding to any intra-cycle volume imbalances, such as those

induced by electroosmosis of solvent, while allowing it to respond to cumulative changes that arise between cycles.

The microcontroller is programmed to maintain a minimum flowrate in each half-cell. In order to force volume transfer to correct for inter-cycle imbalance, pump speeds are adjusted by the PID controller beyond this minimum flowrate. The input to the PID controller is the volume difference between reservoirs, and the output is the applied difference between the pump speeds. The signs of the proportional and integral gains in the PID controller are such that if the positive reservoir has has more electrolyte than the negative reservoir, the speed of the pump on the positive electrolyte flow stream will increase, increasing the hydraulic pressure in the positive half-cell and driving electrolyte back to the negative reservoir. Alternatively, the pump speed is increased on the negative flow stream if the negative reservoir contains more electrolyte than the positive reservoir. In both cases, the pump corresponding to the reservoir with the lower level of electrolyte is maintained at the predetermined minimum flowrate while the other pump operates at a higher speed corresponding to the PID output control signal to rectify imbalance. The time-averaged input signal and the integral term of the controller can create some overshoot and phase lag between the input and output, but this is necessary to avoid oscillations. The derivative gain was always set to zero in the present experiment.

Once the PID controller is properly tuned, unless the major and minor frictional losses are perfectly matched between half-cell fluid paths, there will be some steady-state flow rate differential between the half-cells. This differential could be avoided by designing the system differently and choosing a different pressure-controlling PID output, such as an in-line needle valve, and maintaining equal flowrates with positive-displacement pumps.

10 mL of electrolyte was evenly split between two 10 mL glass vials sealed with rubber septa, making for 5 mL of electrolyte on each side. A piece of 1/8" PTFE tubing was used to connect the headspaces, to equilibrate their pressures and make it easier for the pumps to promote rebalancing through speed adjustment. Charge/discharge cycling took place with a current density of $20\,\mathrm{mA\,cm^{-2}}$ and base

flowrate of 20 mL min^{-1}. A 10 second hold at open circuit was performed in between charge and discharge half-cycles. The high-voltage cutoff for the first 10 cycles was 2.2 V; subsequent cycles applied a constant charging current for 280 seconds, which nearly matched the initial 2.2 V cutoff half-cycle lengths. This change accounted for slight increases in overpotential, which arose from gradual solvent evaporation and/or electrolyte leakage, which can cause the apparent open-circuit potential of the cell to drift. The lower voltage cutoff was always maintained at 1.4 V. The level sensing and PID control script were initiated as cycling started, and controller gains and sampling windows were tuned manually until a steady-state was established. Then, the PID control system was shut off and flow conditions returned to the base flowrate.

2.3.2 Results

Cycling results from this active balancing demonstration are shown in Figure 2.4. Voltage profiles of charge-discharge cycles are shown in Figure 2.5.

For the first 100 cycles, coulombic efficiency is 88.7% ± 0.6%, voltaic efficiency 89.5% ± 0.1%, energy efficiency 79.4% ± 0.5%, and utilization efficiency 22.6% ± 0.1%. Utilization efficiency is defined as the percentage accessed on discharge of the maximum theoretical charge capacity in solution, derived from the active-species concentration and the volume initially contained in each reservoir.

Imbalance versus applied pump duty cycle is shown on the top of Figure 2.4. The diaphragm pumps used take a 0-100% duty cycle to determine pump speed. The pumps were initially set to run at 20 mL/min, which was calibrated to be a 36% duty cycle for the pump/cell/discharged-electrolyte combination. The right vertical-axis reflects the relative change/bias in pump duty cycle from the base value of 36%. A positive value drives the negative flow stream's pump and inversely. The discrete steps in the duty cycle are reflective of the output of the PID control script, which is constrained by the microcontroller's 8-bit pulse width modulation (PWM) output, used in absence of a true digital-to-analog converter.

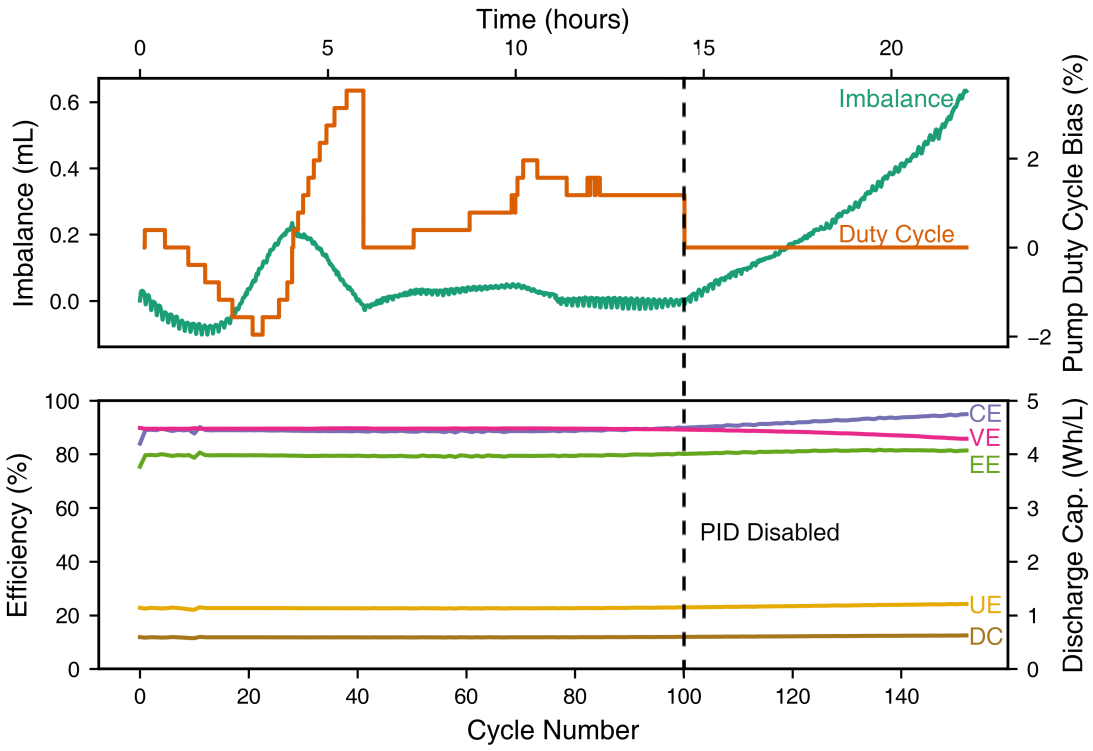


Figure 2.4: Cycle efficiencies and discharge energy capacities plotted simultaneously with imbalance and PID pump speed output control signal.

The microcontroller used was a Teensy 3.5, a sub-$25 ARM-based 120 MHz microcontroller, selected for its small footprint (in a glovebox), low cost, and abundance of GPIO's which allowed for measurement and control of several pumps simultaneously. While an 8-bit PWM signal may be a relatively low resolution compared to commercial offerings, this analog output was internal to the microcontroler and easily programmable and accessible. Additionally, Figure 2.4 shows the resolution of this control signal was sufficient to achieve active balancing and stable reservoir volumes, showing that low-cost hardware is sufficient to control this system.

A closer look at intracycle imbalance during a particularly stable, observable period is shown in Figure 2.6. The first phenomenon observable in the cycling data is the increased stability gained when switching from a high voltage cutoff to a coulomb-based cutoff after 10 cycles. Because the slope of the Nernstian charging plateau is relatively flat, the amount of electrical charge passed during the charging

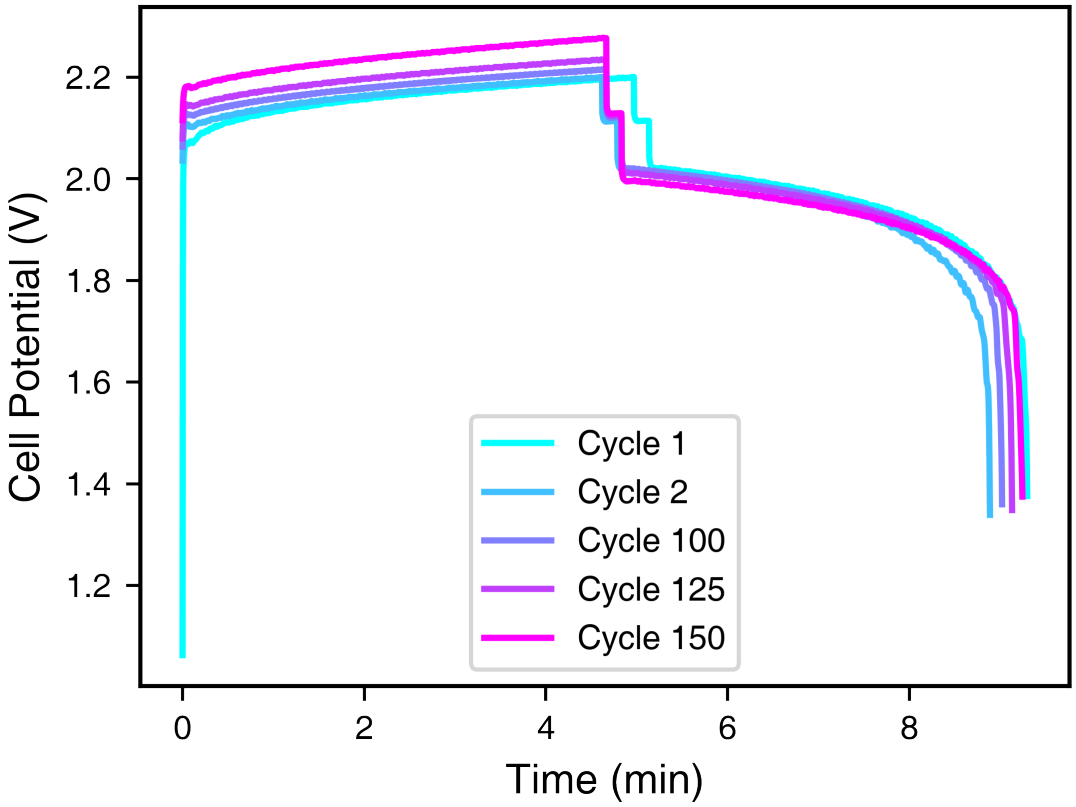


Figure 2.5: Voltage profiles of charge-discharge cycles during active balancing. A 10 second open-circuit hold is performed between charge and discharge steps.

step can be fairly sensitive to millivolt changes in overpotential between cycles, which may arise from various sources including noise. Using a charge-based cutoff avoids this issue and eliminates otherwise premature end conditions for the charging step.

The Ivium potentiostats used in this work have a current resolution of 0.008% of the selected current range (±100 mA), which is 16 µA, and accuracy of 0.2% (in galvanostatic mode). This level of precision is likely unnecessary for the coulomb counting charge step, as the consequences of slight imprecision/inaccuracy are fairly minor. The system has a voltage-based discharge cutoff, meaning that the system begins the charging step from approximately the same state-of-charge each cycle. Consequently, any error in coulomb-counting only means a slightly different maximum state-of-charge is reached each cycle, and there is no significant risk of building up a cumulative error over time as the system is fully discharged each

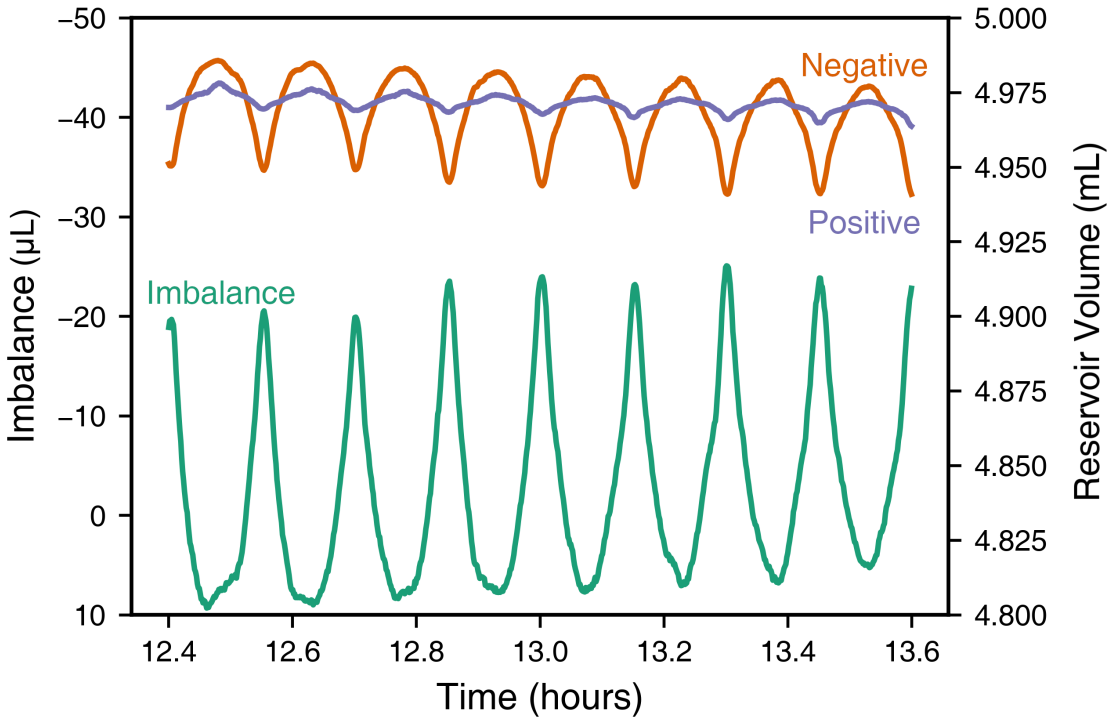


Figure 2.6: Intracycle imbalance and individual reservoir volumes during a stable, balanced period of cycling. Each reservoir had 5 mL of electrolyte initially.

cycle (to the accuracy of the voltage measurement, which is 64 nV resolution and 0.2% accuracy, both sufficient for present purposes).

Figure 2.5 demonstrates the fairly consistent charging and discharging profiles over the almost 24-hour-long experiment and the lack of oxidation state drift due to the constant open circuit potential after the charging step. The first cycle is longer because it starts from a fully discharged electrolyte. After the balancing scheme is disabled, there is is some decrease in voltaic efficiency, seen in the voltage profile as a slight increase in overpotential on charge. This could be due to the volume imbalance developed and other possible factors such as solvent evaporation.

The level-sensing information can be used to examine intra-cycle imbalance, as shown in Figure 2.6. The peak-to-peak amplitude of this volume swing is approximately 30 µL (0.6 % of the reservoir volume). This imbalance could arise for various reasons, not limited to a combination of electroosmotic drag, variable density of the electrolytes with state of charge, or changes in relative viscosity

between half-cells changing the mechanical pressure difference across the cell at a given flowrate and causing bulk permeation of electrolyte across the separator.

The controller takes some time to tune manually and also to stabilize, as setpoint overshoot and oscillations occur in the first 6 hours before reaching a steady state behavior. Even with this initial transient behavior, the fluctuations in reservoir volumes are imperceptible for the experimental conditions in terms of efficiencies and accessible capacity, as seen in Figure 2.4.

No electrolyte leakage was observed anywhere on the exterior of the experimental apparatus, but Figure 2.6 does show the absolute values of the electrolyte volumes decreasing slowly. This can be attributed to solvent evaporation, which is expected to happen at similar rates in both reservoirs so long as charging of the active species does not substantially affect the solution's vapor pressure. As such, the PID controller should be able to compensate for any potential changes in half-cell electrolyte fluid properties as they become more concentrated through solvent evaporation over time. Additionally, the measurement of this value could permit manual or automated solvent top-up procedures if desired.

In this benchtop system, the reservoir headspaces were not perfectly sealed, and throughout the system, there exist several interfaces through which volatile electrolyte components could evaporate from over time. A real system (aqueous or nonaqueous) would possess properly sealed reservoirs capable of withstanding a positive pressure inert head, and stack/hydraulic connections made using more robust methods. As such, the observation of solvent evaporation here, in the absence of detectable side-reactions which consume solvent, is not a significant cause for concern—only motivating the design of better benchtop experimental approaches.

This pump-based reservoir volume-balancing approach is imaginable at scale, where it would continue to enjoy the benefits of no additional wetted components or significant hardware cost. At any SOC above 0%, there will likely be non-negligible transmembrane osmotic pressure. As such, depending on the average SOC, the average pump speed differential applied will be nonzero. This may result in better mass transfer at one electrode at the expense of increased pumping

cost. Increased pumping costs lower the overall round-trip efficiency of the system by imposing an additional parasitic energy penalty. A slightly higher flowrate through one electrode may reduce mass-transfer-related overpotential slightly, but likely not enough to offset the pumping costs. The benefit of not introducing additional components, however, may justify a small drop in efficiency, depending on the relevant technoeconomics.

A control valve could be introduced instead, and while this may allow for equal flowrates, it would result in a similar pumping cost due to the minor loss from the valve, with one electrode missing out on a potential mass transfer enhancement. If electrolyte properties are well-understood, the most efficient solution to maintain balanced reservoirs with minimal pumping penalty may be the careful use of a draw solute to balance the average osmotic transmembrane pressure similar to [87] and [77]. With a symmetric electrolyte configuration (identical discharged half-cell electrolyte compositions, such as in the present study), however, the draw solute would eventually achieve identical concentrations in both reservoirs, complicating matters. In any case, pump-based volume balancing can be used as a backup technique for excursions outside the intended osmotic-pressure range.

If a cell chemistry's nonideality is such that it consistently exerts transmembrane osmotic pressure towards one half-cell (positive or negative), a passive balancing solution may be to hermetically seal the half-cell reservoir possessing the lower osmotic pressure, so that it builds up static pressure head opposing the osmotic pressure difference. Essentially, this makes the lower-osmotic-pressure half-cell reservoir contain zero headspace. Whether or not this is feasible at scale depends on the cost of hermetically sealing the exterior volume of a suitable reservoir to handle excursions above ambient pressure (by the amount of the osmotic pressure difference and any volume expansion). Turning one reservoir into a pressure vessel and/or adding an expansion tank may introduce unnecessary cost to a large-scale system, however.

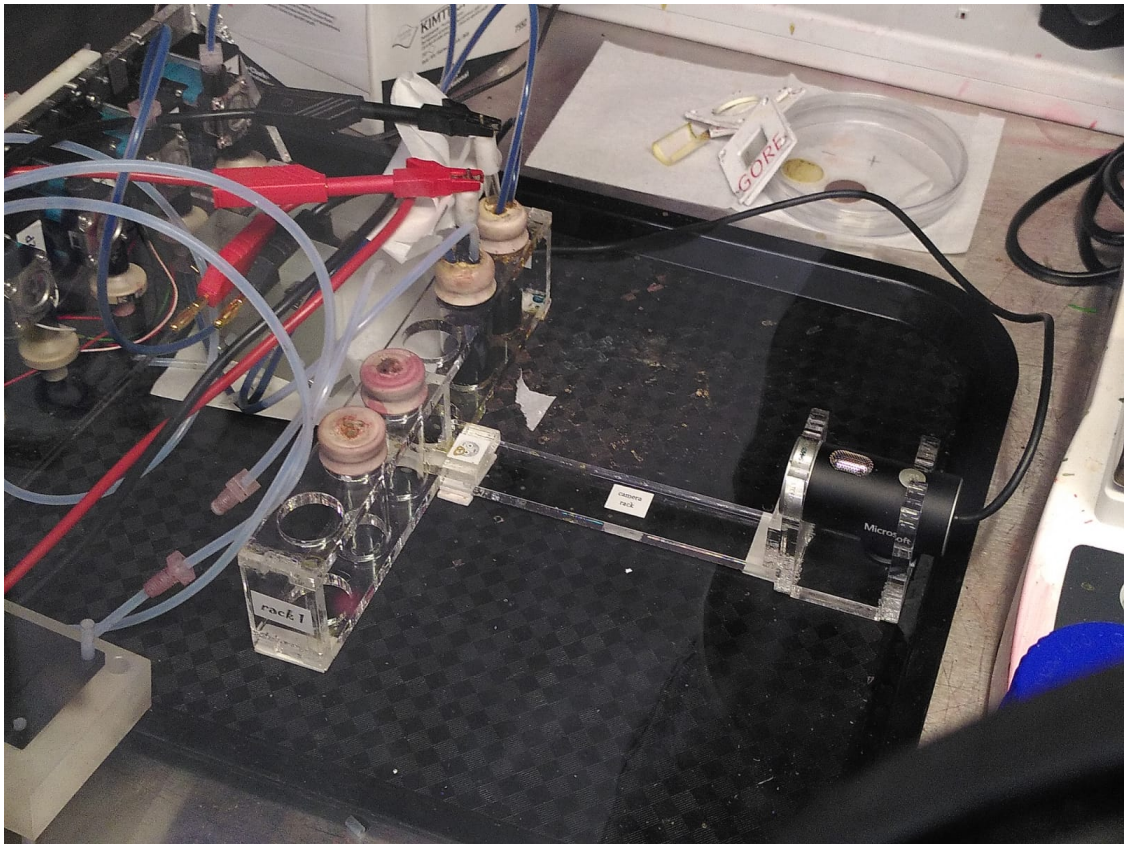


Figure 2.7: Image-based mechanical balancing of multiple flow cells and reservoirs simultaneously with one camera

The balancing system was eventually extended to accommodate multiple cells and their reservoirs simultaneously. An image of this setup in the glovebox is shown in Fig. 2.7, and the camera feed of the same setup in Fig. 2.8

2.4 General Cell Design Developments

The flow cell ultimately used for the majority of the experiments in this thesis was designed and built to combine the advantages of prior cells developed by Milshtein *et al.* [89] and Saraidaridis and Monroe [69]. The biggest challenges in designing a cell for nonaqueous electrolytes were chemical compatibility and adequate sealing to prevent fluid loss by leakage or evaporation on the timescale of several days. Chemical compatibility necessitated the use of very chemically resistant materials by default; materials explored for use with nonaqueous electrolytes based primarily on acetonitrile included amides (nylon), fluorinated polymers such as

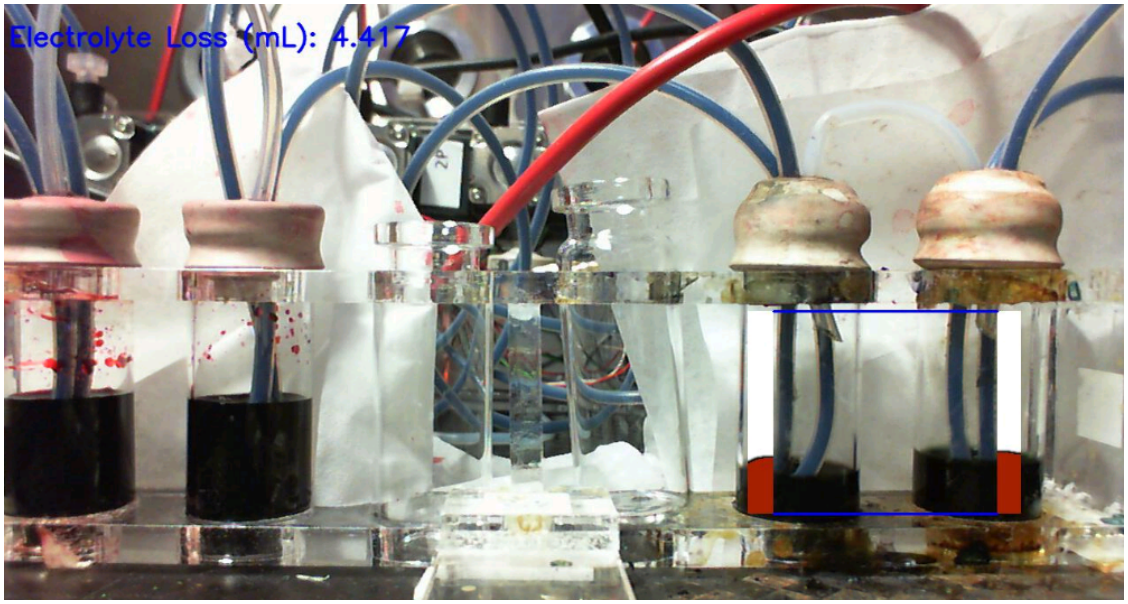


Figure 2.8: Camera feed of setup in Fig. 2.7 showing the virtual sight tubes and level measurement

polytetrafluoroethylene (PTFE) and perfluoroalkoxy alkane (PFA), olefins like polyethylene and polypropylene, borosilicate glass, polyether ether ketone (PEEK), and the like. Notably, care must be taken when storing electrolytes with fluorinated anions in glass containers, as reactions with trace hydrofluoric acid and the container may occur [90]. Natural rubber, Viton, and Tygon polymer blend products were found to be decidedly *not* compatible with acetonitrile for the tasks undertaken in benchtop flow battery research.

Effective sealing *via* novel tubing introduction was achieved with the design in [69], but the cell was not very modular. This made repeated assembly/disassembly burdensome for experiments of the type that will be presented in Chapter 3, which require frequent partial disassembly of cells to swap out membranes or electrodes, followed by reassembly (all in a glovebox).. The cell presented in [89] was modular and easy to handle, but was not leak-proof on the timescale of days. The problematic points in [89] were the NPT adapters connecting the cell to the tubing, and the membrane/gasket interfaces, which relied on incompressible PTFE sheet gaskets to sandwich the membrane.

Merging the Milshtein and Saraidaridis cell designs and making some modifications resulted in a cell which was adequate for longer-duration tests and frequent assembly-disassembly encountered in subsequent chapters of this thesis. Compared to the design of [89], the following changes have been implemented:

- Adoption of flow-through architecture and compressible PTFE membrane gasketing approach of [69]
- Substitution of flanged low-pressure Cheminert® fittings (VICI, USA) for PFA NPT tube connections
- Shortening of tab height on graphite plate current collectors and widening of cutout in plastic block, to allow for cell to be rotated and set down ergonomically in any orientation without risk of fracturing graphite plates
- Minor changes to dimensions and profile of O-ring slots in plastic block to permit manufacture with a manual milling machine

An exploded diagram of the cell used here is shown in Fig. 2.9, and a photograph of a cell running in the glovebox is shown in Fig. 2.10.

A 50 W CO_2 enclosed laser cutter was found to work well for preparing gaskets from sheet PTFE material and carbon felt electrodes. Cutting carbon felt creates a very bright light emission, and direct eye contact should be avoided (as is usually the case for laser cutting—but the light emission is brighter than typical). Additionally, cutting PTFE sheet material with a laser requires active fume extraction. Whatever volatile fluorinated compounds that come off of this process are likely hazardous to health and undoubtedly undesirable to inhale.

Drawings for the present cell are given in Appendix A. The assembly instructions are identical to those given in the theses of Saraidaridis [91] and Milshstein [27].

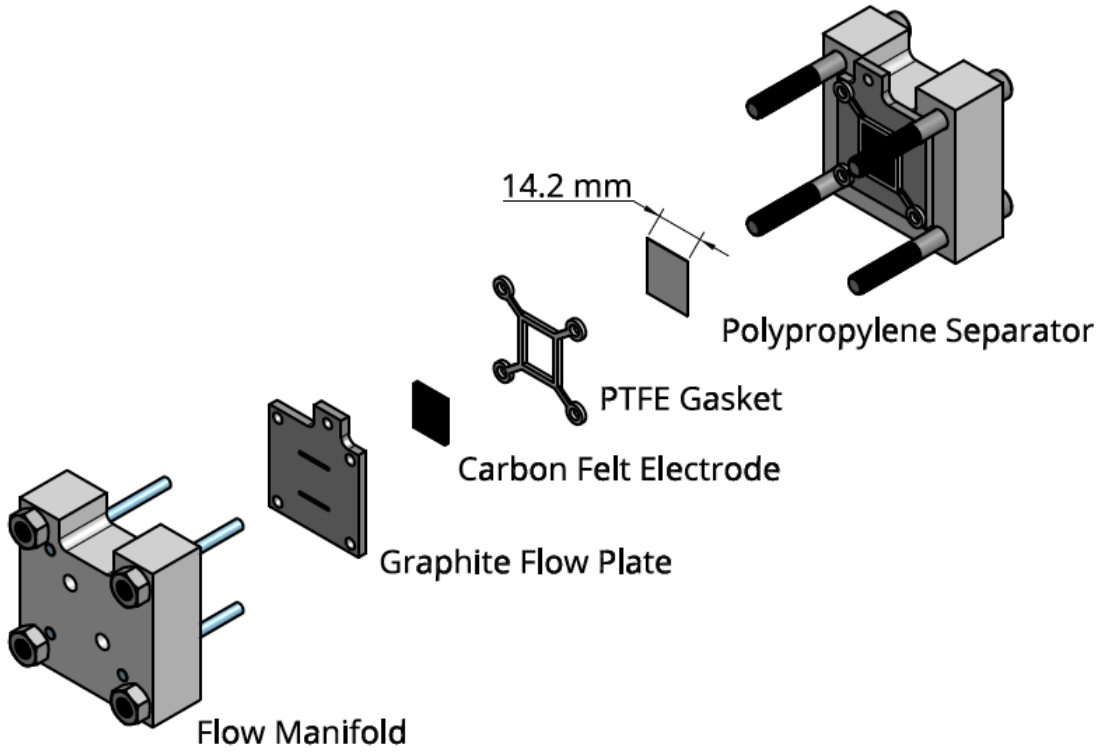


Figure 2.9: Exploded view of the cell used in this thesis

2.5 Conclusion

The techniques described in this chapter were developed to further understand nonaqueous flow batteries with porous separators undergoing self-discharge and make their long-term operation more stable to enable extended cycling experiments. A technique to monitor self-discharge in real-time with the interruption of current was developed and self-discharge current density was shown to be directly proportional to state of charge in the cell. A technique to measure and control reservoir volumes in real-time was developed and shown to function as desired. Existing benchtop cell designs were modified and extended to allow for ergonomic, modular (dis)assembly and prevent electrolyte leakage or solvent evaporation on the timescale of several days. The sum of these developments sought to allow long-term extended cycling of the $V(acac)_3$ compound.

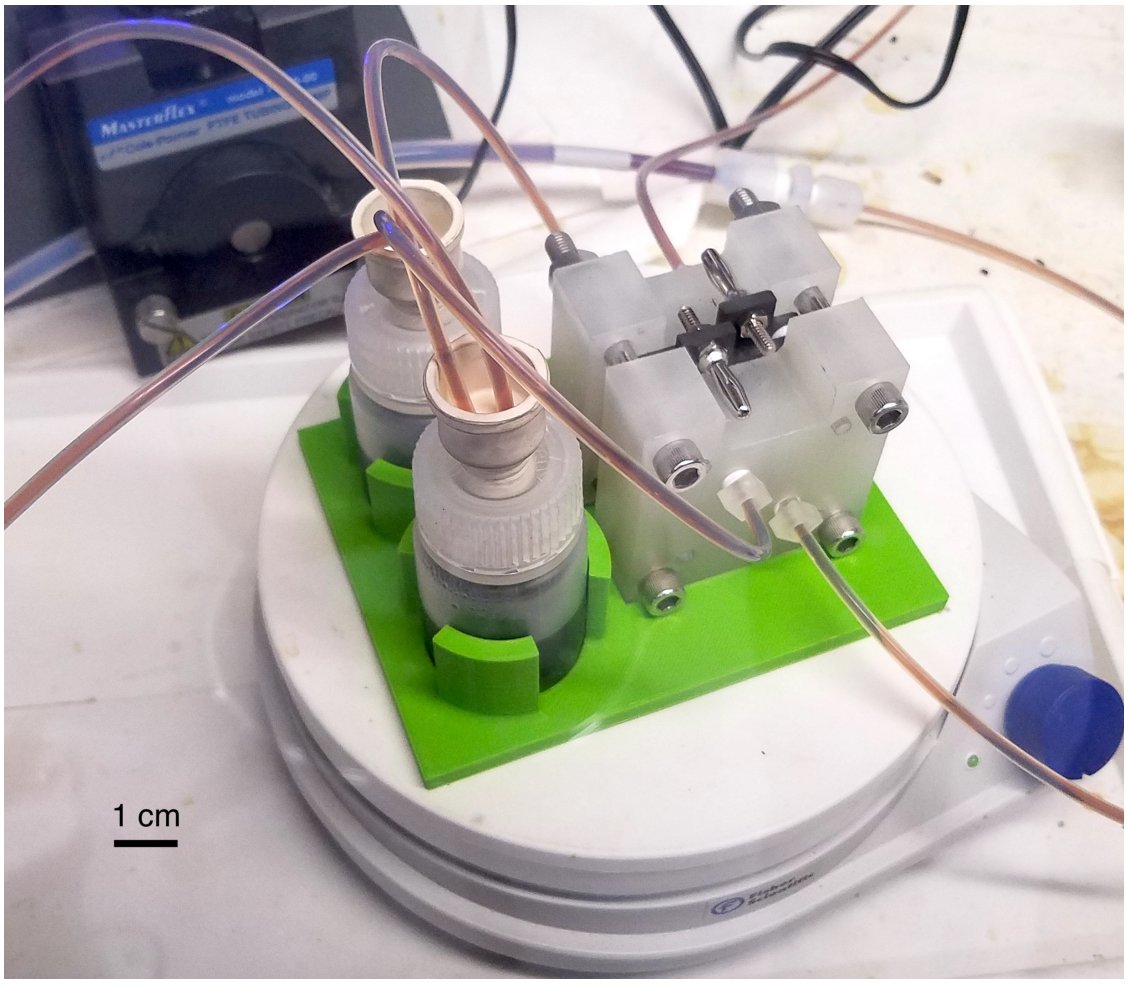


Figure 2.10: Experimental flow cell running in glovebox

3

V(acac)$_3$ Development & Separator Fouling

Contents

3.1 Introduction 77
3.1.1 Context 78
3.2 Solvent Manipulation for Energy Density 79
3.2.1 Solubility & Conductivity Results 84
3.2.2 Cycling Results 90
3.3 Degradation in V(acac)$_3$ systems 93
3.3.1 Effect of Anion Substitution 97
3.3.2 Effect of V(acac)$_3$ Recrystallization 100
3.3.3 Effect of Different Separator Materials 102
3.3.4 Effect of Porous Electrode Replacement 104
3.3.5 Double Reference Electrode Experiments 107
3.3.6 Discussion 124
3.3.7 Approaches to Deconvolute Degradation Phenomena . . 128
3.4 Conclusion 131

3.1 Introduction

This chapter will examine full-cell cycling of the V(acac)$_3$ chemistry in detail, focusing on discrepancies between literature and the present work, ultimately showing that long-term degradation is confined to a surprising component—the

porous separator. First, results will be shared from efforts to improve energy density through cosolvent optimization. Then, data will be presented from charge/discharge cycling experiments which empirically suggest degradation in long-term cycling experiments is confined to the porous separator. Even with long-term cycling once again possible, degradation was not yet completely eliminated, and a combination of electrochemical impedance spectroscopy, ionic diode testing, and reference electrode techniques were used to further define and isolate the mechanism of degradation. These results are discussed and combined with prior incomplete explanations to form a new hypothesis that solutes are precipitating out of solution in the pores of the porous separator over time due to various physicochemical processes. Subsequent charge/discharge cycling with periodic separator replacement lends weight to this hypothesis. Finally, significantly different classes of membrane materials are tested due to insights obtained from the working hypothesis about degradation and are shown to drastically improve the long-term stability of the system, motivating further research. The findings from this chapter are supported in the following chapter on iron-based compounds, which suggests this separator pore-clogging process could be agnostic to cell chemistry.

3.1.1 Context

This thesis chronologically follows and developmentally builds off of those of Saraidaridis [91] and Shinkle [92], both of whom made great efforts to advance nonaqueous symmetric flow batteries based on disproportionation compounds. Some of the most useful findings from their works are their insights as to all the ways a nonaqueous flow battery can fail at the benchtop level [93], and demonstration for the first time of long-term stable cycling [69]. At the outset of the present thesis, research began optimistically with the pretext that the only impediment to long-term cycling of the V(acac)$_3$ chemistry was the management of bulk reservoir imbalance. Indeed, when building benchtop cells with the knowledge developed by Saraidaridis and Shinkle, the primary challenge was the manual rebalancing necessary to keep the cell operational.

Thus, work began on developing the balancing scheme described in Chapter 2. Simultaneously, efforts began to improve the energy density of the system through (co)solvent selection to enhance active-species solubility. During this time period, no active charge/discharge cycling occurred in the laboratory. When the balancing system was operational, and some promising solvent mixtures appeared to afford higher energy density for the symmetric V(acac)$_3$ system, charge/discharge testing resumed. When cycling experiments began, however, a concerning lack of experimental reproducibility was observed. Significant time and effort went in to attempting to reproduce prior results. After substantial remediation efforts, largely related to active species purification, results were obtained that resembled earlier experiments.

Still, however, some transient degradation behavior was observed that had been obscured by imbalancing in prior experiments. To account for these observations, hypotheses were made, tested, and rejected. Performance improved significantly when the V(acac)$_3$ used in experiments was thoroughly purified by recrystallization and washed with anhydrous ether, whereas prior experiments in our group and others had used material from a specific supplier as received. With the issue of V(acac)$_3$ purity addressed, reproducibility was achieved. The balanced, purified system lasted longer than prior experiments had achieved, which led to the observation of new failure mode at longer timescales. This new failure mode had a voltage signature similar to the previous mode, confounding initial attempts to understand and mitigate failure. In short, a problem appeared and was resolved, and a new, longer-term degradation phenomenon appeared at longer timescales.

3.2 Solvent Manipulation for Energy Density

Portions of this section's experimental work and analysis were performed by Luke Petit, a supervised Masters' student.

Nonaqueous redox flow batteries have the potential to be more energy-dense than their aqueous counterparts. The wider electrochemical stability windows of organic solvents enable higher-voltage redox reactions, which have already

been demonstrated to improve molar energy density ($\mathrm{W\,h\,mol^{-1}}$, active species basis). Exceeding the theoretical maximum volumetric energy density of state-of-the-art commercial active liquids ($37.5\,\mathrm{W\,h\,L^{-1}}$ for aqueous vanadium at 1.4 V and 2.0 M, a standard concentration [94]) requires increasing the active-species concentration past a threshold inversely proportional to the nonaqueous cell's redox potential according to

$$E_{\mathrm{vol}} = \frac{1}{2} n F V_{\mathrm{cell}} C_{\mathrm{actives}}, \tag{3.1}$$

where E_{vol} is volumetric energy density ($\mathrm{W\,h\,L^{-1}}$), n is the number of moles of electrons transferred per mole of active species, F is Faraday's constant, V_{cell} is cell voltage, C_{actives} is the molar concentration of active species and the factor of $\frac{1}{2}$ accounts for the symmetry of the cell, in which the negative and positive electrolyte volumes are assumed to be equal.

The theoretical energy density of aqueous vanadium is not realized in practice however, due to non-unity utilization efficiency, and industrial RFB companies don't publicly share their numbers but the author has heard in various forums industrial aqueous vanadium RFBs have energy densities in the upper-20-Wh/L range.

Shinkle *et al.* studied the properties of supporting salts and solvents for use with V(acac)$_3$ [95]. The authors screened twenty supporting salt and solvent mixtures for the maximum solublities of active species and salt using a densitometric method. Conductivities were also determined for each of the mixtures. The solvents investigated were ACN, dimethylformamide (DMF), dimethylcarbonate (DMC), tetrahydrofuran (THF), and hexane. Supporting salts studied include TEABF$_4$, tetrabutyllammonium tetrafluoroborate (TBABF$_4$), tetrabutylammonium hexafluorophosphate (TBAPF$_6$), and (1-butyl, 3-methyl)imidazolium bis(trifluoromethanesulfonyl)imide (BMIMTFSI).

Conductivity data are shown in Table 3.1. ACN consistently offers greater conductivity than DMF, independent of salt, while TEABF$_4$ offers the greatest conductivity in both solvents. DMC, THF and hexane give significantly lower conductivities with all salts.

Table 3.1: Conductivities of 0.1 M salt/solvent mixtures from [95].

Salt	Conductivity (mS cm^{-1})				
	ACN	DMF	DMC	THF	hexane
none	1.63×10^{-3}	7.86×10^{-4}	$<5 \times 10^{-5}$	$<5 \times 10^{-5}$	$<5 \times 10^{-5}$
$TEABF_4$	11.20	5.53	$<5.3 \times 10^{-3}$	$<5 \times 10^{-5}$	$<5 \times 10^{-5}$
$TBABF_4$	9.93	4.76	0.30	0.06	$<5 \times 10^{-5}$
$TBAPF_6$	9.91	4.56	0.57	0.06	$<5 \times 10^{-5}$
BMIMTFSI	10.29	4.76	0.95	0.13	$<5 \times 10^{-5}$

The solubility limits of salts and active species in the solvents are shown in Table 3.2. $TBABF_4$ is the most soluble in ACN and DMF while $TEABF_4$ and $TBAPF_6$ are sufficiently soluble to provide minimum conductivity for subsequent experimental work. $TEABF_4$ offers the highest conductivity per mole and is initially selected for study to minimize material usage. Table 3.2 also shows that the active species is most soluble in ACN, with a maximum concentration of 0.59 M. The paper shows that solutions of V(acac)$_3$ and $TEABF_4$ in ACN will offer the greatest energy density and conductivity. This chemistry will form the reference for experiments presented here.

The motivation to use multi-component solvent stems results from the desire to increase energy density beyond what could be achieved using a single-component solvent while maintaining sufficient conductivity. Solvent mixtures are common in electrochemical systems and an enlightening discussion for nonaqueous electrolytes is given in chapter 2 of [90]. A binary solvent mixture could contain a majority of one solvent with high active-species solubility but poor conductivity combined with a smaller amount of another to dissolve the electrolyte, providing conductivity and maintaining electroneutrality. Here, preferential solvation may play a key role in explaining observations—a clear explanation is given by Ben-Naim [96, 97].

Herr *et al.* investigated the solubility of V(acac)$_3$ in single-component and multi-component solvent mixtures [98]. Solubility limits of the active species were measured using a shake-flask method involving incremental addition of active species to a fixed volume of solvent followed by shaking and shelving overnight. This method cannot measure the change in volume upon addition of active species, so limiting concentrations are expressed in moles per liter of pure solvent, making

Table 3.2: Solubility limits of V(acac)$_3$ and salts in given solvents from [95].

		Maximum solubility (M)				
		ACN	DMF	DMC	THF	hexane
Salt	$TEABF_4$	1.60	1.38	-	-	-
	$TBABF_4$	>3.04	>3.04	-	-	-
	$TBAPF_6$	1.60	0.56	-	-	-
	BMIMTFSI	miscible	miscible	-	-	-
Active species	V(acac)$_3$	0.59	0.54	0.53	0.50	-

it difficult to compare to values reported in other literature. A large number of solvents were tested including ACN, DMF, dimethyl sulfoxide (DMSO), 1,3-DO and dimethoxyethane (DME).

Selected results from the solubility tests are given in Table 3.3. They show that pure dioxolane and pure DMF give a small increase in moles per litre of pure solvent (mol L_{solv}^{-1}). A greater increase was visible with some binary and ternary mixtures, with the highest solubility of 1.10 mol L_{solv}^{-1} achieved by a mixture of ACN, DMSO and 1,3-DO. Based on the experimental results obtained, Herr *et al.* report the following as solvent-mixture criteria for high solubility of active species and high conductivity:

- High amount of acetonitrile
- One solvent with a high donor number and polarizability
- Viscosity should be kept as low as possible

Table 3.3: Solubility of V(acac)$_3$ in different solvent mixtures. Selected results from [98]

Vol % of solvent					Solubility limit (mol $L_{solvent}^{-1}$)
ACN	DMSO	DO	DMF	DME	
100					0.6
	100				<0.3
		100			0.8
			100		0.7
				100	0.6
94.1	5.9				0.90
94.1			5.9		1.00
76.2	4.8			19.0	0.75
76.2	4.8	19.0			1.10

The criteria listed provide useful direction for selecting solvents that should be investigated further. An important conclusion from these results is that small additions of another solvent to ACN can decrease the total volume of solvent required to dissolve a given mass of V(acac)$_3$. It is desirable to explore whether this corresponds to an increase in molarity and therefore energy density, or if it is due to the additional solvent creating a mixture with a greater density than ACN. Comparisons cannot be made regarding maximum solubilities, as the method used does not consider the partial molar volume of the active species. For a given nonaqueous electrolyte, optimization for a given active-species chemistry to achieve maximum volumetric energy density requires careful selection of solvent systems and supporting electrolyte, subject to the constraints of solubility limits (at all oxidation states of the active species), electroneutrality, and conductivity [95, 99, 100].

This section focuses on the V(acac)$_3$ active species, with TEABF$_4$ as the supporting salt. The solubility limit of V(acac)$_3$ in several solvents is determined densitometrically as in [95]. Promising binary mixtures of mutually miscible solvents are explored further, with the aim of choosing one solvent that preferentially solvates V(acac)$_3$ and the other that solvates TEABF$_4$. Optimization of the binary electrolyte identifies a solvent system of ACN and 1,3-DO which offers a maximum V(acac)$_3$ solubility of 0.95 M and a theoretical energy density of 29.3 W h L^{-1}, an improvement of 43.6% over the previous theoretical maximum based on neat ACN.

Methods

Densitometry was used to establish solubility limits in terms of molarity, with the aim of making the solubility limits comparable across solvent systems. This process involves making solutions of solute and solvent at various mass or mole fractions lower than saturation (solubility limit), and a few solutions of undissolved solute and saturated supernatant. The densities of the liquid phases of these samples are recorded and plotted as a density *vs.* concentration curve. This curve is typically linear to a first approximation, allowing a line to be fit through the data. Linear best fits forced through the density of the salt-free solvent mixture were performed

by the method of least squares. A line can then be fit through the density data. The intersection of the best-fit line with the density of saturated supernatant then yields the solubility limit of the solute.

The solute V(acac)$_3$ was weighed with a weighing funnel on an analytical balance, then added to a 16 mL glass vial. The chosen solvent (or solvent mixture) was then added with a syringe through the weighing funnel, while rinsing off any residual V(acac)$_3$ from the funnel. The mass of the added solvent was then recorded. Samples were stirred overnight to ensure that they reached thermodynamic equilibrium, after which their densities were recorded with an Anton Paar DMA 4100M densitometer at 20°C. Care was taken to use neat solvent to rinse the U-tube of the densitometer in between samples and then dry the tube with the instrument's built-in blower.

Conductivity measurements were recorded in an Orion Duraprobe 4-electrode conductivity cell in a 23.5°C water bath using a Thermo Scientific Orion Star A215 pH/conductivity benchtop multiparameter meter.

3.2.1 Solubility & Conductivity Results

Single Solvents

Fig. 3.1 shows a representative density/composition relationship for the solute V(acac)$_3$ in the solvent acetonitrile. This densitometric series of measurements led to a solubility value of 0.7 M.

Table 3.4 shows the solubilities of V(acac)$_3$ and conductivities of $TEABF_4$ in singular solvents.

Table 3.4: Densitometry and conductivity test results for pure solvents as single measurements taken by Luke Petit. *$TEABF_4$ is not entirely soluble at 0.3 M

Compound	V(acac)$_3$ Sol. / M	Cond. 0.3 M $TEABF_4$ / mScm^{-1}
1,3-DO	0.99	0.0*
ACN	0.70	29.9
DMF	0.50	6.5*
DME	0.26	7.3*
DMSO	0.17	7.6

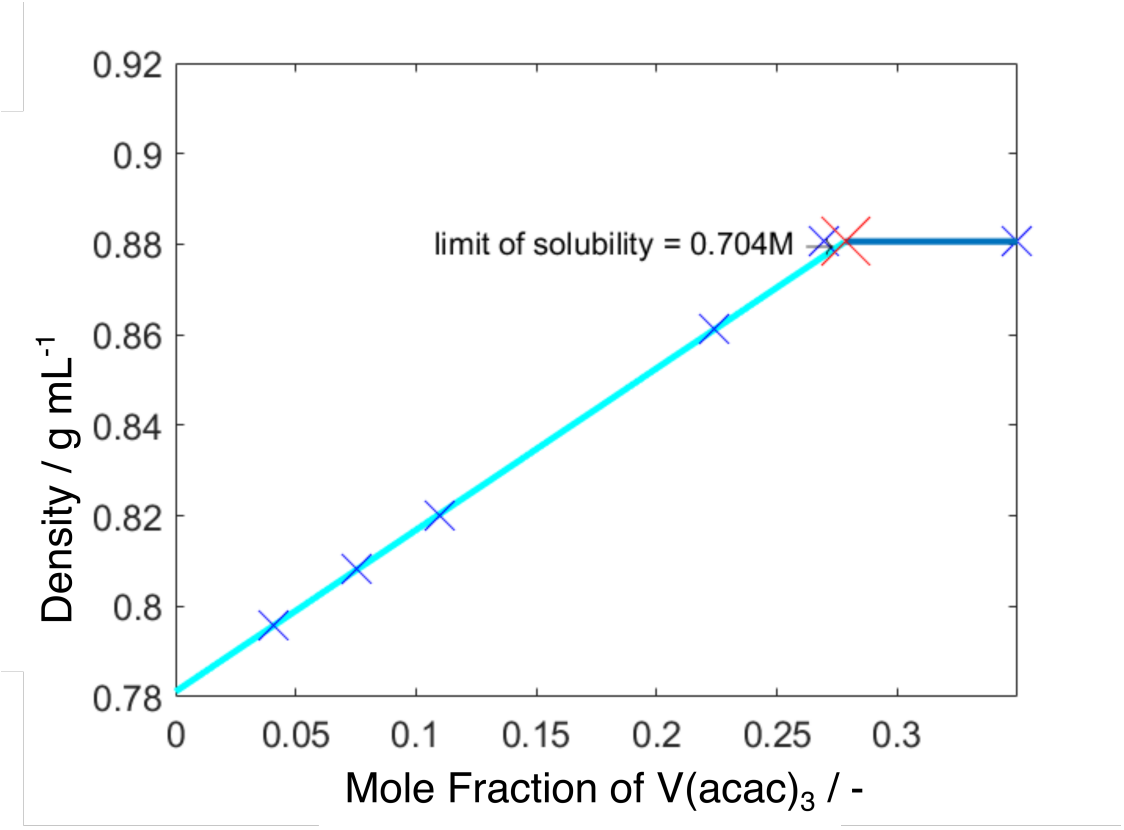


Figure 3.1: Plot of densitometry results showing variation in density with mass fraction of V(acac)$_3$ for pure ACN at 20°C, recorded by Luke Petit

Solvent Mixtures

Herr *et al.* reported V(acac)$_3$ solubility for several solvent mixtures in [98], with the metric of moles V(acac)$_3$ per liter of *solvent*, not per liter of solution. The results indicated that adding small amounts of a cosolvent to ACN could strongly impact the solubility of V(acac)$_3$. The densitometric method of solubility determination used here yields solubility on a solution-volume basis. A series of experiments were performed that explore the effect of small amounts of cosolvent on the molar solubility. The solvent mixtures studied were all 95% ACN: 5% cosolvent on a mole fraction basis. This approach also differs from that of Herr *et al.* who used a neat volume basis when computing the compositions of solvent mixtures. The reasoning for using mole fractions are twofold; one, volume fraction is sensitive to temperature whereas mole and mass fractions are not, and two, volumes of neat solvents are not generally additive when they are combined to form a solution.

Thus mole fractions are a more reliable metric.

Table 3.5 shows the results of five different acetonitrile-rich solvent mixtures. With the exception of ethylene carbonate (EC), which is solid at ambient tem-

Table 3.5: Densitometry test results for solvent mixtures

Solvent / percentage by mole	limit of solubility of V(acac)$_3$	
	M	mol L_{solv}^{-1}
95% ACN 5% DMSO	0.67	0.82
95% ACN 5% DO	0.69	0.83
95% ACN 5% DMF	0.70	0.87
95% ACN 5% DME	0.70	0.86
95% ACN 5% EC	0.54	-

perature and can be considered as a co-solute, no significant change in solubility on a molar basis is seen for any co-solvent system, with all solubilities equal to or less than those observed for pure ACN. The solubilities on a solvent-basis are also shown for comparison, indicating that the trend reported by Herr *et al.* is in fact an artificial effect that owes primarily to the difference in densities between the chosen co-solvent and ACN.

Nevertheless, the work by Herr *et al.* and others suggest 1,3-DO affords higher solubility for V(acac)$_3$ on a molar basis than ACN. Consequently, experiments evaluate the ACN:1,3-DO co-solvent system were conducted. Solubility was determined densitometrically for four intermediate mole fractions between neat ACN and 1,3-DO. These data are shown in Fig. 3.2.

The blue line in Fig. 3.2 is the predicted solubility of V(acac)$_3$ assuming a mixing rule in which the solubility determined by linearly weighting the pure-solvent solubilities by the mole fractions of ACN or 1,3-DO. The red crosses show how experimental data reflect higher solubilities than expected for mole fractions above 0.2 of 1,3-DO. Thus there is some thermodynamic nonideality in the solubility limit. This nonideality could be attributed to a "hydrotrope"-like or "cooperative solubilization" effect, where the presence of a cosolvent (or cosolute) produces a solubility enhancement greater than expected.

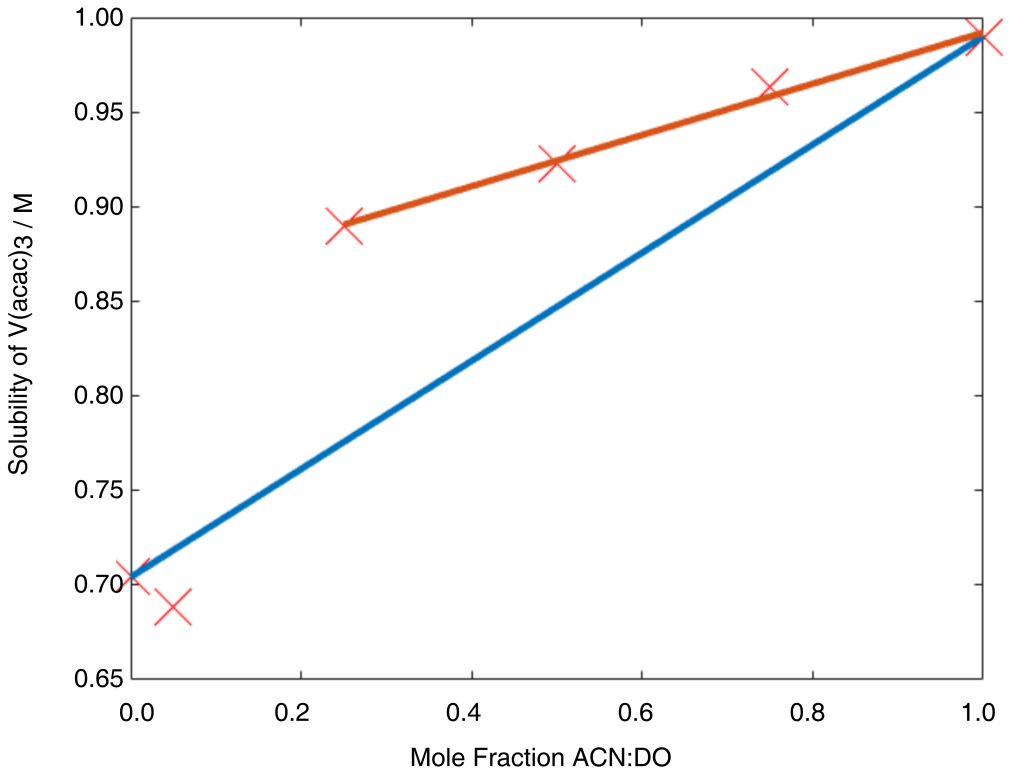


Figure 3.2: Variation in solubility limit of $V(acac)_3$ in ACN/DO solvent mixture with increasing mole fraction of DO. (blue) theoretical relationship (red) experimental data

There is an outlier point at low mole fraction 1,3-DO, where the solubility limit lies below the linear mixing rule. This is odd, but the data for this solvent mixture composition are consistent across the $V(acac)_3$ concentration range, as seen in Fig. 3.3. Future work could double-check this datapoint, though densitometric solubility assays require a nontrivial amount of experimental work, and further, this low mole fraction 1,3-DO region is far from the region where maximum $V(acac)_3$ solubility occurs and as such there is little motivation to do so, when Fig. 3.3 suggests this datapoint is not an outlier.

Fig. 3.3 shows the variation in density of various concentrations across this same composition range. Fig. 3.3 shows that the datapoints at low, nonzero 1,3-DO mole fractions do not seem to be outliers, suggesting the data presented in Fig. 3.2 is valid.

To conclude this series of experiments, the optimum ratio of ACN to 1,3-DO was found according to the following process. To improve theoretical energy density, the

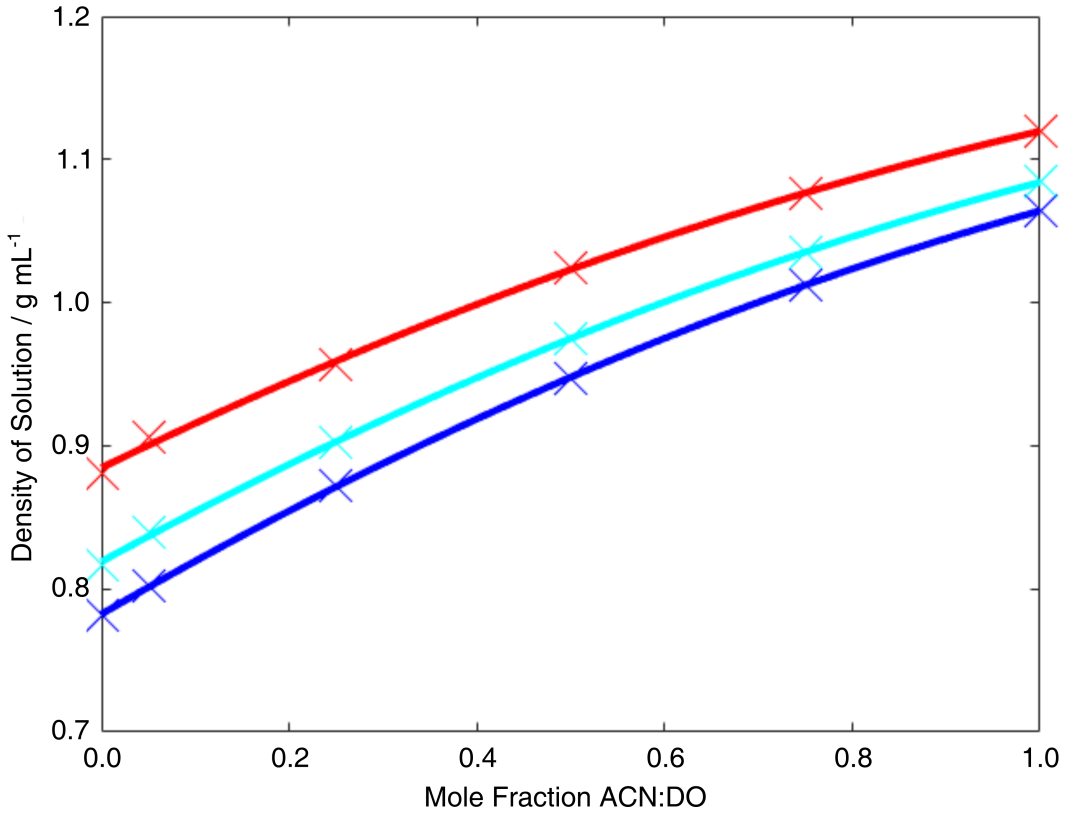


Figure 3.3: Plot showing variation in density of the ACN/DO solvent mixture with increasing mole fraction of 1,3-DO for (dark blue) no V(acac)$_3$ (light blue) 0.1 M V(acac)$_3$ (red) 0.7 M V(acac)$_3$, recorded by Luke Petit

solubility of V(acac)$_3$ must be maximized subject to the constraint that $C_{\text{actives}} \leq 2C_{\text{salt}}$, where C_{actives} is active species concentration and C_{salt} is the concentration of the supporting salt, presuming that the active species undergoes single-electron disproportionation and the supporting electrolyte is a 1:1 salt. This constraint is necessary to ensure a minimum ionic strength to support the maintenance of electroneutrality up to a 100% theoretical SOC. The following equation defines the solubility of V(acac)$_3$ as a function of mole fraction of 1,3-DO, x_{DO}, according to the data in Fig. 3.2, where the solubility limit of V(acac)$_3$ increases linearly past 25% mole fraction 1,3-DO.

$$C_{\text{V(acac)}_3} = 0.135 \times x_{\text{DO}} + 0.857 \qquad \text{if} \qquad 0.25 \leq x_{\text{DO}} \leq 1.00 \tag{3.2}$$

The solubility limit of $TEABF_4$ in ACN is 1.6 M [95], so the amount of $TEABF_4$

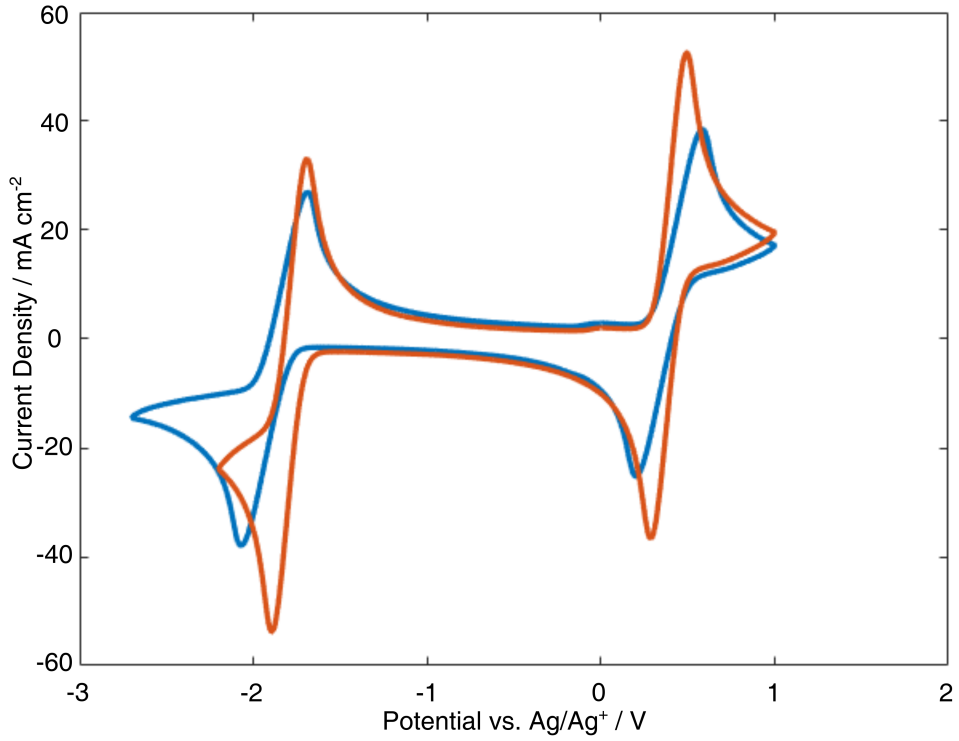


Figure 3.4: Cyclic voltammogram of (red) 0.5 M $TEABF_4$ in ACN with 0.1 M $V(acac)_3$ active species (blue) 0.4 M $TEABF_4$ in 0.3 ACN 0.7 DO by mole fraction with 0.1 M $V(acac)_3$ active species, glassy carbon working electrode, silver/silver nitrate reference, scan rate 400 mVs^{-1}, 25°C, recorded by Luke Petit

solvable by the ACN in an ACN:1,3-DO mixture can be approximated by

$$C_{\mathrm{TEABF_4}} = (1 - x_{\mathrm{DO}}) \times 1.6 \tag{3.3}$$

Solving for the highest possible concentration of $V(acac)_3$ gives an optimal molar ratio of 7:3 for ACN:1,3-DO. This would map to a solubility of $V(acac)_3$ of 0.95 M and allow a concentration of 0.475 M $TEABF_4$, a $\approx 35\%$ improvement in solubility of $V(acac)_3$ of the solvent mixture compared to pure ACN solvent.

Cyclic voltammetry was performed on a more diluted sample at this molar ratio of solvents to observe $V(acac)_3$ redox in the mixed-solvent environment. Fig. 3.4 shows voltammograms of $V(acac)_3$ in a single-solvent ACN system and the 7:3 ACN:1,3-DO molar ratio.

Fig. 3.4 shows qualitatively similar voltammograms between the two solvent systems, with a slightly wider potential difference between reduction and oxidation couples in the mixed system, and slightly wider peak separation (difference in forward/reverse scan peaks for a given couple) for the individual redox couples. This difference in redox potential, a thermodynamic property, is likely due to the different solvation environment around V(acac)$_3$ molecules. Solvent-induced redox-potential changes are common in nonaqueous electrochemistry [101]. The difference in peak separation indicates that redox-reaction kinetics are more sluggish in the mixed-solvent environment, perhaps resulting from an effect of the 1,3-DO co-solvent on the reorganization energy of V(acac)$_3$. The solubility and redox potential differences of the two systems are summarized in Table 3.6, which shows how use of a mixed solvent system could theoretically enable substantial improvements in energy density for nonaqueous flow batteries. Here, an improvement based on nominal cell potential and solubility metrics along confers a 43.6% improvement from 20.4 WhL^{-1} to 29.3 WhL^{-1}. This metric ignores any possible changes to efficiencies or other follow-on effects that may occur in a mixed-solvent system. In particular, the improvement in maximum energy density due to adding 1,3-DO appears to result in higher kinetic overpotentials for vanadium redox; consequently a lower voltage efficiency might be expected for the co-solvent system.

mole fraction	cell potential / V	V(acac)$_3$ sol. / M	Wh L^{-1}
1.00 ACN	2.18	0.70	20.4
0.70:0.30 DO:ACN	2.30	0.95	29.3

Table 3.6: Parameters for calculation of energy density for pure ACN system and 0.70:0.30 DO:ACN system

3.2.2 Cycling Results

Before testing any high-concentration mixed-solvent systems in the benchtop flow cell, a high-concentration ACN-only cell was run with a total electrolyte volume of 9 mL using 0.52 M V(acac)$_3$ and 0.26 M TEABF$_4$, both of which dissolved completely. To drive the flow in these experiments, Cole-Parmer Masterflex peristaltic pumps

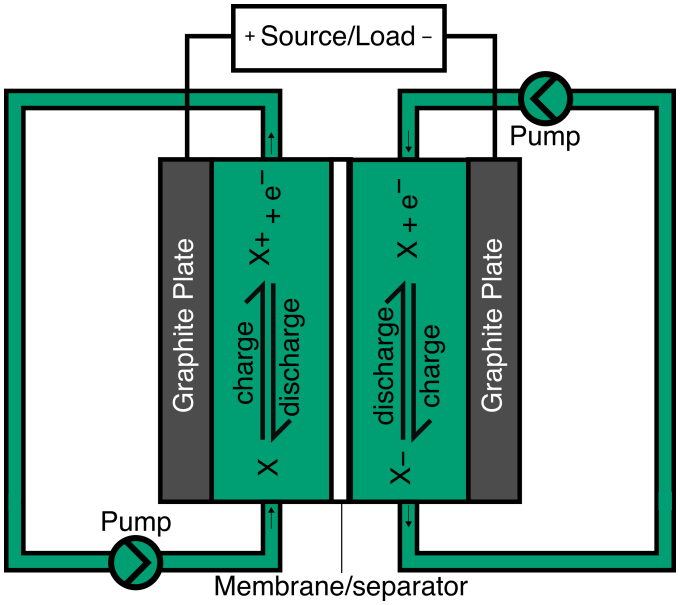


Figure 3.5: Experimental setup of a test cell running without reservoirs in order to minimize solvent evaporation, and because the peristaltic pump tubing occupied sufficient electrolyte volume to facilitate testing

were used as described in [69]. Notably, reservoirs were *not* used in this setup, due to the large dead volume of the pump head tubing required for the peristaltic pumps. This experimental setup is depicted in Fig. 3.5.

This also aided in eliminating solvent evaporation of the nearly-saturated electrolyte, which precipitated out in a previous run using KNF diaphragm pumps and conventional septum-sealed reservoirs. A current density of $50\,\mathrm{mA\,cm^{-2}}$ was applied to the cell. Figs. 3.6 and 3.7 show the cycling behavior and efficiencies of this system,respectively.

Figs. 3.6 and 3.7 show an immediate decay in cycling performance. Note that the noisy voltage profiles in Fig. 3.6 likely owe to the presence of some bubbles in the system, because the lack of reservoirs in this configuration does not allow gas trapped in the flow path to accumulate in reservoir headspace. The first cycle shows a discharge energy capacity of over $8\,\mathrm{W\,h\,L^{-1}}$, at low utilization, coulombic, and energy efficiencies. A $V(acac)_3$ concentration of 0.52 M corresponds to an energy density of $15\,\mathrm{W\,h\,L^{-1}}$, so the utilization efficiency is over 50% on an energy-basis (as opposed to a coulomb-basis, as conventionally used elsewhere in this thesis). Notably, the operating conditions here are not designed to access the majority of active species

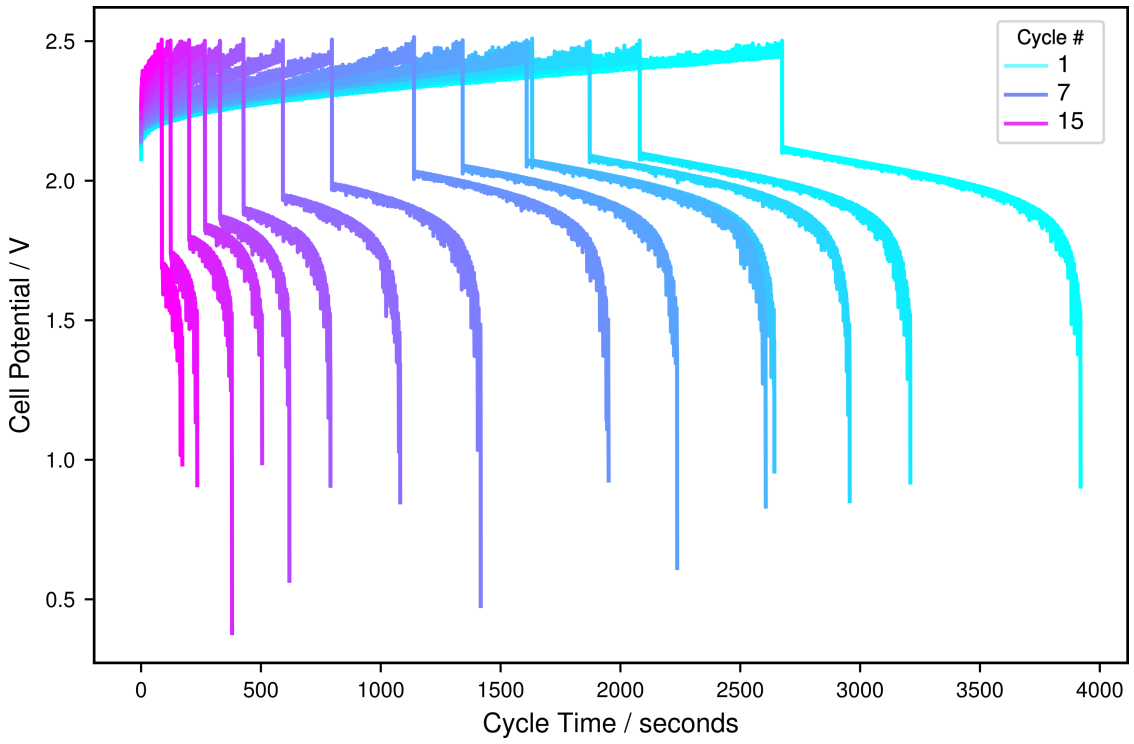


Figure 3.6: Charge/discharge profiles of high concentration V(acac)$_3$ experiment run with peristaltic pumps and no reservoirs

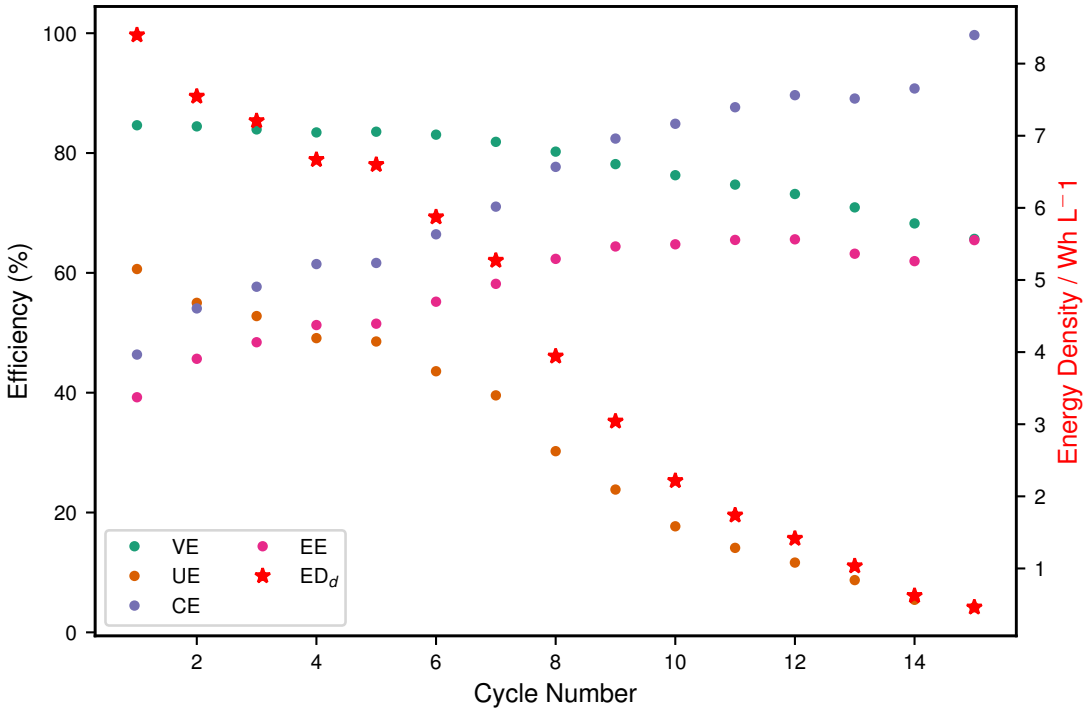


Figure 3.7: Efficiencies of cycles presented in 3.6

dissolved in solution. Because of the strong transient performance decay observed here, further efforts to run high-concentration mixed-solvent V(acac)$_3$ systems were put on hold while efforts were made to understand the rapid performance decay.

3.3 Degradation in V(acac)$_3$ systems

At the outset of the research involved in this thesis, the limiting factor for extended benchtop charge/discharge cycling V(acac)$_3$ experiments was thought to be reservoir imbalancing, an issue mitigated by the developments described in Chapter 2. During development of the balancing system, several months went by without flow-cell charge/discharge experiments using V(acac)$_3$. In this time period, the lab's supply of V(acac)$_3$ was being used to perform the aforementioned mixed-solvent solubility study. When cycling experiments resumed with PID reservoir balancing enabled, very rapid cell failure was unexpectedly observed (such as in Fig. 3.6).

A new stock of V(acac)$_3$ had been purchased since previous cycling experiments, so this was immediately checked. Remnants of the prior stock were still available in the glovebox, and afforded enough residual material to run a flow cell, which did not entirely eliminate the performance fade. Prior to PID balancing development, the cycling protocol had changed from that used in previous experiments by Saraidaridis [69], with constant-current charging at 40 mA cm^{-2} until a HVC of 2.7 V. This was because previous experiments done previously showed no significant performance changes on the timescale of 24-72 hours of cycling. Even switching to a lower voltage cutoff, however, did not completely eliminate the newly observed rapid capacity fade.

In short, stable cycling was initially hindered by reservoir imbalance. This problem was solved, and cycling with newly procured stock of V(acac)$_3$ precursor showed performance fade never seen by the author or previous researchers from the group. The new, higher, voltage cutoff made capacity fade appear sooner, and this fade occurred—although to a lesser extent—even with the old V(acac)$_3$. This combination of events masked the believed origin of this capacity fade for some time, and significant effort was spent modifying and substituting electrolyte and cell components to see if stable cycling could be achieved again.

All cell components (felts, separator, tubing) were remade with no effect. New anhydrous ACN, $TEABF_4$, and $V(acac)_3$ were used with negligible change. Different polymeric separators were tried, along with alternative choices of supporting-electrolyte cation, anion, and solvent (DME). Under all of these conditions, performance decay occurred at different rates, but still occurred in every case. Karl Fischer coulometry was used to confirm quantitatively that water had been excluded from both pre- and post-cycled electrolyte, since rigorous anhydrous conditions are required for stable cycling of $V(acac)_3$ [93].

The investigative effort was taken to some length. The argon atmosphere of the glovebox was sampled and tested using GCMS, on suspicion of a contaminated atmosphere. GCMS results only found argon in the sample. Glovebox purification column material (activated molecular sieves and copper catalyst) were changed with no effect, and attempts were made to perform cycling in an entirely different newly commissioned glovebox. The materials of the reservoirs were changed between borosilicate glass and polypropylene with no effect. NMR was performed on the ACN precursor pre- and post-drying with molecular sieves to determine if molecular sieves were introducing any contaminants (none were found).

While our group has claimed in the past that the chemistry cycles stably [69], and the data presented in the PhD thesis of Milshstein also suggests this [27], there are conflicting reports about the stability of $V(acac)_3$ RFBs [102, 103]. Most attempts at cycling $V(acac)_3$ fail due to insufficient exclusion of water, which causes the formation of vanadyl acetylacetonate ($VO(acac)_2$). Other groups have suggested the fundamental instability of the charged electrolyte as a source of cell failure [104], but these predictions are not commensurate with the cycling stability observed by Milshtein and Saraidaridis.

Nonaqueous electrochemistry is difficult to perform accurately; trace water and oxygen can seriously hinder experimental progress. Based on the demonstrated sensitivity of $V(acac)_3$ to water, and the difficulty of ensuring proper glovebox atmospheres, we attributed the inability of other groups to perform equivalent cycling behavior to their presumed non-rigorous exclusion of contaminants in their

systems. This cannot be the sole explanation, however, because cell failure still occurs with rigorous exclusion of water, in our lab and others. Clegg and Hill show very similar-looking degradation in anhydrous conditions (though they appear to use chemically-incompatible pump head tubing in the experiments) [102]. Clegg and Hill conclude as follows:

> In addition to electrolyte degradation, significant changes to the electrodes are observed post-cycling. XPS reveals the presence of vanadium, fluorine and oxygen containing compounds, as well as small quantities of nitrogen and boron on the negative carbon electrode. The appearance of these features is correlated with a dramatic increase in charge-transfer resistance observed in situ post-cycling. We have shown that even when steps are taken to minimize the impact of moisture, the stability of the non-aqueous vanadium flow battery is limited by degradation processes occurring at the negative electrode. In fact, the rate of degradation observed here is similar to that seen in experiments with much higher background levels of moisture, indicating that this is likely not the primary source of the instability.

Escalante-García *et al.* also suggest the possibility of an electrode process contributing to performance decay [104].

Various hypotheses were formulated after searching the literature. Fluorinated anions are known to intercalate into carbonaceous electrodes at low potentials [90, 105]. Also, electropolymerization of solvent is a common phenomenon. Indeed, Imisides *et al.* offer the following warning: "It is extremely simple to coat an electrode substrate with a polymer. In fact, most electroanalytical chemists have cursed the instances when they have inadvertently achieved electropolymerization" [106]. ACN-based electrolytes have been known to form films upon electropolymerization, although in the present application voltammetry suggests the electrode potentials are insufficient to initiate this process [107].

Electrochemically-induced membrane polymerization was also considered as a source of cell degradation. V(acac)$_3$ is a known Zeigler-Natta polymerization catalyst for olefins like polypropylene and polyethylene, the main component of most porous separators used for nonaqueous RFBs [108]. tetrafluoroborate (BF_4^-) is also known to be unstable in acetonitrile can yield boron trifluoride, another

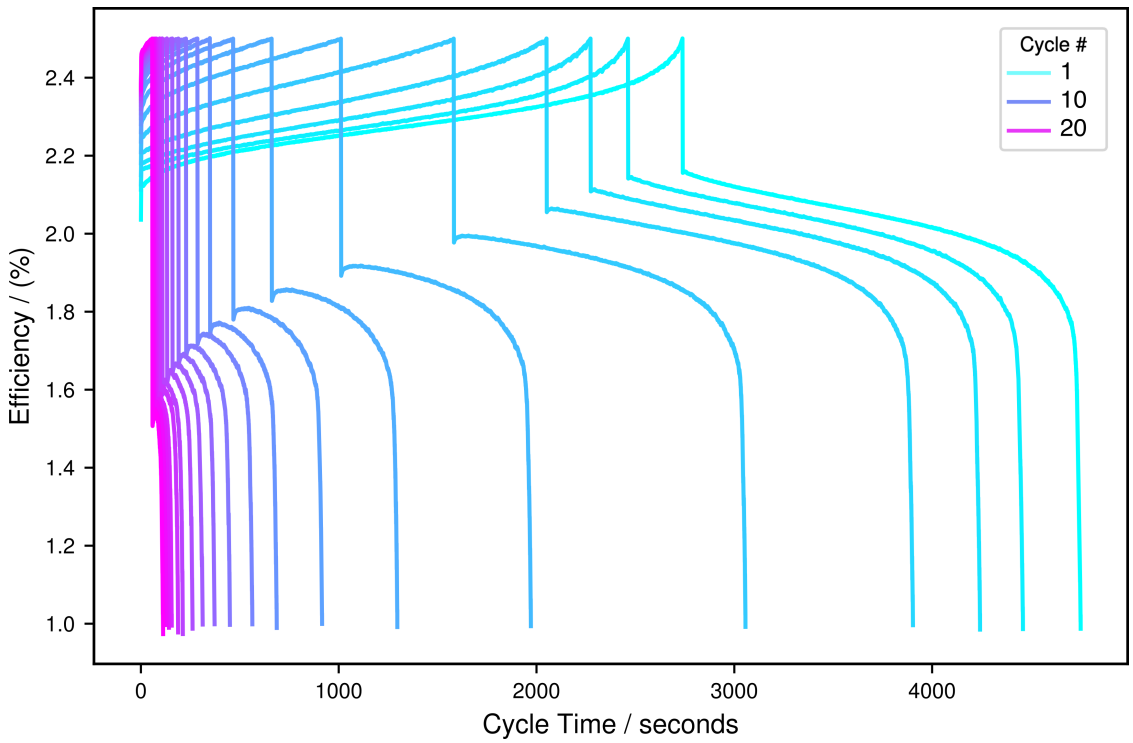


Figure 3.8: Charge/discharge profiles of a representative V(acac)$_3$ system with TEABF$_4$ support undergoing fouling with a constant voltage cutoff of 2.5 V

polymerization agent [109]. The use of inorganic and PEEK separators (which should be immune to action by a polymerization catalyst) failed to alleviate cell degradation, however, seemingly refuting this hypothesis.

Some of the qualitative effects of these various attempts will be shown in the subsequent section, followed by a more comprehensive set of experiments that demonstrate that the degradation phenomenon is confined to the separator and at least partially depends on the separator material.

All the cycling data shown subsequently were recorded with an electrolyte composition of 0.1 M V(acac)$_3$, 0.3 M TEABF$_4$ in ACN using Celgard 4560 separator with an applied current density of 40 mA cm^{-2} in the flow cell described in Chapter 2, unless stated otherwise. When the more rapid cell degradation began occurring after the culmination of the PID balancing development of Chapter 2, the charge/discharge behavior appeared as such in Figs. 3.8 and 3.9, with rapid capacity fade observable within the first 20 cycles.

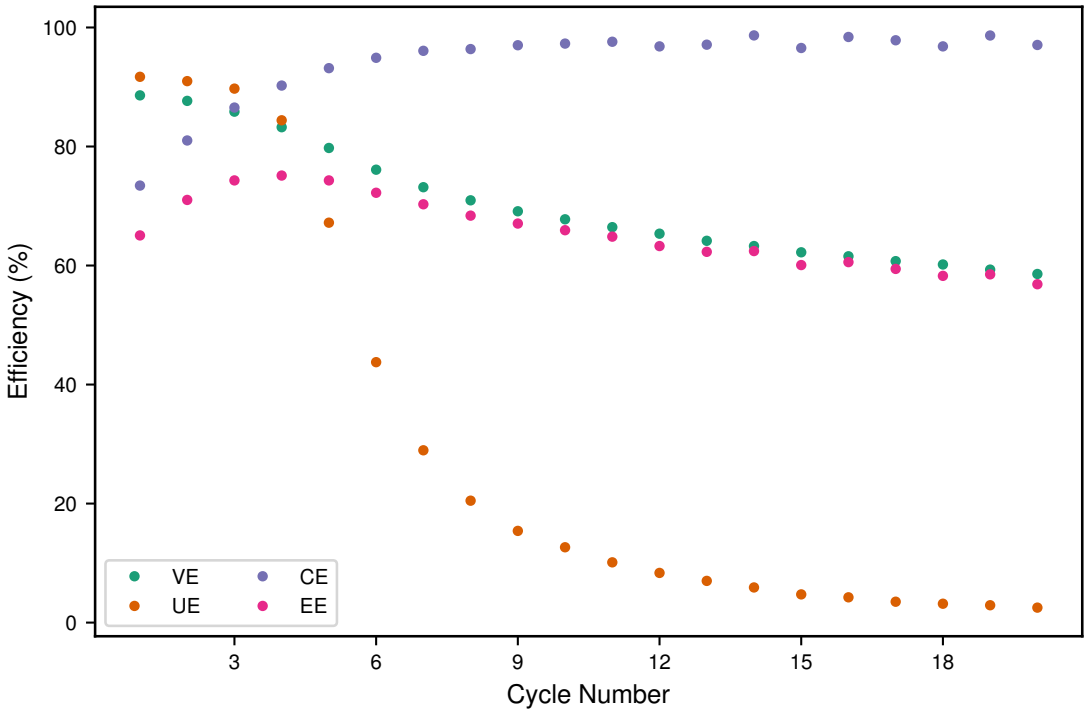


Figure 3.9: Efficiencies of the charge/discharge cycles presented in Fig. 3.8

3.3.1 Effect of Anion Substitution

In efforts to rectify the rapid fade that had previously been observed on a 20-cycle timescale, several attempts were made to achieve cycling which did not exhibit capacity fade, such as remaking/replacing all wetted components, changing glovebox atmospheres, replacing the purification columns of the glovebox, buying new V(acac)$_3$ from the usual (Strem) and other suppliers, scraping the old jar of V(acac)$_3$ for trace material, *etc.* Changing the anion of the support did make a noticeable difference, however. Perchlorate (ClO_4^-) was used instead of BF_4^- as the supporting anion, as BF_4^- is known to react with glass and disproportionate/hydrolyze to some degree [110, 111], and it was thought perhaps the salt had "aged" (even though new salt from multiple manufacturers produced the same results). Also, BF_4^- is known to take part in electrochemical polymerization schemes which could potentially affect the olefin-based Celgard separator [112]. Cyclic voltammetry was performed on both supporting-electrolyte systems to compare the voltammetric responses. Fig. 3.10 shows how both ClO_4^- and BF_4^- systems behave similarly for

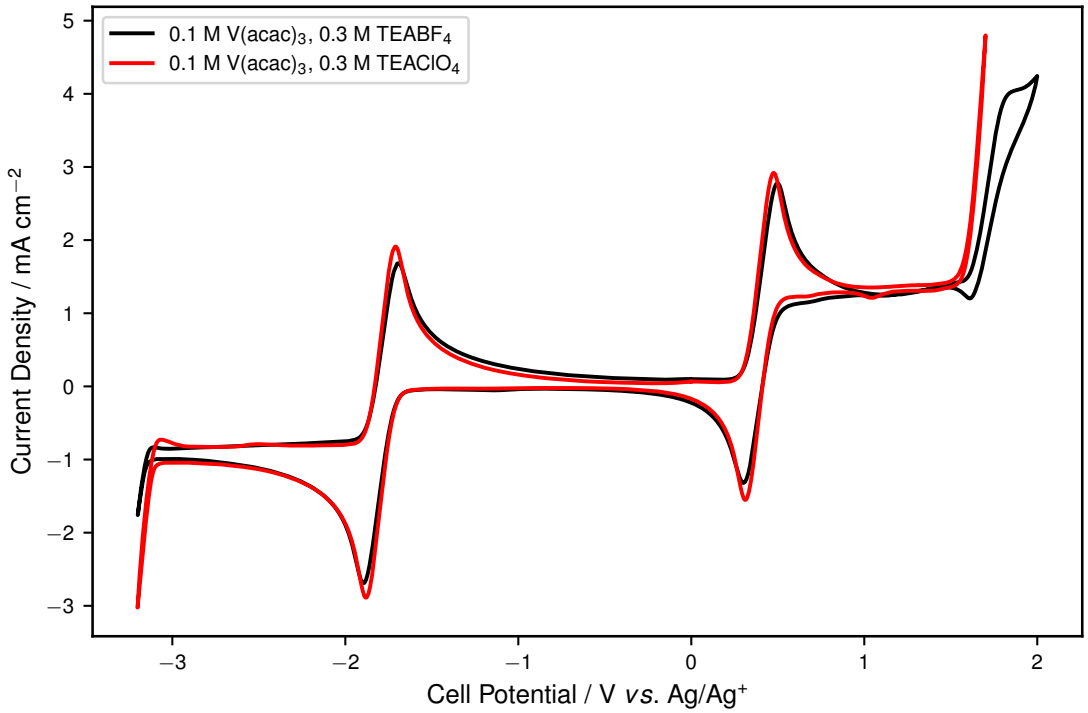


Figure 3.10: Cyclic voltammograms of $V(acac)_3$ with either $TEABF_4$ or $TEAClO_4$ supporting electrolyte in ACN over their entire electrochemical stability windows, GC WE, Pt CE, Ag/Ag^+ RE, scan rate 400 mV s^{-1}

the oxidation/reduction couples known for $V(acac)_3$ in ACN. Voltammograms were recorded at 100 mV s^{-1}, with a 3.0 mm glassy carbon working electrode (BASi), coiled Pt wire counter electrode, and silver/silver nitrate reference electrode.

Fig. 3.10 does show some differing behavior at the anodic (positive) limit of electrochemical stability. The anodic limit of a nonaqueous electrolyte is typically due to coupled solvent/anion breakdown reactions [101]; this figure suggests BF_4^- breaks down at a slightly more positive potential than ClO_4^-. Note that Fig. 3.10 here also demonstrates the extremely wide electrochemical stability window of acetonitrile, also confirming that negligible residual water is present.

Under identical conditions, but using ClO_4^- instead of BF_4^- as the anion, capacity fade occurred at a slower rate, shown in Figs. 3.11 and 3.12 After 20 cycles, the system containing ClO_4^- degraded much less than the BF_4^--containing system, but degradation was still present to a larger degree than the initial experiments at the outset of thesis research. Sodium perchlorate was tried as the supporting

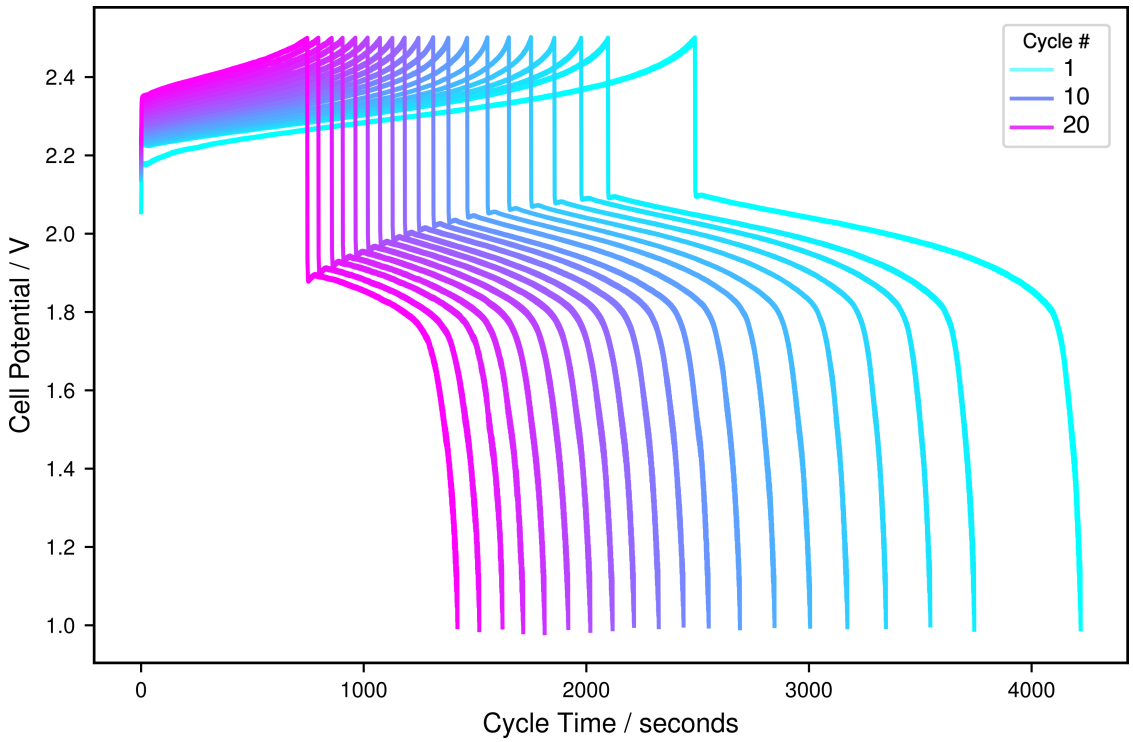


Figure 3.11: Charge/discharge profiles of a representative $V(acac)_3$ system with $TEAClO_4$ support undergoing fouling with a constant voltage cutoff of 2.5 V

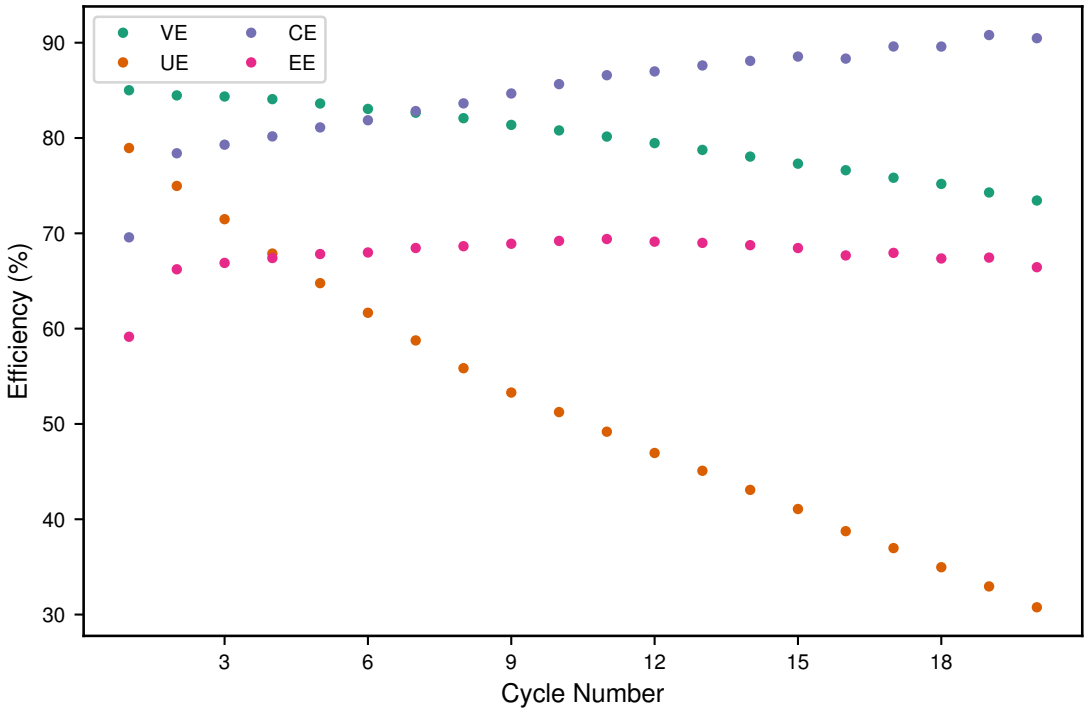


Figure 3.12: Efficiencies of the charge/discharge cycles presented in Fig. 3.11

salt, and voltammograms seemed acceptable within the voltage window of interest, but cycling was not possible. A flow cell using DME and $TBAPF_6$ with $V(acac)_3$ was tried but all performance metrics were poorer. An imidazolium-based cation supporting salt was ordered, to test the absence of a quaternary ammonium cation on this behavior, but this did not arrive in time for testing.

3.3.2 Effect of $V(acac)_3$ Recrystallization

It was thought that there could be purity issues with newly received $V(acac)_3$ or $TEABF_4$ precursor compounds. $V(acac)_3$ cycling was already known to be dependent on supplier—Strem was known to be superior to Sigma-Aldrich, seemingly due to the more rigorous exclusion of the most common degradation product, $VO(acac)_2$, which occurs due to exposure to ambient water from air [91]. Air-free recrystallization and sublimation techniques were learned. The supporting salt $TEABF_4$ was recrystallized from hot acetone without any significant effect on cycling. $V(acac)_3$ was eventually successfully recrystallized in the glovebox from anhydrous acetonitrile and washed with anhydrous diethyl ether, which did seem to make a noticeable difference in cycling performance, but did not fully eliminate capacity fade. Differential scanning calorimetry was performed on as-received $V(acac)_3$ (Strem) and purified compound, showly qualitatively that the purification process did remove something, as the pure sample had one fewer peak than the as-received sample. NMR was attempted as well, but the paramagnetic nature of $V(acac)_3$ caused issues with meaningful interpretation of results.

In any case, purifying $V(acac)_3$ seemed to remove contaminants. Sometimes, when pouring the supernatant off recrystallized $V(acac)_3$ crystals, some blue-ish compound could be seen which had crystallized separately from the $V(acac)_3$. This color resembles that of $VO(acac)_2$, which is known to be moderately soluble in diethyl ether. This justified washing the purified $V(acac)_3$ with diethyl ether after crystallization, to remove any possible residual $VO(acac)_2$.

Cycling results from recrystallized $V(acac)_3$ are shown in Figs. 3.13 and 3.14. Only 5 mL of total electrolyte was split across across hermetically sealed reservoirs

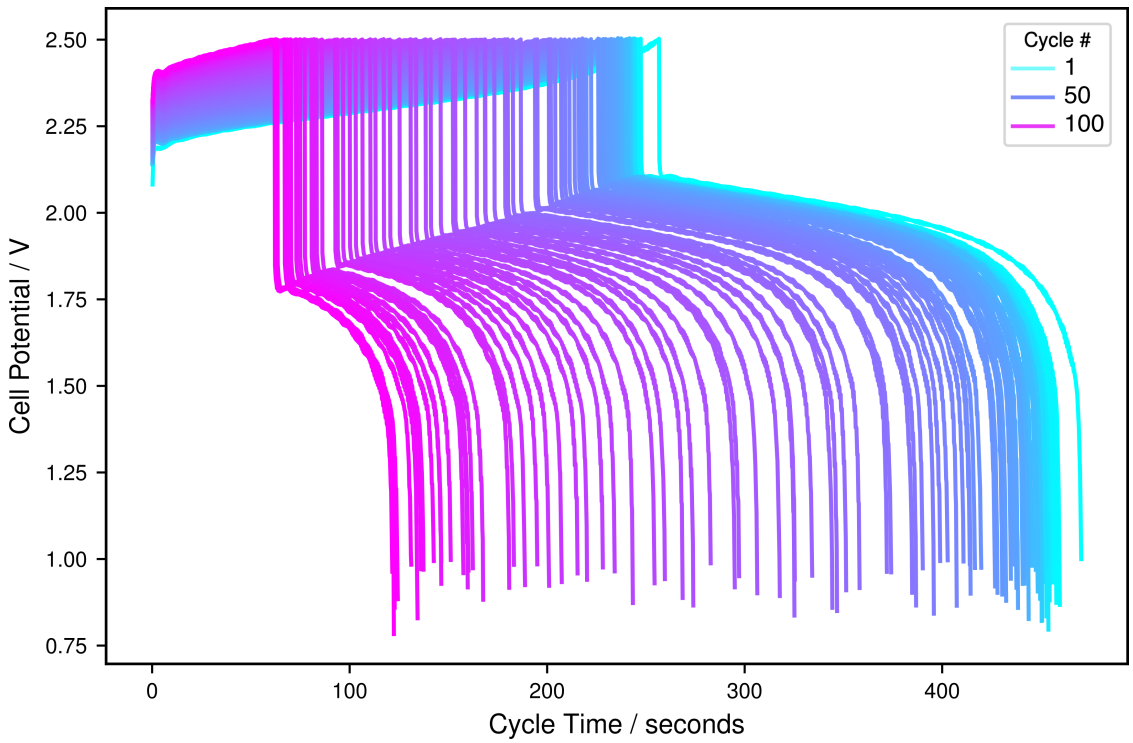


Figure 3.13: Charge/discharge profiles of a flow cell with V(acac)$_3$ purified by recrystallization

(described in Appendix A), which is why cycle times are much shorter than previous experiments.

For the first time here, under voltage-cutoff cycling, a sigmoidal decay in utilization efficiency is observed, along with a clear gradual increase in coulombic efficiency and decrease in voltaic efficiency, which combine to produce a local maximum for energy efficiency. While 100 cycles are observed, cycle times were shorter than previous experiments, so this is not directly comparable. A smaller electrolyte volume was used due to the difficulty of producing large amounts of V(acac)$_3$ through recrystallization. The shorter cycle times do lead to improved resolution of the decay process, however.

Figs. 3.13 and 3.14 led to the formulation of a separator-fouling hypothesis: something is blocking the pores of the porous separator, thereby causing an increase in coulombic efficiency due to lower self-discharge through fewer/smaller pores, but a corresponding decrease in voltaic efficiency. If this is the process for performance decay, then replacing the separator would be expected to restore

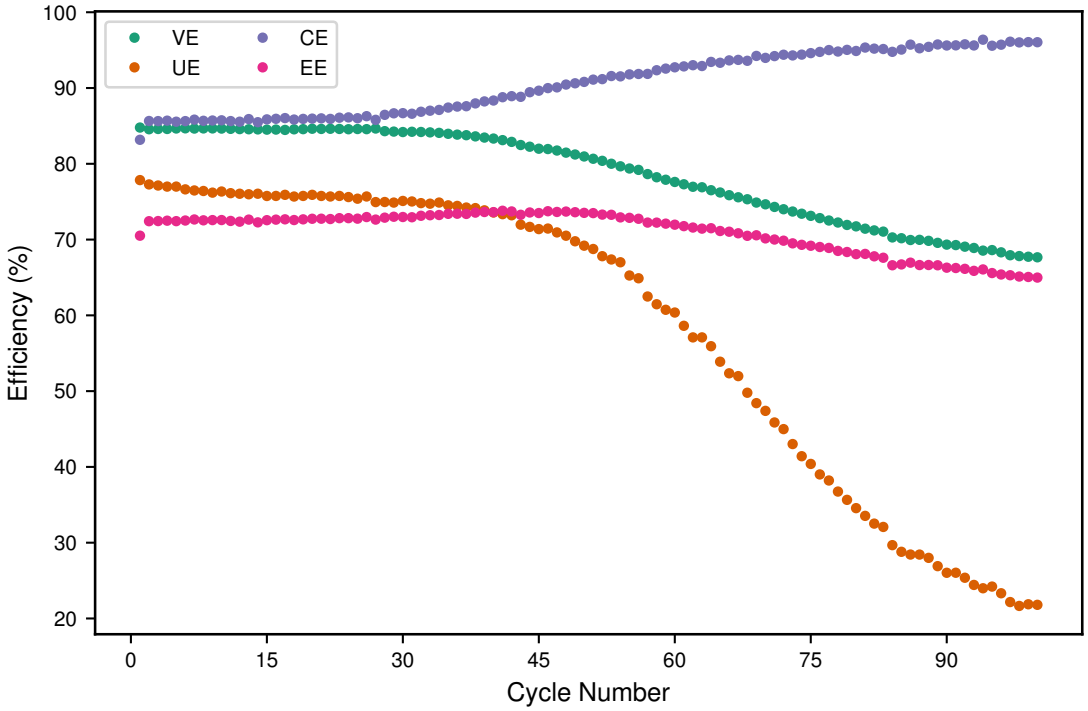


Figure 3.14: Efficiencies of the charge/discharge cycles presented in Fig. 3.13

performance. Indeed, replacing the separator while keeping the electrolyte and electrodes restored performance to almost original cycle capacities. However, this behavior was not always repeatable, and replacing the electrodes while keeping the separator also sometimes restored some performance. Further results regarding separator replacements are given in the following chapter.

3.3.3 Effect of Different Separator Materials

Other polymeric separators were tried using 0.02 µm pore size filtration membranes made from PTFE, PVDF, PEEK, and Nylon, with none of them enabling stable cycling. Use of a 0.02 µm pore size Whatman Anodisc alumina separator did seem to extend performance for longer, however—but did not eliminate this performance decay.

Charge/discharge cycles are shorter in Fig. 3.15 because the cell area was larger due to cell modifications to prevent the brittle ceramic separator from fracturing, and current density was maintained at 40 mA cm^{-2}. Again, a sigmoidal decay of

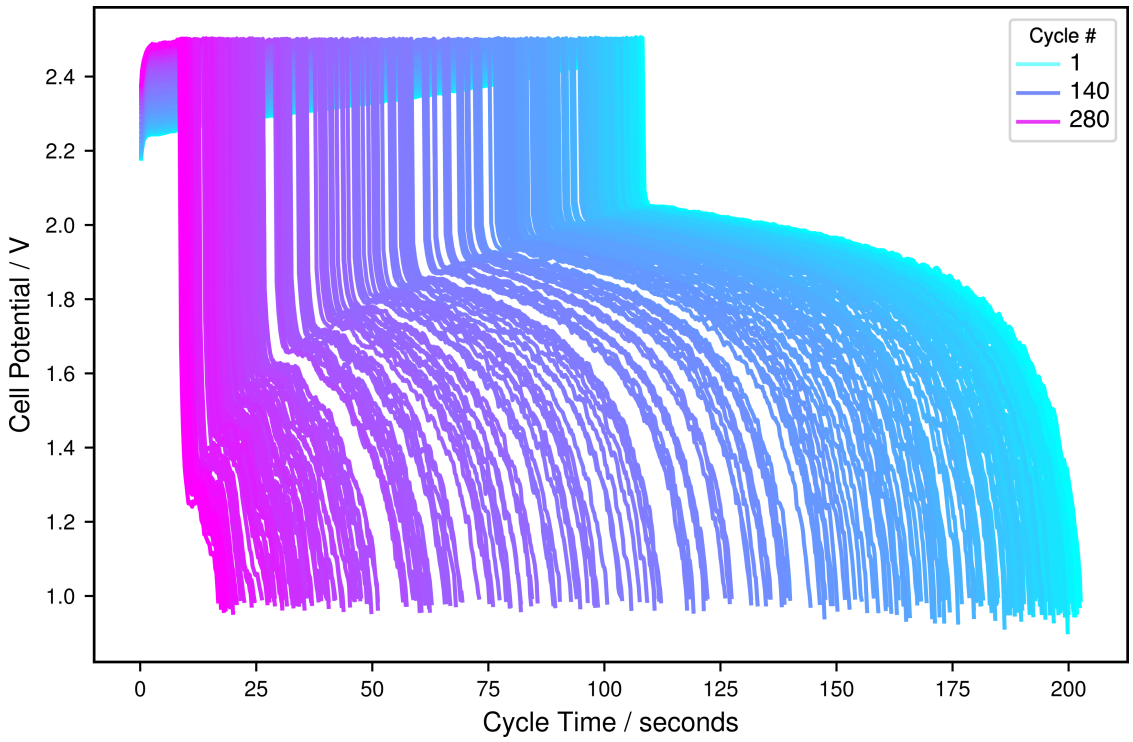


Figure 3.15: Charge/discharge profiles of a V(acac)$_3$ flow cell with an Anodisc alumina separator

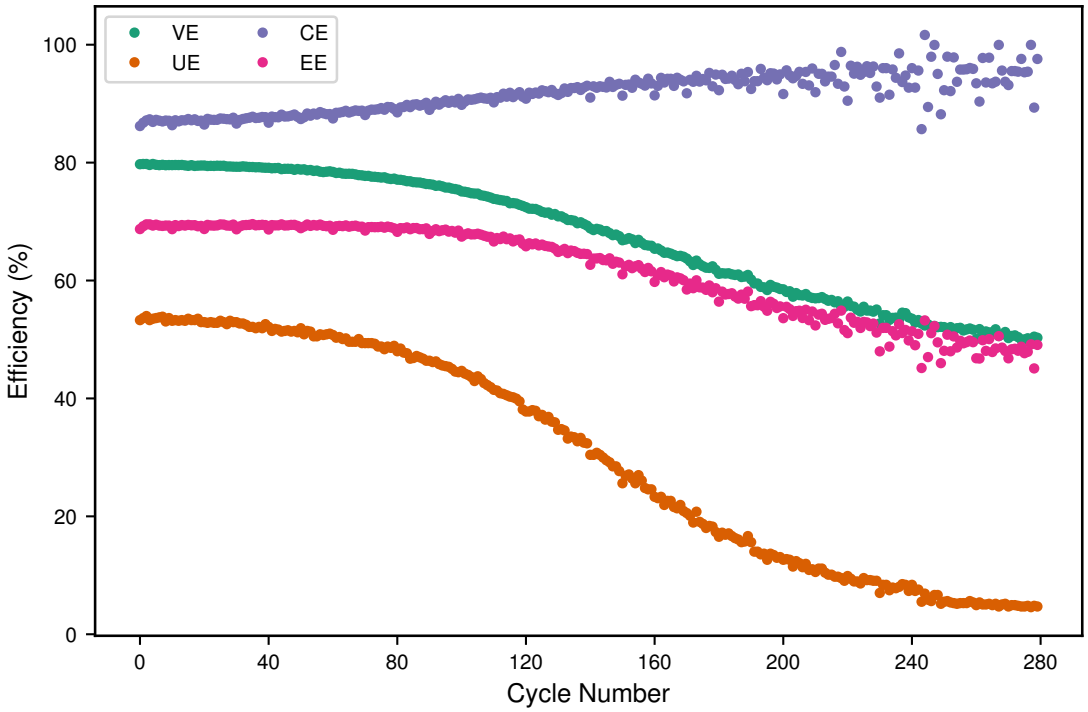


Figure 3.16: Efficiencies of the charge/discharge cycles for a V(acac)$_3$ cell with an Anodisc alumina separator presented in Fig. 3.15

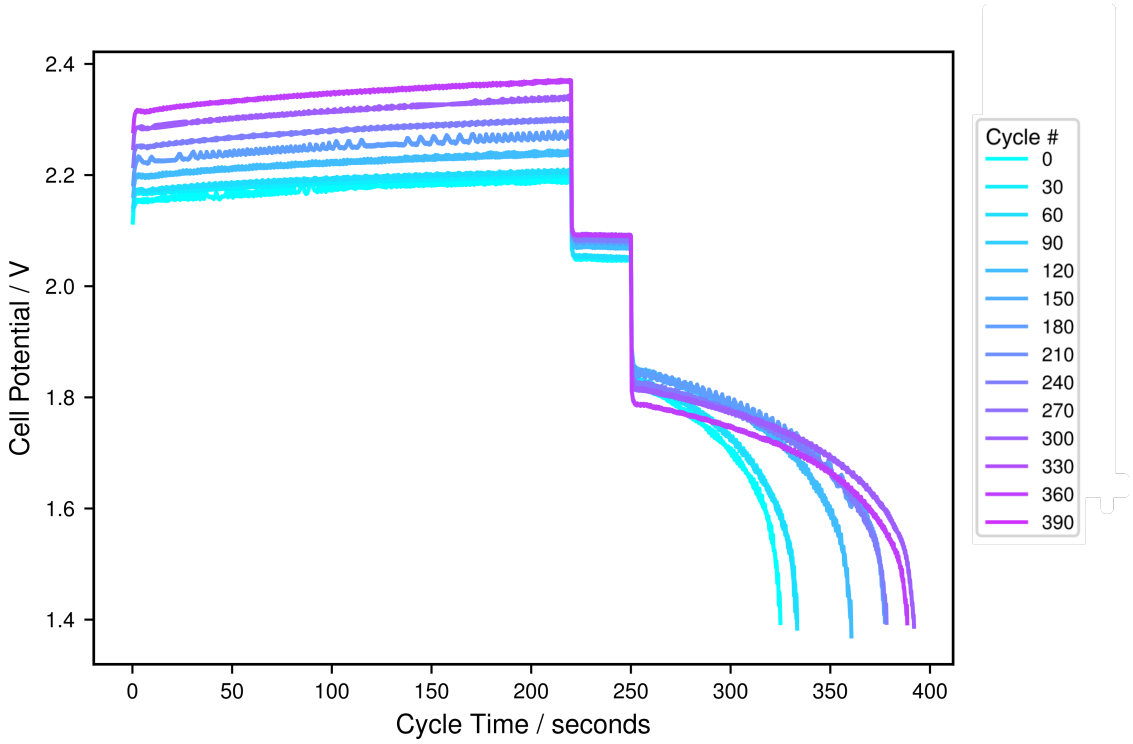


Figure 3.17: Charge/discharge profiles of a V(acac)$_3$ flow cell with a cellulose Dreamweaver Silver 20 separator

utilization efficiency is seen, just as with Celgard 4560, along with an upward trend in coulombic efficiency and downward in voltaic.

A Dreamweaver Silver 20 cellulose membrane was also tried, with a coulomb-based charge step cutoff. Results are shown in Figs. 3.17 and 3.18. Use of a cellulose separator significantly extended cycle life. Also, use of an open-circuit hold between cycles allows for confirmation of absence of SOC drift and observation of the relative overpotentials on charge and discharge. Use of a constant-coulomb charge step is preferable for observing this particular failure mode, believed to be related to pore clogging of the separator. Fig. 3.17 clearly shows both the increasing overpotentials (more so on charge than discharge) as well as increasing discharge durations from the separator's self-discharge current density decreasing over time.

3.3.4 Effect of Porous Electrode Replacement

As mentioned previously, sometimes upon cell performance decay, separators could be replaced and performance would come back, though this was not always repeatable

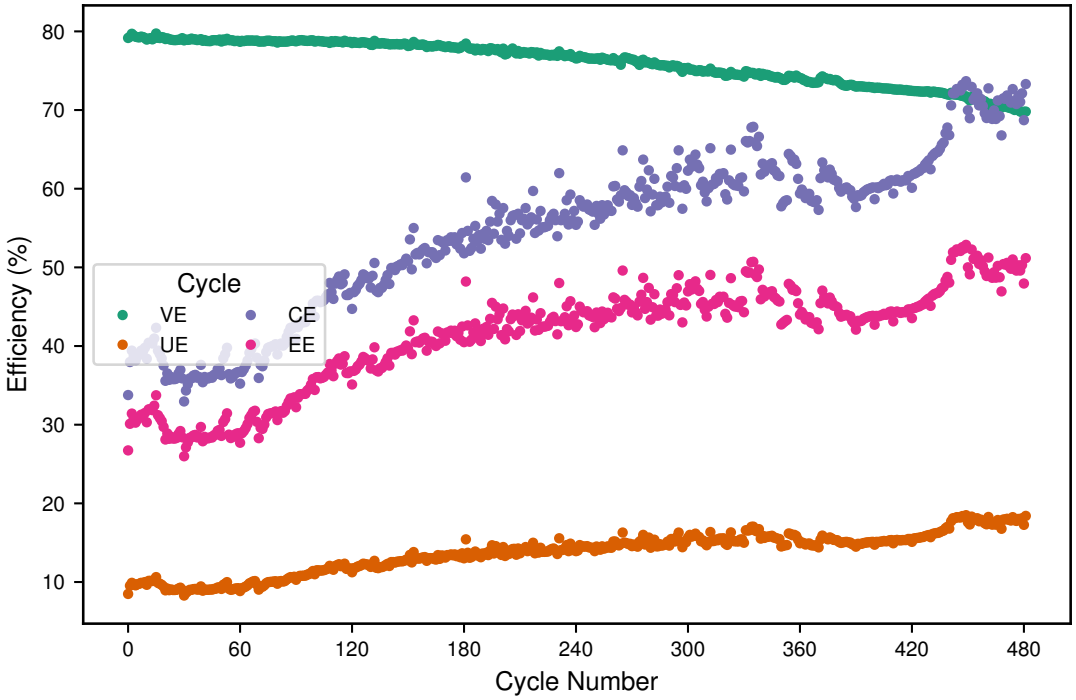


Figure 3.18: Efficiencies of the charge/discharge cycles of a V(acac)$_3$ flow cell with a cellulose Dreamweaver Silver 20 separator presented in Fig. 3.17

and seemed to depend on the extent of degradation at the time of component replacement. Figs. 3.19 and 3.20 show the brief restoration in performance from replacing the porous carbon felt electrodes in a degraded cell. A failed flow cell was carefully disassembled and the electrodes were replaced with fresh ones, while leaving the separator intact. Great care was taken to align the separator with the gaskets exactly as before, so that no "fresh" separator was exposed upon reassembly. Note, the cell shown here already had some use at different operating conditions prior to the data shown below. Applied current density was reduced to 10 mA cm^{-2}, the already partially degraded cell was operated for 40 cycles to show its degraded state, then electrodes replaced and cycling resumed immediately under identical conditions to show any difference in performance.

Fig. 3.19 shows the last cycle of the degraded cell in black, and the first cycle of the same cell with identical electrolyte and porous separator but new porous electrodes in red. Fig. 3.20 shows how the newly rebuilt cell exhibits initially higher performance, but rapidly appears to decay exponentially toward to the

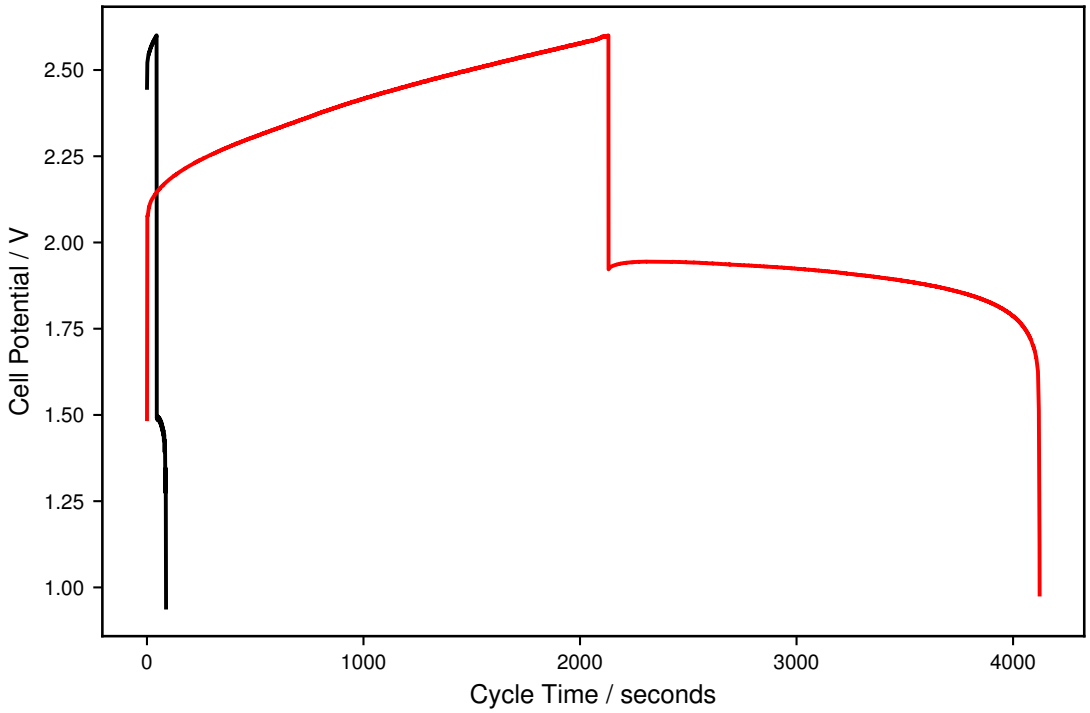


Figure 3.19: Charge/discharge profiles of a degraded V(acac)$_3$ flow cell immediately before (black) and immediately after (red) undergoing an electrode swap

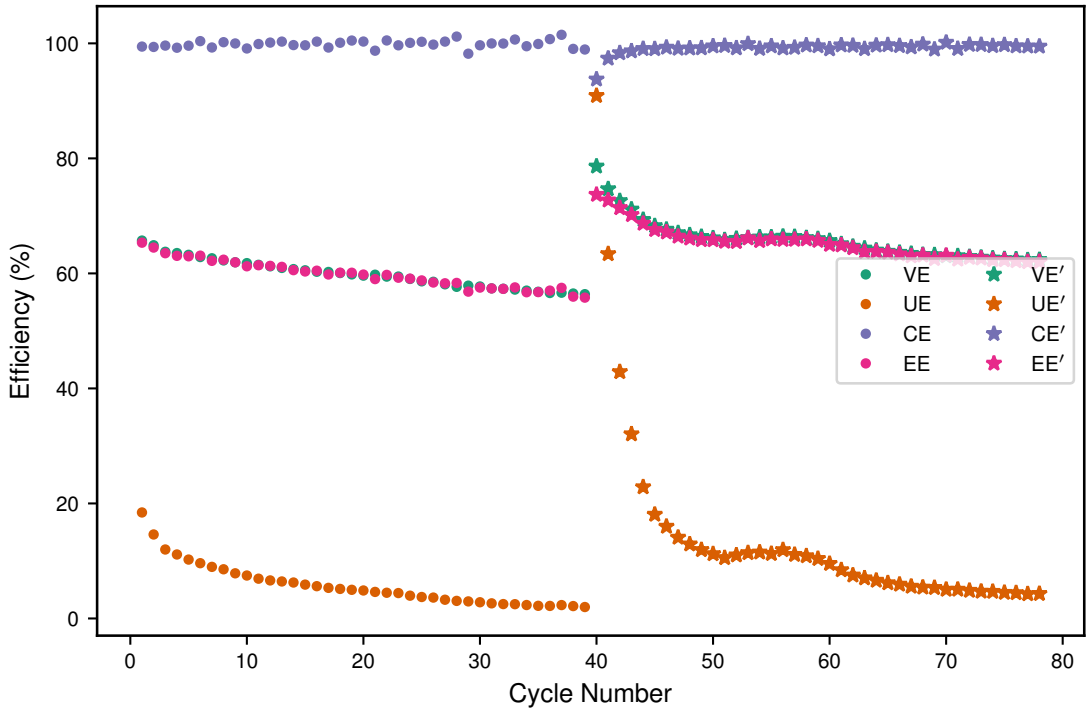


Figure 3.20: Efficiencies of the charge/discharge cycles on either side of and including those presented in Fig. 3.19. Electrode replacement occurs after cycle 40.

behavior of the previous degraded cell (remember, the first cycle in Fig. 3.20 was of a previously degraded cell). The cycle history of this cell at 40 mA cm^{-2} was almost exactly like that presented in Fig. 3.14. So, the cell's initial coulombic efficiency was under 90% before growing to near-unity.

The degradation phenomenon investigated here has been thoroughly demonstrated to involve an increase in coulombic efficiency. Although replacing the porous electrodes briefly restored some performance, it is noteworthy that the initial coulombic efficiency of the cell was still very close to unity upon reassembly. It is reasonable to suggest that the nature of the electrode/electrolyte interface does not affect coulombic efficiency in an all-liquid flow battery, since this efficiency depends primarily on the properties of the separator. Thus, the fouling phenomenon witnessed here—if identical to that seen in the report of Clegg and Hill [102] (and it appears similar)—cannot be explained by the electrode/electrolyte degradation hypothesis presented in that paper.

Indeed, cyclic voltammograms of the cycled electrolyte were identical to voltammograms of the fresh electrolyte, with no detectable changes. SEM with EDX was performed the surface of fresh and partially degraded Celgard 4560 membranes, but again, no change was detected.

Therefore, if both the electrode and electrolyte are not directly related to performance decay, the porous separator seems a more likely culprit.

3.3.5 Double Reference Electrode Experiments

To properly test whether or not there was electrode or electrolyte degradation, an experiment was arranged to directly measure the potentials between the porous electrode surfaces and the bulk electrolytes of their respective half-cells. In this way, growth of any charge-transfer resistance (as postulated by Clegg and Hill [102]) should be observable. If no change was observed, but the full-cell (over)potentials on charge/discharge continue to grow in line with the conventional degradation previously demonstrated, then the growth in overpotential must be happening between the bulk electrolytes of the half cells, *i.e.* within the porous separator.

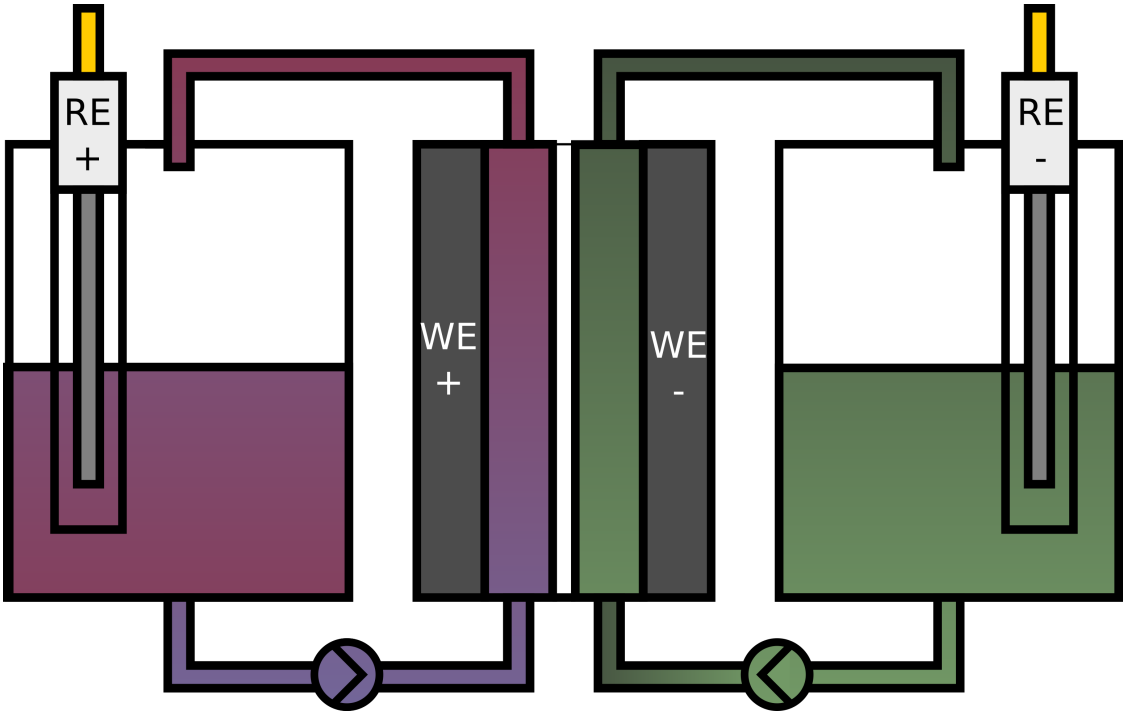


Figure 3.21: Schematic showing double reference electrode setup in a flow battery, with one reference electrode in each reservoir

Methods

The experimental configuration is shown in Fig. 3.21. Fig. 3.21 shows a conventional benchtop flow battery with one reference electrode placed in each reservoir. While it would be ideal to place the reference electrodes as close as possible to the working porous electrode, the cell geometry did not permit this without significant redesign. Consequently, there is a short (≈10 cm) length of 1/16" ID PTFE tubing between the reservoir and the cell. Brief attempts at using a platinum wire sandwiched between two separators within the cell (to use as a single, mutual reference for both electrodes) proved inadequate for the present study. Reference electrodes consisted of the nonaqueous silver/silver nitrate kit from BASi, a silver wire and a filling solution of 0.01 M silver nitrate and 0.1 $TEAClO_4$ in ACN separated from bulk solution with a frit, as commonly used for ACN based electrolyte studies [113]. Three channels of an Ivium Octostat were used: one channel connected to the flow cell as usual, and two other channels connected with only their reference and sensing leads between the reservoir reference electrodes and half-cell porous electrodes.

A constant-current cycling protocol was implemented. Flow rates were 10 mL min^{-1} with PID reservoir balancing. For this experiment, 16 mL total electrolyte volume was used, of 0.1 M V(acac)$_3$ 0.3 M TEABF$_4$ in ACN.

First, the cell was allowed to rest at open circuit for 60 seconds. Then a current density of 40 mA cm^{-2} was applied for 220 s on charge, which corresponds to 50% of the theoretical maximum SOC assuming no self-discharge.

A 60 s open-circuit hold was applied, before performing a "diode test" protocol of approximately 60 s in length, and then an electrochemical impedance measurement, before discharging at the same current density to 1.4 V, and then performing another 60 s hold at open circuit, all while monitoring both half-cell voltages with reference electrodes. The diode test consisted of a sequence of 5 second galvanostatic holds at current densities of ±1, 2, 4, 8, 16, 32, and 64 mA cm^{-2}.

The diode test protocol was implemented because, as seen in the previous experimental charge/discharge curves of this chapter, overpotentials seemed to be increasing more on charge than on discharge, while both post-charge open-circuit holds and reference electrode data can provide evidence for this phenomenon, a bipolar current-step protocol can produce a current-voltage relationship for each cycle. To make a convincing claim of the observation of an "ionic diode" effect would likely require a current-voltage curve akin to a conventional diode. The diode test occurred immediately after a 60 s hold at open circuit after charging, which would correspond to a SOC less than or equal to 50% depending on the transient coulombic efficiency of the cell. Performing the diode test at a SOC near 50% is desirable because the concentration of charged and neutral active species are equal in the respective half cells at this point.

Electrochemical impedance spectroscopic measurements were conducted in galvanostatic mode at 5 frequencies per decade from 10 Hz to 10 or 100 kHz with an applied current of 5 mA. All Bode and Nyquist plots in this thesis were created with the assistance of the `impedance.py` Python package [114].

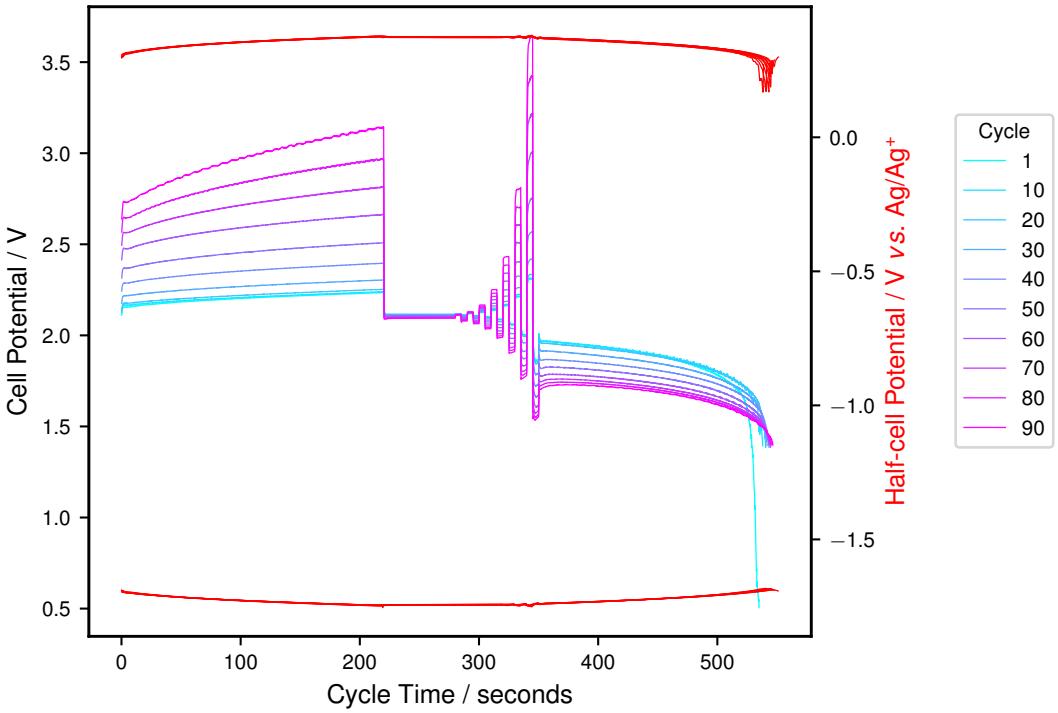


Figure 3.22: Double reference separator fouling experiment with V(acac)$_3$ and Celgard 4560, with OCP hold and diode test in between half-cycles. Red lines show the positive and negative half-cell potentials, which all lie on top of each other.

Celgard 4560

For the first experiment, Celgard 4560 was used as the separator. Fig. 3.22 shows the entire charge/discharge protocol including the open circuit hold and diode test. Fig. 3.23 shows the efficiencies of this system. Fig. 3.24 shows a Bode plot of the impedance data. Fig. 3.25 shows a Nyquist plot of the impedance data.

Fig. 3.22 shows the progression of degradation over the course of nearly 100 cycles, with an open circuit hold and diode test in between charge and discharge. The open circuit hold remains the same over 100 cycles, demonstrating absence of SOC drift which could result from electrolyte degradation. Also, in red, the positive and negative half cell potentials exactly lay on top of each other for every cycle. This seems to directly counter the claims in [102] that there is a growth in charge-transfer resistance on the electrode surface, as the positive and negative half-cell potentials are measured from the bulk half-cell solution to the adjacent working electrodes. Indeed, this half-cell data also confirms that the

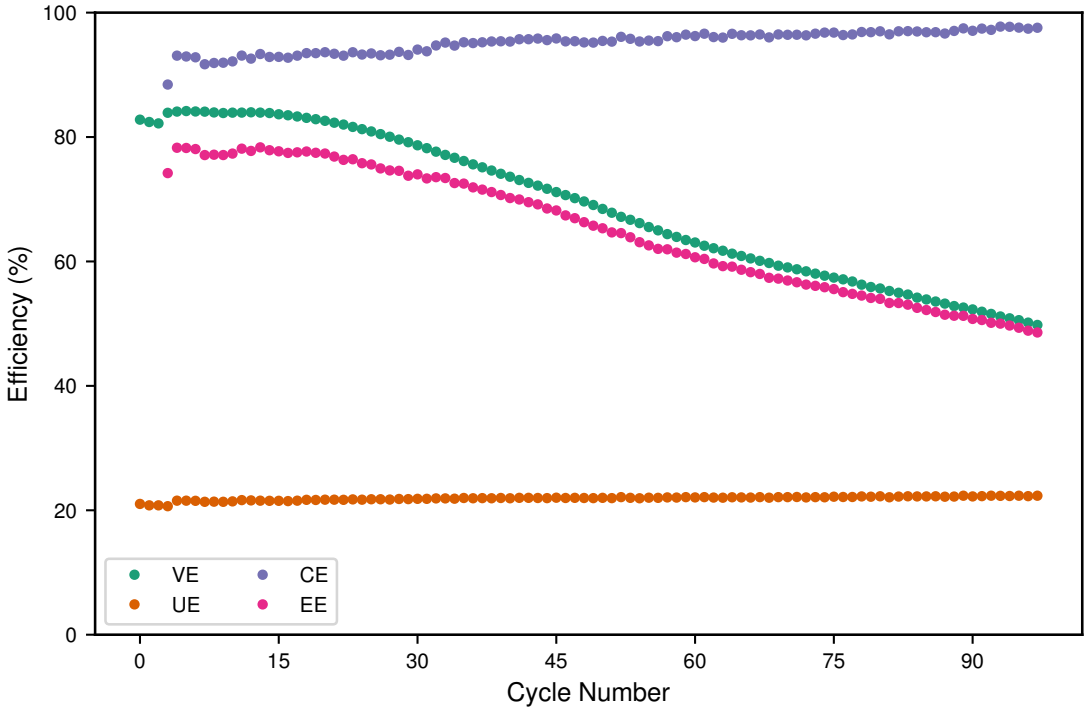


Figure 3.23: Efficiencies of Celgard 4560 separator fouling experiment from Fig. 3.22

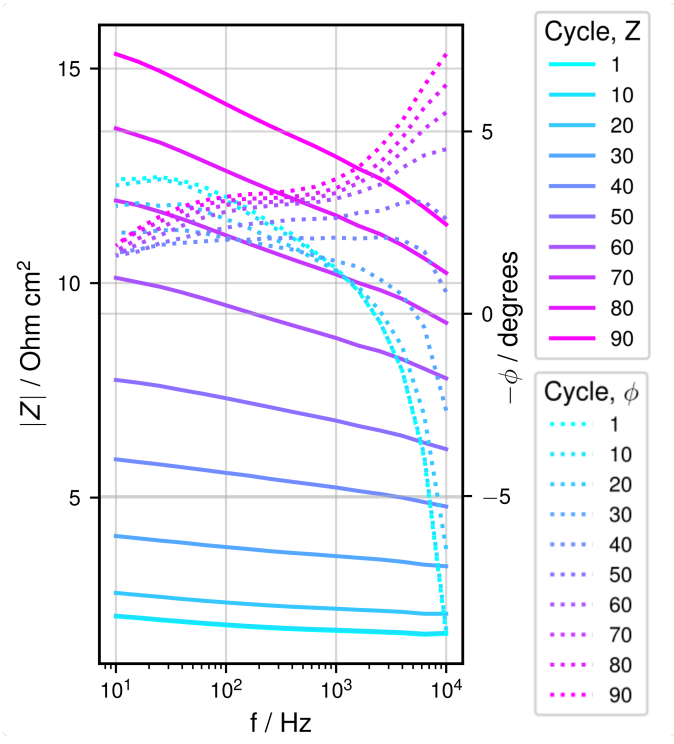


Figure 3.24: Bode plot of impedance spectra from Celgard 4560, V(acac)$_3$ separator fouling experiment

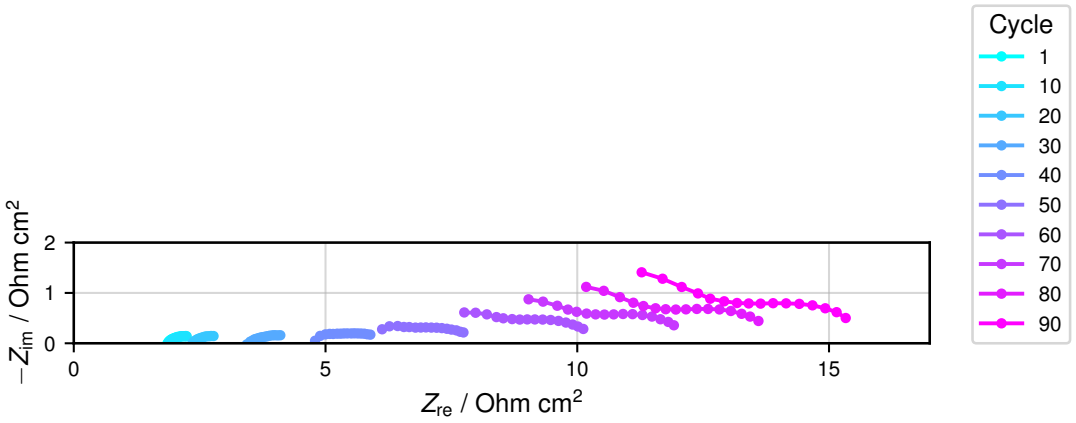


Figure 3.25: Nyquist plot of impedance spectra from Celgard 4560, V(acac)$_3$ separator fouling experiment

cell is far from kinetically limited in the range of current densities applied, as the only noticeable change in half-cell potential seems to come from Nernstian SOC differences. The half-cell voltages are remaining constant as the full cell potential (and overpotential) grows unbounded during the cycles shown. Note also how the overpotential during charge grows more than the overpotential during discharge. Also, note how the diode test is initially symmetric in voltage, then grows asymmetrically with cycling, with more overpotential with a charging current than with a discharging current. These two observations support the ionic diode nature of the separator degradation phenomenon.

This ionic diode effect is even more apparent when presented as a traditional current-voltage relationship. The diode test portion of this cycling experiment is shown in Fig. 3.26. Fig. 3.26 shows how as cycling progresses, overpotential grows more on positive (charging) applied currents than for negative (discharging) currents. The membrane is no longer simply increasing in ohmic resistance over

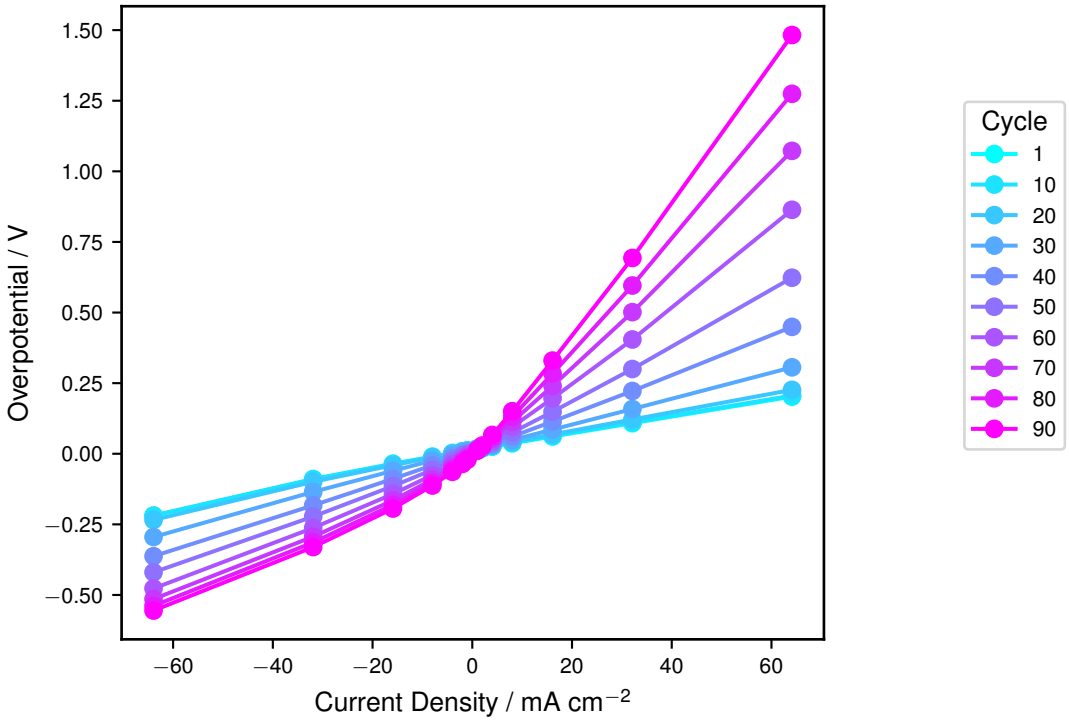


Figure 3.26: Current-voltage relationship of ionic diode membrane fouling signature for V(acac)$_3$ flow cell with Celgard 4560

time, as its behavior starts to depend on the sign of current, such as a resistor with some diode-like properties.

The efficiencies of the system, shown in Fig. 3.23, again demonstrate the increasing couloumbic and decreasing voltaic and energy efficiencies seen before, with some sigmoidal nature possibly apparent. With a constant-coulomb charging step, however, the sigmoidal decay of capacity is replaced by a nearly linear utilization efficiency, which increases slightly in tandem with the coulombic efficiency.

The impedance spectra shown in Figs. 3.24 and 3.25 show a clear change as cycling progresses. Impedance growth continues unbounded, primarily in the real component. Phase shift from negative to positive occurs in the high-frequency region of the Bode plot. The half-cell data, which suggests overpotential growth is confined to the separator, supports the claim that the growth in bulk resistance shown here can be attributed to the separator.

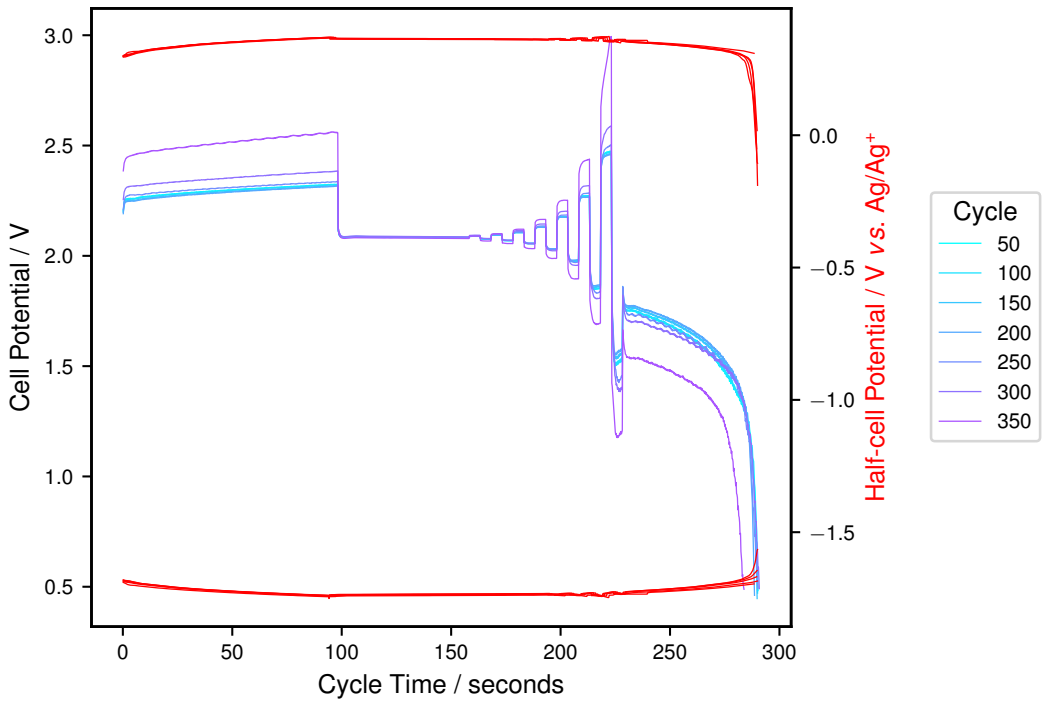


Figure 3.27: Double reference separator fouling experiment with V(acac)$_3$ and Anodisc alumina separator, with OCP hold and diode test in between half-cycles. Red lines show the positive and negative half-cell potentials, which all lie on top of each other.

Alumina

Another double-reference-electrode experiment was performed, using the same circular Whatman Anodisc alumina separator as used previously in this chapter. Upon dissassembly, however, it seemed that accidentally two alumina membranes had been used, as they had stuck together when being removed from their container. This actually proved to be a useful qualitative source of information, however, as shown later. Fig. 3.27 shows the entire charge/discharge protocol including the open-circuit hold and diode test with two layered separators, and Fig. 3.28 shows the efficiencies of this system. Fig. 3.29 shows a Bode plot of the impedance data. Fig. 3.30 shows a Nyquist plot of the impedance data, with Fig. 3.31 showing a closer look at the first 250 cycles. The longevity of the alumina-separated system is again superior to the system with Celgard 4560: the system lasts for nearly 500 cycles. Not visible in this data is the observation that significant solvent evaporation occurred during the experiment. To fit the reference electrodes in the vials, rubber septa were

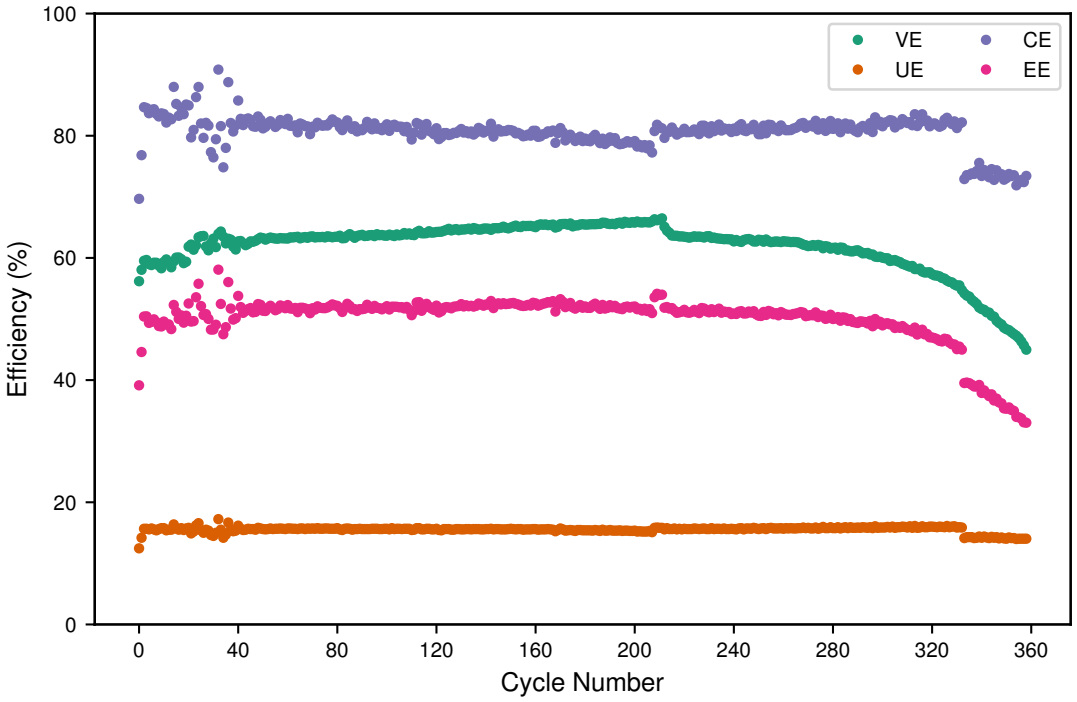


Figure 3.28: Efficiencies of alumina separator fouling experiment from Fig. 3.27

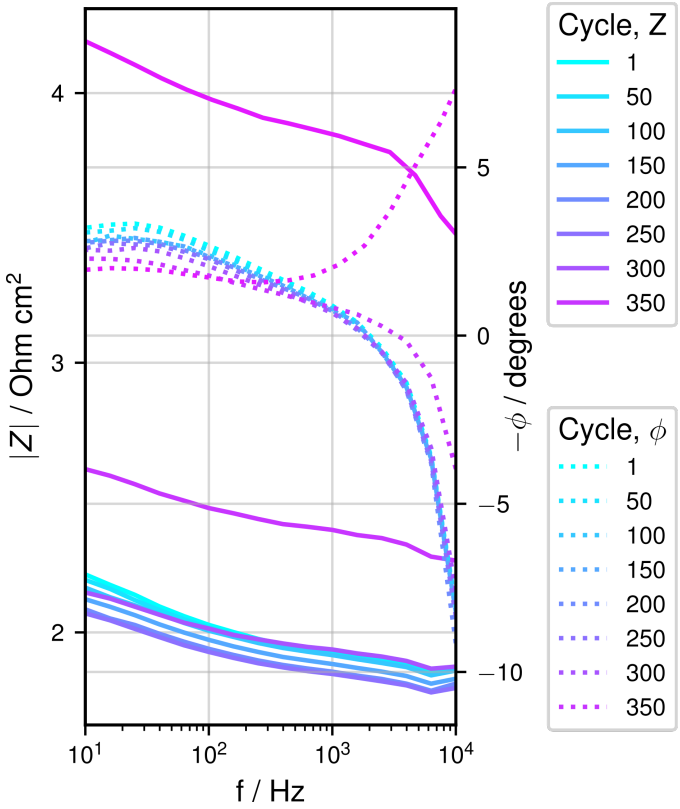


Figure 3.29: Bode plot of impedance spectra from alumina, V(acac)$_3$ separator fouling experiment

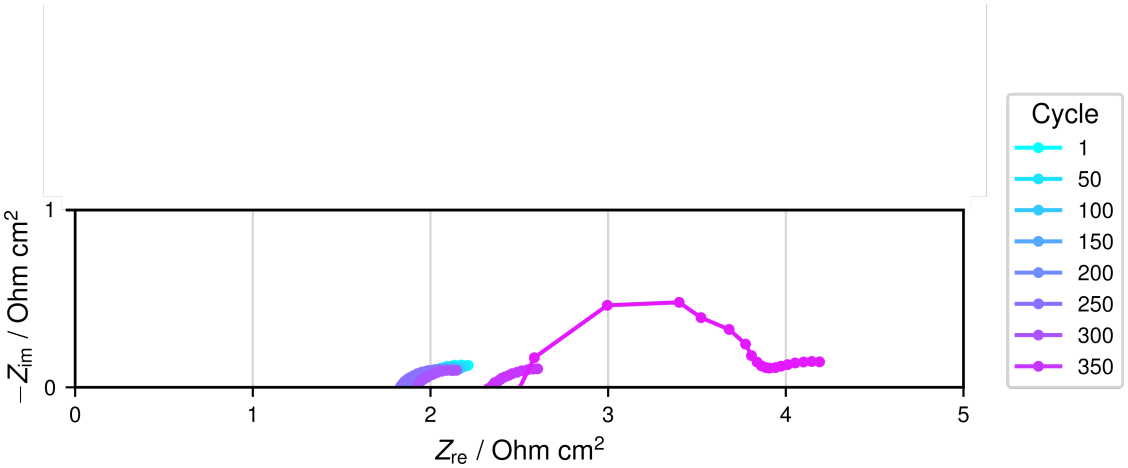


Figure 3.30: Nyquist plot of impedance spectra from alumina, V(acac)$_3$ separator fouling experiment

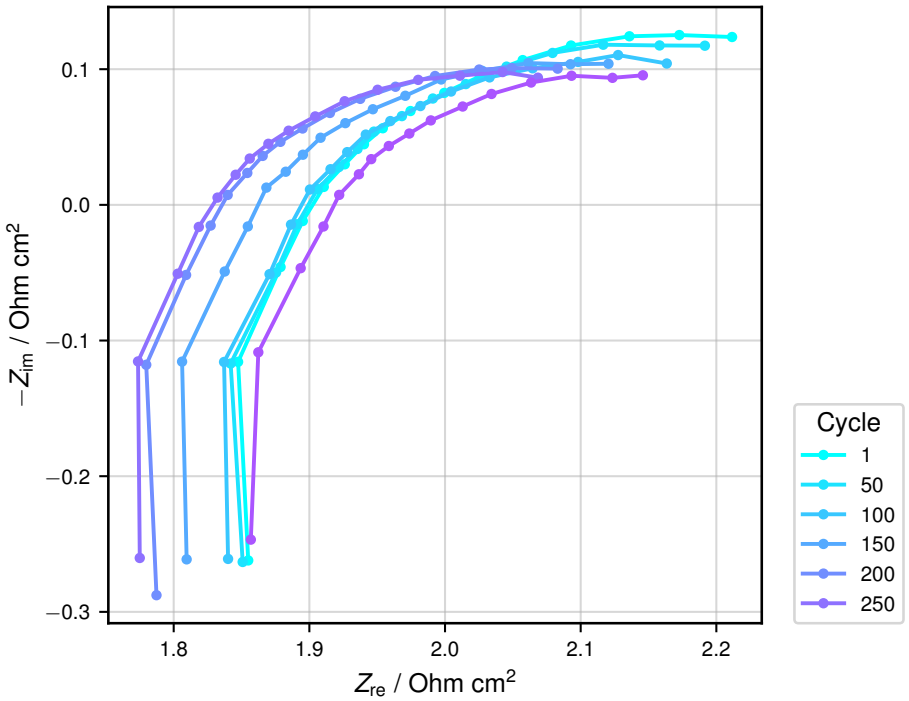


Figure 3.31: Close-up Nyquist plot of first 250 cycles of impedance spectra from alumina, V(acac)$_3$ separator fouling experiment

used which did not create a perfect seal of the headspace. This meant the volatile solvent evaporated into the glovebox (which has an active solvent removal system).

Previous experiments, with different separators, had failed upon the addition of top-up solvent; solvent was not topped up in this system and it was cycled until total failure. The system shows almost no change in performance until cycle 300. Also, overpotential growth appears to be symmetrical between charge and discharge, both in charging/discharging steps and in the diode test. Like before, full-cell and half-cell open-circuit potentials are unchanged over the entire course of the experiment, again supporting the argument of this thesis that the electrode and electrolyte are stable under long-term cycling, and that transient performance decay is primarily attributed to the separator.

The impedance spectra in Figs. 3.29 and 3.30 also show almost imperceptible changes in response until cycle 300, when it is believed solvent evaporation may have made the electrolyte too concentrated. The spectra are also useful in that they are qualitatively similar to those of the immediately previous experiment with identical conditions, except for the use of Celgard 4560 instead of alumina. While the ionic diode nature is not observed in the alumina system, the late-cycle impedance spectra are similar, with a positive phase shift in the Bode plot at high frequencies, and a general increase in the real impedance over time.

The current-voltage relationship of the diode test for alumina is shown in Fig. 3.32.

If the decay phenomenon here is indeed pore clogging of the separator due to electrolyte precipitation, then the qualitative similarity of the impedance spectra suggest that pore clogging may be responsible for the decay in the previous Celgard experiment, even though the cell decayed on a faster timescale than could be explained by electrolyte over-concentration owing to solvent evaporation.

Both Celgard 4560 and alumina double-reference-electrode experiments showed negligible electrode and electrolyte degradation, and confirmed that overpotential and bulk-resistance growth is confined to the separator. The Celgard system develops an ionic diode nature over time, while the alumina system does not.

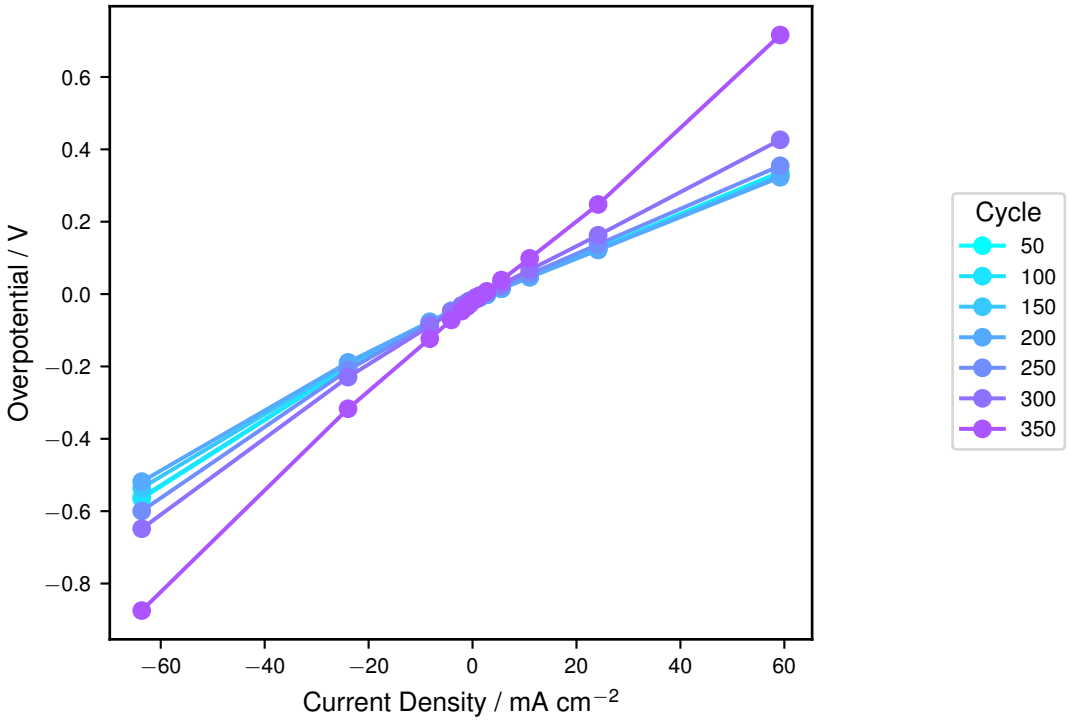


Figure 3.32: Current-voltage relationship of V(acac)$_3$ flow cell with alumina separator, showing absence of ionic diode effect seen with Celgard in Fig. 3.26

As mentioned before, two alumina discs were used as separators accidentally. Upon disassembly of the failed cell, which had a very concentrated electrolyte, only one of the separators seemed to be discolored, and with the color of the neutral V(acac)$_3$ active species (brown), even after thorough rinsing with neat ACN. Leaving separators in electrolyte solutions and then rinsing them with neat solvent removes any color from the separator, *i.e.*, the color shown here is from degradation/pore clogging and not just mere presence of a colored electrolyte solution. This separator was the one closer to the positive electrode. Photographs of both separators are shown in Fig. 3.33.

This accident of using two separators proved useful, as it potentially suggests that solutes from the positive electrolyte precipitated to clog the separator's pores.

Constant Voltage Hold with Celgard 4560

Another double-reference-electrode experiment was performed with Celgard 4560, this time to see if degradation could be induced by means of potentiostatic holds at

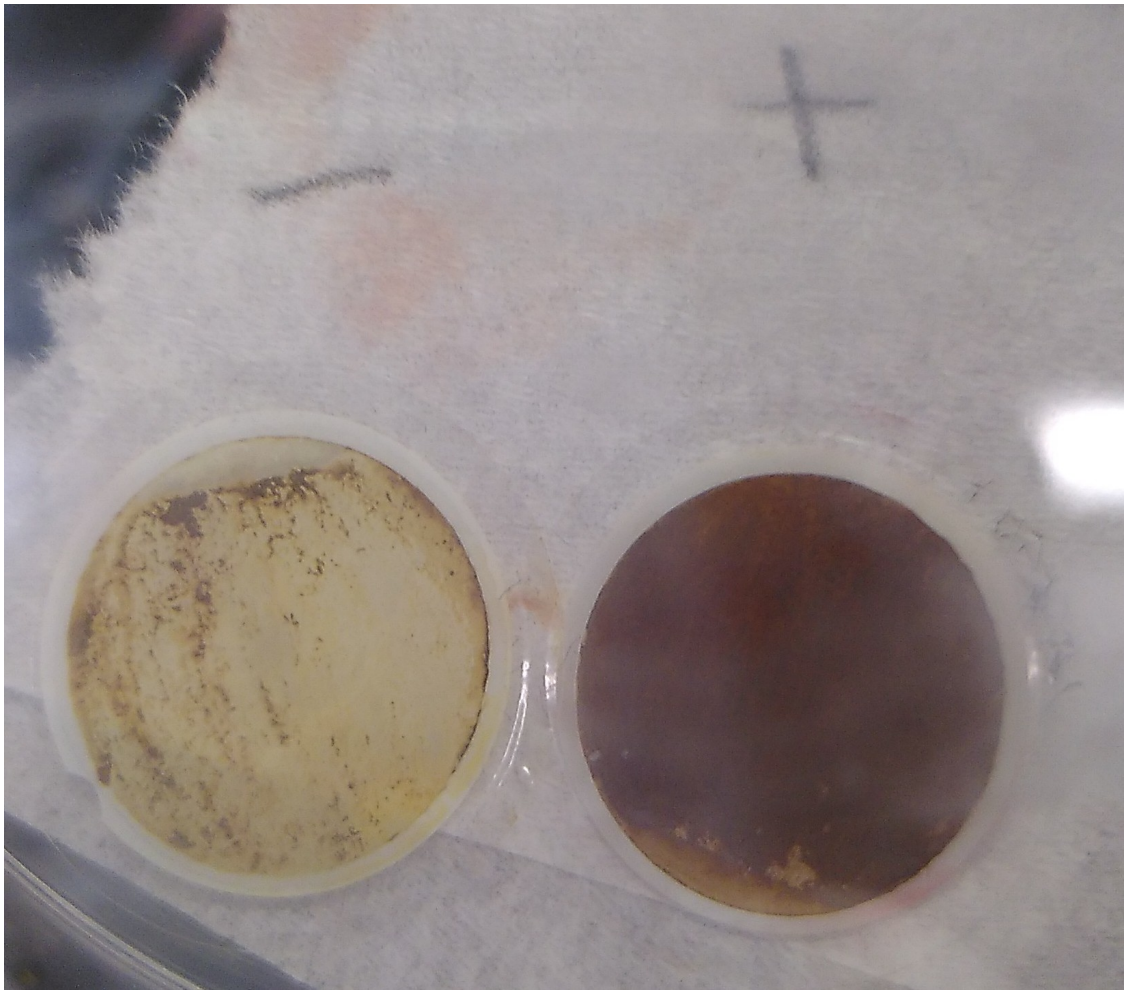


Figure 3.33: Anodisc alumina separators used in V(acac)$_3$ double reference electrode separator fouling experiment. Left separator faced negative electrode, right separator faced positive electrode. Separators were rinsed thoroughly with neat ACN before photo was taken.

a fixed SOC rather than galvanostatic cycling. The motivation for this is remove the effects of reservoir volume, cell/separator geometric area, self-discharge current density, and other factors that would affect the length of cycle times and the accessed capacity so that fouling rates could be decoupled. The experimental protocol was a 2.3 V potentiostatic hold followed by a diode test at the identical current densities as previous ones, following by an impedance measurement, with the entire step taking half an hour.

Fig. 3.34 shows 50 half-hour steps, with full and half-cell data for potentiostatic holds and diode tests. Fig. 3.35 shows a closer look at the diode step. Fig. 3.36

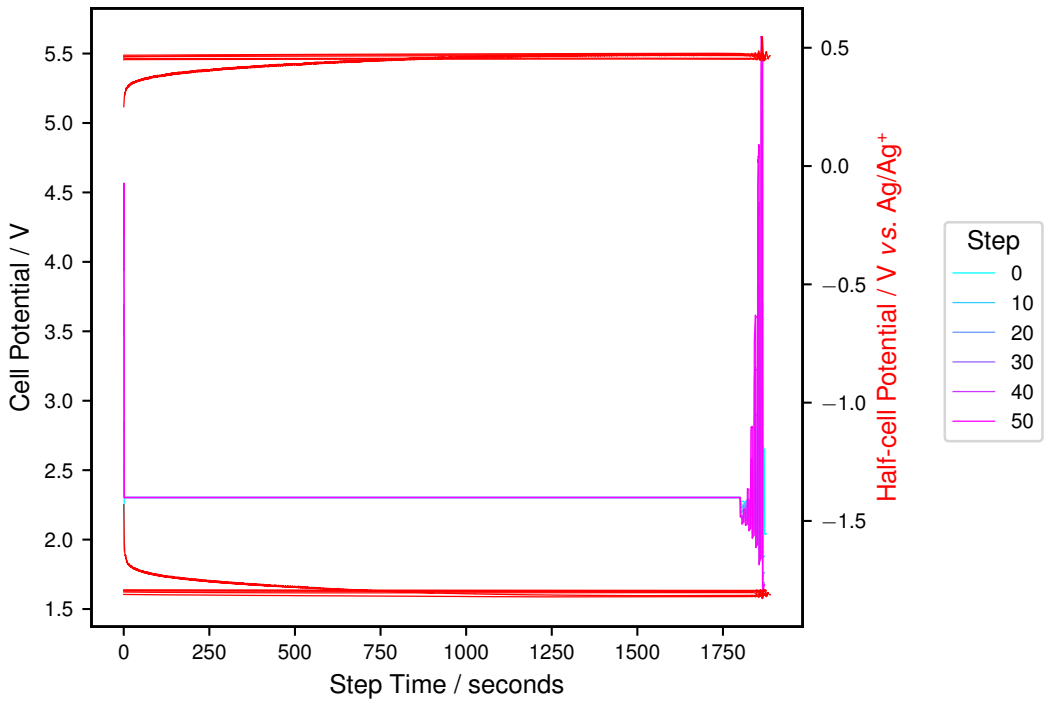


Figure 3.34: Full and half-cell (red) potentials of a V(acac)$_3$ flow battery held at 2.3 V for half-hour steps with a diode test

shows a Bode plot of the impedance data. Fig. 3.37 shows a Nyquist plot of the impedance data. Fig. 3.38 shows the reservoir levels and pump duty-cycle bias over the 25 hours of the experiment.

Visible again in Fig. 3.34 is the clear consistency of half-cell potentials over the 25 hours of the experiment while the cell was constantly held at 2.3 V. The first part of the Nernst curve is visible from the first charging step, which began with a fully discharged electrolyte.

Fig. 3.35 shows a closer look at the diode tests from this experiment. Again, the asymmetric nature of overpotential growth is visible, and the ionic diode properties correlated with separator performance degradation are visible. The first 20 seconds in Fig. 3.35 are the 2.3 V hold, followed by a 5 s open-circuit hold before the diode test begins.

The impedance spectra in Fig. 3.36 and Fig. 3.37 are similar to the ones shown previously for Celgard 4560, Figs. 3.24 and 3.25. Here, impedance spectra were collected from 0.1 Hz to 100 kHz, an expanded range from the charge/discharge

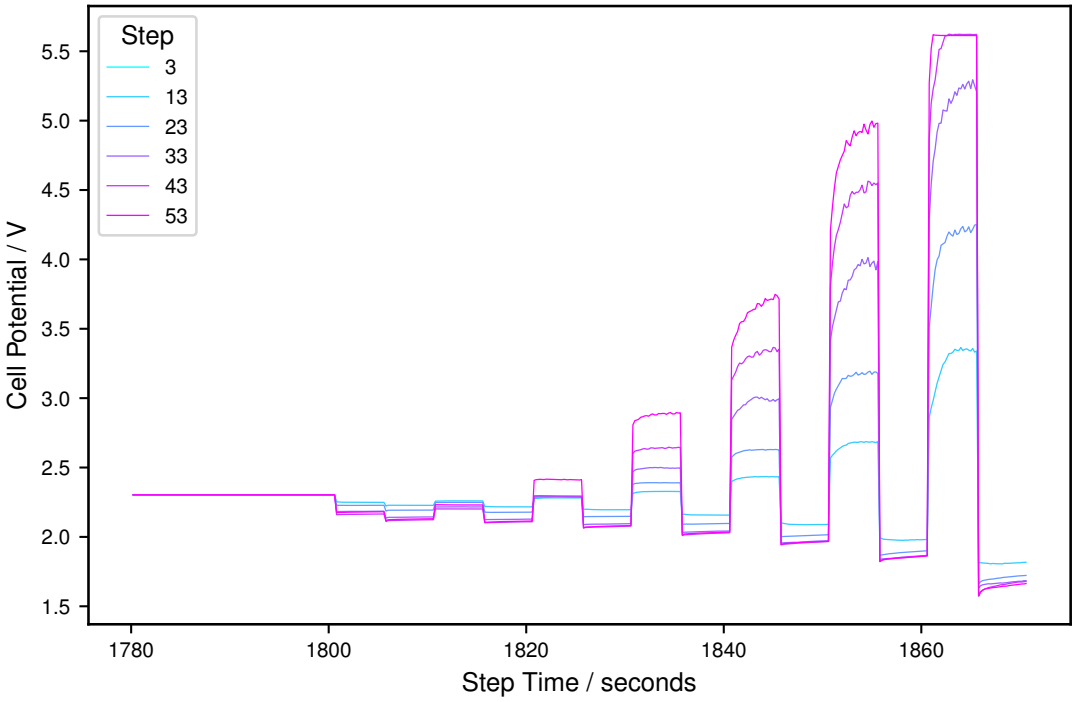


Figure 3.35: Closer look at the diode test portion of 3.34

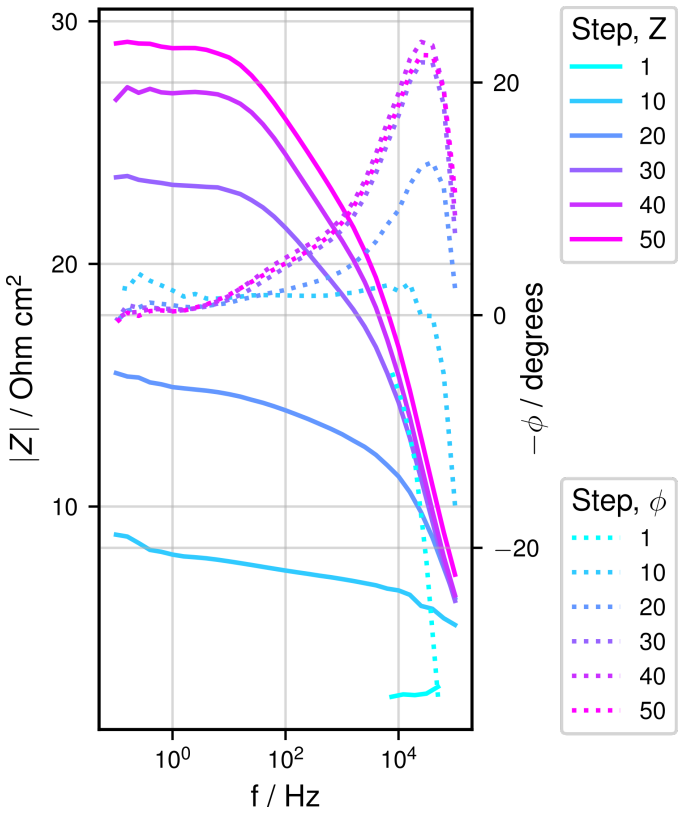


Figure 3.36: Bode plots of the impedance spectra from the 2.3 V hold degradation experiment

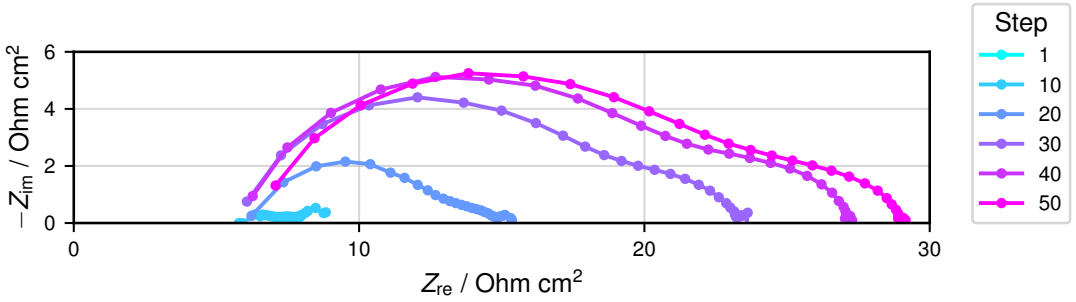


Figure 3.37: Nyquist plots of the impedance spectra from the 2.3 V hold degradation experiment

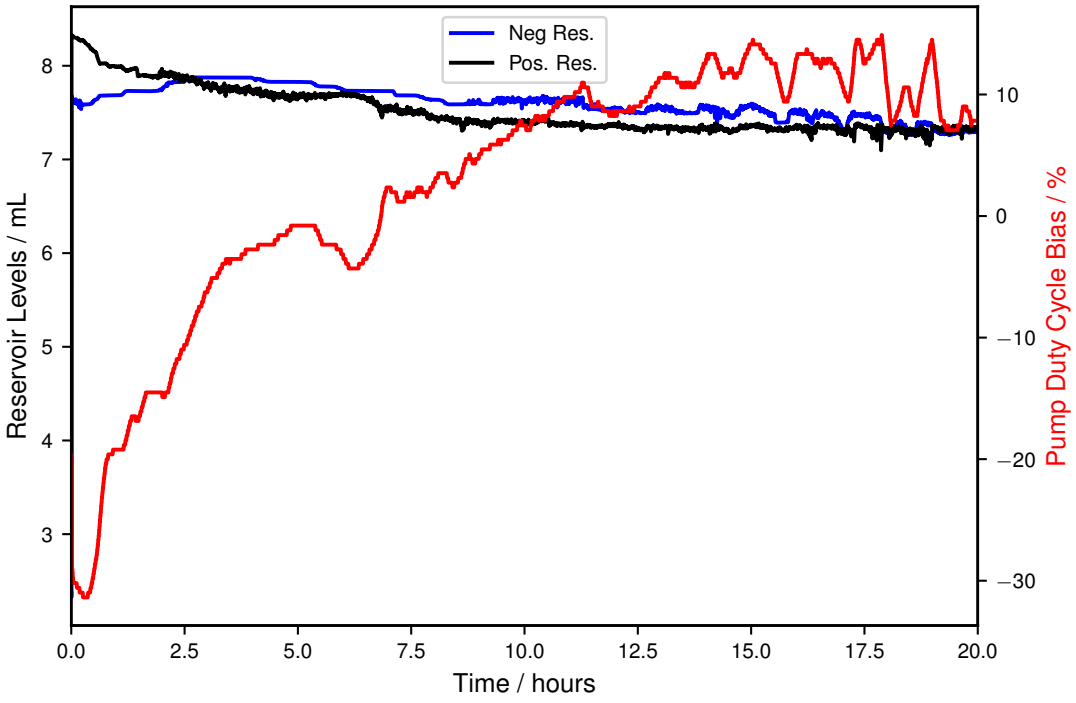


Figure 3.38: Reservoir levels and applied pump duty cycle over the course of the 2.3 V hold degradation experiment

experiment. The overlapping regions are similar though, with a general increase in the real component of impedance over time and positive phase shift at high frequencies, suggesting that the same decay mechanism is present in potentiostatic fouling experiments as with charge/discharge cycling.

Some reservoir balancing phenomena occasionally seen in general experimentation were more pronounced in this constant hold at 2.3 V, during which the electrolyte maintained a higher average SOC than would be typical for a charge/discharge experiment. Specifically, the charged positive electrolyte tended to climb the exterior walls of the tubing and reference electrode, eventually traveling all the way out of the septum sealing the top of the electrolyte reservoir, removing some active material from solution. This apparent change in positive bulk-electrolyte properties could be related to the increase in mechanical pressure required in the negative half-cell to maintain balanced reservoirs—the positive electrolyte could be exerting a significantly higher osmotic pressure than the negative. Fig. 3.38 shows the reservoir levels and applied duty cycle bias between pumps necessary to maintain balanced reservoirs over the course of the experiment. A positive duty cycle bias (expressed as a % change from the baseline duty cycle) corresponds to an increase in the speed of the negative pump, and a negative duty bias means an increase in speed of the positive pump. Initially, the positive pump spun faster than the negative to maintain balance, and as the experiment progressed, the negative pump eventually had to spin faster. Reservoirs were balanced the entire time, and because of the potentiostatic hold, SOC was also confined to a small, fixed window. Thus, the mechanical pressures in the cells were changing over time as the PID controller adjusted to maintain reservoir balance. This artificially applied mechanical pressure may be used to counteract an increasing osmotic pressure in the positive electrolyte, which as just mentioned was exhibiting nonideal behavior (odd surface tension properties, *etc.*). Since the separator seems to be taking on ionic-diode-like properties, it may become selective to certain species over time. While the driving force of (electro)chemical potential of species on either side of the membrane is roughly constant over the course of this potentiostatic experiment

which holds SOC constant, it becomes increasingly difficult for certain species to pass through the separator, which could lead to this increasing osmotic pressure.

3.3.6 Discussion

Degradation manifests as increasing coulombic and decreasing coulombic efficiencies during charge/discharge cycling. Choice of the supporting salt and solvent can affect the rate of degradation. The purity of the active species affects the rate of degradation. The material of the separator affects the rate of degradation. Replacing the electrodes does not reverse degradation. Reference-electrode data gathered during charge/discharge cycling and potentiostatic experiments demonstrate stability of the electrolyte and the electrodes. The separator may attain ionic-diode-like properties with degradation, but this behavior depends on separator material. Impedance spectra suggest that bulk resistance is growing, and reference electrodes suggest that this growth must be within the separator. Degradation may cause an increasing osmotic-pressure difference across the membrane. Polymeric separators exhibit the most degradation and the separator seems to take on ionic-diode like properties. Cellulose separators last longer than polymeric ones but do seem to have some asymmetric behavior. Alumina separators also last much longer than polymeric and exhibit symmetric overpotential growth, *i.e.*, no ionic-diode behavior. Visual inspection of separator membranes after cycling suggests that active species may be depositing within the separator pores, in a way that cannot be reversed by rinsing with neat solvent.

All of these observations lead to the creation of the hypothesis touched upon in the introduction to this section. This hypothesis for the observed degradation is that solutes are coming out of solution within the pores of the separator, according to the mechanism proposed in Fig. 3.39.

The suggested mechanism for this is an established one for the field of membrane (separator) fouling: capillary-induced phase separation, as described by Lindau *et al.* [115]. The first sentence of their paper states that “The flux of ultrafiltration

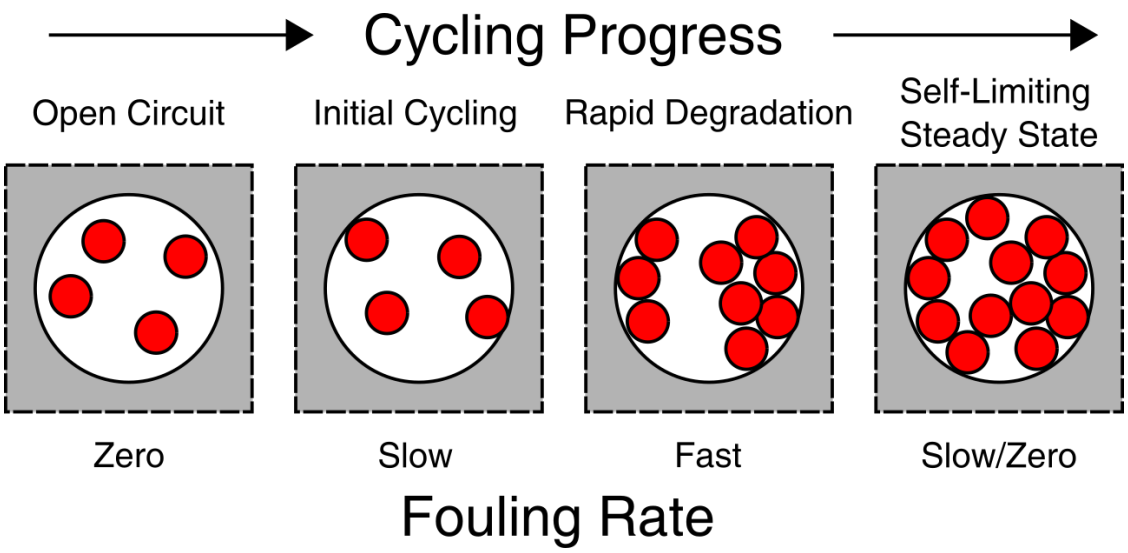


Figure 3.39: Proposed mechanism of porous separator fouling in RFBs resulting in increased coulombic and decreased voltaic efficiencies over time

membranes may be severely reduced when treating low-molecular-weight hydrophobic solutes even though the cut-off of the membrane is orders of magnitudes greater than the size of the solute molecules." In capillary-induced phase separation, solutes with diameters orders of magnitude smaller than separator pore sizes may still clog said pores. The mechanism implies that the bulk solubility properties of solutes do not apply when solutes are contained within small pores, wherein they may develop a long-range order induced by the pore wall and subsequently phase separate (crash out of solution, clog, precipitate *etc.*). The authors found in this study and others that fouling was a function of the solute-concentration/solubility-limit ratio and separator material, and not a function of flowrate. The initial step of pore clogging may be chemical and/or physical adsorption of solute on the pore wall, and then solute-solute layering occurring after this until the pore size is restricted to some critical value. This three-step pore clogging mechanism may correspond with the sigmoidal responses seen in utilization (for voltage-cutoff cycling) and voltaic/energy (for constant-coulomb cycling) efficiencies: efficiency at first decreases slowly as the monolayer of adsorbed solute deposits on pore walls. Then, once this monolayer is established, pore clogging and subsequent efficiency loss progresses more rapidly until it becomes self-limiting, and changes slow down.

Further research into the membrane fouling literature uncovered data with striking similarity to the currently observed phenomenon [116, 117]. Membrane-science vernacular can readily be replaced with flow-battery vernacular, substituting "transmembrane pressure" with "overpotential" and "current density" for "permeate flux," *etc.*

Elimelech and Bhattacharjee in 1998 discuss the difference between filtration (hydrodynamic) theories of flux decline in membrane separation *vs.* thermodynamic (concentration polarization) approaches [118]. They note "cakes are rarely formed during membrane filtration of very small solutes" (interpreted to mean non-colloidal, as in this dissertation) and suggest the validity of concentration polarization models to explain flux decline. In this approach, flux decline occurs as the transmembrane osmotic pressure increases, requiring an increased driving force (applied pressure for membrane filtration, overpotential for RFBs).

Bhattacharjee and Johnston in 2002 [119] cite Elimelech and Bhattacharjee in 1998 [118] however and use transmembrane osmotic pressure build-up from concentration polarization as an example of "rapid decline in permeate flux during the initial stages of filtration" as a counterexample to the form of fouling studied in the 2002 paper: scaling. To describe scaling, they state:

> In sharp contrast to this commonly observed fouling behavior [*i.e.* transmembrane osmotic pressure buildup], the permeate flux during scaling remains relatively unaltered for a considerable period of time, after which there is a sudden and drastic decrease in the flux. This sudden decline in the flux can be attributed to the deposition of a sparingly soluble calcium salt on the membrane once the concentration of the calcium and the coprecipitating anions near the membrane surface attains the solubility product of a specific salt.

The authors attribute scaling to the local concentration of various salts at the membrane surface with the lowest solubility salts scaling out of solution. Charged redox-active species in solution (as in, $V(acac)_3^+$ $V(acac)_3^-$) could have much different solubility limits with their, say, TEA^+ or BF_4^- salt equivalents. Furthermore, the concentration of these species at and inside the membrane is

likely different to their values in the bulk, and, as mentioned by Lindau *et al.* capillary-induced phase separation may further exacerbate the fouling [115].

There could be multiple simultaneous membrane processes occurring. This initial stable period followed by a rapid onset of fouling, as Bhattacharjee and Johnston characterize scaling, corresponds more to the behavior seen, for example, in Fig. 3.14. Scaling, while treated by Bhattacharjee and Johnston as an external membrane layer, can also occur internally.

In contrast, the initial rapid flux decline corresponding to transmembrane osmotic pressure buildup discussed by Elimelech and Bhattacharjee can in part be seen as the rapid increase in coulombic efficiency in early cycles of the first $[Fe(bpy)_3]^{2+}(CF_3SO_3)_2$ cycling experiment shown in Fig. 4.7 of the subsequent chapter and others in literature such as the cycling results given in similar symmetric porous separator RFBs like Duan *et al.* [49] and Liu *et al.* [120]. An increase in coulombic efficiency is a form of flux decline, because the self-discharge flux of the charged active species has reduced. None of these systems seem to reach a true steady-state behavior though, and seem to continue declining linearly in voltaic efficiency after an initial rapid increase in couloumbic efficiency.

Hoek and Elimelech suggested a form of flux decline for reverse osmosis and nanofiltration membranes, called cake-enhanced osmotic pressure [121]. While their foulants were colloidal in nature and resulted in a surface cake not visible in RFB cells, the fouling manifested in part as a restriction on ion transport which came from an increase in transmembrane osmotic pressure— as mentioned previously and possibly visible in Fig. 3.38. Possibly, if internal fouling occurs, a similar increase in transmembrane osmotic pressure could happen and result in the increased mechanical pressure required to achieve balanced reservoirs in Fig. 3.38 and the ionic diode effect.

RFB researchers are already acutely aware of the thermodynamic and kinetic solubility limits of charged and uncharged electrolytes in their systems. The findings discussed here suggest that, when using porous separators, the community must also consider the solubility limit of the charged electrolyte in the membrane pores.

This pore-solubility can be more performance-limiting than the solubility in the bulk solution due to adsorption processes and capillary-induced phase separation which causes internal solute deposition in the membrane. Together, these processes seem to depend on solute concentration, the conventional solute thermodynamic solubility in solution, the membrane pore size, and the membrane-solute interaction properties. Most importantly, the separator material should be solute-phobic.

3.3.7 Approaches to Deconvolute Degradation Phenomena

When assessing the stability of electrolytes through flow cell cycling, both reversible and irreversible degradation phenomena may occur. Bulk electrolyte imbalance may be reversible or not depending on whether or not the battery is symmetric; side reactions, leakage of bulk electrolyte, and chemical decomposition may cause irreversible capacity loss for any RFB system. Solid–electrolyte interfaces may form or membrane structural changes occur and these processes can grow unboundedly to failure or reach self-limiting behavior. Degradation processes can result in net increases or decreases in accessible capacity depending on their growth mechanisms and properties. Volatile solvent may evaporate from the system in the absence of bulk electrolyte leakage, concentrating the electrolyte and changing its electrochemical properties over time even as the moles of redox-active remains constant.

In order to deconvolute as many of these phenomena as possible, the following strategies are recommended.

- Mitigation of bulk electrolyte imbalance through active or passive methods
- Minimization and monitoring of solvent evaporation/electrolyte leakage
- Constant coulomb charge steps
- Periodic open-circuit holds between charge and discharge to monitor overpotential changes with sign of current
- Use of reference electrodes as needed to isolate degradation modes

Notably, incorporation of all of these heuristics most likely will result in non-optimal cycling conditions in terms of efficiencies and/or power capabilities. Optimization of cycling performance is a different task; the present one is to assess the long-term stability of an electrolyte and understand any transient phenomena which preclude steady-state operation.

The outcome of implementing these heuristics is a more complete deconvolution of competing transient phenomena. Maintaining balanced reservoirs eliminates one mode of capacity fade.

Minimizing solvent evaporation and monitoring it, even if only qualitatively, allows for independent observation of possibly increasing electrolyte concentration. Knowledge of electrolyte concentration over time becomes useful if transient charge-discharge behavior appears, especially in the absence of bulk leakage and chemical degradation. If adding solvent to reestablish initial concentration resets the system to its initial behavior, then the electrolyte can be confidently assessed as stable in the absence of other transient degradation modes. If solvent were being consumed in side reactions, presumably one reservoir would gradually become concentration-limiting due to drift in average oxidation states over time—unless the solvent decayed identically in both half-cells.

Applying a constant number of coulombs during charge steps allows for more reliable, complete access of the redox-active material in solution. This can be achieved with constant current or constant current, constant voltage protocols. In practice, this means choosing high and low-voltage cutoffs (HVC/LVC) and current (or current *vs.* time) thresholds to end the constant voltage steps. On discharge, one could implement a constant-current step before hitting the LVC and holding the potential constant until discharge current drops to zero as an end condition. On terminating a constant voltage charging step, in the absence of 100% coulombic efficiency, the risk of setting the cutoff current to zero is that the charging step may never end due to establishment of a steady-state in which the charge current equals the self-discharge, akin to an exchange current at the maximum accessible state of charge. For this reason, on charge, setting the end condition of the constant-voltage

step to a fixed amount of charge or attainment of a sufficiently low or zero $\frac{dI}{dt}$ is more reliable than trying to predict what the self-discharge characteristics may be (especially if the self-discharge characteristics are also changing with time).

These end conditions for charge and discharge ensure that during every cycle, for the given voltage and flowrate, the maximum conversion of active species is reached, which is essential for determining the long-term stability of redox-active compounds. For example, with a conventional constant-current-only cycling protocol, one may observe capacity fade for a number of reasons. If overpotentials are increasing due to solvent evaporation concentrating the electrolyte, causing decreased transport performance, then constant-current charge and discharge steps will end earlier and efficiencies and coulombic capacities will drop. This can be particularly deceptive due to the relatively shallow slope of the Nernstian charging plateau at moderate SOCs; if the charge step only uses constant current with an HVC end condition, a small increase in overpotential can have an outsized effect on prematurely ending the charging half-cycle, while in reality the system may be on a benign transient path towards reaching steady-state cycling behavior. If, in the same system, constant current, constant voltage charge steps were used instead, efficiencies would still drop but coulombic capacity would remain constant. If solvent evaporation is indeed observed, then the transient behavior cannot be attributed to active-species degradation. In this way, constant-coulomb charging steps allows for a more robust assessment of cycling performance.

Finally, laminar flow setups may be used to eliminate the membrane entirely, as a diagnostic tool. While likely impractical at scale, laminar flow RFBs at the benchtop scale do exist [19, 122–125]. A brief inquiry into obtaining or fabricating one for the present application of nonaqueous electrolytes did not identify any promising approaches, in part due to the quite expensive gas-driven pumps required. Still, it would be worthwhile to create an accessible laminar flow/microfluidic test cell to trial active species for chemical degradation in the absence of membrane degradation.

3.4 Conclusion

This chapter has shown that careful choice of cosolvent can lead to electrolyte formulations with higher active-species concentrations and therefore volumetric energy densities. Experimental observations made by the author, previous group members, and external researchers were ultimately repeatable, after material purity constraints were satisfied. Variations in results and occasional lack of reproducibility were explained by the hypothesis of fouling of the porous separator, which appears to depend on multiple variables.

To validate this separator fouling hypothesis further, double-reference-electrode experiments were performed which suggested long-term stability of the charged electrolyte and porous carbon felts, suggesting increasing cell overpotential was confined to the separator alone. The degradation characteristics were qualitatively similar to those studied for industrial membrane separation processes, providing immediate routes for further characterization and mitigation.

Ultimately, the apparent presence of separator fouling in symmetric RFBs with porous separators is concerning, but likely solvable. More promisingly, the previously reported fundamental instability of charged nonaqueous electrolytes against carbon electrodes appears to be not as true as previously thought. With separator fouling identified as the source of long-term degradation, focus turns to the study of more affordable electrolytes for high-voltage nonaqueous flow batteries.

4
Iron-Based Electrolytes

Contents

4.1 Introduction 132
4.2 Synthesis 135
4.3 Voltammetry 137
4.4 Solubility 143
4.5 Cycling 144
4.5.1 HVC Cutoff, Celgard 4560 144
4.5.2 Double RE Celgard 4560 146
4.5.3 Long-term Cycling with Replaceable Cellulose Separators 150
4.6 Fouling Observations and Discussion 159
4.7 Conclusion 161

4.1 Introduction

Two main factors motivate using iron-based compounds in a nonaqueous flow battery. The first is the lower cost of the Fe-based center relative to other elements such as V, Cr, or Mn. The second is the intrinsically ionic nature of the compound, which enables a supporting-salt free configuration; using only a $[Fe(bpy)_3]^{2+}$ salt and solvent such as ACN realizes a two-component electrolyte: one solute, one solvent.

The coordination complex $[Fe(bpy)_3]^{2+}$ is a redox-active cation of the $[M(L)_n][X]$ type, where M is a transition metal cation of Fe, Cr, V, Mn, *etc.* and L is a

chelating ligand. 2,2'–bipyridine (bpy) is a bidentate ligand, meaning it binds to the Fe^{2+} center at two positions. $[Fe(bpy)_3]^{2+}$ has been studied electrochemically in nonaqueous solution since 1958 when Ward claimed the first nonaqueous study of the Fe^{2+}/Fe^{3+} couple of the ClO_4^- salt in ACN [126] (Ward went on to work at Dupont for some years and then quit to develop his own philosophy and movement which inspired the character Anarky in the Batman comic series). The compound consists of an iron (II) center ligated by three bpy ligands and countered by two univalent anions, such as BF_4^-, ClO_4^-, trifluoromethanesulfonate, or triflate ($CF_3SO_3^-$) or others commonly used in electrochemistry. The two nitrogens of each of the three bpy ligands are coordinated octahedrally around the Fe^{2+} center.

The compound exhibits a reversible oxidation couple at 0.7 V *vs.* Ag/Ag^+ attributed to the metal centered process Fe^{2+}/Fe^{3+}, and three reduction couples attributed to the ligand centered process of bpy reduction: the first at -1.7 V, *vs.* Ag/Ag^+, the second 150 mV more negative than the first, and the third 150 mV more negative than the second (according to Fig. 4.3). If utilized in a symmetric configuration the cell would be expected to have an open circuit potential of ≈ 2.4 V (corresponding to the first bpy reduction process), and possibly offer multiple electron transfers on the negative side. The reversibility and observability of the ligand-reduction processes that can be seen in cyclic voltammetry are dependent on the supporting electrolyte and scan rate.

Investigation of the behavior of $[Fe(bpy)_3]^{2+}$ and related compounds quickly jumps into advanced coordination chemistry concepts. The most significant electrochemical feature of this compound is that it allows for one or more reversible negative electron-transfer events at potentials more negative than iron plating/stripping. In other words, the ligand structure confers stability on lower oxidation states of the entire complex, behavior usually attributed to the delocalization of charge over the aromatic rings of the ligands.

Ward studied the positive couple of $[Fe(bpy)_3]^{2+}$ but not the ligand reductions. Herzog and Taube wrote the seminal paper on the stabilization of low-oxidation state transition-metal centers by bpy in 1962 [127]. The first simultaneous preparation

and characterization of the $[Fe(bpy)_3]^{2+}$ compound with reduced ligands seems to have been performed by Hall and Reynolds in 1966 [128]. Singh realized the potential of $[Fe(bpy)_3]^{2+}$ for battery applications in 1984 [129], and by 1988 the Matsumura-Inoue group at Yamaguchi University had studied the positive metal-centered and negative ligand-centered charge-transfer processes of Ru and Fe bpy complexes with voltammetry [130] and built an RFB from tris(bipyridine) ruthenium(II) tetrafluoroborate [131]. This latter paper is not only the original nonaqueous RFB paper, but seems to be the first active attempt to use the reduced ligand-centered bpy couple in a reversible bulk-electrolysis procedure. The team noted the dependence of the system behavior on membrane type, the improvement of performance with flow, and some potential instability of the reduced complex. In this paper, it was found that substituting the bidentate acetylacetonate ($acac^-$) ligand for bpy improved stability, which may explain why future nonaqueous flow battery researchers may have focused more on $acac^-$ compounds.

Indeed, subsequent studies were wary of the reduced $[Fe(bpy)_3]^{2+}$ complex—perhaps unnecessarily so. Mun *et. al* used $[Fe(bpy)_3]^{2+}$ in a flow battery but only for the positive couple, using a nickel equivalent for the negative couple which underwent reversible reduction at a less negative potential than the ligand-centered iron processes [132]. Milshtein *et al.* also investigated this system and intentionally tried to cycle the negative ligand couple of $[Fe(bpy)_3]^{2+}$, performing static bulk electrolysis and flow-cell studies [133]. This study was a thorough investigation that appeared to show stable flow-cell cycling, but the authors faced the confounding observation that the flow cell performance appeared stable while the bulk-electrolysis behavior seemed unstable. They explained it as follows [133]:

> "Notably, the capacity retention during flow-cell cycling is higher than that observed during bulk electrolysis cycling for $[Fe(bpy)_3](BF_4)_2$. This result is counterintuitive given the higher concentration of active species employed in the flow-cell experiment (0.2 M) compared to the bulk electrolysis experiment (5 mM), but can be reconciled by considering differences in the accessed capacity. The bulk electrolysis experiments access nearly 100% of the theoretical capacity, as opposed to less than 33% for the flow-cell experiment. Because a smaller fraction of the theoretical capacity is accessed in the flow-cell experiment, deleterious

> side reactions associated with the less stable, reduced $[Fe(bpy)_3](BF_4)_2$ species do not degrade the observed capacity as rapidly as in the bulk electrolysis experiment. This phenomenon has been reported in prior literature for battery systems with low accessed capacities."

The interpretation of Milshstein *et al.* does not align with the results presented in this chapter. Transient cell degradation was experienced, but shown to be symptomatically confined to the porous separator. Replacing the separator restored performance, as it did with the $V(acac)_3$ chemistry of the previous chapter.

This chapter will detail the synthesis and solubility of $[Fe(bpy)_3]^{2+}(CF_3SO_3)_2$, along with the seemingly insoluble BF_4^- and methanesulfonate, or mesylate ($CH_3SO_3^-$) analogues, and a probably failed but maybe informative attempt at synthesizing the acetate ($CH_3CO_2^-$) analogue. Cyclic voltammetry is performed on $[Fe(bpy)_3]^{2+}(CF_3SO_3)_2$ in ACN, largely without the presence of any supporting salt, in order to demonstrate successful synthesis and similar behavior to that seen in prior literature addressing $[Fe(bpy)_3]^{2+}$ compounds with different anions. Charge/discharge cycling reveals capacity fade similar to that reported in the previous chapter. Use of reference electrodes, cellulose (nonaqueous solute-phobic) separators, and separator replacements all suggest a pore-clogging failure mechanism similar to the $V(acac)_3$ system.

In this way, this chapter tests the hypothesis that, like $V(acac)_3$, the professed instability of $[Fe(bpy)_3]^{2+}$ is a false accusation, and the real culprit for performance degradation is again fouling of the separator.

4.2 Synthesis

NB: the fluorinated acids used in this work require extreme care, and material safety data sheets should be consulted thoroughly. They can dissolve stainless steel and PEEK, amongst other conventionally chemically-resistant materials.

Synthesis of the $CF_3SO_3^-$ salt of $[Fe(bpy)_3]^{2+}$ started with the procedure of Hagen [134]. About 5% (mole basis) excess iron powder was added to a mixture of ACN and triflic acid under heating and stirring. Hydrogen gas is evolved. After

the reaction subsided, the excess iron was filtered off over a Celite pad, and the supernatant concentrated by vacuum. This yielded the acetonitrile-ligated iron (II) triflate salt. The ACN molecules here are equivalent to waters of hydration (and indeed all coordination compound ligands are). Varying degrees of ligation by ACN are observed as in [134] depending on the extent of drying, with a pale off-white free-flowing powder seeming to correspond to a salt with two ACN ligands, and a minty green wet-looking salt seeming to correspond to the salt with four ACN ligands.

Orange compound in the salt, likely Fe^{3+}, can be removed by washing with diethyl ether or acetonitrile. Exposure to ambient air of the Fe^{2+} salts here should be avoided, certainly before ligation by bpy. The intensely red/purple neutral $[Fe(bpy)_3]^{2+}$ compounds may actually resist oxidation of the metal center to Fe^{3+} by air due to protective action of the bpy ligands, but this assertion is based on qualitative observations from looking at piles of dirty glassware—a proper degradation study should be carried out.

Triflic acid exists in the neat, anhydrous form, as does methanesulfonic and (glacial) acetic acid. Fluoroboric acid does not exist in the neat form and was used in aqueous solution. The above procedure was followed for methanesulfonic, acetic, and fluoroboric acids but, before addition of iron, acid and acid/water solutions were sparged for several minutes with argon to remove any dissolved oxygen. This is an important step, since dissolved oxygen will oxidize Fe^{2+} to Fe^{3+}. Triflic acid as received seemed to possess minimal dissolved oxygen and was not sparged beforehand.

In an argon glovebox, the minty green ACN or water-ligated $[Fe(bpy)_3]^{2+}$ salts were then reacted with a slight (5-10%) excess of colorless bpy stock solutions as in [135]. The reaction immediately produces the distinct dark red/purple color of the $[Fe(bpy)_3]^{2+}$ cation. This mixture was left to stir for a few hours before drying under vacuum and washing thoroughly with diethyl ether (to remove excess bpy), and again drying under vacuum—all in a glovebox or on a Schlenk line.

To confirm successful synthesis, voltammetry was used to confirm whether the synthesized compounds had behavior commensurate with literature reports.

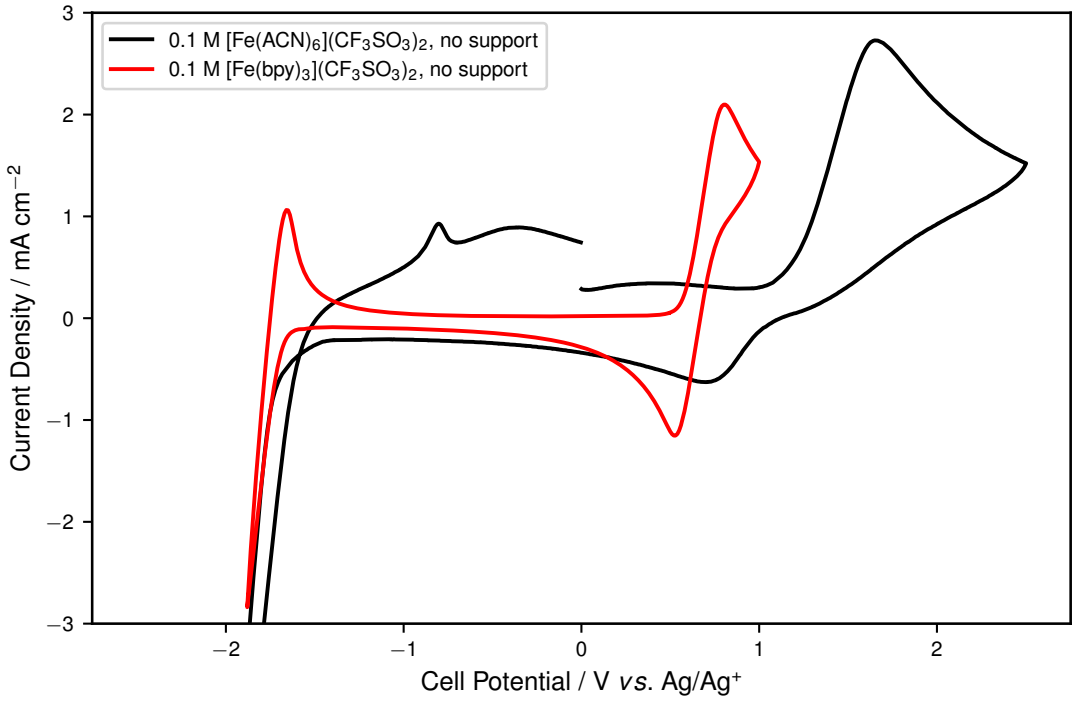


Figure 4.1: Voltammetry of iron (II) triflate in ACN in black, showing irreversible Fe^{2+}/Fe^{3+} couple and Fe^{2+}/Fe^{0} plating stripping in black, and in red, after ligation by bpy, enabling (quasi)reversible Fe^{2+}/Fe^{3+} and absence of plating/stripping negative couple. 400 mV s^{-1}, GC WE, Pt CE, Ag/Ag^{+} RE.

4.3 Voltammetry

Other groups have performed thorough voltammetry on $[Fe(bpy)_3]^{2+}$ compounds in nonaqueous solution with relevant solvents [136, 137]. The focus of the present section is to affirm that the synthesized compounds behave as expected.

After the first seemingly successful synthesis of the ACN-ligated triflate salt, voltammetry was performed in ACN out of curiosity of the author, even though this intermediate compound had not yet been reacted with bpy. Irreversible Fe^{2+}/Fe^{3+} behavior was observed, and plating/stripping behavior of Fe^{2+}/Fe^{0}. This initial voltammogram is shown alongside that of the bpy-ligated desired compound, $[Fe(bpy)_3]^{2+}(CF_3SO_3)_2$, in Fig. 4.1.

Fig. 4.1 clearly illustrates the benefits of nonaqueous flow batteries and the advantages conferrable by coordination electrochemistry. In addition, it demonstrates the elegance of $[Fe(bpy)_3]^{2+}$ and related compounds for the present application. In

black, the initial voltammogram of $[Fe(ACN)_6](CF_3SO_3)_2$ is shown. Though Hagen discussed the $[Fe(ACN)_2](CF_3SO_3)_2$ and $[Fe(ACN)_4](CF_3SO_3)_2$ compounds [134], in solution with excess ACN the compound is almost certainly surrounded by an additional two monodentate ACN ligands, as iron (II) center affords six coordination sites. This first scan started from 0 V in the positive (anodic) direction. Scanning in the positive direction, a textbook example of an irreversible couple is observed, presumably Fe^{2+}/Fe^{3+}. In the negative direction, the voltammetry loop crosses itself after scan reversal, a characteristic signature of metal plating/stripping that presumably can be attributed to the Fe^{2+}/Fe^0 couple.

The red voltammogram in Fig. 4.1 shows the behavior of $[Fe(bpy)_3]^{2+}(CF_3SO_3)_2$ in ACN without any supporting electrolyte. The behavior of this bpy-ligated iron salt is strikingly different from the ACN-ligated salt. The positive couple shifts more negative and appears at least quasireversible, with peak separation decreasing drastically. This shift reflects qualitatively improved kinetics in the iron salt with stronger coordinated bpy ligands.

Outer-shell electron transfers are usually described as having fast kinetics as a consequence of their low reorganization energies. In short, bpy is coordinated to the iron center much more strongly than ACN or water. When the iron center changes oxidation states from II to III without coordinated bpy, the solvation shell around the iron center changes. This change imparts an energy penalty on the charge transfer process, which results in sluggish kinetics. When a strongly-bound ligand like bpy is coordinated around to the iron center, the change in oxidation state does not change the solvation shell of the compound appreciably due to the more rigid geometry of the complex, enabling faster kinetics. This is why flow batteries with aqueous couples are more likely to struggle with kinetics and researchers are constantly developing catalytic electrode treatments, or simply running the whole battery at elevated temperatures (as with Fe/Cr or Fe/O_2 RFBs—aqueous vanadium can't run at high temperatures because of V^{5+} precipitation)

The red voltammogram of Fig. 4.1 shows different behavior on the negative scan as well. Plating/stripping behavior is not witnessed in this potential range, and

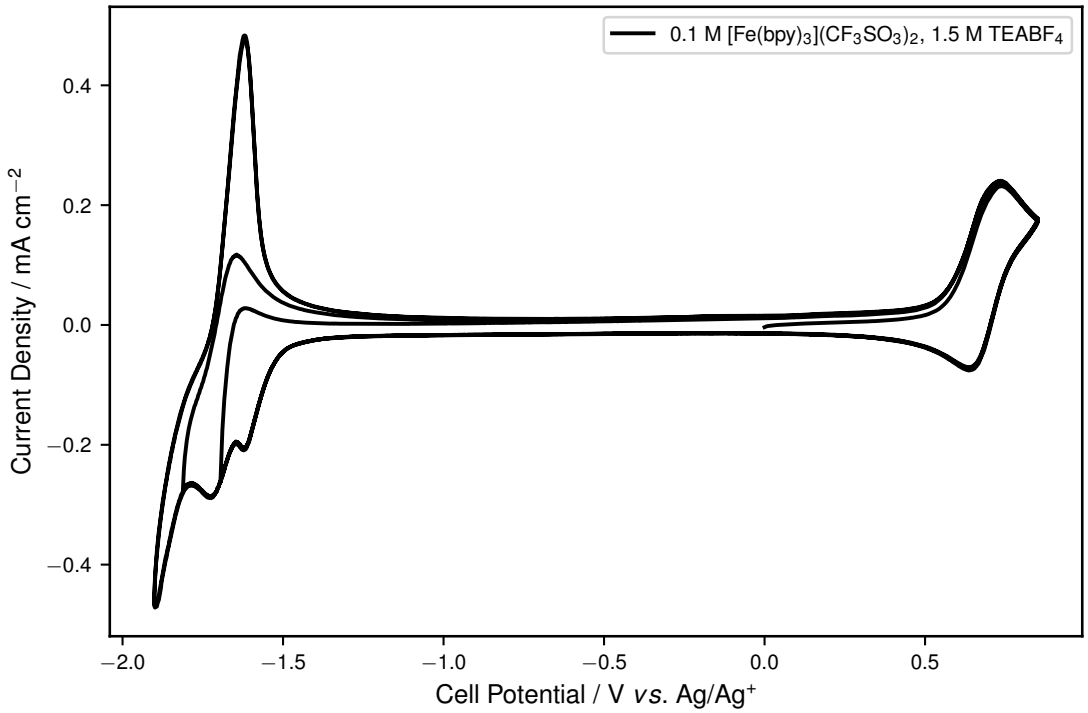


Figure 4.2: Cyclic voltammetry of $[Fe(bpy)_3]^{2+}$ triflate in ACN with various cutoffs, showing sequential ligated bpy reductions. 100 mV s^{-1}, GC WE, Pt CE, Ag/Ag^+ RE.

an atypical reduction event is witnessed around 500 mV more negative than the onset of plating in the non-bpy salt. This reduction process is that of the first bpy ligand reduction process, and detailed further in subsequent voltammograms. Thus, the presence of bpy improves the kinetics of the Fe^{2+}/Fe^{3+} couple and inhibits the Fe^{2+}/Fe^0 plating process, instead allowing potential scans to decrease further without reaction until the reduction of ligand occurs.

Fig. 4.2 shows three scans of 0.1 M $[Fe(bpy)_3]^{2+}(CF_3SO_3)_2$ in ACN with 1.5 M $TEABF_4$ as supporting electrolyte. The three scans have progressively more negative cutoffs for the voltage window. Here, three sequential reduction events corresponding to the three bpy ligands present with tris(bipyridine) compounds [132, 136, 138]. The behavior observed by others depends on the solvent used, with PC showing mass-transfer-limited resolved peaks on the positive scans of the negative couples. Here, in ACN, the forward peak of the reduction couple simply grows in magnitude as more bpy ligands are sequentially reduced, but does not

change significantly in onset potential. Extreme solvent-dependence of charge-transfer processes is quite common in nonaqueous electrochemistry [90, 101]. Also, it must be noted that most voltammetric studies occur with the bulk solution in the fully discharged state (from a battery perspective) and thus, there may be different behavior of these couples as the bulk solution composition changes. A survey of the literature on tris(bipyridine) reduction processes revealed a debate over where the electrons are stored on the reduced complex—on individual ligands or delocalized across all ligands/the complex—and this additionally seems to depend on the nature of the metal center and the solvent [139]. Perhaps there exists some disproportionation equilibria amongst the ligands of the reduced complex with subsequent charge transfers, and the complex is re-oxidized at roughly the same onset potential no matter how many ligands are reduced. This is consistent with the observation that the current for reoxidation increases with the number of ligands that were previously reduced. In any case, the $[Fe(bpy)_3]^{2+}(CF_3SO_3)_2$ compound synthesized shows behavior in ACN commensurate with the literature.

The technique of differential pulse voltammetry (DPV) was used to observe the voltammetric behavior of the $[Fe(bpy)_3]^{2+}(CF_3SO_3)_2$ complex in an attempt to more clearly resolve the ligand reduction processes. DPV superimposes an alternating current waveform on top of a linear-sweep voltammogram. This process seeks to improve the detection of the relevant Faradaic component of the voltammogram relative to the capacitive component [140]. DPV was recorded at $400\,\mathrm{mV\,s^{-1}}$ from +1 to –3 V with a voltage step of 3 mV, pulse amplitude of 10 mV, and pulse time of 10 ms (these are the standard settings in IviumSoft, the potentiostat control software). The voltammogram produced by applying DPV to the same sample as the previous cyclic voltammogram is shown in Fig. 4.3.

In DPV, the signatures of electron-transfer events are expected to be symmetric about their equilibrium potential. Because the scan was entirely in the negative direction, the peaks in Fig. 4.3 have negative currents. The Fe^{2+}/Fe^{3+} couple seems apparent at 0.7 V vs. Ag/Ag^+. Also, six reduction processes are observed in the negative-potential region. The least negative three occur at similar potentials to

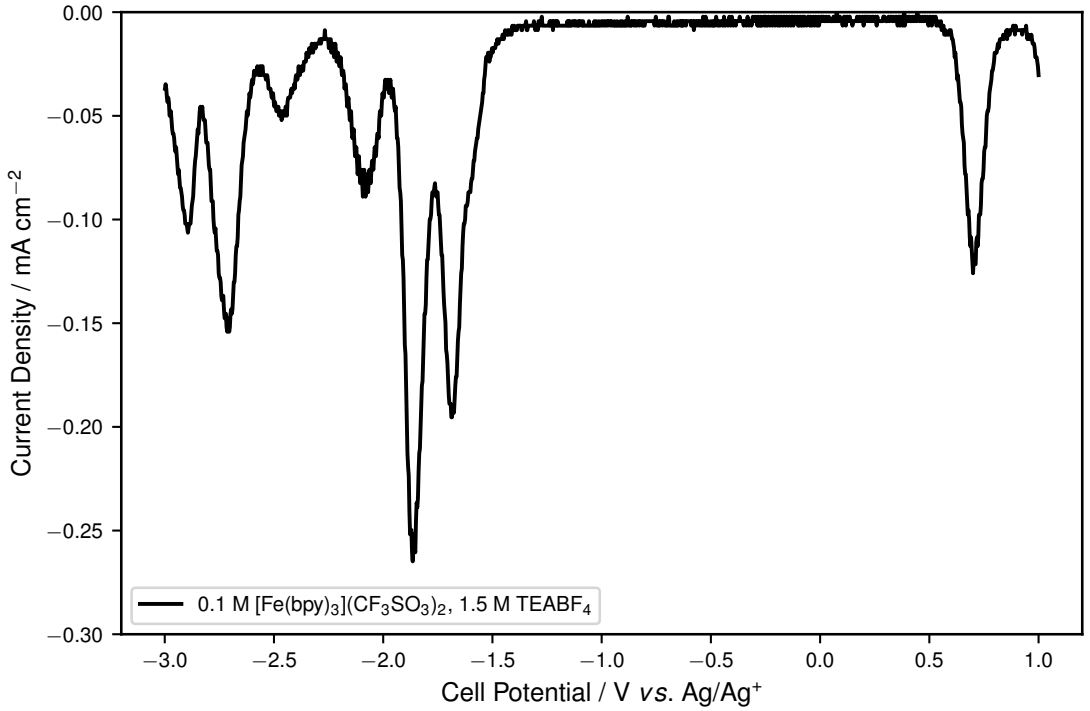


Figure 4.3: Differential pulse voltammetry of $[Fe(bpy)_3]^{2+}$ triflate in ACN showing the iron II/III positive couple, as well as all sequential ligated bpy reductions to their radical anions, and possibly dianions. 400 mV s^{-1}, GC WE, Pt CE, Ag/Ag$^+$ RE. Scan from +1 to –3 V *vs.* Ag/Ag$^+$

those seen in Fig. 4.2 and other reports, and so seemingly correspond to the stepwise reduction of bpy ligands. The most negative three reduction processes also have similar ($\approx$ 150 mV) peak-to-peak separation to the least negative three reduction events. These events likely correspond to the formation of dianions of the bpy ligands. This has been observed for different aromatic ligands coordinated to iron in the past [141].

Fig. 4.4 shows a comparison of $V(acac)_3$ and $[Fe(bpy)_3]^{2+}(CF_3SO_3)_2$ compounds at the same actives concentration and scanrate in ACN. This comparison emphasizes the 200 mV wider couple separation afforded by the iron complex.

Fig. 4.5 compares the voltammograms of $V(acac)_3$ and $[Fe(bpy)_3]^{2+}$ in ACN with a ferrocene reference couple at scanrates of 25, 50, 75, 100, 200, 300, 400, and 500 mV s^{-1}. This shows increasing peak separation with scan rate for both $V(acac)_3$ and $[Fe(bpy)_3]^{2+}$, characteristic of quasireversible half-reaction kinetics.

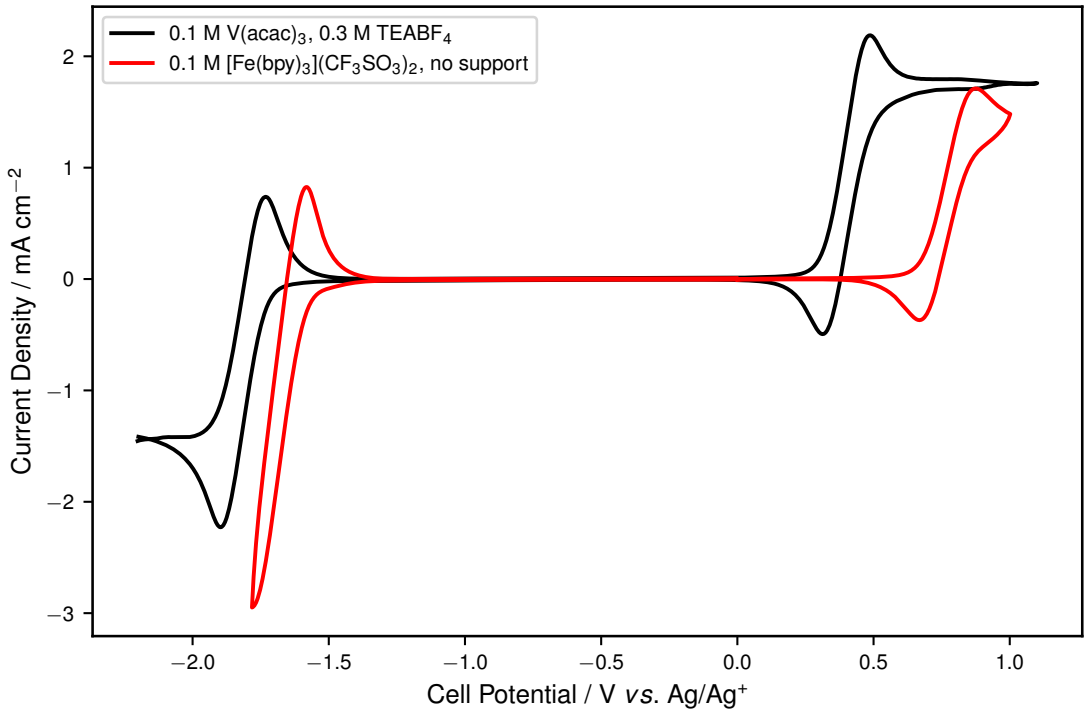


Figure 4.4: A comparison of $V(acac)_3$ and $[Fe(bpy)_3]^{2+}$ in ACN, 100 mV s^{-1}, GC WE, Pt CE, Ag/Ag^+ RE.

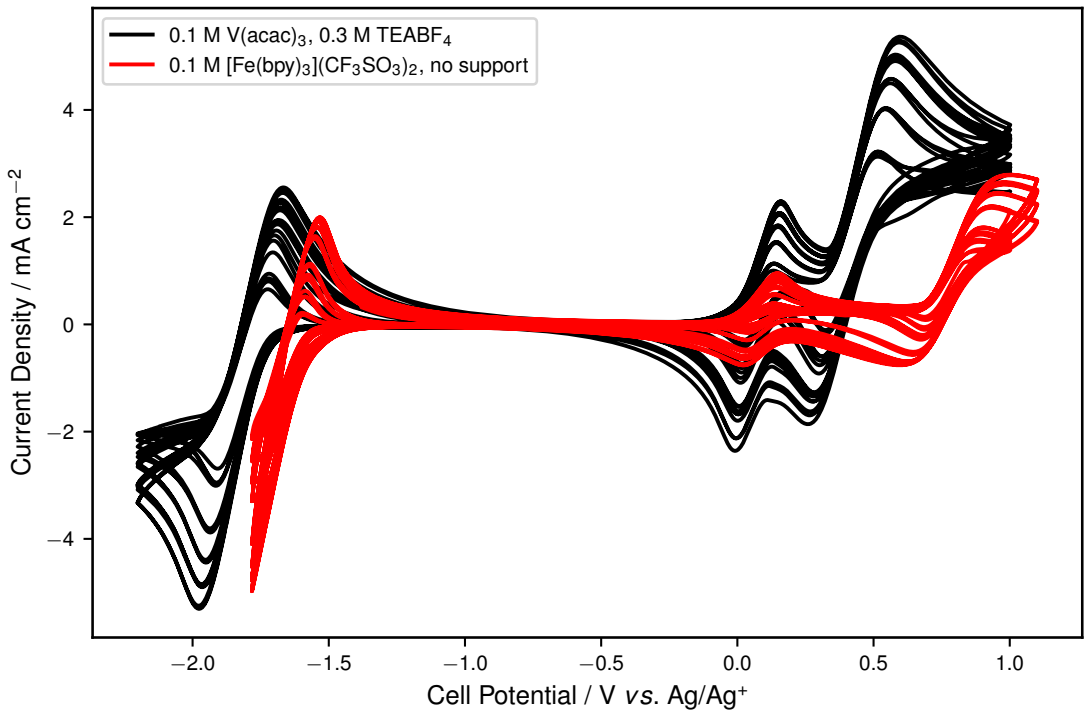


Figure 4.5: A comparison of $V(acac)_3$ and $[Fe(bpy)_3]^{2+}$ in ACN with a ferrocene reference couple at scanrates of 25, 50, 75, 100, 200, 300, 400, and 500 mV s^{-1}, GC WE, Pt CE, Ag/Ag^+ RE.

The rate at which peak separation increases with scan rate is roughly similar between both compounds.

In addition to the triflate salt, iron (II) salts of methanesulfonate, tetrafluoroborate, and acetate were all prepared with the intermediate compounds matching the colors described in literature. The methanesulfonate and tetrafluoroborate salts showed voltammetric behavior qualitatively similar to that shown for the triflate salt, which suggested that synthesis was complete, but as will be shown subsequently, these salts had poor solubility and no further study was attempted.

The acetate salt did not show the expected voltammetric behavior after two synthesis attempts. A brief look at literature revealed that the acetate anion is actually quite a strong coordinating ligand, possibly stronger than bpy—meaning that bpy would be unable to fully ligate the iron center. When examining bpy acetate salts of Zn^{2+}, Cd^{2+}, and Hg^{2+}, even with a tenfold excess of bpy, bpy was unable to displace all the acetate for Hg^{2+} in a study from 2017 [142].

4.4 Solubility

NB: most of the densitometric solubility work here was performed by Tina Mu, an undergraduate intern.

Various salts of $[Fe(bpy)_3]^{2+}$ compounds and solvents were quickly screened for solubility on a visual basis. Promising combinations were then assessed for solubility limits using the densitometric method described in the previous chapter.

Counter to the results of others [143] the BF_4^- salt did not even appear visually soluble in all solvents tested. Synthesis was attempted twice, and voltammetric analysis seemed to confirm the synthesis went as intended. No time was available for structural analysis at an outside facility; the triflate salt worked well enough that further work on BF_4^- was abandoned without pursuing the discrepancy with literature.

The $CH_3SO_3^-$ compound, a cheaper, non-fluorinated version of $CF_3SO_3^-$ used as an ionic-liquid anion, was also not very soluble in any solvent attempted even though voltammetric analysis showed the behavior expected for $[Fe(bpy)_3]^{2+}$.

Table 4.1: Solubilities of iron bipyridine salts with different anions in various solvents

Solubilites in M	BF_4^-	$CF_3SO_3^-$	$CH_3SO_3^-$
Acetone	-	0.040	-
ACN	-	0.47 (0.57)	.058
Benzene	-	0.080	-
Benzonitrile	-	-	-
DME	-	-	-
DMF	-	0.55	.042
1,3-DO	-	-	-
DMSO	-	0.37	0.025
PC	-	0.53 (0.38)	0.10
THF	-	-	-

Table 4.1 summarizes these results. The main results relevant here are that the $CF_3SO_3^-$ salt is soluble to around 0.5 M in ACN and PC, more than enough to allow for benchtop RFB work. Note that the author's own prior measurements of $[Fe(bpy)_3]^{2+}(CF_3SO_3)_2$ in these two solvents do not agree with the measurements of the intern, though identical techniques were used. The author's two measurements are shown in parentheses. It could be that the u-tube of the densitometer was not properly flushed with neat solvent between some measurements, which could be a large source of error. Nonetheless, the experiments confirmed the suitability of the triflate salt for benchtop cycling experiments in two common electrochemical solvents, ACN and PC.

4.5 Cycling

4.5.1 HVC Cutoff, Celgard 4560

Charge/discharge cycling was first attempted with 0.1 M $[Fe(bpy)_3]^{2+}(CF_3SO_3)_2$ in ACN without supporting electrolyte, using 20 mL of total electrolyte at $20\,mA\,cm^{-2}$ with a 2.6 V charging cutoff. Celgard 4560 was used as the separator. Over 100 cycles were achieved, but performance fade appeared in a fashion looking similar to that of previous $V(acac)_3$ experiments. Charge/discharge profiles are shown in Fig. 4.6 and the corresponding efficiencies, in Fig. 4.7. Fig. 4.7 shows the increasing coulombic and decreasing voltaic/utilization efficiencies witnessed with the $V(acac)_3$

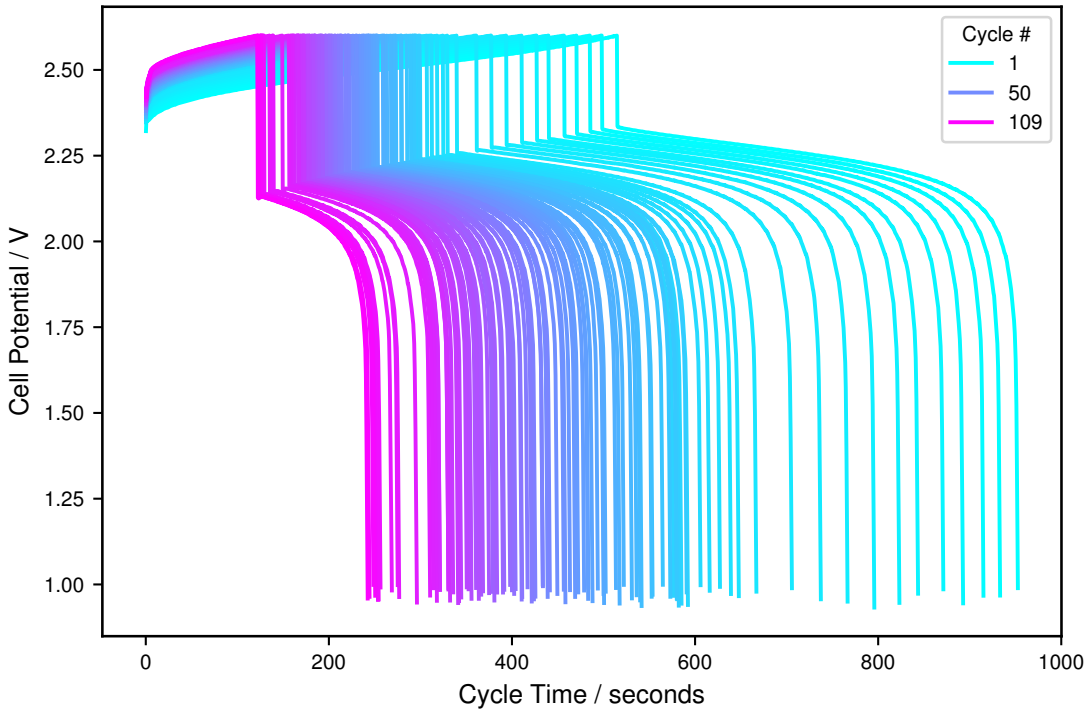


Figure 4.6: 109 charge/discharge profiles of 0.1 M $[Fe(bpy)_3]^{2+}(CF_3SO_3)_2$ in ACN without supporting electrolyte. 20 mA cm^{-2}, 2.6 V cutoff

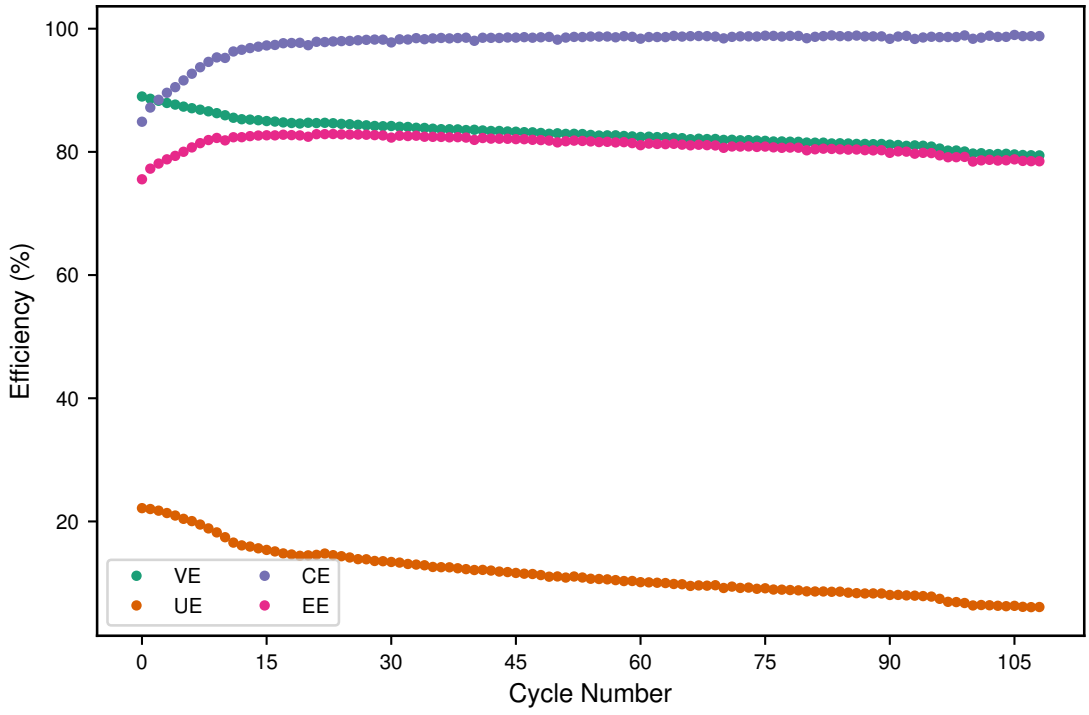


Figure 4.7: Charge/discharge efficiencies of Fig. 4.6

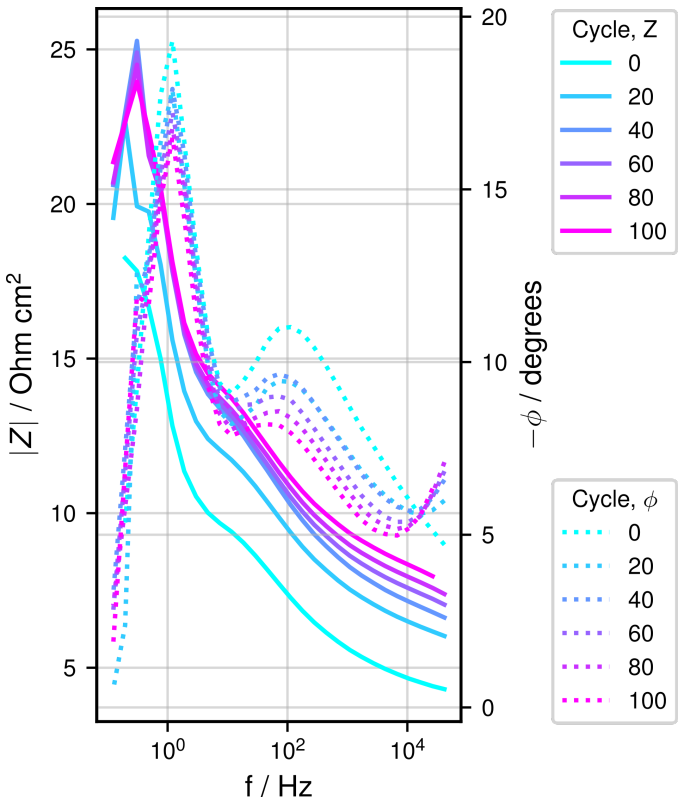


Figure 4.8: Bode plots of EIS scans taken every 10 cycles during experiment of Fig. 4.6

chemistry. Before the experiment and every 10 cycles, an impedance scan was recorded. Bode plots are shown in Fig. 4.8 and Nyquist plots in Fig. 4.9.

Like $V(acac)_3$, both figures show an increase in the real component of impedance with continued cycling. To determine where this impedance growth originated, double-reference electrode charge/discharge experiments were performed similar to the previous chapter.

4.5.2 Double RE Celgard 4560

16 mL of total electrolyte was used for the following double-reference electrode experiments. Charging was performed at $20\,mA\,cm^{-2}$ to 25% theoretical SOC assuming no self-discharge, followed by a 60 s OCP hold, and then discharge to 1.4 V at the same current, followed by another 60 s hold at OCP. Charge/discharge profiles over more than 50 cycles are shown in Fig. 4.10 and corresponding efficiencies in Fig. 4.11.

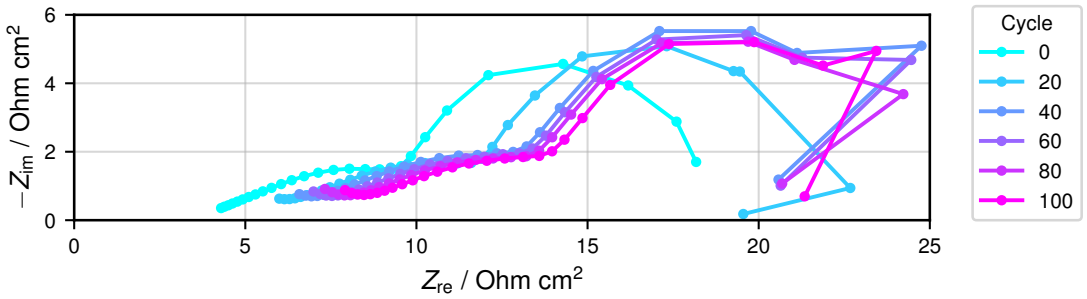


Figure 4.9: Nyquist plots of EIS scans taken every 10 cycles during experiment of Fig. 4.6. Noise in the low-frequency response appears in the final cycles, with a heavily fouled separator, indicating the EIS settings are likely no longer suitable for the system.

Fig. 4.10 shows how, with a constant amount of charge entering the battery every half-cycle, the OCP-hold voltage remains constant, suggesting that the cell is not experiencing any oxidation-state drift. This in part supports the claim that the $[Fe(bpy)_3]^{2+}$ ligand-reduction process is indeed stable. Clear overpotential growth is shown on both charge and discharge, but appears to be more symmetric in nature than Celgard 4560 cells using $V(acac)_3$ and $TEABF_4$ in ACN. The end-of-discharge OCP hold does increase slightly with cycling—this is because as overpotential grows with cycle count, the cell is not discharging as much as previous cycles due to premature cutoff. Later cycles show unusual, non-monotonic behavior on charge. This could be due to the relaxation of concentration polarization/dynamic film process on the membrane—an extreme case of pore clogging growing beyond the membrane surface, for example.

Fig. 4.11 shows typical behavior for a system undergoing gradual separator degradation, with coulombic efficiency increasing and voltaic decreasing with cycle

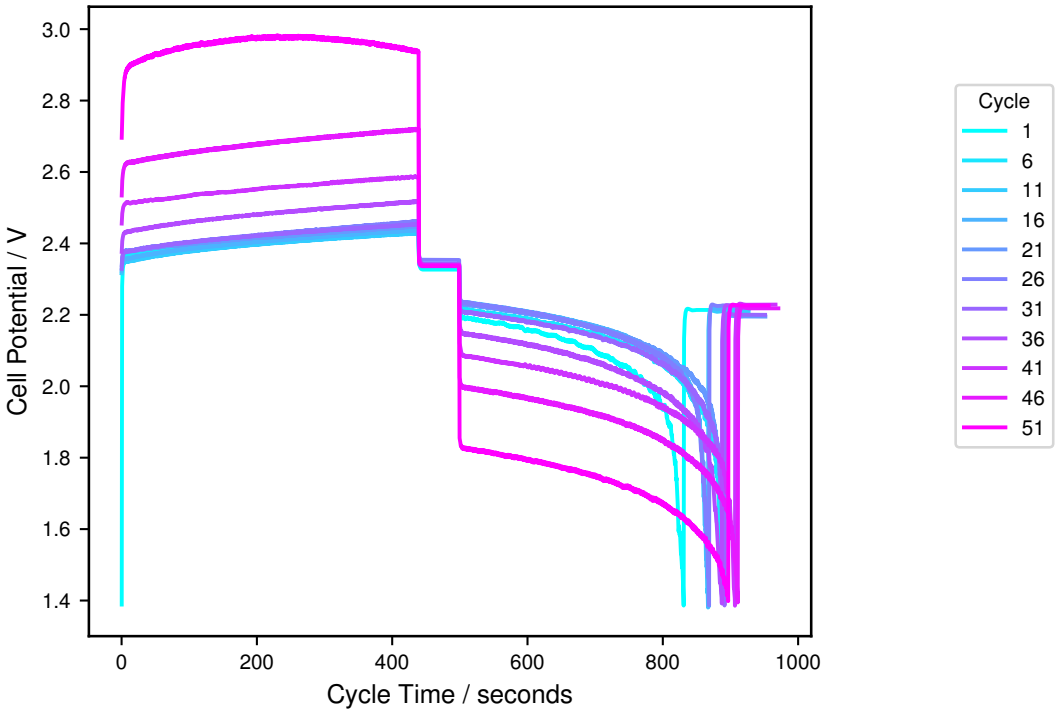


Figure 4.10: Over 50 charge/discharge profiles of 0.1 M $[Fe(bpy)_3]^{2+}(CF_3SO_3)_2$ in ACN without supporting electrolyte. 20 mA cm^{-2} to 25% theoretical SOC, open-circuit hold between cycles

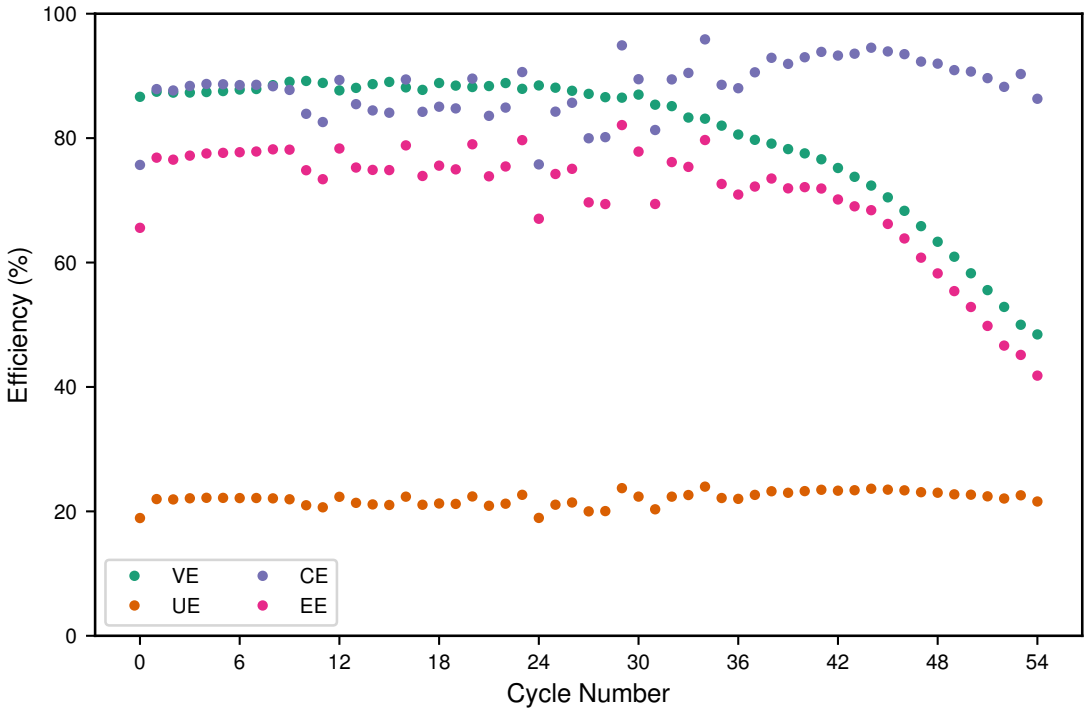


Figure 4.11: Charge/discharge efficiencies of Fig. 4.10

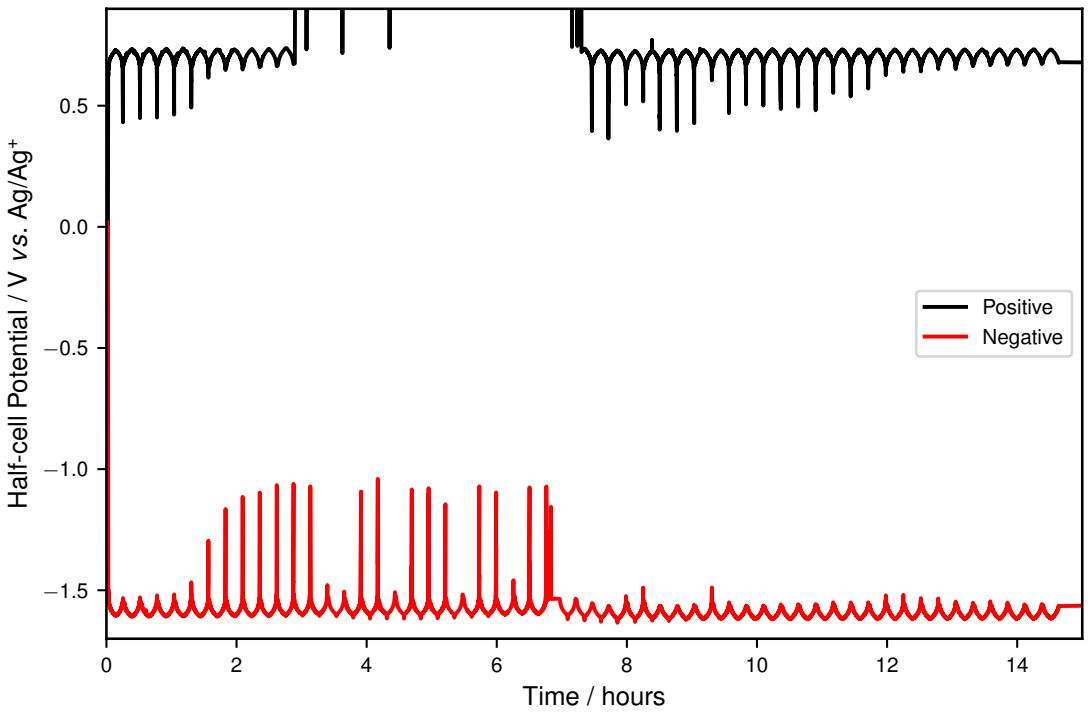


Figure 4.12: Half-cell data from Fig. 4.10 showing constant and repeatable Nernstian behavior and lack of overpotential growth from electrode surfaces to bulk solutions

count. Utilization efficiency remains roughly constant, because of the coulomb-counting nature of the cycling protocol and the lack of chemical degradation or oxidation state drift.

Fig. 4.12 shows the half-cell data from this cycling experiment. Again there is remarkable stability of the voltage between the carbon felt electrodes and the bulk electrolyte half-cell solution. A clear Nernstian charge/discharge behavior is seen in each half-cell. No overpotential growth is witnessed between the carbon felts and the reservoirs of either half-cell, suggesting the overpotential growth obvious in Fig. 4.10 must be confined to the component existing between the carbon felts and bulk solutions: the porous separator. The period between 3 and 7 hours shows erratic behavior because one of the reference electrodes lost contact with the reservoir volume due to solvent evaporation overnight. Pushing the positive reservoir reference electrode further down in the reservoir restored ionic contact with the electrolyte solution.

4.5.3 Long-term Cycling with Replaceable Cellulose Separators

NB: the author is grateful to fellow labmate Andrew Wang for his assistance with some of the following experiments when the author had to leave the UK on short notice.

$[Fe(bpy)_3]^{2+}$ was cycled with Dreamweaver cellulosic separators because those gave the most stable performance for $V(acac)_3$ systems. The current working hypothesis for the performance degradation of both $V(acac)_3$ and $[Fe(bpy)_3]^{2+}$ flow batteries is gradual adsorption of solute molecules on pore walls, followed by more rapid codeposition of further solute on the initial adsorbed layer of solute, which gradually blocks the pores, making the coulombic efficiency higher and voltaic lower due to increased difficulty for all species to traverse the membrane. Thus, the material of the separator has a strong effect on this fouling, with conventionally "hydrophilic" membranes like alumina and cellulose taking much longer to foul than polymeric membranes. These systems are anhydrous, so instead "solutephobic" is used to describe the desired behavior of the separator pore walls.

PC was used instead of ACN for these experiments exclusively because of its lower vapor pressure. Previous experiments with ACN would run into issues with solvent evaporation before significant cell failure, while PC did not evaporate from the system at all in the timescale studied, which was several weeks. Also, voltammetric studies by others of $[Fe(bpy)_3]^{2+}$ in PC and ACN suggested the PC system yielded commensurate or higher stability than ACN [133, 136]. PC electrolytes are usually more viscous and less conductive than ACN-based ones, so electrochemical performance is not optimal.

Like $V(acac)_3$, the cellulose separators enabled much longer cell lifetimes, but were not completely immune to fouling. However, with the PC system maintaining its volume over time, electrolyte maintenance was trivial due to the stability of the $[Fe(bpy)_3]^{2+}(CF_3SO_3)_2$ compound. After each cell had been cycled to the point of significant separator fouling, separators would be replaced, while maintaining the same carbon felt electrodes and electrolyte. This was accomplished by pumping

out the electrolyte into external vials. The cell was then rinsed with neat ACN and split open, carefully removing the failed separator and inserting a new one. The cell was reassembled and rinsed once more with neat ACN, and pumped dry for a short period to "blow out" as much ACN as possible. The electrolyte from the previous build was then pumped back into the original reservoirs and through the rebuilt cell, which contained the previously used electrodes but a new separator. Every experiment in this subsection was performed using the exact same batch of 16 mL of 0.1 M $[Fe(bpy)_3]^{2+}(CF_3SO_3)_2$ electrolyte in PC and the same carbon felt electrodes, demonstrating the remarkable stability of the $[Fe(bpy)_3]^{2+}(CF_3SO_3)_2$ compound used here.

Dreamweaver Silver 40

A single sheet of Dreamweaver Silver 40, a 40 µm thick cellulosic battery separator, was used for the initial experiment at a current density of $5\,mA\,cm^{-2}$ to 25% theoretical SOC, followed by 30s OCP hold, and then discharge to 1.4 V at the same voltage. EIS scans were recorded every 10 cycles, but unfortunately the settings were inappropriate for the system, and the results are not meaningful. Charge/discharge profiles of the system are shown in Fig. 4.13 and corresponding efficiencies in Fig. 4.14.

Fig. 4.13 shows the system lasting over 150 cycles, with each cycle lasting between 20 and 30 minutes. A clear increase in cycle length is observed with cycling, and this is reflected by the increasing couloumbic efficiency shown in Fig. 4.14 below. Overpotentials are greater than ACN-based systems even at this lower current density due to the lower conductivity of PC-based electrolytes.

Fig. 4.14 shows, like previous efficiency plots, the gradual increasing coulombic and utilization and decreasing voltaic efficiencies of a gradually degrading porous separator flow battery experiment which operates with a coulomb-counting charge step. There is apparent noise in the coulombic/energy efficiencies, however. Recall that this experiment attempted to perform EIS scans every 10 cycles, though the settings were inappropriate. This means every 10 cycles there was a substantial

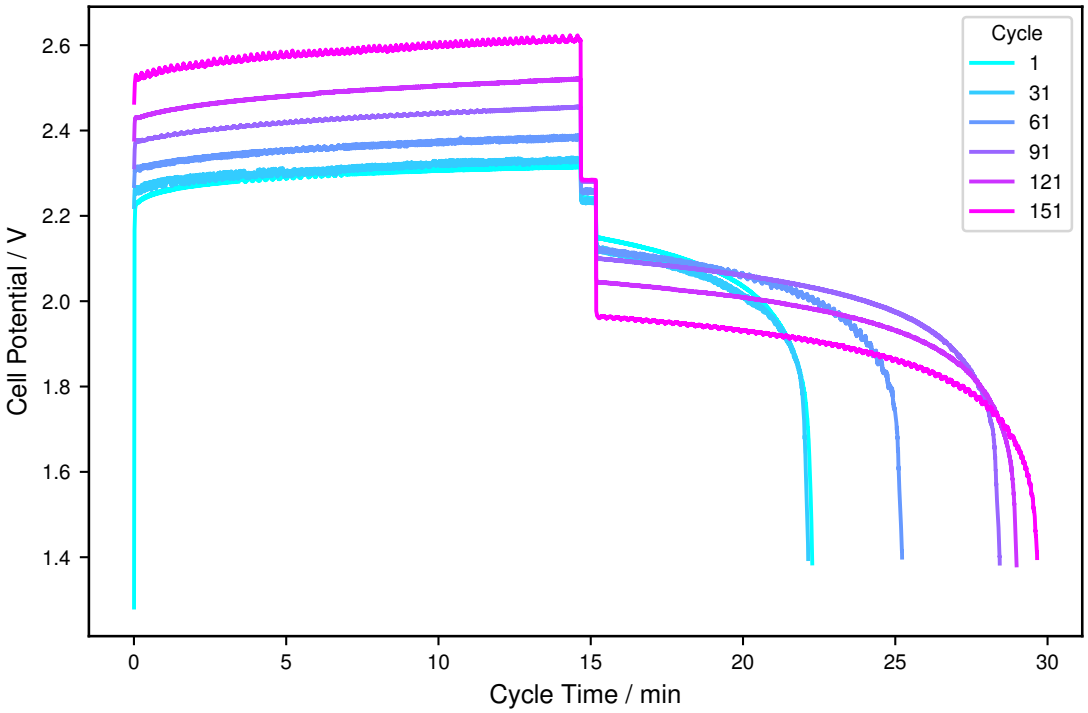


Figure 4.13: Over 150 charge/discharge profiles of 0.1 M $[Fe(bpy)_3]^{2+}(CF_3SO_3)_2$ in PC without supporting electrolyte. Dreamweaver Silver 40 cellulose separator, 5 mA cm^{-2} to 25% theoretical SOC, 30s OCP hold

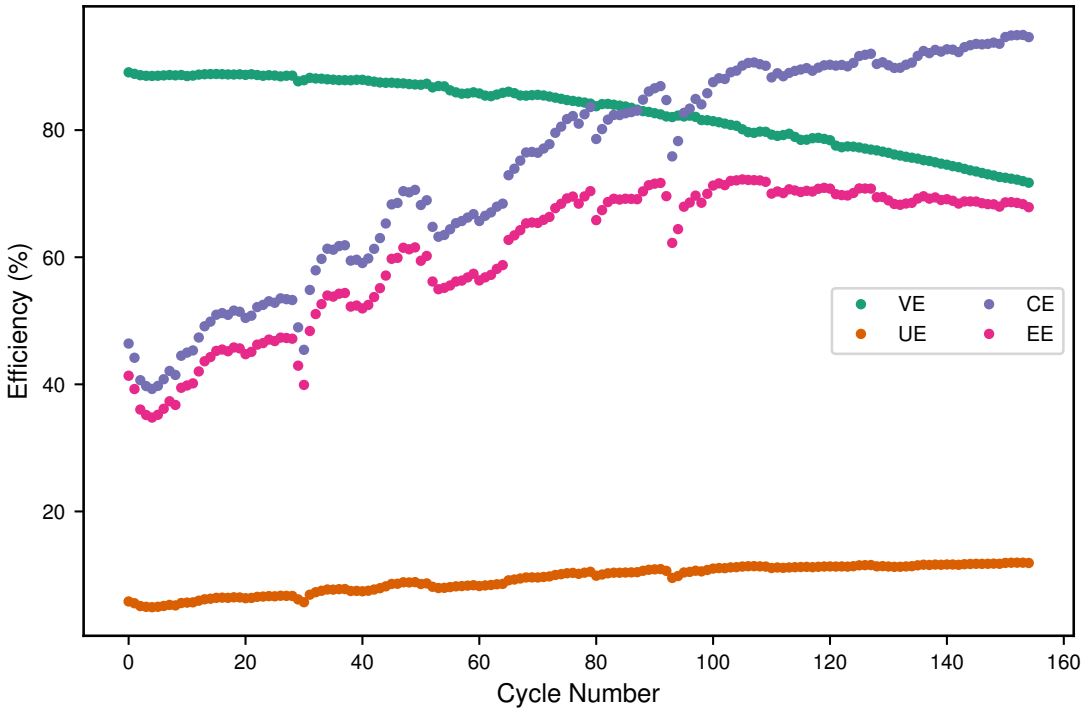


Figure 4.14: Charge/discharge efficiencies of 4.13

rest step, which allowed the system to relax. These fluctuations in couloumbic efficiency occur every 10 cycles.

Often, in conventional membrane separation systems, fouling can be classified into reversible and irreversible fouling. Here, it seems a rest period alleviates some reversible fouling process—possibly internal or external concentration polarization, a film or gel on the membrane surface, *etc.*—and this is visible in the jumps and discontinuities in the coulombic efficiencies. Voltaic efficiency continues to decrease monotonically, however, suggesting irreversible fouling also occurs (or at least irreversible without further mitigation strategies).

Dreamweaver Silver 40 with separator puncture

The cell was rebuilt with another sheet of Dreamweaver Silver 40 as the separator and operated with the same conditions as the previous experiment. Due to a seemingly random error/memory overflow after several days of running the previous cell, after the first 8 cycles or so, the PID reservoir balancing control script crashed and the controller had to be reset. It took a couple cycles to notice the script had crashed, and in that time a small amount of reservoir imbalance had accumulated. Upon restarting the balancing script, the PID controller reacted strongly to the sudden imbalance and immediately applied an extreme bias to the flowrate. This sudden bias caused a pressure fluctuation which punctured the membrane, evident in the sudden drop in efficiencies after cycle 7 in Fig. 4.16. Cycle 11 in Fig. 4.15 shows the nonexistent discharge capacity of this short period of cycles at the original current density of $5\,\mathrm{mA\,cm^{-2}}$ after the PID controller reset appears to have punctured the membrane, or exfoliated it somehow.

In order to see if the cell could still function, current density was doubled to $10\,\mathrm{mA\,cm^{-2}}$ in the hopes the cell with a much leakier separator could still hold some charge, and it could. In fact, the system lasted an additional 65 cycles, and the membrane continued to experience whatever degradation mechanism had been seen in previous tests.

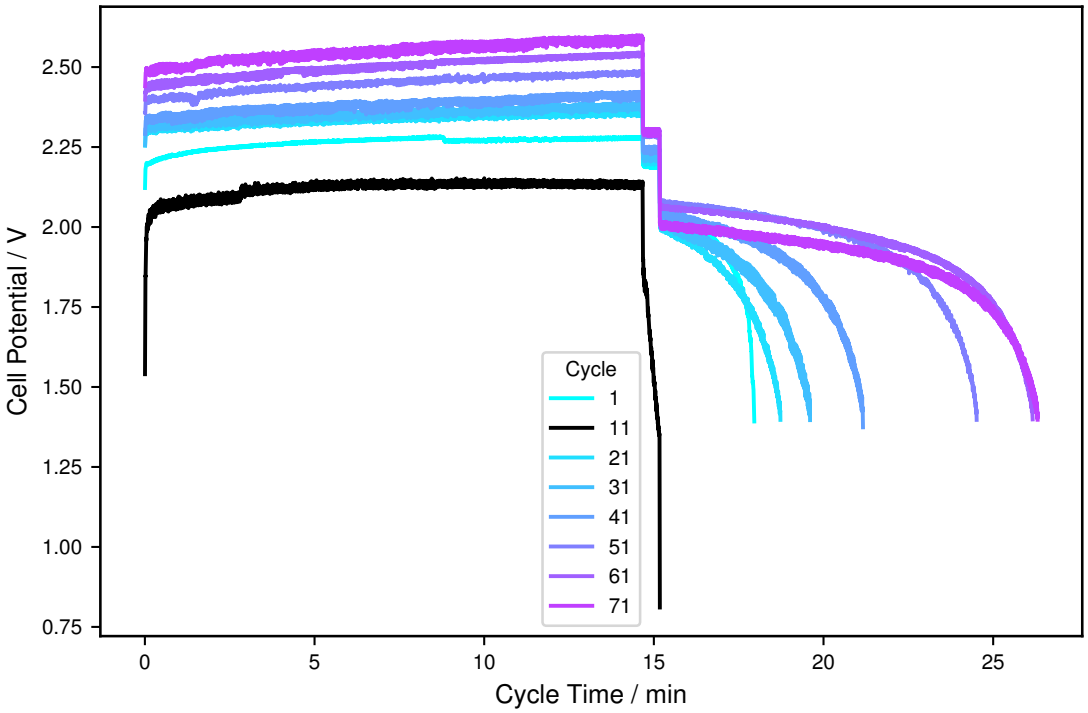


Figure 4.15: Charge/discharge profiles of 0.1 M $[Fe(bpy)_3]^{2+}(CF_3SO_3)_2$ in PC without supporting electrolyte, in same cell as Fig. 4.13 with new separator. Dreamweaver Silver 40 cellulose separator, 5 mA cm^{-2} to 25% theoretical SOC for first 15 cycles, then 10 mA cm^{-2} to to 50% theoretical SOC, 30s OCP hold

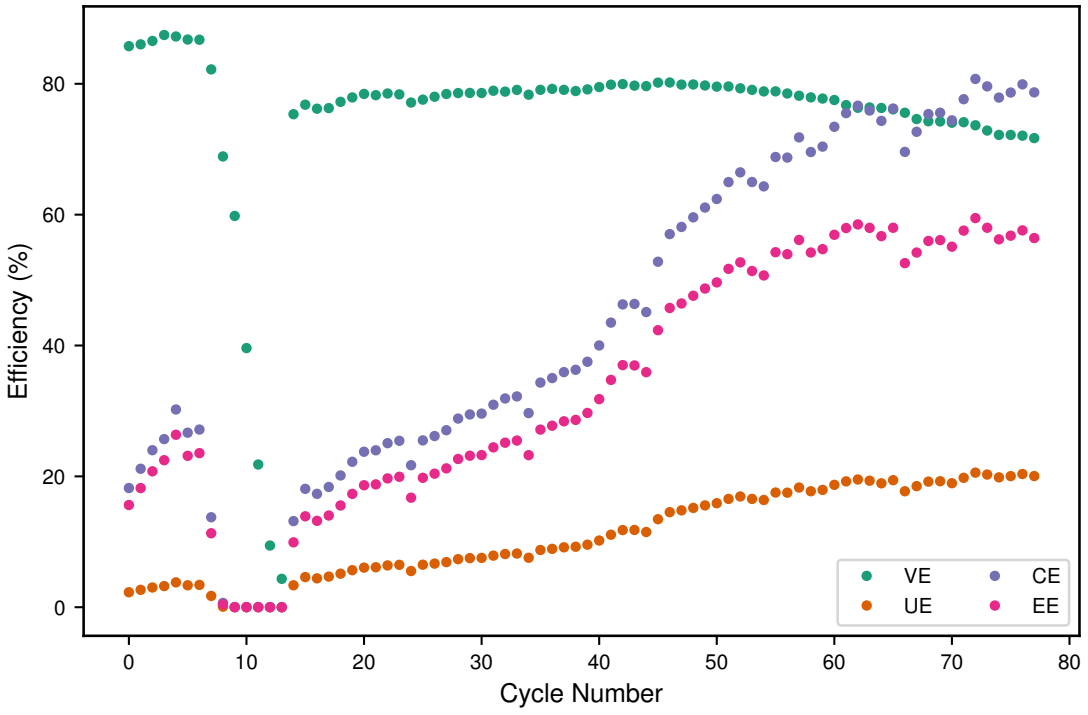


Figure 4.16: Charge/discharge efficiencies of Fig. 4.15

Fig. 4.16 shows how after the current density was doubled post-separator-puncture after cycle 15, the system continued to show normal behavior with increasing coulombic, energy, and utilization efficiencies as the separator continued to close up. Optimists may call this behavior "self-healing," but it is likely still the same fouling mechanism experienced previously in this thesis—starting from a much more initially porous punctured state.

Dreamweaver Silver 20

Both previous experiments with this batch of electrolyte and electrodes started at initially low coulombic efficiencies below 50%—unacceptable for a real system, but the aim here is to probe long term stability, not optimize single-cycle performance. Dreamweaver Silver 40 is 40 µm thick, and Dreamweaver Silver 20 is 20 µm thick. With the anticipation that a thinner membrane may possess even lower coulombic efficiency than the previous ones, Dreamweaver Silver 20 was used in the hope that a thinner membrane might eventually reach a steady-state fouled condition with higher coulombic efficiency and a stable voltaic efficiency. In this way, the goal was to form a "self-forming dynamic membrane" of sorts grafted onto the initial separator matrix, a practice common in wastewater treatment and bioreactors [144]. Fig. 4.17 shows the initial cycles at $20\,\mathrm{mA\,cm^{-2}}$, revealing barely any discharge capacity because of the very thin membrane.

Consequently, current density on charge only was doubled to $40\,\mathrm{mA\,cm^{-2}}$ in the hopes the cell could hold an appreciable amount of charge. Discharge current density was maintained at $20\,\mathrm{mA\,cm^{-2}}$. Fig. 4.18 shows the charge/discharge profiles from this experiment.

Fig. 4.18 shows significant overpotentials because of the higher current density and the less conductive PC-based electrolyte. Unusual non-monotonic behavior is again seen during later cycles on the charging step, possibly due various mechanisms already proposed related to film formation/concentration polarization. Noticeable also in these profiles is the decreasing potential recorded during the OCP hold. A constant amount of charge was introduced into the system, so this voltage should be

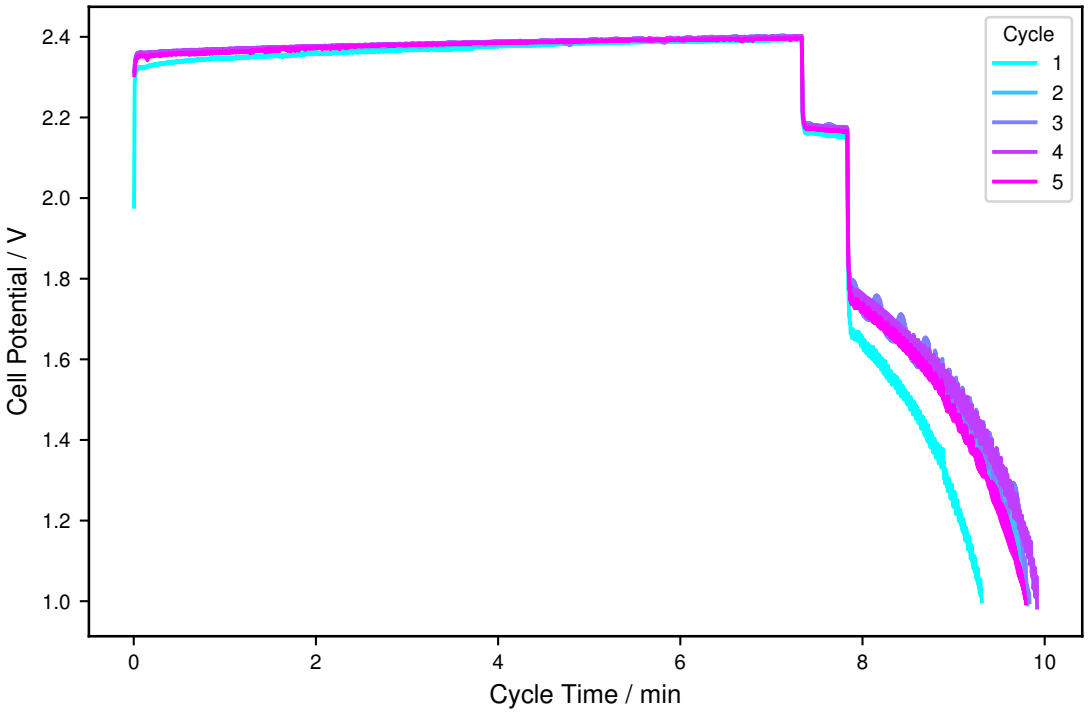


Figure 4.17: Initial charge/discharge profiles of 0.1 M $[Fe(bpy)_3]^{2+}(CF_3SO_3)_2$ in PC without supporting electrolyte, in same cell as Fig. 4.15 with new separator. Dreamweaver Silver 20 cellulose separator, 20 mA cm^{-2} to 50%, 30s OCP hold

only Nernstian and unchanging in the absence of chemical degradation or oxidation-state drift. Previous and subsequent experiments seemed to rule out drift, however, supporting the thought that this OCP drift is due to incomplete relaxation of concentration polarization across the membrane. Fig. 4.19 shows the efficiencies from the cycles shown in Fig. 4.18. Fig. 4.19 shows the continually decreasing voltaic efficiency of this system, suggesting a stable operating point was not reached.

Four Dreamweaver Silver 40 separators in series ("Dreamweaver 160")

The opposite approach was taken for the final separator replacement experiment; a very thick separator assembly was used, and intentionally operated at a low current density. Four sheets of Dreamweaver Silver 40 were stacked in series and used to replace the previous separator, and a current density of 5 mA cm^{-2} was used. After cycle 45, when it was apparent the system was still suffering from the same fouling mechanism, a fluid mechanical fouling mitigation approach was trialed

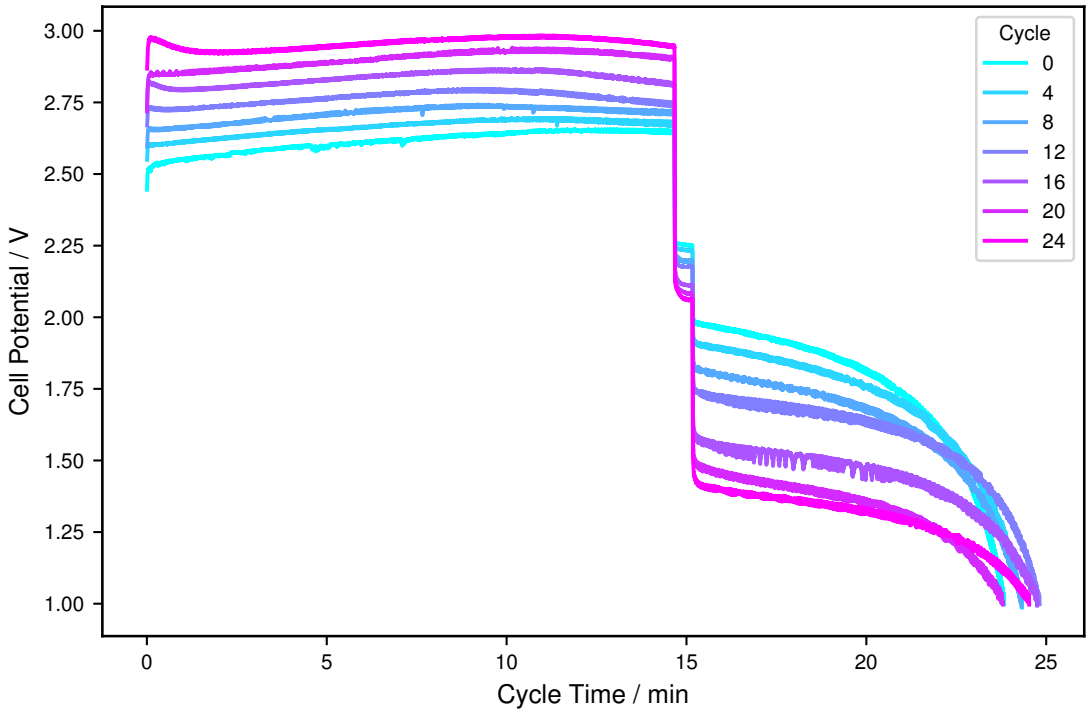


Figure 4.18: Charge/discharge profiles of 0.1 M $[Fe(bpy)_3]^{2+}(CF_3SO_3)_2$ in PC without supporting electrolyte, in same cell as Fig. 4.15 with new separator after initial cycles of Fig. 4.17. Dreamweaver Silver 20 cellulose separator, 40 mA cm^{-2} to 50% SOC, 30s OCP hold

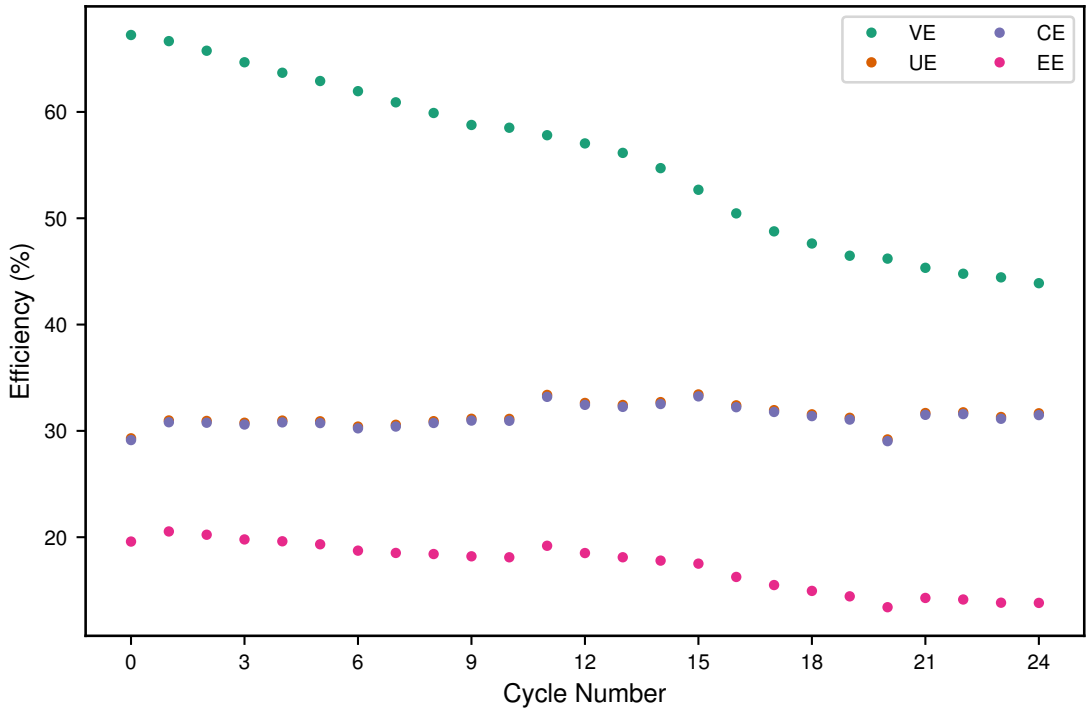


Figure 4.19: Charge/discharge efficiencies of Fig. 4.18

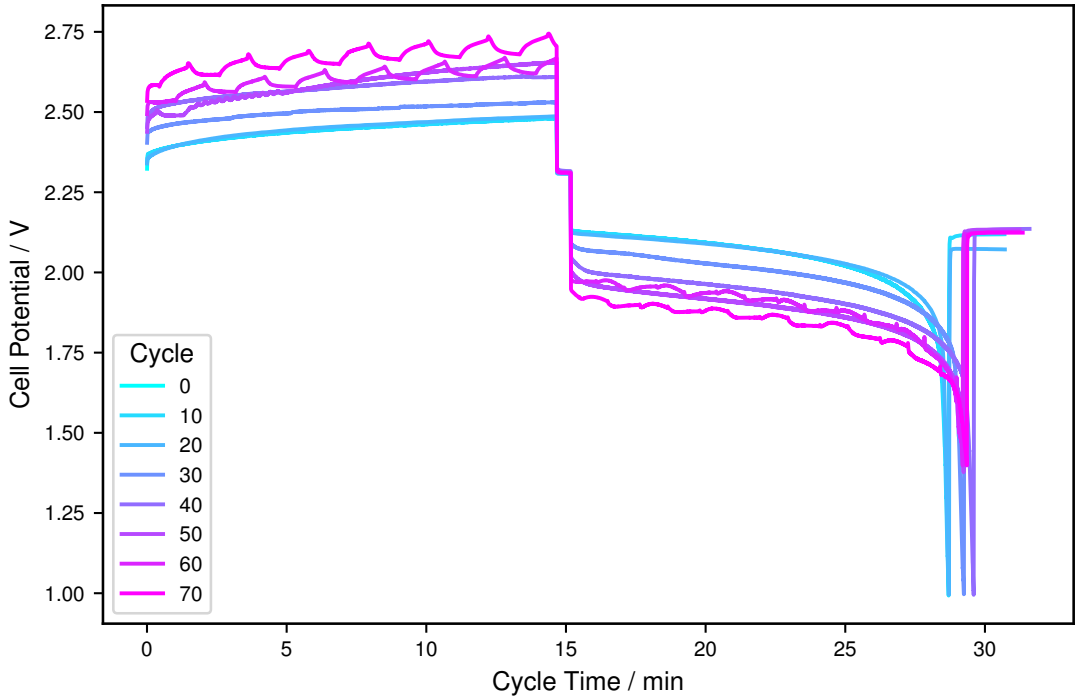


Figure 4.20: Charge/discharge profiles of 0.1 M $[Fe(bpy)_3]^{2+}(CF_3SO_3)_2$ in PC without supporting electrolyte, in same cell as Fig. 4.18 with new separator. 4 pieces of Dreamweaver Silver 40 cellulose separator, 5 mA cm^{-2} to 25% SOC, 30s OCP hold

unsuccessfully. Flowrate was set to maximum on one half-cell and maintained at a low flowrate on one side for one minute, alternating between sides, in an attempt to generate the maximum possible transmembrane mechanical pressure to "wash off" any dynamic films that may have formed. Fig. 4.20 shows the charge/discharge profiles of this experiment.

Visible in Fig. 4.20 are the charge/discharge profiles after cycle 45 which were subjected to the alternating flowrate treatment. This produced some sawtooth waves superimposed on the regular charge/discharge profiles. Fig. 4.21 shows the efficiencies of the cycles shown in Fig. 4.20.

Apparent in Fig. 4.21, which otherwise shows normal fouling behavior, is the sudden discontinuity in efficiency trends around cycle 45 when "pressure washing" was attempted. Coulombic efficiency does decrease, but then climbs back up to near unity. Voltaic efficiency briefly recovers but continues on a downward trajectory at the same rate as before. Thus, this crude attempt at fouling mitigation did produce

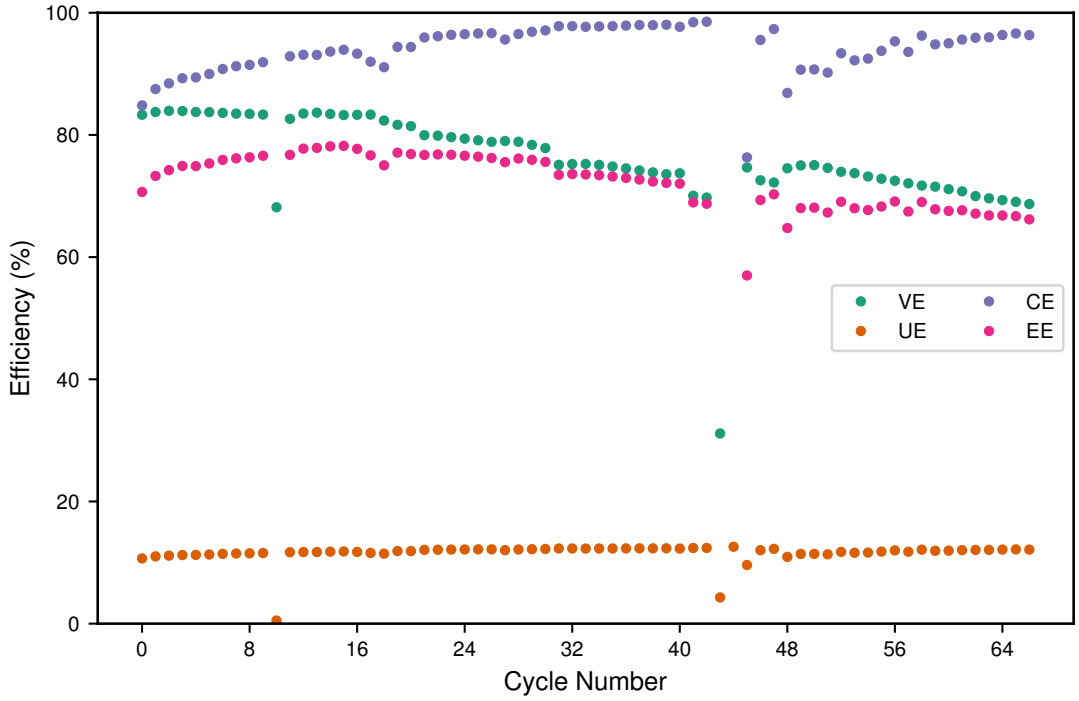


Figure 4.21: Charge/discharge efficiencies of Fig. 4.20

a measurable change, but was not able to rectify fouling completely.

4.6 Fouling Observations and Discussion

After disassembly of a failed cell, separators can be visually examined. Even after rinsing failed separators with neat solvents, stirring and/or sonicating in solvent overnight, *etc.*, fouled separators continue to retain a color that is close to the color of the respective active species. Fig. 4.22 shows fouled Celgard 4560 separators after thorough attempts at cleaning.

The $V(acac)_3$-fouled separator retains the dark brown color of the $V(acac)_3$ species, while the $[Fe(bpy)_3]^{2+}(CF_3SO_3)_2$-fouled separator retains the red-purple color of that system. This is not simple "staining" from being in contact with colored electrolyte. Cells were assembled and uncharged electrolyte pumped through with no current passed, then disassembled. After rinsing with neat solvent, separators maintain their original white/off-white colors. Thus, it appears that a chemical or electrochemical reaction process has occurred to stain the membranes as shown in

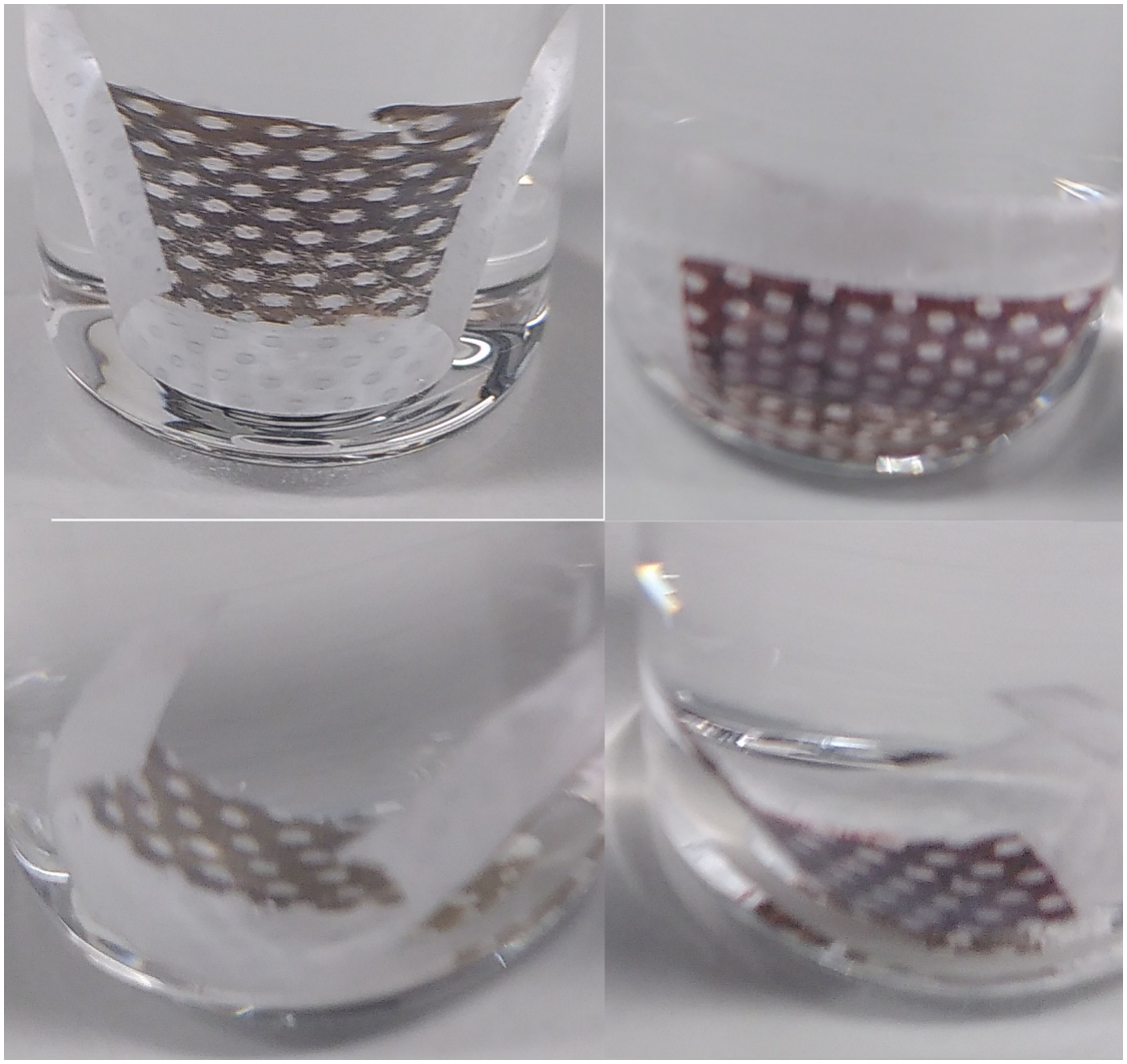


Figure 4.22: Fouled Celgard 4560 separators with adsorbed active species in their pores after stirring and sonicating in neat ACN. $V(acac)_3$ on left, $[Fe(bpy)_3]^{2+}(CF_3SO_3)_2$ on right

the figure. Indeed, cells could be assembled and pumps turned on while the cell rests discharged at open-circuit, and initial cycling performance seemed independent of the time spent at open-circuit after cell assembly. In other words, separator fouling does not occur before current is passed. This also suggests that fouling may be caused by a reaction involving a charged state of the active species.

4.7 Conclusion

This chapter sought to revisit the $[Fe(bpy)_3]^{2+}$ chemistry, a promising, more affordable active species for symmetric RFBs which does not require a supporting salt. Specifically, $[Fe(bpy)_3]^{2+}$ was revisited with the knowledge that current porous separators used for benchtop nonaqueous RFBs are susceptible to fouling, and that this can occur without irreversible degradation of the electrolyte or electrodes. This chapter showed that the $[Fe(bpy)_3]^{2+}$ compound cycles stably in ACN and PC, and that the transient performance decay witnessed is attributable to the fouling of the porous separator, identical to that experienced by $V(acac)_3$ systems. Replacement of fouled separators restored system performance, suggesting long-term stability of $[Fe(bpy)_3]^{2+}$.

$[Fe(bpy)_3]^{2+}(CF_3SO_3)_2$ may be an ideal candidate compound for further optimization and studies on nonaqueous symmetric RFBs with porous separators. The compound's current chemical composition, with two non-utilized bipyridine ligands and fluorinated anions, is however prohibitively expensive for the application of grid-scale energy storage. Encouragingly, coordination chemists are well-equipped to substitute cheaper ligands and counterions into the compound, while also optimizing for solubility, redox potential, and other properties. The proposition of a high-voltage, iron-based active species in a symmetric RFB with a fouling-resistant separator certainly motivates further study in this application.

5
Conclusion

This thesis attempted to further the understanding of symmetric nonaqueous flow batteries with porous separators. Various challenges were encountered initially, such as a lack of understanding of self-discharge behavior, uncontrolled reservoir imbalance, and questionable stability of various vanadium and iron-based active species. In Chapter 1, models were developed to understand self-discharge behavior and couple this to technoeconomic models to understand relevant trade-offs. In Chapter 2, a technique was developed to measure self-discharge in real-time, and a control system to maintain balanced reservoirs was successfully designed and built. This enhanced stability allowed for more long-term testing of $V(acac)_3$ chemistries in Chapter 3.

In Chapter 3, the effects of several factors on the transient performance decay of $V(acac)_3$ flow batteries were investigated. A set of double-reference-electrode cycling experiments was carried out and showed that the growth of the internal resistance within the system was confined to the porous separator. These results contrast those published in the literature by other research groups professing the fundamental instability of the $V(acac)_3$ species at the negative carbon-felt electrode interface. Experiments presented in Chapter 3 and Chapter 4 confirmed the strong effect of separator material on performance decay and longevity. Hydrophilic, or "so-

lutephobic" membranes like alumina and cellulose fared much better than polymeric separators made of polypropylene/polyethlene, PEEK, PTFE, nylon, and the like.

Chapter 4 sought to explore the cycling stability of $[Fe(bpy)_3]^{2+}$ compounds to create a "supporting-electrolyte free" flow-battery chemistry. $[Fe(bpy)_3]^{2+}(CF_3SO_3)_2$ was synthesized: its voltammetric behavior matched that of other $[Fe(bpy)_3]^{2+}$ compounds, and its solubilities in ACN and PC were sufficient to enable benchtop testing. With the reservoir balancing of Chapter 2 and the separator fouling knowledge of Chapter 3, cycling of the synthesized $[Fe(bpy)_3]^{2+}(CF_3SO_3)_2$ compound began. Cycling performance was similar to that of $V(acac)_3$, in that the compound appeared chemically stable, absent of oxidation-state drift, with transient performance decay confined to resistance growth within the separator as before. Long-term cycling experiments of $[Fe(bpy)_3]^{2+}(CF_3SO_3)_2$ were carried out by periodically replacing cellulose separators while keeping the used carbon felts and used electrolyte for the next experiment. This demonstrated chemical stability of $[Fe(bpy)_3]^{2+}$ in a nonaqueous flow battery, and contrasts with prior published literature by others that has professed instability of the bpy ligands in reduced $[Fe(bpy)_3]^{2+}$ electrolytes.

In these ways, understanding of nonaqueous symmetric flow batteries with porous separators seems to have been furthered. Benchtop flow-battery researchers now have a rudimentary model of self-discharge for porous separators and an accessible method for maintaining balanced reservoirs without any additional wetted components. If appropriate purity of precursors is guaranteed, $V(acac)_3$ and $[Fe(bpy)_3]^{2+}$ and the porous carbon electrodes which facilitate their heterogeneous reactions appear to be stable across several hundreds of cycles, on the timescales of several days and multiple weeks of cumulative time, in contradiction with existing literature. The porous separators used here, however, do not appear stable on this same timescale. Ironically, they were initially used in nonaqueous flow battery research due to their professed chemical stability in harsh nonaqueous electrolyte solutions. Indeed, they appear stable in the discharged, flux-free conditions in electrolytes, but the passage of current may expose their interior surface area to concentrations of solutes which, possibly due to capillary-induced phase separation, slowly chemisorb on pore

walls, gradually restricting pore diameters and closing up the separator, increasing coulombic and decreasing voltaic efficiency.

As such, there is both hope for the future of nonaqueous flow battery development and a large amount of future work remaining to gain sufficient understanding to enable a symmetric chemistry. Following are some thoughts and suggestions on how future research could proceed.

No IEMs were used in this thesis. Perhaps they are immune to this fouling mechanism. If they are, their cost/performance relationship will justify whether or not they are an appropriate substitute for porous separators.

The author believes there is insufficient interaction between the membrane fouling community and the nonaqueous redox-flow-battery community, which uses porous separators that are ultimately products of the research of the membrane-science community. There are myriad approaches to mitigate reversible and irreversible membrane fouling in various membrane processes. One or more of them can hopefully solve this issue for nonaqueous flow batteries. Promisingly, redox flow batteries are closed systems with respect to mass; membranes here are not subject to a continuous process stream which constantly introduces new foulants.

If membrane fouling could be mitigated in these systems, there does not appear to be another obvious degradation mode present inhibiting truly uninterrupted, perpetual charge/discharge cycling—though one may certainly appear on a longer timescale. The wide electrochemical stability windows of these nonaqueous solvents and chemical stability of active species at all charge states means there is no detectable oxidation-state drift—an issue well-known in the aqueous flow battery domain.

Additionally, the $[Fe(bpy)_3]^{2+}$ compound seems to hold significant promise. It offers an open-circuit voltage of 2.4 V and allows for operation without a supporting salt, conventionally the most expensive electrolyte component in nonaqueous flow batteries. Presently, the anions investigated for $[Fe(bpy)_3]^{2+}$ compounds are mostly fluorinated ones, and thus expensive. Crude attempts at using non-fluorinated anions in Chapter 4 of this thesis were unsuccessful, but the author is far from a synthetic chemist and others with more knowledge or skill can certainly succeed.

Perchlorate appears as an immediately obvious candidate for a nonaqueous-soluble, electrochemically stable, affordable anion to be paired with $[Fe(bpy)_3]^{2+}$ for this application. Indeed, the perchlorate salt was the one used by Ward in his 1958 thesis and by many others in subsequent years. Perchlorate salts fell out of favor over time due to their sometimes unstable, explosive nature, and their use was often substituted for fluorinated anions. Research groups with wash-down fumehoods capable of doing safe perchlorate work should explore the solubility of these compounds and test their actual safety properties. It is possible that the ligated iron perchlorates could be reasonably stable for the present application, and are likely even more stable in solution.

Nonaqueous all-liquid iron flow batteries which use the Fe^{2+}/Fe^{3+} couple with a ligand reduction process may actually be a viable energy-storage technology, especially if they can be constructed from affordable, sustainable components. Carbon felt and porous separators, especially cellulosic ones, may be fabricated from a variety of carbonaceous starting materials. The facile kinetics of nonaqueous chemistries may allow for less carbon felt to be used per unit area compared to aqueous systems, possibly decreasing areal reactor cost. Importantly, the iron kinetics witnessed here seem to obviate the need for catalytic treatments or actual catalysts or elevated-temperature operation. The avoidance of plating/stripping enables a true all-liquid flow battery without morphology constraints. Nonaqueous electrolytes may eliminate need for SOC remediation. Pumps, tanks, pipes, and other relevant process equipment already exist at scale. The $[Fe(bpy)_3]^{2+}$ cation is not composed of anything particularly exotic or expensive—only iron, carbon, nitrogen and hydrogen. Ligand modifications may allow for cheaper and more soluble chemistries. Surely coordinated research efforts could provide an affordable, sustainable counterion for the $[Fe(bpy)_3]^{2+}$ cation or variants thereof. Fouling must still be mitigated, however, and swapping from aqueous system to nonaqueous does have safety considerations with a now-flammable electrolyte, though these appear manageable from a chemical-engineering perspective. There appears to still be promise for nonaqueous symmetric flow batteries, but many research tasks remain.

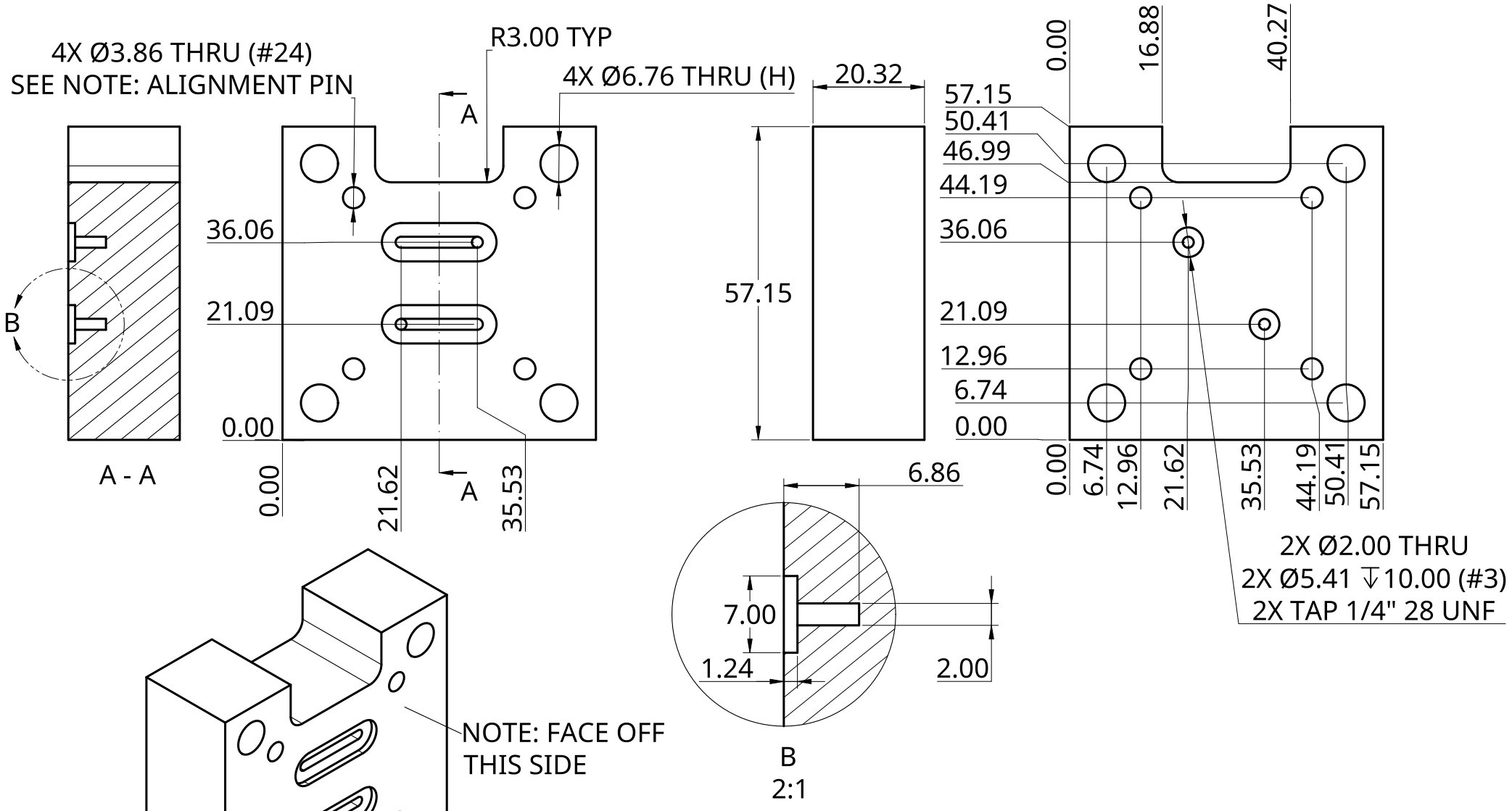
Appendices

A

Flow Cell and Hermetically Sealed Reservoir Drawings

The first two drawings attached here are of the flow cell and current collector used in this thesis. Design is primarily from the thesis of Milshtein [27], while the actual flow-through electrochemical cell with compressible PTFE gaskets and carbon felt electrodes was from the thesis of Saraidaridis [91].

The latter two drawings are for a hermetically sealed reservoir made from polypropylene rod. This reservoir was designed to be sealed with a 20 kHz ultrasonic horn welder. The reservoirs were successfully fabricated and leak-free but only used for one experiment presented in this thesis. They are included here for completeness and possible extension by others.



		NAME	SIGNATURE	DATE
	DRAWN	KIRK SMITH		2018-12-12
	CHECKED			
	APPROVED			
DO NOT SCALE DRAWING				

MATERIAL	FINISH
POLYPROPYLENE	

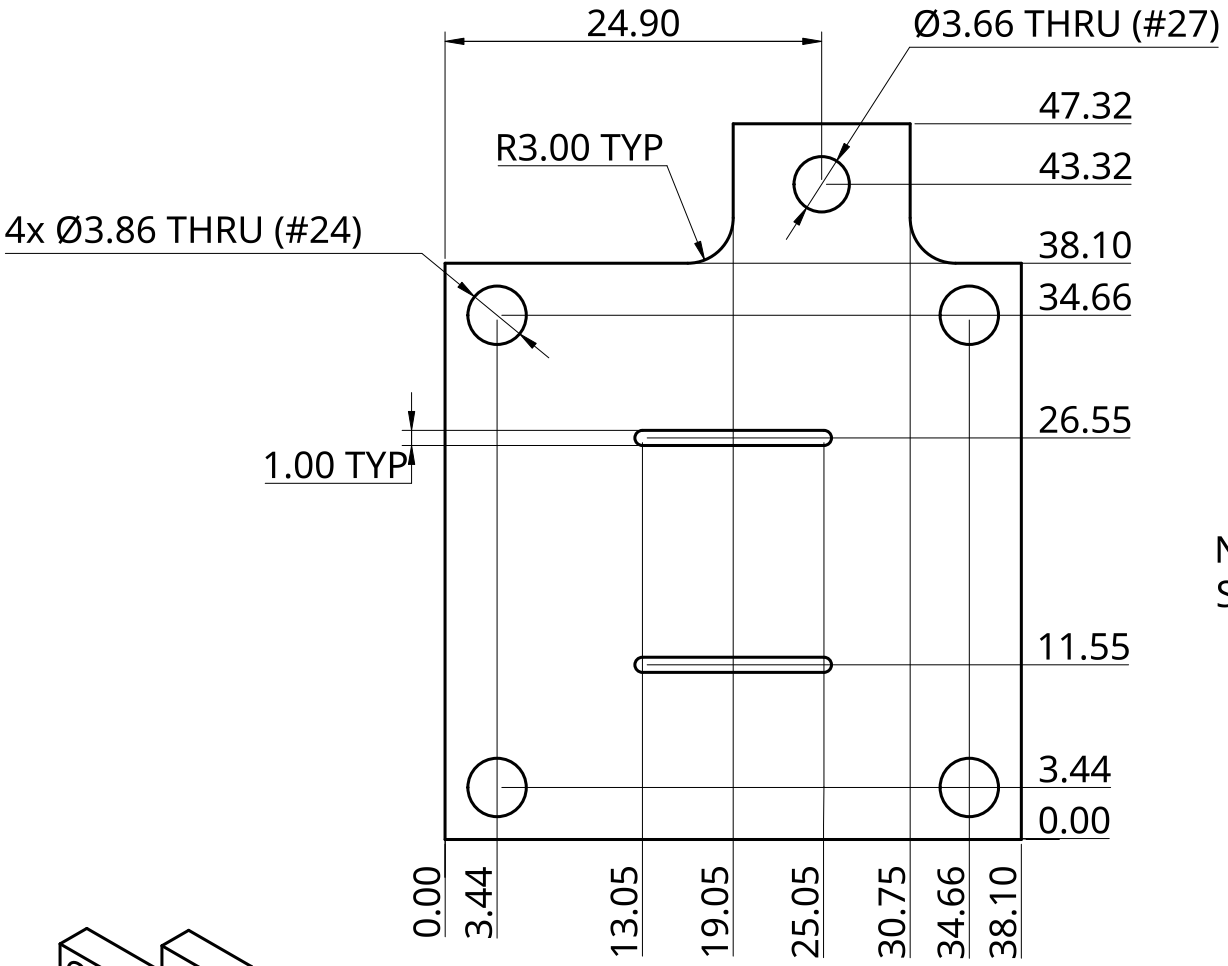
DIFFUSER

TITLE

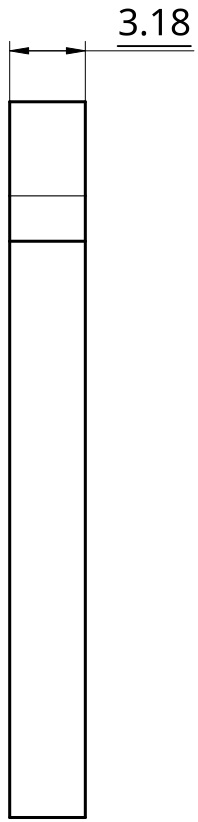
KIRK.SMITH@ENG.OX.AC.UK

SIZE	DWG NO.	REV.
A4		

SCALE	WEIGHT	SHEET
1:1		1 of 1

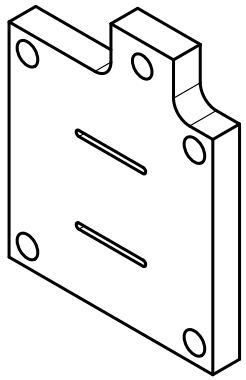


2:1



2:1

NOTE: FACE OFF BOTH SIDES FROM STOCK

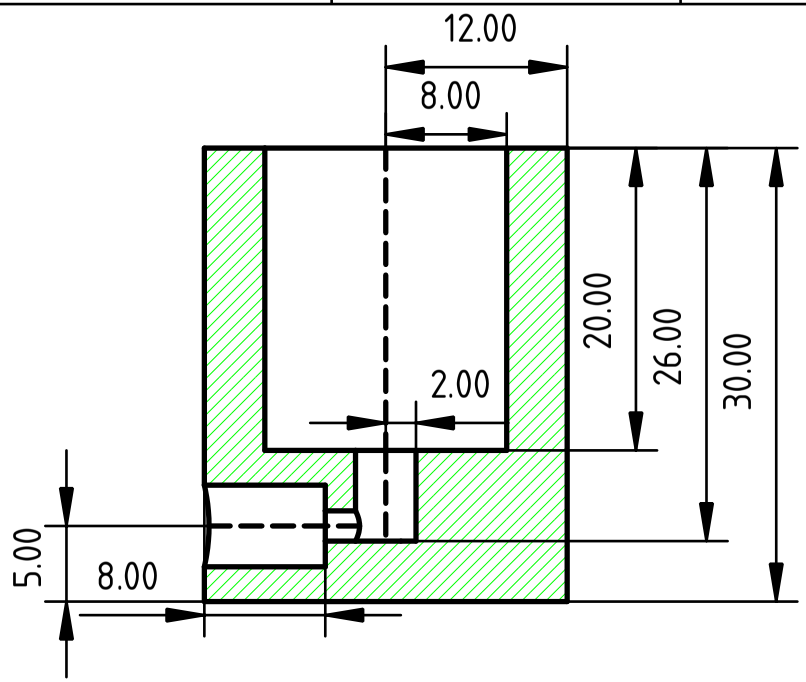


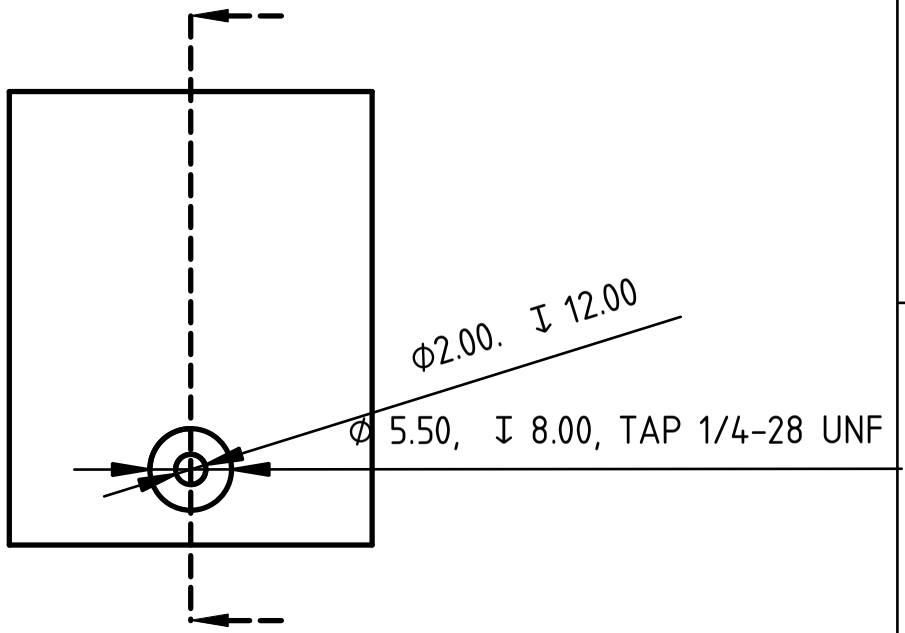
1:1

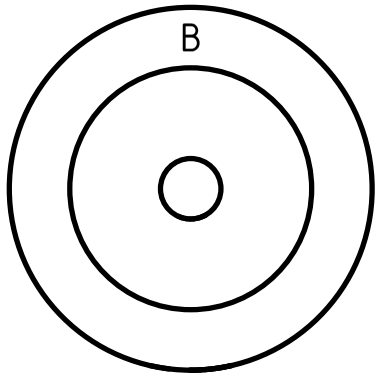
UNLESS OTHERWISE SPECIFIED, DIMENSIONS ARE IN MILLIMETERS		NAME	SIGNATURE	DATE
	DRAWN	KIRK SMITH		April 2021
	CHECKED			
	APPROVED			
DO NOT SCALE DRAWING				

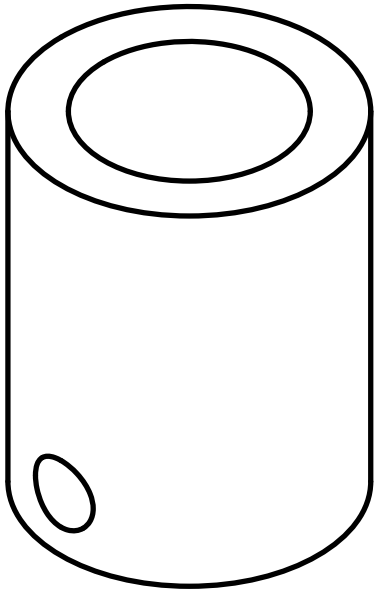
MATERIAL	FINISH
Aluminium 1050 /resin-impregnated graphite	

TITLE	CURRENT COLLECTOR		
SIZE A4	DWG NO.		REV.
SCALE 2:1	WEIGHT	SHEET 1 of 1	



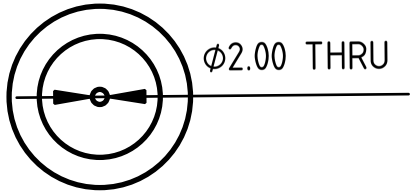


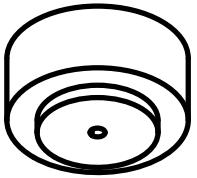


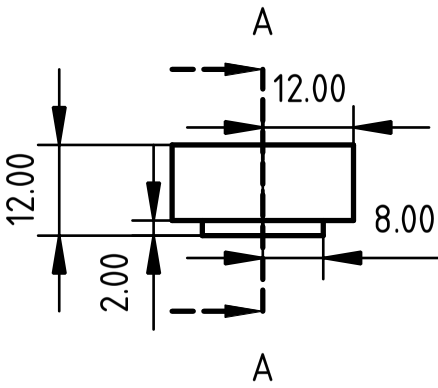


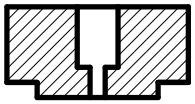
DESIGNED BY:		2 PORT VIAL - LOWER	
DATE:		ALL DIMENSIONS IN MM	
SIZE A4			
SCALE 2:1	WEIGHT (kg)	DRAWING NUMBER KIRK.SMITH@ENG.OX.AC.UK	SHEET

This drawing is our property; it can't be reproduced or communicated without our written consent.

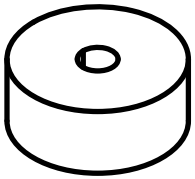


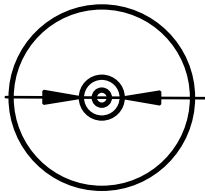






8.00 NOTE: REDUCE AS NECESSARY FOR MANUAL PRESS FIT WITH LOWER PART





DESIGNED BY:		2 PORT VIAL - UPPER	
DATE:		ALL DIMENSIONS IN MM	
SIZE A4			
SCALE 2:1	WEIGHT (kg)	DRAWING NUMBER KIRK.SMITH@ENG.OX.AC.UK	SHEET

This drawing is our property; it can't be reproduced or communicated without our written consent.

B

Publications and Presentations Given

This thesis resulted in multiple articles and presentations. They are listed here:

1. K. P. Smith, D. A. Howey, P. Ascencio, and C. W. Monroe, "Real-Time Reservoir Balancing and Leak-Free Nonaqueous Cell Design for Flow Batteries," *ECS Meeting Abstracts*, vol. MA2019-01, no. 3, pp. 455–455, May 2019, doi: 10.1149/ma2019-01/3/455.

2. K. P. Smith, P. Ascencio, D. A. Howey, and C. W. Monroe, "Online Characterization of Porous Separators for Disproportionation Redox Flow Batteries," *ECS Meeting Abstracts*, vol. MA2019-04, no. 4, p. 182, Jun. 2019, doi: 10.1149/MA2019-04/4/182.

3. P. Ascencio, K. Smith, C. W. Monroe, and D. Howey, "Adaptive Observer for Charge-State and Crossover Estimation in Disproportionation Redox Flow Batteries undergoing Self-Discharge," in *2019 American Control Conference (ACC)*, Jul. 2019, pp. 5452–5457. doi: 10.23919/ACC.2019.8814764.

4. P. Ascencio, K. Smith, D. Howey, and C. W. Monroe, "Augmented State Observer for Simultaneous Estimation of Charge State and Crossover in Self-Discharging Disproportionation Redox Flow Batteries," in *2019 IEEE*

Conference on Control Technology and Applications (CCTA), Aug. 2019, pp. 481–486. doi: 10.1109/CCTA.2019.8920467

5. K. P. Smith and C. W. Monroe, "Image-Based Mechanical Balancing of Reservoir Volumes During Benchtop Flow Battery Operation," *Frontiers in Chemical Engineering*, vol. 3, p. 56, 2021, doi: 10.3389/fceng.2021.748865.

References

[1] Jens Noack, Nataliya Roznyatovskaya, Tatjana Herr, and Peter Fischer. "The Chemistry of Redox-Flow Batteries". In: *Angewandte Chemie - International Edition* 54.34 (2015), pp. 9776–9809. DOI: 10.1002/anie.201410823.

[2] Xiao-Zi Yuan, Chaojie Song, Alison Platt, Nana Zhao, Haijiang Wang, Hui Li, Khalid Fatih, and Darren Jang. "A review of all-vanadium redox flow battery durability: Degradation mechanisms and mitigation strategies". en. In: *International Journal of Energy Research* 43.13 (2019), pp. 6599–6638. DOI: 10.1002/er.4607.

[3] Robert M. Darling, Kevin G. Gallagher, Jeffrey A. Kowalski, Seungbum Ha, and Fikile R. Brushett. "Pathways to low-cost electrochemical energy storage: a comparison of aqueous and nonaqueous flow batteries". In: *Energy Environ. Sci.* 7.11 (2014), pp. 3459–3477. DOI: 10.1039/C4EE02158D.

[4] John Newman. *Electrochemical Systems*. en. 2004.

[5] Mani Ulaganathan, Vanchiappan Aravindan, Qingyu Yan, Srinivasan Madhavi, Maria Skyllas-Kazacos, and Tuti Mariana Lim. "Recent Advancements in All-Vanadium Redox Flow Batteries". en. In: *Advanced Materials Interfaces* 3.1 (Jan. 2016), p. 1500309. DOI: 10.1002/admi.201500309.

[6] Piergiorgio Alotto, Massimo Guarnieri, and Federico Moro. "Redox flow batteries for the storage of renewable energy: A review". en. In: *Renewable and Sustainable Energy Reviews* 29 (Jan. 2014), pp. 325–335. DOI: 10.1016/j.rser.2013.08.001.

[7] Ruijie Ye, Dirk Henkensmeier, Sang Jun Yoon, Zhifeng Huang, Dong Kyu Kim, Zhenjun Chang, Sangwon Kim, and Ruiyong Chen. "Redox Flow Batteries for Energy Storage: A Technology Review". en. In: *Journal of Electrochemical Energy Conversion and Storage* 15.1 (Sept. 2017), p. 010801. DOI: 10.1115/1.4037248.

[8] Yu Ding, Changkun Zhang, Leyuan Zhang, Yangen Zhou, and Guihua Yu. "Molecular engineering of organic electroactive materials for redox flow batteries". In: *Chemical Society Reviews* 47.1 (2018), pp. 69–103. DOI: 10.1039/c7cs00569e.

[9] P. Leung, A. A. Shah, L. Sanz, C. Flox, J. R. Morante, Q. Xu, M. R. Mohamed, C. Ponce de León, and F. C. Walsh. "Recent developments in organic redox flow batteries: A critical review". en. In: *Journal of Power Sources* 360 (Aug. 2017), pp. 243–283. DOI: 10.1016/j.jpowsour.2017.05.057.

[10] Bin Li and Jun Liu. "Progress and directions in low-cost redox-flow batteries for large-scale energy storage". In: *National Science Review* 4.1 (2017), pp. 91–105. DOI: 10.1093/nsr/nww098.

[11] Feng Pan and Qing Wang. "Redox Species of Redox Flow Batteries: A Review". en. In: *Molecules* 20.11 (Nov. 2015), pp. 20499–20517. DOI: 10.3390/molecules201119711.

[12] Minjoon Park, Jaechan Ryu, Wei Wang, and Jaephil Cho. "Material design and engineering of next-generation flow-battery technologies". In: *Nature Reviews Materials* 2.1 (2016), p. 16080. DOI: 10.1038/natrevmats.2016.80.

[13] Sung-hee Shin, Sung-hyun Yun, and Seung-hyeon Moon. "RSC Advances A review of current developments in non-aqueous redox flow batteries : characterization of their". In: (2013), pp. 9095–9116. DOI: 10.1039/c3ra00115f.

[14] Grigorii L. Soloveichik. "Flow Batteries: Current Status and Trends". en. In: *Chemical Reviews* 115.20 (Oct. 2015), pp. 11533–11558. DOI: 10.1021/cr500720t.

[15] Adam Z. Weber, Matthew M. Mench, Jeremy P. Meyers, Philip N. Ross, Jeffrey T. Gostick, and Qinghua Liu. "Redox flow batteries: a review". en. In: *Journal of Applied Electrochemistry* 41.10 (Sept. 2011), p. 1137. DOI: 10.1007/s10800-011-0348-2.

[16] L. F. Arenas, C. Ponce de León, and F. C. Walsh. "Engineering aspects of the design, construction and performance of modular redox flow batteries for energy storage". In: *Journal of Energy Storage* 11 (2017), pp. 119–153. DOI: 10.1016/j.est.2017.02.007.

[17] William A. Braff, Martin Z. Bazant, and Cullen R. Buie. "Membrane-less hydrogen bromine flow battery". en. In: *Nature Communications* 4 (Aug. 2013), p. 2346. DOI: 10.1038/ncomms3346.

[18] Korey Cook, Ethan Lau, Jordan Thayer, Shane Mann, Tom Guarr, and Andre Benard. "Development of a Membraneless Organic Redox Flow Battery". en. In: *Volume 6A: Energy*. Pittsburgh, Pennsylvania, USA: American Society of Mechanical Engineers, Nov. 2018, V06AT08A029. DOI: 10.1115/IMECE2018-88024.

[19] Rosaria Ferrigno, Abraham D. Stroock, Thomas D. Clark, Michael Mayer, and George M. Whitesides. "Membraneless Vanadium Redox Fuel Cell Using Laminar Flow". In: *Journal of the American Chemical Society* 124.44 (Nov. 2002), pp. 12930–12931. DOI: 10.1021/ja020812q.

[20] Victor Gold, ed. *The IUPAC Compendium of Chemical Terminology: The Gold Book*. en. 4th ed. Research Triangle Park, NC: International Union of Pure and Applied Chemistry (IUPAC), 2019. DOI: 10.1351/goldbook.

[21] Sean E. Doris, Ashleigh L. Ward, Artem Baskin, Peter D. Frischmann, Nagarjuna Gavvalapalli, Etienne Chénard, Christo S. Sevov, David Prendergast, Jeffrey S. Moore, and Brett A. Helms. "Macromolecular Design Strategies for Preventing Active-Material Crossover in Non-Aqueous All-Organic Redox-Flow Batteries". en. In: *Angewandte Chemie International Edition* 56.6 (2017), pp. 1595–1599. DOI: 10.1002/anie.201610582.

[22] L. W. Hruska and R. F. Savinell. "Investigation of Factors Affecting Performance of the Iron-Redox Battery". en. In: *Journal of The Electrochemical Society* 128.1 (Jan. 1981), p. 18. DOI: 10.1149/1.2127366.

[23] H. S. Lim, A. M. Lackner, and R. C. Knechtli. "Zinc-Bromine Secondary Battery". en. In: *Journal of The Electrochemical Society* 124.8 (Aug. 1977), p. 1154. DOI: 10.1149/1.2133517.

[24] Ahmed Hazza, Derek Pletcher, and Richard Wills. "A novel flow battery: A lead acid battery based on an electrolyte with soluble lead(ii) Part I. Preliminary studies". en. In: *Physical Chemistry Chemical Physics* 6.8 (2004), pp. 1773–1778. DOI: 10.1039/B401115E.

[25] Rylan Dmello, Jarrod D. Milshtein, Fikile R. Brushett, and Kyle C. Smith. "Cost-driven materials selection criteria for redox flow battery electrolytes". en. In: *Journal of Power Sources* 330 (Oct. 2016), pp. 261–272. DOI: 10.1016/j.jpowsour.2016.08.129.

[26] Sydney M. Laramie, Jarrod D. Milshtein, Tanya M. Breault, Fikile R. Brushett, and Levi T. Thompson. "Performance and cost characteristics of multi-electron transfer, common ion exchange non-aqueous redox flow batteries". In: *Journal of Power Sources* 327 (Sept. 2016), pp. 681–692. DOI: 10.1016/j.jpowsour.2016.07.015.

[27] Jarrod David Milshtein. "Electrochemical engineering of low-cost and high-power redox flow batteries". PhD thesis. Massachusetts Institute of Technology, 2017.

[28] Shaurjo Biswas, Aoi Senju, Robert Mohr, Thomas Hodson, Nivetha Karthikeyan, Kevin W. Knehr, Andrew G. Hsieh, Xiaofang Yang, Bruce E. Koel, and Daniel A. Steingart. "Minimal architecture zinc–bromine battery for low cost electrochemical energy storage". en. In: *Energy & Environmental Science* 10.1 (Jan. 2017), pp. 114–120. DOI: 10.1039/C6EE02782B.

[29] Paul Albertus, Joseph S. Manser, and Scott Litzelman. "Long-Duration Electricity Storage Applications, Economics, and Technologies". en. In: *Joule* 4.1 (Jan. 2020), pp. 21–32. DOI: 10.1016/j.joule.2019.11.009.

[30] Feng Pan, Jing Yang, Qizhao Huang, Xingzhu Wang, Hui Huang, and Qing Wang. "Redox Targeting of Anatase TiO2 for Redox Flow Lithium-Ion Batteries". en. In: *Advanced Energy Materials* 4.15 (Oct. 2014), p. 1400567. DOI: 10.1002/aenm.201400567.

[31] Curt M. Wong and Christo S. Sevov. "All-Organic Storage Solids and Redox Shuttles for Redox-Targeting Flow Batteries". In: *ACS Energy Letters* (Mar. 2021), pp. 1271–1279. DOI: 10.1021/acsenergylett.1c00143.

[32] Elena Zanzola. "Aqueous Redox Flow Batteries Enhanced by Solid Boosters". en. PhD thesis. EPFL, June 2020.

[33] Hongzhang Zhang, Huamin Zhang, Xianfeng Li, Zhensheng Mai, and Jianlu Zhang. "Nanofiltration (NF) membranes: the next generation separators for all vanadium redox flow batteries (VRBs)?" en. In: *Energy & Environmental Science* 4.5 (2011), pp. 1676–1679. DOI: 10.1039/C1EE01117K.

[34] Pablo J. Cabrera, Xingyi Yang, James A. Suttil, Krista L. Hawthorne, Rachel E. M. Brooner, Melanie S. Sanford, and Levi T. Thompson. "Complexes Containing Redox Noninnocent Ligands for Symmetric, Multielectron Transfer Nonaqueous Redox Flow Batteries". In: *The Journal of Physical Chemistry C* 119.28 (July 2015), pp. 15882–15889. DOI: 10.1021/acs.jpcc.5b03582.

[35] Mike L. Perry, James D. Saraidaridis, and Robert M. Darling. "Crossover mitigation strategies for redox-flow batteries". en. In: *Current Opinion in Electrochemistry* 21 (June 2020), pp. 311–318. DOI: 10.1016/j.coelec.2020.03.024.

[36] Robert M. Darling and Mike L. Perry. "Half-Cell, Steady-State Flow-Battery Experiments". en. In: *ECS Transactions* 53.7 (May 2013), pp. 31–38. DOI: 10.1149/05307.0031ecst.

[37] Chanyong Choi, Hyungjun Noh, Soohyun Kim, Riyul Kim, Juhyuk Lee, Jiyun Heo, and Hee-Tak Kim. "Understanding the redox reaction mechanism of vanadium electrolytes in all-vanadium redox flow batteries". In: *Journal of Energy Storage* 21 (Feb. 2019), pp. 321–327. DOI: 10.1016/j.est.2018.11.002.

[38] Bin Li, Qingtao Luo, Xiaoliang Wei, Zimin Nie, Edwin Thomsen, Baowei Chen, Vincent Sprenkle, and Wei Wang. "Capacity Decay Mechanism of Microporous Separator-Based All-Vanadium Redox Flow Batteries and its Recovery". en. In: *ChemSusChem* 7.2 (Feb. 2014), pp. 577–584. DOI: 10.1002/cssc.201300706.

[39] Qingtao Luo, Liyu Li, Wei Wang, Zimin Nie, Xiaoliang Wei, Bin Li, Baowei Chen, Zhenguo Yang, and Vincent Sprenkle. "Capacity Decay and Remediation of Nafion-based All-Vanadium Redox Flow Batteries". en. In: *ChemSusChem* 6.2 (Feb. 2013), pp. 268–274. DOI: 10.1002/cssc.201200730.

[40] Kara E. Rodby, Thomas J. Carney, Yasser Ashraf Gandomi, John L. Barton, Robert M. Darling, and Fikile R. Brushett. "Assessing the levelized cost of vanadium redox flow batteries with capacity fade and rebalancing". en. In: *Journal of Power Sources* (Apr. 2020), p. 227958. DOI: 10.1016/j.jpowsour.2020.227958.

[41] Tino Hagemann, Jan Winsberg, Bernhard Häupler, Tobias Janoschka, Jeremy J. Gruber, Andreas Wild, and Ulrich S. Schubert. "A bipolar nitronyl nitroxide small molecule for an all-organic symmetric redox-flow battery". en. In: *NPG Asia Materials* 9.1 (Jan. 2017), e340–e340. DOI: 10.1038/am.2016.195.

[42] Rebecca A Potash, James R McKone, Sean Conte, and Héctor D Abruña. "On the benefits of a symmetric redox flow battery". In: *Journal of The Electrochemical Society* 163.3 (2015), A338.

[43] Yihan Zhen, Cuijuan Zhang, Jiashu Yuan, Yicheng Zhao, and Yongdan Li. "Ferrocene/anthraquinone based bi-redox molecule for symmetric nonaqueous redox flow battery". en. In: *Journal of Power Sources* 480 (Dec. 2020), p. 229132. DOI: 10.1016/j.jpowsour.2020.229132.

[44] Gabriel Sikukuu Nambafu. "Organic molecules as bifunctional electroactive materials for symmetric redox flow batteries: A mini review". en. In: *Electrochemistry Communications* 127 (June 2021), p. 107052. DOI: 10.1016/j.elecom.2021.107052.

[45] Harry D. Pratt, Nicholas S. Hudak, Xikui Fang, and Travis M. Anderson. "A polyoxometalate flow battery". en. In: *Journal of Power Sources* 236 (Aug. 2013), pp. 259–264. DOI: 10.1016/j.jpowsour.2013.02.056.

[46] Qinghua Liu, Alice E S Sleightholme, Aaron A. Shinkle, Yongdan Li, and Levi T. Thompson. "Non-aqueous vanadium acetylacetonate electrolyte for redox flow batteries". In: *Electrochemistry Communications* 11.12 (2009), pp. 2312–2315. DOI: 10.1016/j.elecom.2009.10.006.

[47] Qinghua Liu, Aaron A. Shinkle, Yongdan Li, Charles W. Monroe, Levi T. Thompson, and Alice E S Sleightholme. "Non-aqueous chromium acetylacetonate electrolyte for redox flow batteries". In: *Electrochemistry Communications* 12.11 (2010), pp. 1634–1637. DOI: 10.1016/j.elecom.2010.09.013.

[48] Alice E S Sleightholme, Aaron A. Shinkle, Qinghua Liu, Yongdan Li, Charles W. Monroe, and Levi T. Thompson. "Non-aqueous manganese acetylacetonate electrolyte for redox flow batteries". In: *Journal of Power Sources* 196.13 (2011), pp. 5742–5745. DOI: 10.1016/j.jpowsour.2011.02.020.

[49] Wentao Duan, Rama S. Vemuri, Jarrod D. Milshtein, Sydney Laramie, Rylan D. Dmello, Jinhua Huang, Lu Zhang, Dehong Hu, M. Vijayakumar, Wei Wang, Jun Liu, Robert M. Darling, Levi Thompson, Kyle Smith, Jeffery S. Moore, Fikile R. Brushett, and Xiaoliang Wei. "A symmetric organic-based nonaqueous redox flow battery and its state of charge diagnostics by FTIR". en. In: *Journal of Materials Chemistry A* 4.15 (2016), pp. 5448–5456. DOI: 10.1039/C6TA01177B.

[50] Rocco Peter Fornari, Murat Mesta, Johan Hjelm, Tejs Vegge, and Piotr de Silva. "Molecular engineering strategies for symmetric aqueous organic redox flow batteries". In: *ACS Materials Letters* 2.3 (2020), pp. 239–246.

[51] Gabriel Sikukuu Nambafu, Kumar Siddharth, Cheng Zhang, Tianshou Zhao, Qing Chen, Khalil Amine, and Minhua Shao. "An organic bifunctional redox active material for symmetric aqueous redox flow battery". en. In: *Nano Energy* 89 (Nov. 2021), p. 106422. DOI: 10.1016/j.nanoen.2021.106422.

[52] N. Harsha Attanayake, Zhiming Liang, Yilin Wang, Aman Preet Kaur, Sean R. Parkin, Justin K. Mobley, Randy H. Ewoldt, James Landon, and Susan A. Odom. "Dual Function Organic Active Materials for Nonaqueous Redox Flow Batteries". en. In: *Materials Advances* (2021), 10.1039.D0MA00881H. DOI: 10.1039/D0MA00881H.

[53] Pieter Geysens, Yun Li, Ivo F. J. Vankelecom, Jan Fransaer, and Koen Binnemans. "Highly soluble 1,4-diaminoanthraquinone derivative for non-aqueous symmetric redox flow batteries". In: *ACS Sustainable Chemistry & Engineering* (Feb. 2020). DOI: 10.1021/acssuschemeng.9b07244.

[54] James D. Saraidaridis, James A. Suttil, and Charles W. Monroe. "High-Voltage Metal-Free Disproportionation Flow Batteries Based on 9,10-diphenylanthracene". en. In: *Journal of The Electrochemical Society* 167.7 (Jan. 2020), p. 070517. DOI: 10.1149/1945-7111/ab6a8d.

[55] Craig G. Armstrong, Ross W. Hogue, and Kathryn E. Toghill. "Application of the dianion croconate violet for symmetric organic non-aqueous redox flow battery electrolytes". en. In: *Journal of Power Sources* 440 (Nov. 2019), p. 227037. DOI: 10.1016/j.jpowsour.2019.227037.

[56] Ting Ma, Zeng Pan, Licheng Miao, Chengcheng Chen, Mo Han, Zhenfeng Shang, and Jun Chen. "Porphyrin-Based Symmetric Redox-Flow Batteries towards Cold-Climate Energy Storage". en. In: *Angewandte Chemie* 130.12 (2018), pp. 3212–3216. DOI: 10.1002/ange.201713423.

[57] Craig G Armstrong. "Novel Non-Aqueous Symmetric Redox Materials for Redox Flow Battery Energy Storage". en. PhD thesis. Lancaster University, 2020.

[58] Csaba P. Keszthelyi, Hiroyasu Tachikawa, and Allen J. Bard. "Electrogenerated chemiluminescence. VIII. Thianthrene-2,5-diphenyl-1,3,4-oxadiazole system. Mixed energy-sufficient system". en. In: *Journal of the American Chemical Society* 94.5 (Mar. 1972), pp. 1522–1527. DOI: 10.1021/ja00760a014.

[59] Chinmaya Ramachandra, Raja Murugan, Vasudevarao Pasala, Sethuraman Sankararaman, and Kothandaraman Ramanujam. "Functionalised carbazole as cathode for high voltage non-aqueous organic redox flow battery". en. In: *New Journal of Chemistry* (July 2020). DOI: 10.1039/D0NJ02543G.

[60] Donghan Xu, Cuijuan Zhang, Yihan Zhen, Yicheng Zhao, and Yongdan Li. "A high-rate nonaqueous organic redox flow battery". en. In: *Journal of Power Sources* 495 (May 2021), p. 229819. DOI: 10.1016/j.jpowsour.2021.229819.

[61] Donghan Xu, Cuijuan Zhang, Yihan Zhen, and Yongdan Li. "Liquid Nitrobenzene-Based Anolyte Materials for High-Current and -Energy-Density Nonaqueous Redox Flow Batteries". In: *ACS Applied Materials & Interfaces* 13.30 (Aug. 2021), pp. 35579–35584. DOI: 10.1021/acsami.1c05564.

[62] Bo Yang, Advaith Murali, Archith Nirmalchandar, Buddhinie Jayathilake, G. K. Surya Prakash, and S. R. Narayanan. "A Durable, Inexpensive and Scalable Redox Flow Battery Based on Iron Sulfate and Anthraquinone Disulfonic Acid". en. In: *Journal of The Electrochemical Society* 167.6 (Apr. 2020), p. 060520. DOI: 10.1149/1945-7111/ab84f8.

[63] S. Selverston, R. F. Savinell, and J. S. Wainright. "Zinc-Iron Flow Batteries with Common Electrolyte". en. In: *Journal of The Electrochemical Society* 164.6 (2017), A1069–A1075. DOI: 10.1149/2.0591706jes.

[64] Zhipeng Xie, Qingchao Liu, Zhiwen Chang, and Xinbo Zhang. "The developments and challenges of cerium half-cell in zinc–cerium redox flow battery for energy storage". en. In: *Electrochimica Acta* 90 (Feb. 2013), pp. 695–704. DOI: 10.1016/j.electacta.2012.12.066.

[65] Venkat Pavan Nemani and Kyle C. Smith. "Analysis of Crossover-Induced Capacity Fade in Redox Flow Batteries with Non-Selective Separators". en. In: *Journal of The Electrochemical Society* 165.13 (Jan. 2018), A3144–A3155. DOI: 10.1149/2.0701813jes.

[66] Robert Darling, Kevin Gallagher, Wei Xie, Liang Su, and Fikile Brushett. "Transport Property Requirements for Flow Battery Separators". In: *Journal of The Electrochemical Society* 163.1 (2016), A5029–A5040. DOI: 10.1149/2.0051601jes.

[67] Ryan P. O'Hayre, Suk-Won Cha, Whitney G. Colella, and F. B. Prinz. *Fuel cell fundamentals*. en. Third edition. Hoboken, New Jersey: Wiley, 2016.

[68] Aaron A. Shinkle, Alice E. S. Sleightholme, Levi T. Thompson, and Charles W. Monroe. "Electrode kinetics in non-aqueous vanadium acetylacetonate redox flow batteries". en. In: *Journal of Applied Electrochemistry* 41.10 (Oct. 2011), pp. 1191–1199. DOI: 10.1007/s10800-011-0314-z.

[69] James D. Saraidaridis and Charles W. Monroe. "Nonaqueous vanadium disproportionation flow batteries with porous separators cycle stably and tolerate high current density". en. In: *Journal of Power Sources* 412 (Feb. 2019), pp. 384–390. DOI: 10.1016/j.jpowsour.2018.11.058.

[70] Patrick J. Cappillino, Harry D. Pratt, Nicholas S. Hudak, Neil C. Tomson, Travis M. Anderson, and Mitchell R. Anstey. "Application of Redox Non-Innocent Ligands to Non-Aqueous Flow Battery Electrolytes". In: *Advanced Energy Materials* 4.1 (2014), p. 1300566. DOI: 10.1002/aenm.201300566.

[71] Nicholas S. Hudak, Leo J. Small, Harry D. Pratt, and Travis M. Anderson. "Through-Plane Conductivities of Membranes for Nonaqueous Redox Flow Batteries". In: *Journal of The Electrochemical Society* 162.10 (2015), A2188–A2194. DOI: 10.1149/2.0901510jes.

[72] Ao Tang, Jie Bao, and Maria Skyllas-Kazacos. "Studies on pressure losses and flow rate optimization in vanadium redox flow battery". In: *Journal of Power Sources* 248 (2014). DOI: 10.1016/j.jpowsour.2013.09.071.

[73] John Newman, Paul G. Hoertz, Christopher A. Bonino, and James A. Trainham. "Review: An Economic Perspective on Liquid Solar Fuels". en. In: *Journal of The Electrochemical Society* 159.10 (Aug. 2012), A1722. DOI: 10.1149/2.046210jes.

[74] Piyasak Poonpun and Ward T. Jewell. "Analysis of the Cost per Kilowatt Hour to Store Electricity". In: *IEEE Transactions on Energy Conversion* 23.2 (June 2008), pp. 529–534. DOI: 10.1109/TEC.2007.914157.

[75] MARK Johnson. "Gridscale rampable intermittent dispatchable storage (grids) program". In: *DOE annual storage R&D review meeting*. 2010.

[76] *Duration Addition to electricitY Storage (DAYS) Overview*. May 2018.

[77] Vasudevarao Pasala and Kothandaraman Ramanujam. "On In–situ Redox Balancing of Vanadium Redox Flow Battery Using D-Fructose as Negative Electrolyte Additive". en. In: *ChemistrySelect* 2.2 (2017), pp. 720–727. DOI: https://doi.org/10.1002/slct.201601417.

[78] Ai Quoc Pham and On Kok Chang. "Systems and methods for rebalancing redox flow battery electrolytes". en. US8980454B2. Mar. 2015.

[79] S. Rudolph, U. Schröder, and I.M. Bayanov. "On-line controlled state of charge rebalancing in vanadium redox flow battery". en. In: *Journal of Electroanalytical Chemistry* 703 (Aug. 2013), pp. 29–37. DOI: 10.1016/j.jelechem.2013.05.011.

[80] Katharina Schafner, Maik Becker, and Thomas Turek. "Capacity balancing for vanadium redox flow batteries through continuous and dynamic electrolyte overflow". en. In: *Journal of Applied Electrochemistry* (May 2021). DOI: 10.1007/s10800-021-01572-y.

[81] S. Selverston, E. Nagelli, J. S. Wainright, and R. F. Savinell. "All-Iron Hybrid Flow Batteries with In-Tank Rebalancing". en. In: *Journal of The Electrochemical Society* 166.10 (Jan. 2019), A1725–A1731. DOI: 10.1149/2.0281910jes.

[82] Nestor A. Sepulveda, Jesse D. Jenkins, Aurora Edington, Dharik S. Mallapragada, and Richard K. Lester. "The design space for long-duration energy storage in decarbonized power systems". en. In: *Nature Energy* 6.5 (May 2021), pp. 506–516. DOI: 10.1038/s41560-021-00796-8.

[83] Pedro Ascencio, Kirk Smith, Charles W. Monroe, and David Howey. "Adaptive Observer for Charge-State and Crossover Estimation in Disproportionation Redox Flow Batteries undergoing Self-Discharge". In: *2019 American Control Conference (ACC)*. July 2019, pp. 5452–5457. DOI: 10.23919/ACC.2019.8814764.

[84] Arjun Bhattarai, Nyunt Wai, Rüdiger Schweiss, Adam Whitehead, Günther G. Scherer, Purna C. Ghimire, Tuti M. Lim, and Huey Hoon Hng. "Vanadium redox flow battery with slotted porous electrodes and automatic rebalancing demonstrated on a 1kW system level". In: *Applied Energy* 236 (Feb. 2019), pp. 437–443. DOI: 10.1016/j.apenergy.2018.12.001.

[85] Ke Wang, Le Liu, Jingyu Xi, Zenghua Wu, and Xinping Qiu. "Reduction of capacity decay in vanadium flow batteries by an electrolyte-reflow method". en. In: *Journal of Power Sources* 338 (Jan. 2017), pp. 17–25. DOI: 10.1016/j.jpowsour.2016.11.031.

[86] Ron MOSSO, Sumitha Durairaj, Jay SHA, and Jeremy MEYERS. "Pressure balancing of electrolytes in redox flow batteries". US20140057141A1. Feb. 2014.

[87] Ligen Yan, Dan Li, Shuaiqiang Li, Zhi Xu, Junhang Dong, Wenheng Jing, and Weihong Xing. "Balancing Osmotic Pressure of Electrolytes for Nanoporous Membrane Vanadium Redox Flow Battery with a Draw Solute". en. In: *ACS Applied Materials & Interfaces* 8.51 (Dec. 2016), pp. 35289–35297. DOI: 10.1021/acsami.6b12068.

[88] G. Bradski. "The OpenCV library". In: *Dr. Dobb's Journal of Software Tools* (2000).

[89] Jarrod D. Milshtein, John L. Barton, Robert M. Darling, and Fikile R. Brushett. "4-acetamido-2,2,6,6-tetramethylpiperidine-1-oxyl as a model organic redox active compound for nonaqueous flow batteries". en. In: *Journal of Power Sources* 327 (Sept. 2016), pp. 151–159. DOI: 10.1016/j.jpowsour.2016.06.125.

[90] Doron Aurbach. *Nonaqueous Electrochemistry*. English. 1999.

[91] James D. Saraidaridis. "Analysis and Performance of Symmetric Nonaqueous Redox Flow Batteries". DPhil. University of Oxford, 2017.

[92] Aaron A. Shinkle. "Non-Aqueous Single-Metal Redox Flow Batteries". PhD thesis. University of Michigan, 2013.

[93] Aaron A. Shinkle, Alice E S Sleightholme, Lucas D. Griffith, Levi T. Thompson, and Charles W. Monroe. "Degradation mechanisms in the non-aqueous vanadium acetylacetonate redox flow battery". In: *Journal of Power Sources* 206 (2012), pp. 490–496. DOI: 10.1016/j.jpowsour.2010.12.096.

[94] Christine Minke and Thomas Turek. "Materials, system designs and modelling approaches in techno-economic assessment of all-vanadium redox flow batteries – A review". en. In: *Journal of Power Sources* 376 (Feb. 2018), pp. 66–81. DOI: 10.1016/j.jpowsour.2017.11.058.

[95] Aaron A. Shinkle, Timothy J. Pomaville, Alice E S Sleightholme, Levi T. Thompson, and Charles W. Monroe. "Solvents and supporting electrolytes for vanadium acetylacetonate flow batteries". In: *Journal of Power Sources* 248.January 2015 (2014), pp. 1299–1305. DOI: 10.1016/j.jpowsour.2013.10.034.

[96] A. Ben-Naim. "Preferential solvation in two- and in three-component systems". en. In: *Pure and Applied Chemistry* 62.1 (Jan. 1990), pp. 25–34. DOI: 10.1351/pac199062010025.

[97] Gayani N. Pallewela and Paul E. Smith. "Preferential Solvation in Binary and Ternary Mixtures". en. In: *The Journal of Physical Chemistry B* 119.51 (Dec. 2015), pp. 15706–15717. DOI: 10.1021/acs.jpcb.5b10139.

[98] T. Herr, P. Fischer, J. Tübke, K. Pinkwart, and P. Elsner. "Increasing the energy density of the non-aqueous vanadium redox flow battery with the acetonitrile-1,3-dioxolane–dimethyl sulfoxide solvent mixture". In: *Journal of Power Sources* 265 (Nov. 2014), pp. 317–324. DOI: 10.1016/j.jpowsour.2014.04.141.

[99] Musbaudeen O. Bamgbopa, Nir Pour, Yang Shao-Horn, and Saif Almheiri. "Systematic selection of solvent mixtures for non-aqueous redox flow batteries – vanadium acetylacetonate as a model system". In: *Electrochimica Acta* 223 (2017), pp. 115–123. DOI: 10.1016/j.electacta.2016.12.014.

[100] T. Herr, J. Noack, P. Fischer, and J. Tübke. "1,3-Dioxolane, tetrahydrofuran, acetylacetone and dimethyl sulfoxide as solvents for non-aqueous vanadium acetylacetonate redox-flow-batteries". In: *Electrochimica Acta* 113 (Dec. 2013), pp. 127–133. DOI: 10.1016/j.electacta.2013.09.055.

[101] Kōsuke Izutsu. *Electrochemistry in nonaqueous solutions*. en. 2nd., rev. and enlarged ed. Weinheim: Wiley-VCH, 2009.

[102] Charlotte Clegg and Ian G. Hill. "Characterizing Degradation in Non-aqueous Vanadium(III) Acetylacetonate Redox Flow Batteries". en. In: *Journal of The Electrochemical Society* 167.12 (Aug. 2020), p. 120510. DOI: 10.1149/1945-7111/aba932.

[103] Craig G. Armstrong, Ross W. Hogue, and Kathryn E. Toghill. "Characterisation of the ferrocene/ferrocenium ion redox couple as a model chemistry for non-aqueous redox flow battery research". en. In: *Journal of Electroanalytical Chemistry*. Dr. Richard Compton 65th birthday Special issue 872 (Sept. 2020), p. 114241. DOI: 10.1016/j.jelechem.2020.114241.

[104] I. L. Escalante-Garcia, J. S. Wainright, L. T. Thompson, and R. F. Savinell. "Performance of a Non-Aqueous Vanadium Acetylacetonate Prototype Redox Flow Battery: Examination of Separators and Capacity Decay". In: *Journal of the Electrochemical Society* 162.3 (2014), A363–A372. DOI: 10.1149/2.0471503jes.

[105] P.W. Ruch, M. Hahn, F. Rosciano, M. Holzapfel, H. Kaiser, W. Scheifele, B. Schmitt, P. Novák, R. Kötz, and A. Wokaun. "In situ X-ray diffraction of the intercalation of (C2H5)4N+ and BF4 into graphite from acetonitrile and propylene carbonate based supercapacitor electrolytes". en. In: *Electrochimica Acta* 53.3 (Dec. 2007), pp. 1074–1082. DOI: 10.1016/j.electacta.2007.01.069.

[106] Mark D. Imisides, Richard John, Peter J. Riley, and Gordon G. Wallace. "The use of electropolymerization to produce new sensing surfaces: A review emphasizing electrode position of heteroaromatic compounds". en. In: *Electroanalysis* 3.9 (1991), pp. 879–889. DOI: https://doi.org/10.1002/elan.1140030903.

[107] Gerard Tourillon, Pierre-Camille Lacaze, and Jacques-Emile Dubois. "Electrochemical formation of thin polyacetonitrile films on a Pt surface: Pmt, ir, xps and sims analyses and study of formation mechanism". In: *Journal of Electroanalytical Chemistry and Interfacial Electrochemistry* 100.1-2 (1979), pp. 247–262.

[108] Yinlin Ma, Damien Reardon, Sandro Gambarotta, Glenn Yap, Hayder Zahalka, and Catherine Lemay. "Vanadium-Catalyzed EthylenePropylene Copolymerization: The Question of the Metal Oxidation State in ZieglerNatta Polymerization Promoted by (-diketonate) $_3$ V". en. In: *Organometallics* 18.15 (July 1999), pp. 2773–2781. DOI: 10.1021/om9808763.

[109] J Brennan. "Oligomerization of olefins with boron trifluoride". 3,769,363. 1973.

[110] Gino Bontempelli, Renato Seeber, Sandro Zecchin, and Gilberto Schiavon. "Electroanalytical evidences for the instability of hydrogen tetrafluoroborate in acetonitrile". In: *Journal of Electroanalytical Chemistry and Interfacial Electrochemistry* 73.3 (1976), pp. 295–302.

[111] Mara G. Freire, Catarina M. S. S. Neves, Isabel M. Marrucho, João A. P. Coutinho, and Ana M. Fernandes. "Hydrolysis of Tetrafluoroborate and Hexafluorophosphate Counter Ions in Imidazolium-Based Ionic Liquids". In: *The Journal of Physical Chemistry A* 114.11 (Mar. 2010), pp. 3744–3749. DOI: 10.1021/jp903292n.

[112] Kyung Moon Choi, Chung Yub Kim, and Keu Hong Kim. "Polymerization mechanism and physicochemical properties of electrochemically prepared polyindole tetrafluoroborate". en. In: *The Journal of Physical Chemistry* 96.9 (Apr. 1992), pp. 3782–3788. DOI: 10.1021/j100188a040.

[113] György Inzelt, Andrzej Lewenstam, and Fritz Scholz, eds. *Handbook of Reference Electrodes*. en. Berlin, Heidelberg: Springer Berlin Heidelberg, 2013. DOI: 10.1007/978-3-642-36188-3.

[114] Matthew D. Murbach, Brian Gerwe, Neal Dawson-Elli, and Lok-kun Tsui. "impedance.py: A Python package for electrochemical impedance analysis". In: *Journal of Open Source Software* 5.52 (2020), p. 2349. DOI: 10.21105/joss.02349.

[115] J Lindau, A. -S Jönsson, and A Bottino. "Flux reduction of ultrafiltration membranes with different cut-off due to adsorption of a low-molecular-weight hydrophobic solute-correlation between flux decline and pore size". en. In: *Journal of Membrane Science* 149.1 (Oct. 1998), pp. 11–20. DOI: 10.1016/S0376-7388(98)00161-6.

[116] Viktoria Lindstrand, Göran Sundström, and Ann-Sofi Jönsson. "Fouling of electrodialysis membranes by organic substances". en. In: *Desalination* 128.1 (Mar. 2000), pp. 91–102. DOI: 10.1016/S0011-9164(00)00026-6.

[117] Viktoria Lindstrand, Ann-Sofi Jönsson, and Göran Sundström. "Organic fouling of electrodialysis membranes with and without applied voltage". en. In: *Desalination* 130.1 (Sept. 2000), pp. 73–84. DOI: 10.1016/S0011-9164(00)00075-8.

[118] Menachem Elimelech and Subir Bhattacharjee. “A novel approach for modeling concentration polarization in cross¯ow membrane ®ltration based on the equivalence of osmotic pressure model and ®ltration theory”. en. In: *Journal of Membrane Science* (1998), p. 19.

[119] Subir Bhattacharjee and Glen M. Johnston. “A Model of Membrane Fouling by Salt Precipitation from Multicomponent Ionic Mixtures in Crossflow Nanofiltration”. In: *Environmental Engineering Science* 19.6 (Nov. 2002), pp. 399–412. DOI: 10.1089/109287502320963391.

[120] Bin Liu, Chun Wai Tang, Fu Kit Sheong, Guochen Jia, and Tianshou Zhao. “Artificial Bipolar Redox-Active Molecule for Symmetric Nonaqueous Redox Flow Batteries”. In: *ACS Sustainable Chemistry & Engineering* (Dec. 2021). DOI: 10.1021/acssuschemeng.1c07190.

[121] Eric M. V. Hoek and Menachem Elimelech. “Cake-Enhanced Concentration Polarization: A New Fouling Mechanism for Salt-Rejecting Membranes”. en. In: *Environmental Science & Technology* 37.24 (Dec. 2003), pp. 5581–5588. DOI: 10.1021/es0262636.

[122] William Allan Braff. “Membraneless hydrogen bromine laminar flow battery for large-scale energy storage”. PhD thesis. Massachusetts Institute of Technology, 2014.

[123] Marc-Antoni Goulet and Erik Kjeang. “Co-laminar flow cells for electrochemical energy conversion”. en. In: *Journal of Power Sources* 260 (Aug. 2014), pp. 186–196. DOI: 10.1016/j.jpowsour.2014.03.009.

[124] Ranga S. Jayashree, Daniela Egas, Jacob S. Spendelow, Dilip Natarajan, Larry J. Markoski, and Paul J. A. Kenis. “Air-Breathing Laminar Flow-Based Direct Methanol Fuel Cell with Alkaline Electrolyte”. en. In: *Electrochemical and Solid-State Letters* 9.5 (May 2006), A252–A256. DOI: 10.1149/1.2185836.

[125] Martin Z. Bazant William A. Braff and Cullen R. Buie. “Membrane-less hydrogen bromine laminar flow battery”. In: *Nature Communications* 4 (2014), p. 2346.

[126] WALLACE WARD. “Electrode Potential Measurements in Anhydrous Acetonitrile”. English. Ph.D. United States – Iowa: The University of Iowa, 1958.

[127] Siegfried Herzog and Rudolf Taube. “Neutralkomplexe des 2,2-Dipyridyls Teil I Darstellung und Eigenschaften”. de. In: *Zeitschrift für Chemie* 2.6-7 (1962), pp. 208–214. DOI: 10.1002/zfch.19620020608.

[128] Frank S. Hall and Warren L. Reynolds. “Preparation of an Iron(0) Complex with 2,2’-Bipyridine”. en. In: *Inorganic Chemistry* 5.5 (May 1966), pp. 931–932. DOI: 10.1021/ic50039a046.

[129] P. Singh. “Application of non-aqueous solvents to batteries”. en. In: *Journal of Power Sources* 11.1-2 (Jan. 1984), pp. 135–142. DOI: 10.1016/0378-7753(84)80079-8.

[130] Masayuki Morita, Yoshinori Tanaka, Keisuke Tanaka, Yoshiharu Matsuda, and Takeko Matsumura-Inoue. “Electrochemical Oxidation of Ruthenium and Iron Complexes at Rotating Disk Electrode in Acetonitrile Solution”. In: *Bulletin of the Chemical Society of Japan* 61.8 (Aug. 1988), pp. 2711–2714. DOI: 10.1246/bcsj.61.2711.

[131] Y. Matsuda, K. Tanaka, M. Okada, Y. Takasu, M. Morita, and T. Matsumura-Inoue. "A rechargeable redox battery utilizing ruthenium complexes with non-aqueous organic electrolyte". en. In: *Journal of Applied Electrochemistry* 18.6 (Nov. 1988), pp. 909–914. DOI: 10.1007/BF01016050.

[132] Junyoung Mun, Myung-Jin Lee, Joung-Won Park, Duk-Jin Oh, Doo-Yeon Lee, and Seok-Gwang Doo. "Non-Aqueous Redox Flow Batteries with Nickel and Iron Tris(2,2-bipyridine) Complex Electrolyte". en. In: *Electrochemical and Solid State Letters* 15.6 (Apr. 2012), A80. DOI: 10.1149/2.033206esl.

[133] Jarrod D. Milshtein, Sydney L. Fisher, Tanya M. Breault, Levi T. Thompson, and Fikile R. Brushett. "Feasibility of a Supporting-Salt-Free Nonaqueous Redox Flow Battery Utilizing Ionic Active Materials". en. In: *ChemSusChem* 10.9 (May 2017), pp. 2080–2088. DOI: 10.1002/cssc.201700028.

[134] Karl S. Hagen. "Iron(II) Triflate Salts as Convenient Substitutes for Perchlorate Salts: Crystal Structures of [Fe(H2O)6](CF3SO3)2 and Fe(MeCN)4(CF3SO3)2". In: *Inorganic Chemistry* 39.25 (Dec. 2000), pp. 5867–5869. DOI: 10.1021/ic000444w.

[135] Joung-Won Park, Myung-Jin Lee, Seung-Sik Hwang, Doo-yeon Lee, and Duk-Jin Oh. "REDOX FLOW BATTERY". en. US20120171541A1. July 2012.

[136] Diogo Moulin Cabral, Patrick C Howlett, and Douglas R MacFarlane. "Electrochemistry of the tris(2,2'-bipyridine) complex of iron(II) in ionic liquids and aprotic molecular solvents". en. In: *Electrochimica Acta* 220 (Dec. 2016), pp. 347–353. DOI: 10.1016/j.electacta.2016.10.126.

[137] Shuo Dong, Diogo Moulin Cabral, Jennifer M. Pringle, and Douglas R Macfarlane. "Exploring the electrochemical properties of mixed ligand Fe(II) complexes as redox couples". en. In: *Electrochimica Acta* 362 (Dec. 2020), p. 137109. DOI: 10.1016/j.electacta.2020.137109.

[138] Pablo J. Cabrera, Xingyi Yang, James A. Suttil, Rachel E. M. Brooner, Levi T. Thompson, and Melanie S. Sanford. "Evaluation of Tris-Bipyridine Chromium Complexes for Flow Battery Applications: Impact of Bipyridine Ligand Structure on Solubility and Electrochemistry". en. In: *Inorganic Chemistry* 54.21 (Nov. 2015), pp. 10214–10223. DOI: 10.1021/acs.inorgchem.5b01328.

[139] Carol Creutz. "Bipyridine Radical Ions". en. In: *Comments on Inorganic Chemistry* 1.5 (Apr. 1982), pp. 293–311. DOI: 10.1080/02603598208078100.

[140] Richard G Compton and Craig E Banks. *Understanding Voltammetry*. en. 3rd ed. WORLD SCIENTIFIC (EUROPE), Aug. 2018. DOI: 10.1142/q0155.

[141] T Saji and S Aoyagui. "Electrochemical evidence for aromatic dianion ligands of iron and ruthenium complexes". In: *Journal of Electroanalytical Chemistry and Interfacial Electrochemistry* 110.1-3 (1980), pp. 329–334.

[142] José Antônio do Nascimento Neto, Cameron Capeletti da Silva, Leandro Ribeiro, Géssica Adriana Vasconcelos, Boniek Gontijo Vaz, Vinicius Sousa Ferreira, Luiz Henrique Keng Queiroz Júnior, Lauro June Queiroz Maia, Ariel M. Sarotti, and Felipe T. Martins. "Probing the competition between acetate and 2,2-bipyridine ligands to bind to d-block group 12 metals". en. In: *New J. Chem.* 41.21 (2017), pp. 12843–12853. DOI: 10.1039/C7NJ02393F.

[143] Jarrod D. Milshtein, Aman Preet Kaur, Matthew D. Casselman, Jeffrey A. Kowalski, Subrahmanyam Modekrutti, Peter L. Zhang, N. Harsha Attanayake, Corrine F. Elliott, Sean R. Parkin, Chad Risko, Fikile R. Brushett, and Susan A. Odom. "High current density, long duration cycling of soluble organic active species for non-aqueous redox flow batteries". en. In: *Energy & Environmental Science* 9.11 (2016), pp. 3531–3543. DOI: 10.1039/C6EE02027E.

[144] Bin Fan and Xia Huang. "Characteristics of a Self-Forming Dynamic Membrane Coupled with a Bioreactor for Municipal Wastewater Treatment". In: *Environmental Science & Technology* 36.23 (Dec. 2002), pp. 5245–5251. DOI: 10.1021/es025789n.